Autonomous University of San Luis Potosí

Faculty of Science

Wireless Perception using Deep Learning for Vehicular and Human Detection

DISSERTATION FOR THE DEGREE OF

DOCTOR OF ENGINEERING SCIENCE

PRESENTS:

M.Sc. JORGE DANIEL CÁRDENAS AMAYA

ADVISORS:

Dr. Carlos Adrián Gutiérrez Díaz de León
Dr. Ruth Mariela Aguilar Ponce

San Luis Potosí, S. L. P., México, September 2023

Dedicatory

A mis padres Jorge Cárdenas Estrada y Genoveva Amaya Mendoza por sus consejos, sus valores, por la motivación constante que me ha permitido ser una persona de bien y por ser siempre un ejemplo de perseverancia y constancia. Todo esto es gracias a ustedes que me enseñaron el valor del trabajo y que aún en mis momentos más difíciles me ayudaron a seguir adelante. Su confianza en mí me ha dado la fortaleza para superar obstáculos y perseguir mis pasiones. Esta dedicatoria es un humilde homenaje a su dedicación y sacrificio. Todo lo que soy se los debo a ustedes por lo que siempre les estaré agradecido, los amo.

A mis hermanas Nallely Roxana y Saraly Nohemí por estar conmigo y apoyarme siempre a lo largo de todos estos años. El amor y cariño que nos tenemos como familia nos ha fortalecido para ser lo que nuestros padres siempre desearon y el apoyo que ustedes me dieron espero poder devolvérselos de igual manera. El amor de hermanos es el que nos permite hacer grandes cosas con nuestras vidas y por eso les estoy agradecido.

Finalmente a toda mi familia, profesores, amigos y compañeros quienes participaron directa o indirectamente en la elaboración de este trabajo. Nada de esto hubiese sido posible sin su apoyo ya que a su lado compartí buenos momentos y supere todo los malos. Ustedes fueron para mi una guía que me ayudó a alcanzar todas mis metas y que sin duda me alentaron a proponerme retos cada vez mayores. Por todo esto, les doy las gracias.

Acknowledgments

To the Faculty of Sciences of the Autonomous University of San Luis Potosí for being the site where I concluded all my professional studies and to CONACYT for the support received during this time.

To my advisors, Dr. Carlos Adrián Gutiérrez Díaz de León and Dr. Ruth Mariela Aguilar Ponce, for all the time invested and patience they gave me throughout the completion of this work. I am also grateful for the trust you have placed in me and the opportunity to collaborate on research and development projects that have allowed me to broaden my horizons and gain valuable experiences. All my admiration for you.

To my external synodal, Dr. Carolina del Valle Soto, for allowing me to collaborate with you during my stay at the Universidad Panamericana and for the care provided in carrying out this work. To my synodal Dr. Bersaín Alexander Reyes and Dr. Francisco Rubén Castillo Soria for all their comments and suggestions, I also appreciate the time they dedicated to evaluating this work.

To my friends Francisco Javier, Iván Israel, Raúl Iván, José, Raúl Machuca, Diomar, Emanuel, Ricardo, Óscar, José Mata, Dr. Ulises, Edoardo, Erik, Sandra, Laura, and to all the people who were present throughout of my life giving me his support and friendship at all times.

To Mariana for supporting me during these last years and giving me all her love and confidence. Thank you for proudly celebrating my successes, as well as giving me comfort and encouragement to keep going through difficult times. I love you.

It is very hard to thank all the people who were directly or indirectly involved. However, I apologize for any unintentional omissions.

Contents

List of Figures

List of Tables

List of acronyms

RS Radio Sensing

RF Radio-Frequency

AoA Angle of Arrival

LOS Line of Sight

JRSAC Joint RS and Communications

V2X Vehicle-to-Everything

WLAN Wireless Local Area Network

AP Access Points

DL Deep Learning

ML Machine Learning

AI Artificial Intelligence

FT Fourier Transform

STFT Short-Time Fourier transform

FFT Fast Fourier Transform

IF intermediate frequency

CW Continuous Waveform

ADL Activities of Daily Living

T_X Transmitter

R_X Receiver

HH Horizontal-to-Horizontal

VV Vertical-to-Vertical

RSSI Received Signal Strength Indicator

CSI Channel State Information

PCA Principal Component Analysis

ANN Artificial Neural Network

KNN K-nearest neighbors

QSVM Quadratic Support Vector Machine

NLOS non-LOS

PLF Polarization Loss Factor

SVD Singular Value Decomposition

SVM Support Vector Machine

WBAN Wireless Body Area Network

QoS Quality of Service

LSTM Long-Short-Term Memory Network

CNN Convolutional Neural Network

BoF Bag-of-Feature

SISO Simple Input Simple Output

OFDM Orthogonal Frequency Division Multiplexing

TP True Positive

TN True Negative

FN False Negative

FP False Positive

ROC Receiver-Operating Characteristic

AUC Area Under the ROC Curve

VCS Vehicular Communication Systems

DSRC Dedicated Short-Range Communications

C-V2X Cellular Vehicle-to-Everything

GPS Global Positioning System

TF Time-Frequency

RNN Recurrent Neural Networks

3GPP Third Generation Partnership Project

5G fifth-generation

CCE channel complex envelope

CDF	cumulative distribution function
CV2X	cellular-based V2X
DSRC	dedicated short-range communication
ETSI	European Telecommunications Standards Institute
FCC	Federal Communications Commission
IF	intermediate frequency
ITS	intelligent transportation system
LTE	long-term evolution
LTV	linear time-varying
MIMO	multiple-input multiple-output
NLOS	non-line-of-sight
PDF	probability distribution function
PDP	power delay profile
RBW	resolution bandwidth
SA	spectrum analyzer
SDR	software-defined radio
TF	time and frequency
TOA	time-of-arrival
UPS	uninterruptible power supply
V2I	vehicle-to-infrastructure
V2V	vehicle-to-vehicle
VBW	video bandwidth
VSA	vector spectrum analyzer
VNA	vector network analyzer

Abstract

In the wireless perception of events, Radio Sensing (RS) has been positioned as an alternative technology that does not have major limitations under several environmental conditions or lack of line of sight. However, there are techniques and approaches to the RS that have not yet been widely explored and that can improve its sensing capabilities for characterization and recognition applications. Furthermore, within the new paradigm of joint radio sensing and communications (JRSAC), it is a priority to find alternatives that facilitate the integration of these two technologies. In this dissertation, I present an RS platform based on the analysis of Doppler signatures of a radio-frequency continuous wave signal. Specifically, the platform was used for two relevant wireless perception applications: the detection of human falls and the detection of approaching vehicles. In fall detection, I present a systematic analysis of the influence of antenna orientation on RS systems and how it directly affects classification performance. For this, I compared the performance of two classification algorithms based on deep learning (DL): a long-short-term memory (LSTM) network and a convolutional neural network (CNN). Both models were tested using data collected from experiments with different antenna orientations and activities. The highest accuracy rates achieved were 92.10% for the implemented algorithms. This represents that the majority of events were correctly identified. The results obtained contribute to improving the design of the sensing platforms and increase the accuracy to identify fall events. On the other hand, the same platform was used for the detection of approaching vehicles in a vehicle-to-vehicle dispersion scenario. In this case, the feasibility of using an alternative sensing approach where a vehicle receives the signal transmitted by a second vehicle to characterize the event was verified. Combining this approach with the DL models, an accuracy of 98.60% detecting vehicles was achieved with the LSTM and 94.50% with the CNN. The high accuracy rates demonstrate the potential of Doppler signatures and DL algorithms in detecting oncoming vehicles.

Chapter 1

Introduction

Wireless perception refers to the technologies used for objects or people sensing present in a particular scenario without requiring physical sensors that have to be installed on each target. Wireless sensing has applications in indoor environments such as smart homes, hospitals, universities, or industry 4.0. In addition, this technology encompasses outdoor environments such as smart cities for vehicle detection or traffic monitoring. The traditional methods with which these wireless perception systems have been developed are those that collect information from the scenario through video images [1, 2], lasers [3], sonars [4], or sensors embedded in the environment [5]. However, most of these technologies are limited by environmental conditions, expensive implementation, privacy vulnerabilities, or the low line of sight (LOS) they have with the target. This has motivated the development of new wireless sensing technologies that mitigate these practical issues.

Radio sensing (RS) has emerged as a detection alternative that is based on the analysis of the propagation effects of radio frequency (RF) signals. In these systems, the RF signals transmitted in the environment are reflected, refracted, and diffracted when interfered with by the objects present. The registered changes are characterized to determine the unique patterns of each movement and thus identify the activity that caused them. The different paths that RF signals take from the moment they are interfered with until the receiver captures them are known as the multipath effect. This means that, in environments with low or no LOS due to objects that inhibit it, RS systems take advantage of the multipath effect to perform the sensing. This is an advantage over other methods such as those based on video sensors, lasers, or sonars where specific lighting conditions and a constant direct LOS to the target are required to maintain sensing. Furthermore, by not requiring the capture of images of the objective, the user's privacy is preserved. Finally, the RF signals used by RS systems can be transmitted through objects such as walls, so they can cover a greater range of environments without increasing the number of sensors, as is the case with systems environmental sensing [6].

Parallel to RS, wireless communication technologies have been developing significantly with limited interaction with each other. However, with the deployment of 5G networks and beyond, the integration of sensing and communication applications is a concept that has started to play a very important role [7]. This is known as Joint RS and Communications (JRSAC). In the new JRSAC paradigm, the cooperation and coexistence of both technologies are possible due to their commonalities in terms of signal processing, devices, and architecture [8,9]. Although there are sensing schemes that consider the transmission of two separate communication and RF signals in the same system, this represents a greater consumption of hardware resources and high-performance signal processing. Therefore, the JRSAC paradigm represents a more viable solution by reusing the hardware of communication devices and adapting them for sensing purposes.

Due to the characteristics of JRSAC systems, these have the potential to be implemented in all kinds of environments where at least there is already simple point-to-point communication between wireless devices, as shown in Figure 1.1. Some applications are focused on human monitoring or the interaction of smart devices with the environment, as is the case of the vehicle-to-everything (V2X) scenario. With the almost ubiquitous deployment of wireless local area networks (WLAN), the development of technologies, such as JRSAC systems, could represent the beginning of a large-scale sensor network. However, there are still gaps and limitations in the analysis of communication signals that can be used for RS. For example, the antenna orientation used for the transmission of RF signals can affect the sensing performance, but its influence has not been systematically analyzed. On the other hand, it is necessary to explore RS systems that simplify the extraction of information on the effects of signal propagation and that use the most advanced classification techniques. Furthermore, when it is required to increase the accuracy rate of the systems, information diversification is accomplished through the implementation of more hardware consuming more resources. Finally, another concern is to preserve continuous sensing without affecting communication performance, especially in scenarios where sensing interruption can compromise human life.

1.1 Motivation

The variety of applications that wireless perception has are extensive, especially in indoor environments for recognizing human behavior. Some of the applications range from human gesture recognition [10, 11] to healthcare [12, 13]. Most human behavior has been monitored by these systems to provide more comfortable and interactive living conditions. However, activity recognition is essential not only to assist in people's daily lives but also to record unusual behaviors caused by accidents or medical emergencies. These events can put people's lives or quality of life at risk if they are not detected

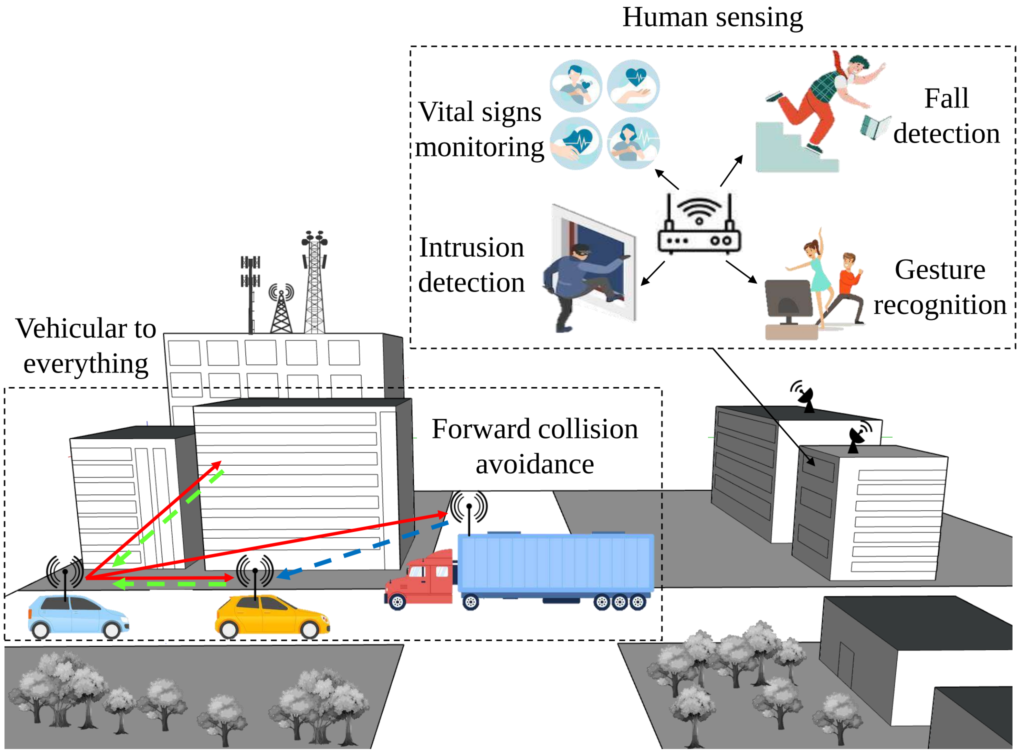

Figure 1.1: Overview of the applications of JRSAC systems in smart cities and smart homes.

promptly and have become a priority for detection systems.

Several schemes have been proposed based on the analysis of the propagation effects of WiFi RF signals. Some of these effects include changes in amplitude, phase, angle of arrival, or received power. To extract information on these effects, analysis techniques of the characteristics of the communication channel have been used, such as the Channel State Information [12] and the Received Signal Strength Indicator [14]. However, the hardware suitable for the extraction and digital processing of the CSI is limited to a few models of access points, such as those shown in [15] and [16]. This is because, to obtain these parameters, it is necessary to calculate the orthogonal frequency division multiplexing (OFDM) of the signal in offline processing, which is an exhaustive process. Furthermore, for an accurate calculation of the CSI, measurements have to be made with a high sampling rate, which can reduce the network performance [17]. On the other hand, RSSI is a complementary parameter to the link quality indicator (LQI) and provides a measure of signal power. Although the processing required to extract the RSSI information is less complex, the power is a parameter that can be attenuated by the lack of LOS with the target or by the interference of the signal with the objects. This can cause the extracted information to be complex to characterize by not being able to guarantee homogeneous measurements when the scenario has a change in its dynamics of static and moving objects [18]. Another limitation is that for the extraction of the CSI and the RSSI, the Access Points (AP) have to work in data transmission mode for the OFDM calculation, which cannot always be guaranteed [19]. Therefore, alternatives have been explored to simplify the analysis of WiFi signals for detection applications.

There is another propagation effect of RF signals that has been scarcely explored in RS JRSAC systems that is caused by the Doppler effect and is known as the Doppler signature [20, 21]. Doppler signatures are frequency dispersions that transmitted signals undergo when interfered by a moving body and that increase with more prominent speed. However, it is necessary to determine if the extraction of its information in a JRSAC system is less complex than with other techniques. A JRSAC system of this type can have practical issues in its implementation because the capture of the Doppler signatures has to be with a high definition that allows one to distinguish the changes caused by the different accelerations of the objects. This can be achieved by implementing a capture and analysis system that has a good trade-off between acquisition time and resolution. Furthermore, it has to be analyzed if the event detection performance is of high accuracy if Doppler signatures are used as the main feature in a classification system. Therefore, there is a whole field of research on the use of Doppler signatures for RS purposes.

On the other hand, most devices already deployed for indoor environments WiFi communications were not designed for sensing purposes. This means that it is necessary to carry out a study of the sensing capabilities of the systems that seek to integrate into the JRSAC paradigm. One of the concerns on this topic is the omnidirectional antennas used by most WiFi AP, whose radiation and polarization patterns can play an important role. The spatial positioning and orientation of the antennas have not been addressed in depth and represent a gap in the knowledge of the JRSAC. Therefore, it is necessary to carry out a systematic analysis of the influence that the antennas have on the RS.

The use of multiple antennas has also been a technique used to diversify the information gathered from RF signals. In this case, some of the limitations in the observation angle that the antennas have of the events that occur in an indoor environment and the scarce data that can be collected from the real world have been mitigated by implementing more hardware. However, this has caused RS systems to become more expensive or demand a higher consumption of computational resources. Therefore, it is necessary to explore alternatives in the diversification of the information gathered from the signals using a scheme that does not require increasing the number of antennas.

JRSAC systems have also been developed in outdoor environments, mainly in vehicular communication scenarios. Vehicle sensing has aimed to alert autonomous vehicles, or drivers, of other moving objects approaching their position to avoid a potential collision. Based on the precepts of RS, a vehicle with a communication system takes advantage of the variations in the transmitted signals for sensing tasks. In contrast to indoor environments, in this scenario, the conditions are changing every time the vehicles move from one point to another and it is necessary to consider other types of approaches. For example, in the centralized approach, each vehicle simultaneously performs sensing and communication independently. However, following current vehicular communication standards [22, 23], the only way not to significantly affect the operation of communication systems is to follow the Communication-Centric Design. This is not a trivial process and its implementation is a topic that is still in development. On the other hand, implementing an approach using a Joint Design is a subject-matter that has not been tested experimentally. This is known as a decentralized approach. In this approach, a vehicle that is receiving an RF signal transmitted by a second vehicle can take advantage of it for sensing applications. Therefore, it is of great interest to carry out an experimental demonstration to test the efficiency of this approach within JRSAC systems for vehicular applications.

The key to the operation of the JRSAC systems lies directly in how to optimize the use of the information collected through sensing approaches during an activity or event for its correct identification. As can be seen in Figure 1.2 with the sensing data captured by the JRSAC system, the recognition of classes or activities can be carried out through different classification techniques. Nowadays, Deep Learning (DL) is considered one of the hot topics in the area of data science due to its capability of learning from given data [24]. The DL technique is a subset of Machine Learning (ML) and Artificial Intelligence (AI) that relies on multi-layer artificial neural networks to represent data through abstractions and thus build computational models. Furthermore, DL is the core of AI and plays an important role in the process of finding meaning in data of a particular sensing problem due to its intelligent decision-making. On the other hand, distinct from ML, where the construction of analytical models is sought from a series of characteristics of the given signals, DL can automatically extract the features directly from the data. The discriminative deep architectures of the DL are commonly used for classification applications due to their great power to recognize patterns. Therefore, it is understandable to consider DL models as a fundamental part of the design and development of JRSAC systems for indoor and outdoor applications.

1.2 Problem statement

In this dissertation, I present an analysis and proof of concept of two RS systems based on the JRSAC paradigm: *Human Fall Detection* and *Vehicle Forward Collision Avoidance*. Human fall detection is a highly relevant application because falls cause health problems worldwide [25]. Furthermore,

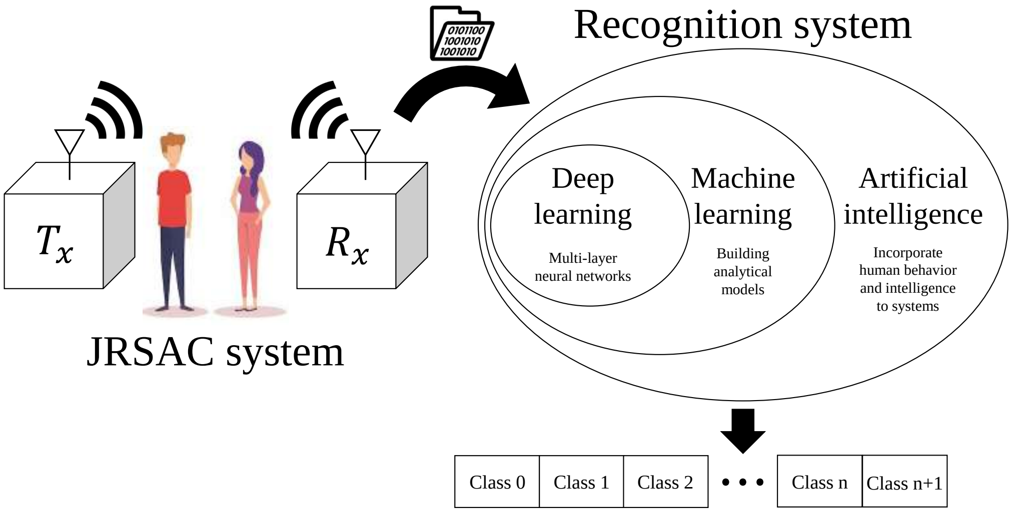

Figure 1.2: Event classification system using a JRSAC approach and a recognition model based on deep learning.

falls are one of the leading causes of unintentional death in the elderly. Therefore, it is a priority to present in this work a fall detection system that addresses some of the gaps in the design and development of these.

Specifically, I focus on the influence of antenna orientation on fall detection performance in a RS system. This analysis has not been performed before in a JRSAC-based system. It is necessary to determine if the information gathered in the RF signals is affected by the positioning of the antennas. Furthermore, the use and feasibility of Doppler signatures as the principal feature of the classification models considered in the detection system have not been proven. For this, it is necessary to demonstrate experimentally that, based on the analysis of Doppler signatures, a multi-class classification model can achieve high levels of accuracy. Finally, the information gathered for fall detection by RS systems has been diversified using multiple antennas to improve the quality of the extracted features. Therefore, it is necessary to use alternative techniques, such as signal diversity, to improve the quality of the extracted features without the need to increase the hardware.

On the other hand, the vehicle forward collision avoidance as well as fall detection is based on the same precepts of wireless perception. However, the building and design of these systems must consider changing scenarios where the transmitting and receiving devices are subjected to high speeds. Furthermore, beyond the centralized sensing approach, no other has been verified that matches satisfactorily with the JRSAC principles. Experimentally, the task of demonstrating the operation of a forward collision warning system from the decentralized approach is challenging. Nevertheless, there are multiple advantages over the centralized one, particularly in scenarios where one of the vehicles must remain in transmission mode, inhibiting its sensing capabilities. Therefore, approaches such as decentralized require probing their feasibility empirically.

1.3 General objective

The objective of this dissertation is to establish a methodology that allows the use of the Doppler signature as a main feature for the classification of events detected by analyzing the transmitted signal in a joint sensing and communication scheme using deep learning techniques. As a proof of concept, the developed methodology is applied in the detection of human falls as well as in a collision warning system where car approaching events are detected.

1.3.1 Specific objectives

- Develop an RS platform based on general-purpose measurement equipment that allows capturing event data in indoor and outdoor environments.
- Present a systematic analysis of the influence of antennas orientation on the classification performance of fall detection systems.
- Propose a methodology to characterize human fall events based on the Doppler signatures of RF signals and a multi-class deep learning framework for their classification.
- Use signal diversity techniques to diversify the information collected from Doppler signatures in a fall detection system to demonstrate that implementation of a more significant number of sensors is not required.
- Explore an alternative to automatic forward collision warning that follows the decentralized approach for vehicular applications.
- Fuse DL models and decentralized approach Continuous Waveform (CW) RS to evaluate their performance for detecting oncoming vehicles.

1.4 Hypothesis

Wireless perception, based on the analysis of the Doppler signatures registered in the RF signals, can be exploited to identify and classify several events of daily life such as human falls or potential forward vehicular collisions. Furthermore, the use of DL models in conjunction with alternative sensing methods has the potential to be integrated into the new JRSAC paradigm.

1.5 Contributions

This dissertation contributes to the state of the art of wireless perception systems in the empirical demonstration of various methodologies, concepts, and approaches that impact the accuracy and robustness of event detection applications. I demonstrated this by implementing a sensing platform that is not based on the use of specialized measurement equipment whose adaptation within the new JRSAC paradigm is more complex. The sensing platform is based on the analysis of Doppler signatures, whose principal features can be extracted using the hardware and processing resources of consumer electronics such as WiFi AP. Unlike other approaches such as CSI or RSSI, my proposal does not require off-line processing or working in data transmission mode since Doppler signatures can be extracted from the pilot carriers used for channel estimation. Therefore, RS system integration has low implications for the performance of wireless communication networks.

On the other hand, the hardware and processing used by the platform can be used for applications in indoor and outdoor environments where simple point-to-point communication is established. The platform uses probe signals transmitted in a range of frequencies within the IEEE 802.11 communication protocols. This allows for the different applications that are based on this standard to have interoperability in the communication network. My contributions in indoor environments focused on fall detection using the WiFi AP. For outdoor environments, efforts were focused on detecting approaching vehicles that have a communication system that can coexist with WiFi protocol.

Because the radiation pattern and polarization of the antennas are altered by changing their position, mismatch or misalignment effects can occur between the transmitter and receiver. These effects alter the quality of the signals received and can cause a loss of information that reduces the performance of a recognition system. In this dissertation, I theoretically and empirically analyzed the influence of the spatial orientation of the antennas of a RS system for detecting human falls. The analysis was carried out systematically to compare the changes in the Doppler signatures under different orientations. The quality of the information extracted from the different configurations was evaluated through intelligent classification systems. Furthermore, I presented a comparison between the performance of different DL-based classification architectures to provide different considerations that have to be taken into account for the design of detection applications. In fall detection, I evaluated the signal diversity techniques to increase the accuracy rate in these systems, which had not been reported in the literature. Finally, I introduced an empirical demonstration of the decentralized approach for sensing in vehicle scenarios that have not been shown before and that can be taken as a basis for the development of warning applications in autonomous vehicles. This demonstration also adopted the same precepts of the DL used for fall detection.

1.5.1 Performance evaluation metrics

The performance of the DL algorithms within the RS platform presented in this work for fall detection and oncoming vehicle detection applications was evaluated using specific critical tools in machine learning. These tools are known as performance evaluation metrics, which are a quantitative measure of how well a classification model fits. To compute them, I based myself on the information from the confusion matrix. The confusion matrix is a table that shows the number of correct and incorrect predictions. Furthermore, this tool provides a detailed view of how well the classes were classified, the model errors, and the areas where improvement is required. Therefore, my assessments are based on this analysis.

Specifically, specific metrics can be extracted from the confusion matrix that helps in the evaluation of the effectiveness of the classification model. In this work, the metrics of accuracy, precision, recall, and specificity were used. The accuracy was taken because it tells us how accurate the RS platform was in general terms. Precision focuses on determining how many of our predictions were correct. This metric helps us measure the performance of our platform in specific terms for each class of classified event. It is necessary to consider precision as falling events and oncoming vehicles will be evaluated with this metric. Recall measures the model's ability to identify the largest number of events relevant to the study. Finally, the specificity measures the number of false alarms that the classification model generated. The formulas and a summary of these performance metrics can be consulted in [20] and [26].

1.6 Structure of the dissertation

The rest of the dissertation has the following organization of the chapters.

Chapter 2 [18] contains a journal paper published in MDPI Sensors, 2021. In this work, I analyze the classification performance of a fall detection application concerning the antennas' orientation and the associated effects, such as polarization and radiation patterns. Furthermore, I implemented a wireless sensing platform based on transmitting an RF probe signal. I processed the received signal to extract the Doppler signatures generated by human movement during a fall and its principal features. In this research, I explored two types of antenna orientation: horizontal and vertical. Using the information from the Doppler signatures as input to a classification algorithm, I compared performance parameters to determine if there were significant changes between the two orientations. The results showed that some of the limitations of fall detection systems can be mitigated by considering the effects produced by the orientations of the antennas.

Chapter 3 [20] contains the second journal article published in the MDPI International Journal of Environmental Research and Public Health, 2023.

In this research, I proposed a methodology to monitor human activity in an indoor environment with a focus on fall detection. For this, I implemented an RS platform that uses a CW RF probe signal. In this way, it is not required that people have to wear any kind of sensors adapting to the concepts of wireless perception. The transmitted pilot carrier has similarities to the subcarriers transmitted by commercial WiFi systems, as a result, it can be easily integrated into the JRSAC paradigm. I innovated in this methodology by not depending on the CSI or RSSI to extract the necessary information for fall detection, I followed an alternative method based on Doppler signatures. Although Doppler signatures have been widely used in radar-based detection applications, they have rarely been studied for JRSAC systems. To evaluate the performance and accuracy of this methodology, I used and compared the results of two DL models. The results showed the feasibility of this methodology to detect human falls with a high accuracy rate.

In Chapter 4, the third journal article is presented. This work was submitted for possible publication in the IEEE Consumer Electronics Magazine, 2023. My objective with this work was to present a scheme for fall detection based on analyzing the Doppler signatures in WiFi RF signals using a frequency diversity technique to diversify the collected information. I intend to demonstrate that the precision in fall detection can be increased without the need to use more sensors or antennas that diversify the information of the observed events. I use a frequency diversity technique on a series of pilot subcarriers that can be transmitted in a single communication frame. Furthermore, for the characterization of the Doppler signatures that are registered in each of the subcarriers, I implemented a classification model based on DL. The evaluation of my results showed that the accuracy rate of an RS system based on Doppler signatures is increased concerning the results obtained in the scheme using a single pilot carrier.

Chapter 5 contains the fourth journal article that was submitted for possible publication in IEEE Intelligent Transportation Systems Magazine, 2023. In this work, I explored an alternative of RS for the detection of oncoming vehicles based on the decentralized approach. I used a CW transmitted by a second vehicle as a probe signal to detect and classify the variations corresponding to a vehicle that could provoke a possible collision. I contributed to the experimental demonstration of this proposal which had not been performed before. I determined the feasibility of this approach by fusing the sensing platform with two DL-based classification algorithms. The results of these algorithms showed that a high accuracy rate can be obtained, capable of preventing drivers from a possible forward collision. Furthermore, I compute the response time that a driver has to maneuver using this platform, demonstrating that it is enough to make the system a feasible alternative.

Finally, in Chapter 6 the conclusions of this dissertation and future work are presented.

1.7 Additional works

During my Ph.D., two more papers were published in which I collaborated. Furthermore, these papers are directly related to the central topic of wireless perception. Therefore, these publications had important contributions and are briefly discussed below.

The work in [27] is a conference paper published in 2020 and presented at the IEEE Latin American Communications Conference (LATINCOM) proceedings and is shown in Appendix A. In this paper, I present a systematic analysis of the effects of antenna orientation within fall detection systems. Furthermore, I detail the changes that occur when changing the orientation of the antennas in terms of the radiation pattern and polarization. I show how the power received by the antennas decreases or increases depending on the orientation as well as the features that can be extracted from the signals. Therefore, I give an approach to the readers of the importance of having a correct configuration of the fall detection platforms so as not to affect the classification algorithms in the posterior stages.

The work in [28] corresponds to a journal article published in IEEE Access in 2022 and is shown in Appendix B. In this article, the implementation of a sensing platform for narrowband frequency-dispersive vehicle-to-vehicle channels was described. The results of the work demonstrated that the platform was able to characterize and identify the relevant road safety scenario Doppler signatures. One of the events could be characterized was the vehicles approaching from the opposite direction that had the potential to cause a collision. Finally, the empirical statistics of the instantaneous mean Doppler shifts and the Doppler spread for three different propagation scenarios were analyzed.

Chapter 2

Theoretical framework

In this dissertation, I will guide the research by presenting the concepts, techniques, and approaches that will provide a solid understanding of wireless perception. The present theoretical framework focuses on people and vehicle sensing in indoor and outdoor environments, respectively, via the JRSAC paradigm. These applications share characteristics in their hardware and signal processing components that are used for specific recognition of certain events [9]. Therefore, I designed a methodology to delve into three fundamental stages: the RS of movements, pre-processing of the signals, and pattern recognition for classification.

An overview of the methodology used is shown in Figure 2.1. Regardless of the scenario where the wireless perception platform is implemented, monitoring of human or vehicle activities will be carried out using RS techniques. With this platform, the information gathered in the RF signals will be collected through a transmitter module (T_x) and a receiver module (R_x) to form a system with characteristics similar to those of the JRSAC. The collected data set will go through a pre-processing stage to reduce some of the practical issues during the transmission and reception of signals. Finally, I relied on the design of DL models for the data characterization and classification according to the specific application.

2.1 Doppler effect observed in the RS of movement objects

Doppler analysis was originally used in laser radar systems to measure changes in amplitude, frequency, phase, or polarization of signals when they were reflected by objects. In these systems, the phase of the signal is sensitive to the variations caused when the signal is returned by an object. Furthermore, the maximum Doppler frequency is determined by

$$max\{f_D\} = \frac{2}{\lambda} D_v f_v, \tag{2.1}$$

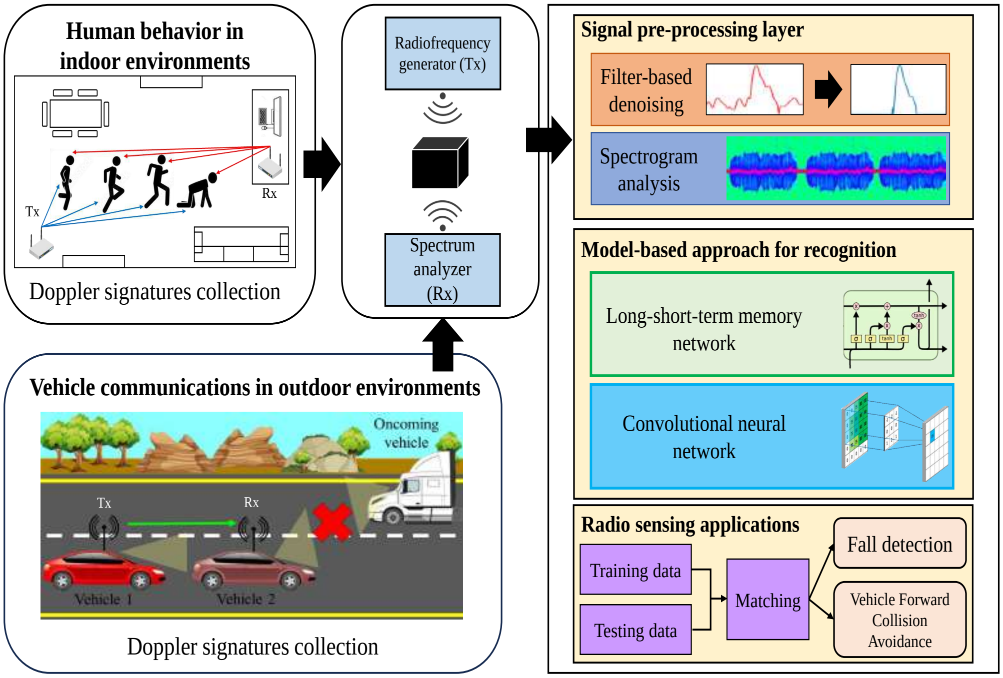

Figure 2.1: Principal RS applications and the overview of the implemented methodology.

where f_v is the frequency dispersion, D_v is the amplitude of that dispersion and λ is the wavelength. As a result of this equality, if the frequency of the wave is high, a phase change occurs even when f_v and D_v are very low. Therefore, Doppler shifts can be easily detected.

These principles can be applied in RS systems, where the Doppler effect affects the frequency band of an RF signal. In these systems, Doppler shifts are known as Doppler signatures because it is a term commonly used to refer to the appearance of a particular pattern. The Doppler signatures generated by the reflection of the signal with a moving object can be characterized and classified to form a detection system. For this, a non-stationary analysis of the signals can be used. For example, for a real value signal $s(t)$, it is associated with a complex value $z(t)$ and is defined by

$$z(t) = s(t) + jH\{s(t)\} = a(t)exp[\varphi(t)], \tag{2.2}$$

where H is the Hilbert transform of the signal given by

$$H\{s(t)\} = \frac{1}{\pi}\int_{-\infty}^{\infty}\frac{s(\tau)}{t-\tau}d\tau, \tag{2.3}$$

$z(t)$ is the analytical signal associated with $s(t)$, $a(t)$ is the amplitude of the function, and $\varphi(t)$ is the phase function. The instantaneous frequency of the signal z(t) can be calculated using the Fourier transform resulting in

$$f(t) = \frac{1}{2\pi}\frac{d}{dt}\varphi(t), \tag{2.4}$$

it is the derivative time of the uniquely defined phase function $\varphi(t)$. This allows us to describe the instantaneous frequency of the signal and analyze its behavior. However, when the spectral composition of the signal varies in time, conventional Fourier Transform (FT) methods cannot provide a time-dependent spectral description. Therefore, I have chosen to use other methods that provide a better representation of the Doppler signatures.

Spectrogram is a method that has been widely used to analyze non-stationary and time-varying RF signals. Furthermore, the spectrogram generates a graphical representation of the spectral changes over time of the RF signal. To calculate the spectrogram, it is required to use the Short-Time Fourier transform (STFT) of the signal, such that

$$Spectrogram(t, f) = |STFT(t, f)|^2, \tag{2.5}$$

where the STFT calculates the Fourier transform in a short time window and is represented by the squared magnitude. Because the window size can vary, the resolution of the spectrogram will be compromised between the trade-off between sampling time and frequency span. Furthermore, the spectrogram is less affected by cross-product interference, unlike other transformations, such as the Wigner-Ville distribution [29].

2.2 Spectrum analysis

The platform design is adapted for the transmission and reception of RF signals through the use of general-purpose measurement equipment. Considerations in selecting this equipment were being able to transmit a CW RF probe signal and capture the Doppler signatures produced by the motion. Furthermore, the collection of signals must allow the calculation of spectrograms for subsequent analysis. In this case, we select a radio frequency generator for the RF module capable of transmitting in the range of IEEE 802.11 g, n, communication protocols that cover up to 2.5 GHz. This is because these protocols constitute one of the most common technologies available, and by considering a multi-carrier scheme, they allow different problems to be addressed.

On the other hand, a spectrum analyzer was used to receive the signals since these instruments are frequently used to perform radio communications measurements. Furthermore, spectrum analyzers can provide values of average noise, frequency range, and power, among others. To perform these tasks, the frequency spectrum of an input signal must be calculated in the time domain. As has already been explained, conventional TF methods can provide a spectral description of the signals but, in practice, require using optimized algorithms to reduce the number of operations. A spectrum analyzer uses the Fast Fourier Transform (FFT) in its configuration which is shown in Figure 2.2. This is because, with this operation, no phase or magnitude information is lost, allowing complex spectra to be analyzed. To

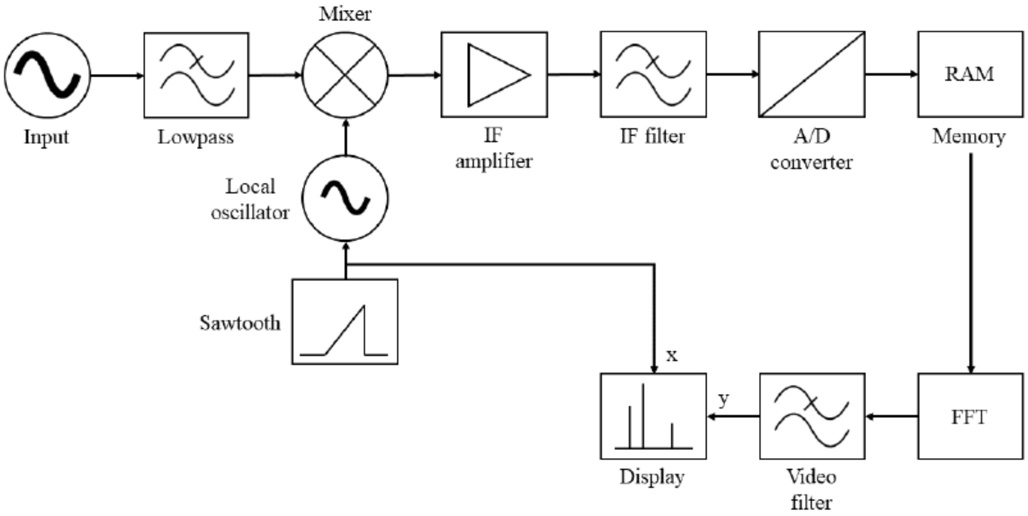

Figure 2.2: Block diagram of a spectrum analyzer and its configuration.

calculate the FFT, the analog signal passes through an A/D converter, and the values are saved in memory. These values are used to calculate the new signal in the frequency domain, and it is subsequently displayed.

Due to bandwidth limitations of A/D converters, analyzers can only perform low-frequency measurements. This is a drawback for RS platforms seeking to integrate into wireless communication systems that operate in high-frequency ranges. To mitigate this problem the signal has to be decomposed into its individual components through the heterodyne receiver principle. The heterodyne receiver converts the input signal into an intermediate frequency (IF) with the help of a mixer and a local oscillator. If the oscillator is adjustable, a constant IF can be obtained [30]. Subsequently, the signal is amplified and filtered by two additional blocks. The filter bandwidth used will determine the bandwidth resolution of the analyzer. However, to minimize IF power and local oscillator re-radiation at the RF input a low pass filter is needed at the beginning.

Once the internal workings of this measuring instrument are known, some of the configurations can be analyzed to avoid measurement errors caused by the use of digital or analog filters. The sweep time, for example, is limited by the operating time of the IF filters and the video filtering. The minimum sweep time is given by

$$T_{sweep} = k \cdot \frac{\Delta f}{B_{IF}^2}, \tag{2.6}$$

where f is the span, B is the bandwidth resolution and k is a proportionality factor that depends on the type of filter. Notably, there is a linear relationship between bandwidth resolution and sweep time. Reducing the bandwidth will result in a longer sweep time. Therefore, this configuration will be decisive in the design of the RS platform because events such as falls require a low sweep time.

Finally, another characteristic that must be considered by spectrum analyzers to improve their performance is inherent noise. Inherent noise is the thermal noise generated by the analyzer, and the sensitivity with which it can operate depends on its reduction. The total noise factor can be reduced with the use of attenuators at the input and the total noise factor will depend on it. Therefore, it is important to set the gain of this component to ensure that noise does not affect the analysis of the signals.

2.3 Doppler signature sampling

The platform experiments for collecting data containing Doppler Signature information were carried out following two different methodologies. In the fall detection application, a selection of participants was carried out using purposive sampling. I focused on middle-aged individuals in good physical condition. Furthermore, I aimed to have diversity among the participants that would guarantee the representativeness of the results. The experimental protocol and the informed consent letter used for the experiments are presented in Appendix C. Finally, the vehicle detection application protocol only requires one car trip and constant signal sampling. Details of this protocol are found in Chapter 6.

2.4 Pre-processing

The pre-processing of the signals acquired during the experimental protocol of the RS platform for the wireless perception of events is necessary to condition and improve the quality of the information gathered in the Doppler signatures. At this stage, several techniques and operations can be applied to address particular signal aspects to eliminate or improve its components. This depends on whether a contribution from them is required. In this work, we focus on applying filtering based on thresholding certain signal levels to eliminate the contributions of inherent noise. For this process, Equation 2.1 was used to calculate the maximum Doppler of each activity or event recorded by the platform and determine the threshold that eliminates most of the noise without affecting the Doppler signatures. Details about this process are shown in Chapter 5. Furthermore, a segmentation stage was applied where the signal information was divided into segments containing only the events of interest. This stage depends on the application but was carried out using video recording and positioning equipment to have a time stamp and know the samples where the events were recorded. Finally, through a manual process, outliers caused by measurement equipment errors that are not representative of the signal were removed.

2.5 Pattern recognition

In the last part of the methodology, Artificial Neural Network (ANN) was used as the central component of data processing to extract the principal patterns and develop an intelligent system that can recognize them. In this way, for the main applications of RS, an event detection or warning system is obtained. A set of data is entered into these networks for training. This means that the network will learn from the data gathered. The data is learned automatically as it propagates through the network, passing through different layers where operations are applied to extract or preserve its most relevant features. In the next stage, the difference between the output produced and the input is calculated to evaluate the network performance. This error is taken to provide feedback to the network, where it is decreased using optimization algorithms. The entire process becomes iterative until the network manages to retain or learn the data with a given minimum error. The learning has a hierarchical representation of the principal patterns that originated with the data, so predominant values extraction is obtained automatically. Finally, the network is tested using a new data set to validate its performance. To ensure that the system's accuracy is high, neural networks require large data sets. Therefore, the applications presented in this work seek to gather and provide an adequate database for this type of algorithms. Details and considerations in the implementation of these models are presented in the next sections.

Chapter 3

Influence of the Antenna Orientation on WiFi-Based Fall Detection Systems

The growing elderly population living independently demands remote systems for health monitoring. Falls are considered recurring fatal events and therefore have become a global health problem. Fall detection systems based on WiFi radio frequency signals still have limitations due to the difficulty of differentiating the features of a fall from other similar activities. Additionally, the antenna orientation has not been taking into account as an influencing factor of classification performance. Therefore, we present in this chapter an analysis of the classification performance in relation to the antenna orientation and the effects related to polarization and radiation pattern. Furthermore, the implementation of a device-free fall detection platform to collect empirical data on falls is shown. The platform measures the Doppler spectrum of a probe signal to extract the Doppler signatures generated by human movement and whose features can be used to identify falling events. The system explores two antenna polarization: horizontal and vertical. The accuracy reached by horizontal polarization is 92% with a false negative rate of 8%. Vertical polarization achieved 50% accuracy and false negatives rate.

3.1 Introduction

Improvement on quality of life has resulted in an increment on life expectancy. In 2019, the population over 65 years had a 3% growth compared to 1990. Projected population expansion indicates that elderly people will represent 16% of the world population by 2050 [31]. Much of this sector of society tend to live independently. For this reason, it is necessary to pro-

---

This chapter forms part of the paper titled "Influence of the Antenna Orientation on WiFi-Based Fall Detection Systems" published in *MDPI, Sensors*. The authors gave their consent to use their work as an integral part of this dissertation.

vide systems for remote healthcare and monitoring. Several systems have been developed for this purpose using well-established sensing techniques, such as acoustic sensors, video cameras, vibration sensors, and wearable devices [4, 5, 32–34]. However, an innovative technique has emerged in the last years: device-free monitoring based on radio-frequency (RF) signals. An RF signal shows fluctuations at the receiver due to absorption and reflections by moving persons wondering in the proximities of the transmitting and receiving antennas [35, 36]. These fluctuations can be characterized to identify Activities of Daily Living (ADL) or to detect important sporadic events, such as the presence of burglars or the occurrence of accidents. RF monitoring systems are noninvasive because users do not need to carry a sensor and they also preserve user privacy since no image is recorded.

According to the World Health Organization, 37.3 million elderly people require medical attention each year for injuries caused by falls [25]. In contrast to ADL, like walking, running, or going up and downstairs, falls are rare or transient events. This implies that the detection of these events should be approached from a different perspective, seeking to provide prompt medical attention when a fall occurs.

In device-free monitoring, the presence of WiFi access points (AP) in indoor environments has been used to collect and classify RF signals [37, 38]. Despite recent advances in the design of WiFi-based fall detection systems, most of the work has focused on developing algorithms for feature extraction and classification. Previous research has not addressed the impact of some important physical layer factors on the system's sensing capabilities, such as the variations of the antenna response with spatial orientation. These variations stem from the angular dependence of the antenna's radiation pattern, and also from the polarization mismatch between the Transmitter (T_X) and the Receiver (R_X) due to channel depolarization effects [39]. To the best of the authors knowledge, a detailed investigation of the impact of the radiation pattern's anisotropy and antenna polarization mismatch on the performance of WiFi-based fall detection systems has not been conducted so far. However, in [40], Wang *et. al* analyzed the influence of antenna height on the system's performance, and they concluded that the detection rate improves by raising the antenna height. In [21], a fall detection system was presented taking into consideration the polarization of the received signal. Nonetheless, the system was developed using Doppler radars, and the results presented there cannot be extrapolated directly to WiFi-based systems. A preliminary analysis of the effects of antenna orientation in the performance of fall detection system built around the Doppler signatures of WiFi signals was presented in [27]. There, it was empirically demonstrated that fall detection platforms are highly sensitive to antenna orientation. However, the analysis presented in [27] needs to be revisited by considering a complete implementation of feature extraction and classification algorithms to determine the accuracy of the system.

This chapter presents a systematic analysis of the effects of the antenna orientation in a fall detection system based on the Doppler signatures of WiFi signals. The results of this work are intended to help researchers to determine the best antenna orientation, and to promote the design multi-polarized antennas that improve the system's sensing capabilities without increasing the number of sensors (antennas) or the classification algorithms' complexity. To assess these effects, an experimental fall detection platform is presented that replicates the operating conditions of a system based on the transmission of WiFi-signals. This experimental platform allows to compute the Doppler signatures of the transmitted signal so that the features of the signal's variations in presence of human movements can be identified and classified. A series of experiments were conducted to gather empirical data about the Doppler signatures produced by falls from a three-step ladder. The experiments comprised two different antenna orientation configurations: Horizontal-to-Horizontal (HH) and Vertical-to-Vertical (VV). The detection accuracy obtained for the HH configuration amounts to a 92% with a false negative rate of 8%. The VV configuration produced a 50% accuracy and a 50% false negatives rate. The obtained results provide evidence of the importance of considering the effects of antenna orientation for the design of WiFi-based fall detection systems.

The remainder of the chapter has the following organization. Section 3.2 provides a review of related work. Section 3.3 details the mains components of a WiFi-based fall detection system. The mathematical model of the probe signal is presented in Section 3.4. In Section 3.5 the implementation of our experimental platform is described. Section 3.6 addresses the feature extraction and event classification algorithms. The results obtained are presented in Section 3.7. In Section 3.8 the results are discussed. Finally, the conclusions are given in Section 3.9.

3.2 Related work

There are different sensing techniques that can be used to design and develop fall detection systems. Table 3.1 shows an overview of some of the most common techniques and their characteristics. Vision-based systems comprise principally digital image processing [32]. The optimization of this processing can be affected by the resolution of the images that are collected by the video recording equipment. This implies that the use of high resolution equipment is necessary, which can be expensive. Furthermore, the feature extraction process is essential for vision-based fall detection systems. First, a simple model of a human body needs to be obtained, encompassing only head, torso and legs. However, partial occlusion of a user affects the construction of such model. Additionally, camera projection artifacts must be considered to avoid a misdetection. Then a description of movement of this human body model is used for analysis. Feature analysis can be static

Table 3.1: Approaches to fall detection systems

Technique	Article & Year	Characteristics
Vision-Based	J. Zhang [32](2020) K.I. Withanage [44] (2016)	Needs to have a direct line of sight with the target, privacy concerns.
Wearable-Based	J. Hauth [33] (2021) N. Zurbuchen [43] (2021) O. Kerdjidj [45](2020)	The device has to be wear by the user at all times.
Environment-Based	C. Liu [5] (2019) J. Mun [4] (2015)	Require specialized and expensive implementation.
Radio Frequency-Based	Y. Wang [40] (2017) M. Huang [37] (2019) W. Wang [38](2017)	Provides data without the need to wear a device, it can be adapted to existing hardware.

or dynamic. In the static analysis, a morphological model of the behavior of the fall is made [41]. In the case of dynamic analysis, the movement change determines the presence of abnormal events in the general movements. This analysis allows to identify the speed and direction of movement of the human body. In this way, the trajectories can be used to detect the behavior of a fall. Occlusions in the target's vision also make this process difficult, making necessary to implement complex classification algorithms. Therefore, vision-based systems present drawbacks such as highly complex analysis algorithms, which require high performance computer system and a line of sight (LOS) to user compromising their privacy.

Wearable devices use accelerometers, gyroscopes, magnetometers and tilt sensors embedded in general-purpose devices that can be carried by people. These sensors operate at different frequencies, which can vary the sampling rate of the system. For this reason, it is necessary to determine the rate at which the falling event can be registered and select the sensor that best suits these conditions. However, the placement of the sensor on the human body directly affects the detection performance of the system [33, 42, 43]. Furthermore, wearable sensors can produce discomfort for users that are not used to wear such devices.

On the other hand, environment-based systems use sensors embedded in the indoor surroundings. These sensors can be acoustic, where the transmission of sound waves is affected by changes in trajectory caused by obstacles in the environment [4]. In this way, changes in the trajectory are recorded and characterized to determine if a fall occurred. However, due to the nature of sound waves, the transmission can be degraded by the multi-path effect. Therefore, monitoring more than one indoor environment requires the implementation of a large number of sensors. The measurement of floor vibration signals through sensors such as accelerometers or piezoelectrics is another alternative for environment-based systems. Sensors mounted on the floor structure collect the variations in vibration induced by the movement of the human body to classify them. However, environment-based systems tend to be expensive due to their exhaustive implementation and the large number of sensors employed.

An alternative to all these approaches are systems based on radio frequency signals. Some proposals for the design of fall detection systems are based on Doppler radars to measure and analyze changes in signals caused by human movement. [21]. However, the cost and complexity of such specialized equipment make the deployment of these monitoring systems an expensive solution. Other proposals capitalize on the ubiquity of wireless local area networks [38,46,47]. The idea underlying these fall detection systems is to employ the signals transmitted by commercial WiFi AP as probe signals to scan the environment and detect anomalies in the received power that could be produced by a fall event. The attributes of the received signal that can be considered for anomaly detection are the Received Signal Strength Indicator (RSSI) [36], the Channel State Information (CSI) [37,40], and the Doppler spectral signatures [14].

A RF monitoring system based on the RSSI of WiFi signals was presented in [36]. This system analyzes the received signal to identify irregularities in the RSSI that could be produced by human movement. A limitation of this approach is that the system's performance is sensible to changes in the environment's characteristics. A fall detection system that considers the CSI of WiFi signals, and which is referred to as WiFall, was presented in [40]. In its simplest form (WiFall-one link), the system is composed of a single transmitting antenna and a single receiving antenna. The results presented in [40] show that WiFall-one link is capable of detecting falls, but with a rather high false alarm rate 16%. This problem is caused by the limited angle of observation of the single antenna configuration [48]. To reduce the false alarm rate, the authors proposed an enhanced version (WiFall-two links) that incorporates a second receiving antenna as a means to reduce ambiguities due to the angle of observation. A similar system, referred to as Fall Sense, was presented in [37]. The CSI is also considered in that paper as the detection parameter, but a third receiving antenna was incorporated to increase detection accuracy and further reduce the percentage of false alarms. Nevertheless, increasing the number of antennas adds complexity to the overall detection system. A proof-of-concept of a device-free fall detection system based on the Doppler signatures of WiFi signals was presented in [14]. The results obtained in that paper suggest that such spectral signatures

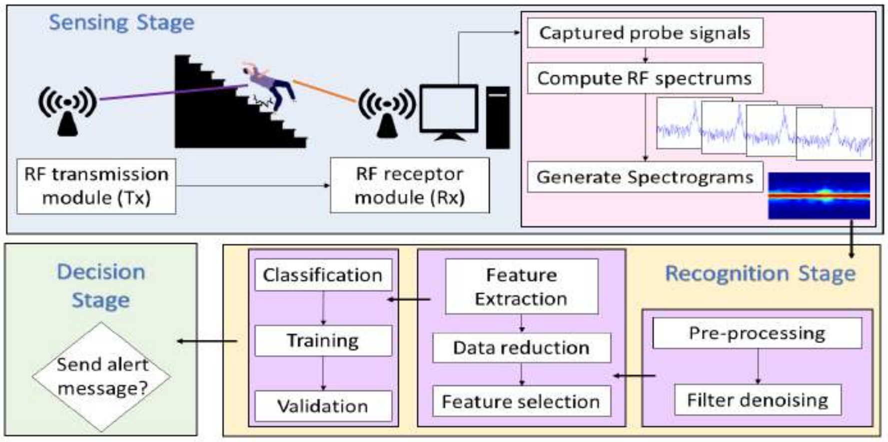

Figure 3.1: General diagram of a fall detection system based on RF signals.

allow differentiation between activities and falling events.

3.3 General structure of a WiFi-based fall detection system

Fall detection by RF monitoring comprises three phases: sensing, recognition, and decision. Figure 3.1 shows a block diagram of these three stages for a system based on the Doppler signatures of WiFi signals. In the sensing phase, a probe signal is radiated by the transmitting antenna. This signal is not intended to carry data, it is simply a means to interact—by the mechanism of electromagnetic wave reflection—with the objects in the vicinity of the receiving antenna. If the probe signal impinges on a moving body, e.g., a falling person, then the reflected signal will suffer an apparent frequency shift due to the Doppler effect [14]. This frequency shift depends on the speed and acceleration of the moving/falling body and it therefore produces a spectral (Doppler) signature whose features can be used to detect a fall event. The Doppler signature of the received probe signal can be computed, e.g., by following the spectrogram concept [49]. Spectrograms provide information about the spectral density of a signal within a short observation time interval. In fall detection, the signals are time-varying and non-stationary. Therefore, spectrograms are excellent tools to analyze such signals.

Figure 3.2 shows an example of an empirical spectrogram of a CW probe signal during a fall event. This figure shows static scenarios within the first 4.5 seconds and the last 3 seconds where no human movement is observed. The power density of the received signal is therefore concentrated in the origin. On the other hand, a fall occurs during a time interval spanning 4.5 to 7 seconds. The acceleration of the falling body produces a frequency drift of received power. Such a frequency drift can be analyzed to identify characteristic patterns of fall events. The example shown in Figure 3.2 con-

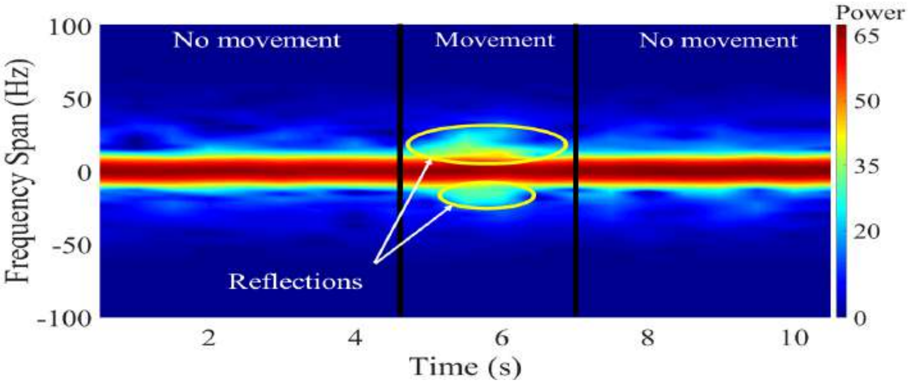

Figure 3.2: Spectrogram during a falling event.

siders motion of a single body. This scenario is relevant for fall detection of elderly people living independently, as these individuals have no one around and therefore rely on an automatic wireless monitoring system to get assistance in case of a fall. The single-person scenario shown in Fig. 3.2 may not be relevant for ADL applications, in which several persons, each producing a different Doppler signature, could be around the receiving antenna. For these latter applications, the goal of the system is to isolate and identify the activities realized by each person.

Classification stage is performed after acquiring a spectrogram. In this stage, the signals are classified based on the information extracted from their features. The feature extraction is based on finding the dataset that allows quantitatively differentiating if the signals correspond to a falling event or other activity. A dimensionality-reduction technique widely used for feature extraction is Principal Component Analysis (PCA). Spectrograms are high-dimensional data that can be further explored into a lower dimensional space that retains most of the information. Therefore, PCA is applied to the acquired spectrogram. The extracted principal components can be used by classification algorithms as features to recognize falling events. However, the number of techniques and approaches that can be used for data analysis at this stage is very extensive. The feature selection in RF-WiFi signals and the techniques used for the training phases must be balanced to the needs of the detection system. In [46], Di Domenico *et. al.* explore different training approaches for motion sensing platforms based on RF signals and Doppler spectrum. Furthermore, they show that it is necessary to establish the necessary trade-offs in terms of performance, time-consuming, complexity, and the number of features in these applications. A fall detection platform implemented in [50] shows the performance of different classification algorithms using six features extracted of the instantaneous Doppler frequency of a RF signal. Detection accuracy was increased by implementing different classification algorithms such as ANN, K-nearest neighbors (KNN), Quadratic Support Vector Machine (QSVM), or ensemble bagged tree. Fall detection systems have been proposed that implement novel classification algorithms, e.g., adversarial data argumentation [51], recurrent neural networks [52], among others, which positively impact accuracy rates. However, this area has been under intensive research, while the sensing has been vaguely explored. This is in spite of the fact that the quality of the signal features are directly related to the sensing capabilities of the platform.

Finally, the decision stage comprises decision algorithms aimed at issuing alerts when falls occur. This stage processes the data in real-time to determine when a fall is detected. In this way, the user will receive medical attention as soon as possible. The emergency alert is part of the final system process and therefore represents a device-level implementation. Therefore, the decision stage is outside the scope of this work and remains as future work.

3.4 Signal model

The influence of the antenna orientation on the sensing and feature extraction stages of a WiFi-based fall detection system is analyzed in this chapter by considering the transmission of a CW probe signal in an indoor environment. This signal could be one of the pilot signals defined within the WiFi physical protocol data unit [53], or a specific purpose signal transmitted by the AP when there is not an active communication session with a user node. We assume the probe signal is received by another WiFi device that acts as the system's sensor and which is located in a different position than the AP. Also, we assume the received probe signal comprises a LOS component and a non-line-of-sight (NLOS) component due to single reflections from K static objects (e.g., walls and furniture) and a moving object (falling person), as illustrated by Fig. 3.3.

The received signal can be written in the complex base-band equivalent as:

$$y(t) \;=\; n_\sigma(t) + y_{\mathrm{los}} + y_{\mathrm{nlos}}^{(s)} + y_{\mathrm{nlos}}^{(m)}(t). \tag{3.1}$$

In this equation, $n_\sigma(t) \in \mathbb{C}$ is additive white Gaussian noise with power density σ^2; $\mathbb{C}$ stands for the set of complex-valued numbers. The LOS component of $y(t)$ is a time-invariant signal modeled by

$$y_{\mathrm{los}} = E\left(\vec{u}_0\right) V\left(-\vec{u}_0\right) X_{\mathrm{los}} g_0 e^{-j\theta_0}, \tag{3.2}$$

where $E\left(\vec{u}_0\right) \in \mathbb{R}_0^+$ is the transmitting antenna's radiation pattern evaluated in the direction of the unit vector, $\vec{u}_0$, that points toward the R_X from the position of the T_X; the symbol $\mathbb{R}_0^+$ stands for the set of non-negative real numbers. In turn, $V\left(-\vec{u}_0\right) \in \mathbb{R}_0^+$ is the vector effective length of the receiving antenna evaluated in the direction from the R_X to the T_X. Signal attenuation due to path loss is modeled by $g_0 \in \mathbb{R}_0^+$, and $\theta_0 = 2\pi D_0/\lambda$ is a phase shift that depends on the signal's wavelength λ and the distance D_0 between the T_X and the R_X. The absolute value of $X_{\mathrm{los}} \in \mathbb{C}$

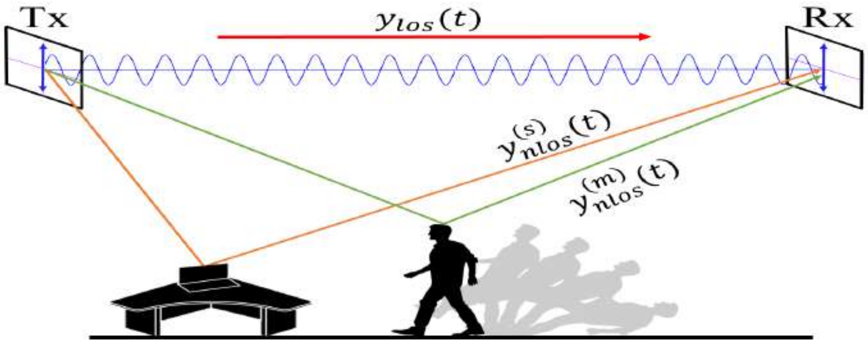

Figure 3.3: Schematic propagation of an RF signal in a real test scenario.

is the Polarization Loss Factor (PLF), which characterizes the polarization mismatch between the transmitting and receiving antennas. We note that $|X_{\text{los}}| \leq 1$, and $|X_{\text{los}}| = 1$ if the antennas are co-polarized, whereas $|X_{\text{los}}| = 0$ if they are cross-polarized.

The NLOS component of $y(t)$ due to single reflections from the K static objects is characterized as a time-invariant signal

$$y^{(s)}_{\text{nlos}} = \sum_{k=1}^{K} E\left(\vec{u}^{(s)}_k\right) V\left(\vec{v}^{(s)}_k\right) X^{(s,k)}_{\text{nlos}} g^{(s)}_k e^{-j\left[\phi^{(s)}_k + \theta^{(s)}_k\right]} \tag{3.3}$$

where $\vec{u}^{(s)}_k$ and $\vec{v}^{(s)}_k$ are unit vectors that point toward the kth static reflector from the position of the T_X and the R_X, respectively. The scalar variable $g^{(s)}_k \in \mathbb{R}^+_0$ accounts for the combined effects of path loss and signal attenuation due to the interaction with the k_{th} reflector. Likewise, $\phi^{(s)}_k$ accounts for the phase shift that results from such an interaction. The phasor $g^{(s)}_k \exp\{j\phi^{(s)}_k\}$ can therefore be described as a weighted version (weighted by the path loss) of the reflection coefficient that characterizes the reflection of electromagnetic waves from lossy dielectrics [54]. The phase $\theta^{(s)}_k$ is given as $\theta^{(s)}_k = 2\pi D^{(s)}_k/\lambda$, where $D^{(s)}_k$ is the total length of the path among the T_X, the k_{th} reflector, and the R_X. The absolute value of $X^{(s,k)}_{\text{nlos}} \in \mathbb{C}$ also characterizes the PLF between T_X and R_X. However, the difference between $X^{(s,k)}_{\text{nlos}}$ and X_{los} is that the former incorporates effects of depolarization caused by the reflection from the k_{th} static object [39]. In turn, the NLOS component of $y(t)$ stemming from the reflection off the falling person is modeled by

$$y^{(m)}_{\text{nlos}}(t) = E\left(\vec{u}^{(m)}\right) V\left(\vec{v}^{(m)}\right) X^{(m)}_{\text{nlos}} g^{(m)} e^{-j\left[\phi^{(m)} + \theta^{(m)} - \varphi^{(m)}(t)\right]}. \tag{3.4}$$

Except for the time-varying phase $\varphi^{(m)}(t)$, the variables on the right-hand side of (3.4) are defined as their counterparts with the (s) superscript but considering the moving (falling) person as the reflector. The phase $\varphi^{(m)}(t)$ is given as $\varphi^{(m)}(t) = 2\pi \int_0^t \nu_d(x)\,\mathrm{d}x$, where $\nu_d(t)$ is the total time-varying Doppler frequency shift caused by the velocity of the person during a fall [55]. Assuming that the person falls with a constant acceleration, $\varphi^{(m)}(t)$ can be characterized as a quadratic phase $\varphi^{(m)}(t) = 2\pi\left[\nu_s t + \widehat{\nu}_a t^2/2\right]$, where ν_s is the Doppler frequency shift produced by the initial speed of the falling person, and $\widehat{\nu}_a$ is a frequency drift having units of hertz per second. Thereby, the total Doppler shift can be written as

$$\nu_d(t) = \nu_s + \nu_a(t) \tag{3.5}$$

with $\nu_a(t) = \widehat{\nu}_a t$ accounting for the component of the time-varying Doppler shift due to acceleration [56].

The spectrogram of the received probe signal is given as

$$S(t';\nu) = |Y(t';\nu)|^2 \tag{3.6}$$

where t' is an arbitrary observation time, $Y(t';\nu) = \int_{-\infty}^{\infty} y(t)w(t-t')e^{-j2\pi\nu t}\,\mathrm{d}t$ is the STFT of $y(t)$, and $w(t)$ is an even and positive windowing function of unit energy [49]. For the signal defined by (3.1)–(3.4), we have

$$Y(t';\nu) = N_\sigma(t';\nu) + A^{(s)}W(t';\nu) + Y_{\text{nlos}}^{(m)}(t';\nu) \tag{3.7}$$

where $W(t';\nu)$, $Y_{\text{nlos}}^{(m)}(t';\nu)$, and $N_\sigma(t';\nu)$ are the STFT of $w(t)$, $y_{\text{nlos}}^{(m)}(t)$, and the noise signal, respectively, whereas $A^{(s)} = y_{\text{los}} + y_{\text{nlos}}^{(s)}$. In this chapter, we consider a Gaussian window function $w(t) = (\sqrt{\pi}\sigma_s)^{-1/2}e^{-t^2/(2\sigma_s^2)}$, with spread parameter σ_s [56], due to its good frequency resolution and reduced spectral leakage. This window results in wide peaks and low sidelobes, which allows a better frequency resolution. The Gaussian window is widely used in applications of time-frequency analysis. For a Gaussian pulse window, it can be shown (see [56]) that

$$W(t';\nu) = \sqrt{2\sigma_s\sqrt{\pi}}e^{2\pi[j\nu t' - \pi(\sigma_s\nu)^2]} \tag{3.8}$$

$$Y_{\text{nlos}}^{(m)}(t';\nu) = \frac{A^{(m)}}{\pi^{\frac{3}{4}}\sigma_y\sqrt{2\sigma_s}}e^{-\frac{[\nu-\nu_d(t')]^2}{2\sigma_y^2}}e^{j[\varphi^{(m)}(t')-\varphi^{(m)}-\theta^{(m)}-2\pi\nu t']} \tag{3.9}$$

where $\sigma_y^2 = [1 - j2\pi\sigma_s^2\widehat{\nu}_a]/(2\pi\sigma_s)^2$, and

$$A^{(m)} = E\left(\vec{u}^{(m)}\right)V\left(\vec{v}^{(m)}\right)X_{\text{nlos}}^{(m)}g^{(m)}. \tag{3.10}$$

By substituting (3.7) into (3.6), we find

$$S(t';\nu) = S_n(t';\nu) + |A^{(s)}|^2 S_w(t';\nu) + S_y^{(m)}(t';\nu) + C(t';\nu). \tag{3.11}$$

In this equation,

$$S_n(t';\nu) = |N_\sigma(t';\nu)|^2 \tag{3.12}$$

$$S_w(t';\nu) = |W(t';\nu)|^2 = 2\sigma_s\sqrt{\pi}e^{-[2\pi\sigma_s\nu]^2} \tag{3.13}$$

$$S_y^{(m)}(t';\nu) = \left|Y_{\text{nlos}}^{(m)}(t';\nu)\right|^2 = \frac{\left|A^{(m)}\right|^2}{\sqrt{2\pi}\gamma}e^{-\frac{[\nu-\nu_d(t')]^2}{2\gamma^2}} \tag{3.14}$$

for $\gamma^2 = [1+(2\pi\sigma_s^2\widehat{\nu}_a)^2]/[2(2\pi\sigma_s)^2]$, and $C(t';\upsilon)$ is a complex-valued function accounting for the cross-products among $N_\sigma(t';\nu)$, $A^{(s)}W(t';\nu)$, $Y_{\text{nlos}}^{(m)}(t';\nu)$ and their corresponding complex conjugates [56].

Equation (3.11) shows that the spectrogram of the received signal is composed of two Gaussian pulses plus a noise term and artifacts resulting from the cross-products of the $C(t';\upsilon)$ function. The Gaussian pulse $|A^{(s)}|^2S_w(t';\nu)$ is an origin-centered pulse whose amplitude is scaled by the combination of $y_{\text{los}}(t)$ and $y_{\text{nlos}}^{(s)}(t)$. The second Gaussian pulse, $S_y^{(m)}(t';\nu)$ is centered at the Doppler frequency $\nu_d(t)$ and it amplitude depends on the antenna characteristics involved in the definition of $A^{(m)}$ (see(3.10)).

The combined spectrogram of the LOS and static-reflectors NLOS signals does not contribute meaningful information for fall detection. This is because such signals remain unchanged during a fall event as they are not influenced by the Doppler effect. All the relevant information about the direction and speed of the fall is embedded in the spectrogram of the moving-reflector NLOS signal through the dependence of $S_y^{(m)}(t';\nu)$ on the time-varying Doppler shift $\nu_a(t)$. However, a proper detection of $S_y^{(m)}(t';\nu)$ depends not only on a good match between the polarization of both antennas, but also on a good alignment between the radiation pattern of the transmitting antenna and the vector effective length of the receiving antenna. The alignment of the radiation pattern and polarization during transmission depends on the antenna orientation, as illustrated in Fig. 3.4. By changing the position of T_X and R_X, mismatches occur and change the effective radiation zones where the signal arrives [57, 58]. Misalignments that decrease $S_y^{(m)}(t';\nu)$ strength can be mitigated by varying the orientation of the antennas and analyzing changes in the spectrogram of the received signal.

From an analytical perspective, it is a complex process to analytically compute the optimal antenna placement and orientation that maximize the value of $\left|A^{(m)}\right|^2$ for any given indoor environment. However, the performance of the antennas can be measured and compared empirically to find the optimum zone of radiation with which it will be possible to receive high-quality features for fall detection. We implemented a fall detection platform that considers two experimental scenarios: one with a VV antenna orientation (Fig. 3.4a) and another with an HH orientation (Fig. 3.4b). The platform will capture a series of falls and then extract the Doppler signatures from the RF signals to classify them through machine learning-based classification algorithms. Misalignment effects will be measured by comparing the precision values obtained to determine the orientation that best mitigates variability in polarization and radiation patterns. Therefore, using a systematic analysis of Doppler signatures captured by a radio-sensing system, the influence of antennas on performance in classification algorithms for a fall detection application can be determined.

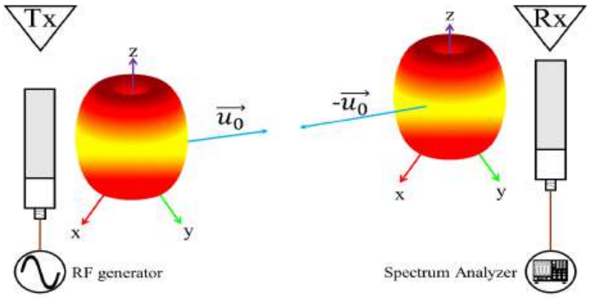

(a) Radiation pattern of antennas in VV scenario

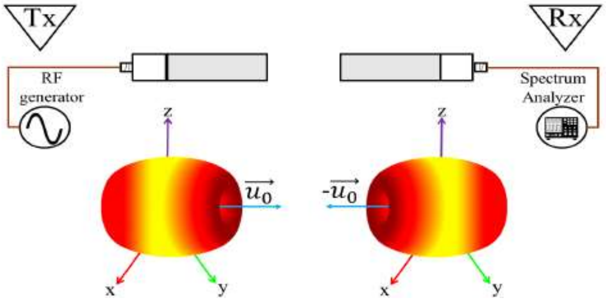

(b) Radiation pattern of antennas in HH scenario

Figure 3.4: Radiation pattern and polarization of antennas configuration in both scenarios.

3.5 System design

3.5.1 Hardware setup

The T_X module of our experimental platform comprises a RF signal generator connected to a monopole antenna whose radiation pattern is omnidirectional in any plane perpendicular to the monopole's axis. The R_X module is composed of a monopole antenna connected to a spectrum analyzer. Both antennas were empirically characterized to ensure a proper coupling with the measurement equipment. The results are shown in Table 3.2. The antennas obtained the best parameters at a frequency of 2.42 GHz using an RG-58 coaxial cable. This operating frequency is within the range of commercial WiFi systems (IEEE 802.11b). Our T_X module emits a pure tone with this frequency. In our case, we used a Keysight N9310A RF generator with a transmission power of 20 dBm. The transmitted probe signal is received by a second monopole antenna with the same characteristics. Afterward, the signal is processed by a spectrum analyzer. We use a spectrum analyzer FieldFox N9912A. This analyzer allows us to capture a series of snapshots of the signal. Thereby, it is possible to record the Doppler signatures of the probe signal caused by fall event. The configuration used for the capture is shown in Table 3.3. This configuration allows a balanced trade-off between

Table 3.2: Transmission parameters in antennas

Parameter	**Value**
Frequency	2.42 GHz
Return losses	32.4 dB
Impedance	$50 + j0.70$
Voltage standing wave ratio	1.042

Table 3.3: Spectrum analyzer configuration

Parameter	**Value**
Central frequency	2.42 GHz
Sweep time	271ms
Sample points	1001
Frequency span	1 kHz

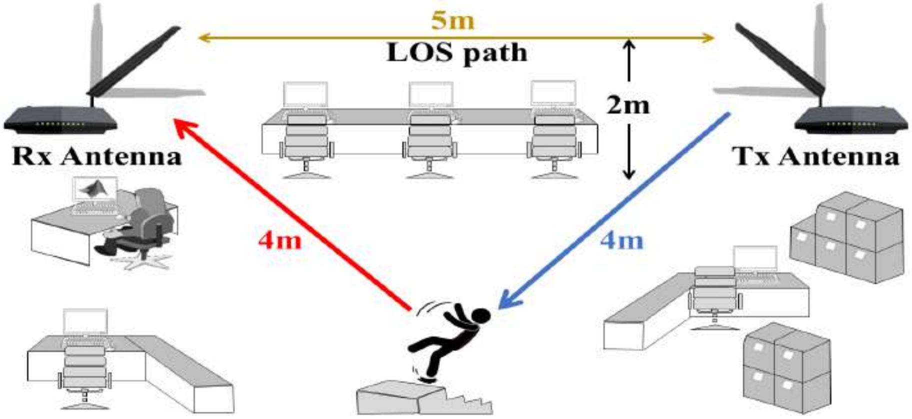

Figure 3.5: Schematic of the test scenario.

the signal resolution and the sweep time.

The experiments with falls were conducted in an indoor environment with fixed furniture. Figure 3.5 shows the position of the transmitting and receiving modules during the experiments. The T_X module is installed in the top right corner and the receiver in the top left corner of the room 5m apart from each other. Both antennas are located at a height of 2m and maintain an unobstructed LOS. This indoor environment corresponds to an office room and has a ladder in the center of the room where falling are performed (Figure 3.6). The platform allows changing the antenna orientation according to test VV and HH settings.

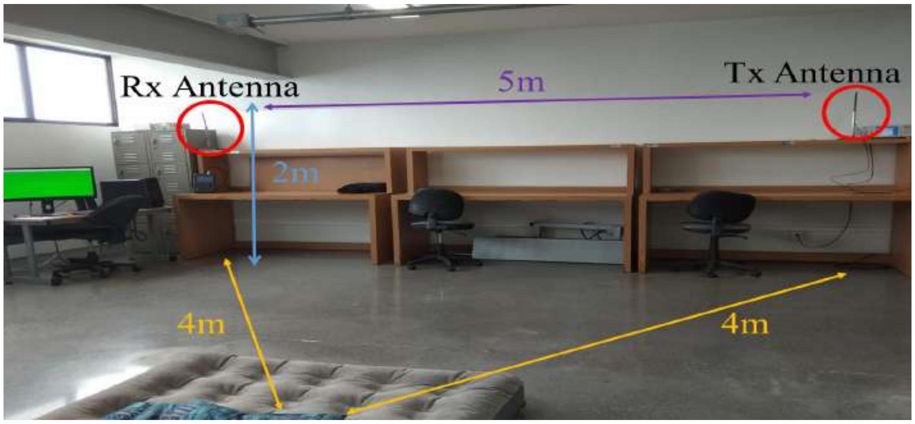

Figure 3.6: Indoor environment for the test experimentation.

3.5.2 Experimental protocol

Our experimentation protocol seeks to replicate the typical conditions of indoor environments that independent elderly people face daily. To that end, it is necessary to consider that the experiments have to be developed in the presence of a single individual in the environment and surroundings. Furthermore, the inclusion of other activities in the protocol such as running, jumping, or waving the arms is beyond the scope of the work. On the other hand, the activities carried out daily such as crouching down, raising the arms, or getting dressed do not produce an acceleration of the body compared to that of a fall. Then, our protocol focuses on the static and falling state of the participants.

The empirical data were collected for a group of people falling from different heights in the VV and HH scenario. The participant's age range from 23 to 48 years old. This represents a general demographic sample of middle-aged people who have different physical conditions to perform falling movements or other activities relevant to the study. The selection was conducted based on a random process to reduce biases and increase the possibility that the results are applied to the general population of older adults. Furthermore, the group was composed of 3 males and 3 females. All participants were previously evaluated to validate that they were in good physical condition. The physical characteristics of each individual are shown in Table 3.4. Due to the nature of experimentation, selecting subjects with a higher age range can put their health at risk.

The experimentation protocol consists of a sequence of falls from a height of 59cm. This height was determined according to the specifications of the third step of a ladder. In total, the participants performed a sequence of 10 falls for each scenario.

The experiment starts with a participant placed immobile on the ladder. A visual and audible signal was configured to notify the participants of the beginning and end of the experimentation. At the beginning of the test, the

Table 3.4: Physical characteristics of test subjects

Subject	Age	Gender	Height (m)	Weight (Kg)	Fall tests
1	23	Female	1.61	60	20
2	24	Male	1.75	77	20
3	27	Male	1.72	73	20
4	38	Female	1.55	58	20
5	47	Female	1.55	65	20
6	48	Male	1.71	85	20

participants remain in a static state until a signal is sent indicating the start of the falling movement. The participants were also instructed to remain immobile once the falling movement has been performed. The notifications of preparation, start, and end of the tests were triggered automatically by the system to avoid the presence of more people near the test scenario. Finally, the signal notifies the end of the test to the subjects. The information collected in the experiments is used in the subsequent stages of the system to identify falling events.

3.6 Feature extraction and classification algorithm

The classification stage in our platform involves the pre-processing, extraction, and classification of the acquired signals. In our system, the analyzed features must contain the information necessary to determine the antenna orientation with which the misalignment in fall detection can be mitigated. Our signal model indicates that frequency drifts recorded in the spectrograms as Doppler signatures can be used as detection features. The considered scenarios as described earlier consist of VV and HH antenna disposition. Each set is composed of 60 spectrograms computed during the experiments. In order to extract the most relevant information from the spectrograms, a dimensionality-reduction technique is employed.

We selected a PCA algorithm given its wide application in data analysis problems [59–65]. PCA is based on Singular Value Decomposition (SVD) technique, which generates a low-dimensional approximation of a high-dimensional data set in terms of its dominant patterns [66]. The PCA algorithm reduces the dimension of the features and orders them hierarchically. Furthermore, this technique can be used to represent the correlation of high-dimensional data through a coordinate system.

The first step in the PCA algorithm is to pre-process the calculated spectrograms. The pre-processing in our system first reduces the frequency span of the spectrums to a total bandwidth of 200 Hz. This is because the frequency drifts of the probe signal do not exceed this bandwidth value. Moreover, denoising filter is applied to smooth the additive white Gaussian noise in the CW probe signal. The data set is then organized as a matrix $X \in \mathbb{C}^{m \times n}$, where the rows $x_k \in \mathbb{C}^n$ contain the instantaneous spectrum of the probe signal received during the k_{th} time instant, $k \in \{1, 2, \ldots, m\}$. The next step is to compute the mean of the n elements of row x_k and subtract it from X. This standardization process results in the mean-subtracted data B:

$$B = X - \overline{X}, \tag{3.15}$$

where $\overline{X}$ is the matrix of means. Then, it is necessary to compute the covariance matrix of the rows of B given by

$$C = B^T B. \tag{3.16}$$

The covariance matrix describes all relationships between pairs of variables in the data set [67]. In the next step, the eigen-decomposition of the covariance matrix C is computed and resulting:

$$CV = VD, \tag{3.17}$$

in this case V and D correspond to the eigenvectors and eigenvalues respectively. Finally, the matrix of principal components is defined as,

$$T = BV, \tag{3.18}$$

where T corresponds to the matrix of principal components. Furthermore, matrix B can be defined by the SVD as:

$$B = U \Sigma V^T \tag{3.19}$$

in this case, $U \in \mathbb{C}^{n \times n}$ and $V \in \mathbb{C}^{m \times m}$ are unit matrices with orthonormal columns, and $\Sigma \in \mathbb{R}^{n \times m}$ is a matrix with non-negative real integers on the diagonal and zeros off the diagonal [66]. Therefore, when substituting (3.19) in (3.18), the matrix of principal components would be given by:

$$T = U \Sigma \tag{3.20}$$

The numerical values resulting from the PCA for the spectrogram data set can be represented in a coordinate system. These values have a logarithmic distribution as in Fig 3.7. In our case, the resulting number of principal components r corresponds to the 200 frequency values measured for each instantaneous Doppler spectrum captured during the experiments. And σ_r are the elements on the diagonal of Σ that correspond to the singular values. Furthermore, the first three singular values σ_r resulting from the PCA are taken as the features of the received signal. This is because the greater variance of the values of our Doppler spectrums is concentrated in these components. The first principal component in our case generally comprises

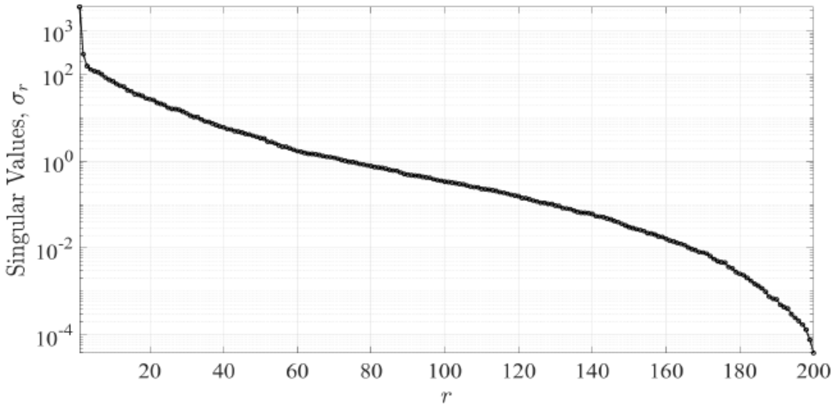

Figure 3.7: Principal components of the frequency of a Doppler spectrum.

99%, the second 0.01%, and the third 0.002%. The rest of the components can be omitted because they will represent a minimum of information loss. Therefore, our system uses these components as the particular features of each spectrum that will be used in the classification process.

The resulting low-dimension feature space is used for classification. At this stage, it is necessary to classify the extracted features into different classes. Support Vector Machine (SVM) was employed due to its balance between complexity and accuracy. Additionally, SVM has demonstrated its effectiveness in fall detection [40, 50]. SVM classification allow us to measure the impact of the antenna orientation in the accuracy of the overall fall detection system. SVM algorithms are learning machines that analyze and recognize patterns in a set of features. This supervised learning model allows us to distinguish between different classes. Then, we can determine if the data introduced belongs to a falling event or a static scenario. The implementation was developed using Matlab™ classification learner toolbox. Based on the feature space generated by PCA, we selected a quadratic kernel to maximize the geometric margin of our training data.

We evaluate the performance of the classification using a re-sampling process known as the cross-validation method. The data introduced is randomly shuffled and divided into K folds. The first fold is used for validation and the rest for training. When the process concludes, the performance score is preserved and the model is discarded. Afterward, the process is iterated K times. Therefore, the model can be trained $K-1$ times. Finally, the performance scores are averaged to reduce randomness and obtain an accurate result. Performance scores were obtained using 5 folds of the cross-validation method.

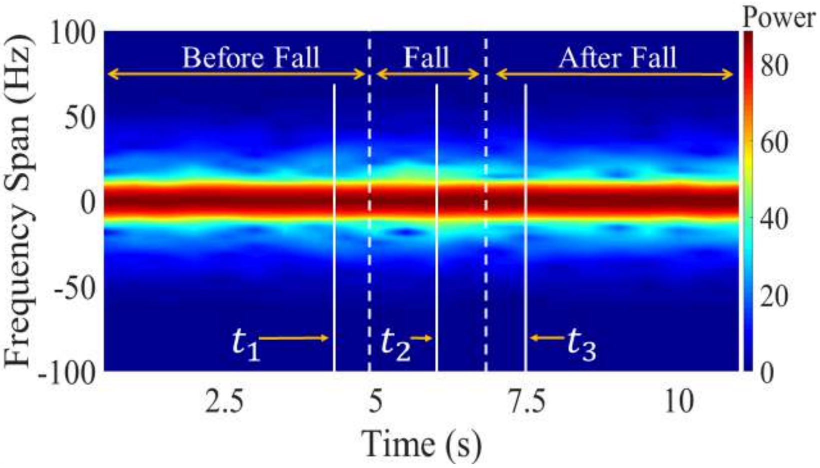

(a) Doppler signatures captured in the spectrograms.

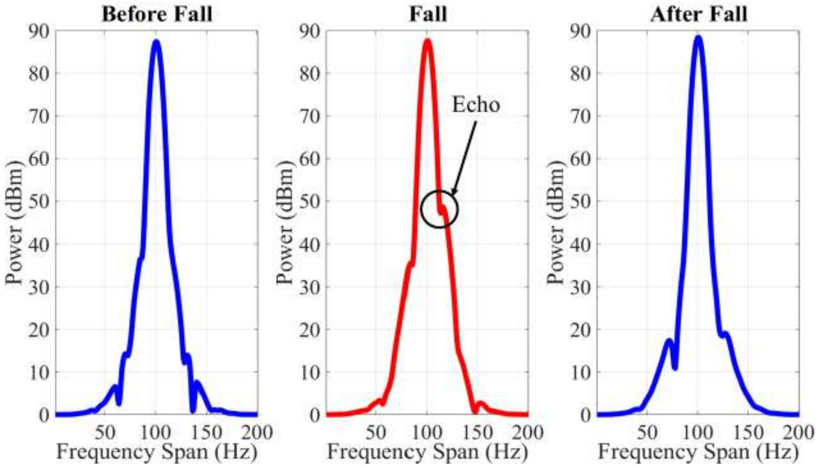

(b) Sequence of Doppler spectrums at a time $t_1 = 4.5s$ (before fall), $t_2 = 6s$ (fall) and $t_3 = 7.5s$ (after fall).

Figure 3.8: Experimental results using VV scenario setup: a) spectrogram, b) sequence of spectrums.

3.7 Results

The results obtained by our platform allow us to assess the impact of antenna polarization in the fall detection rate. The pre-processing results of the signals are shown in Figure 3.8 and Figure 3.9. Frequency dispersions caused by human movement during tests are notable in each spectrogram time sample.

Figure 3.8 shows the results obtained during one of the experiments with the VV orientation of the antennas. The falling event was recorded at 6 seconds of the experimentation. In the spectrogram of Figure 3.8a, the Doppler signatures captured during falling, cause a dispersion of the probe signal.

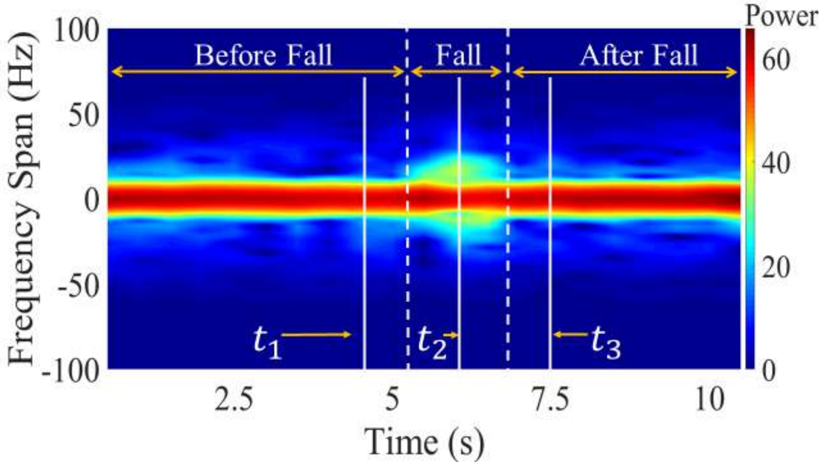

(a) Doppler signatures captured in the spectrograms.

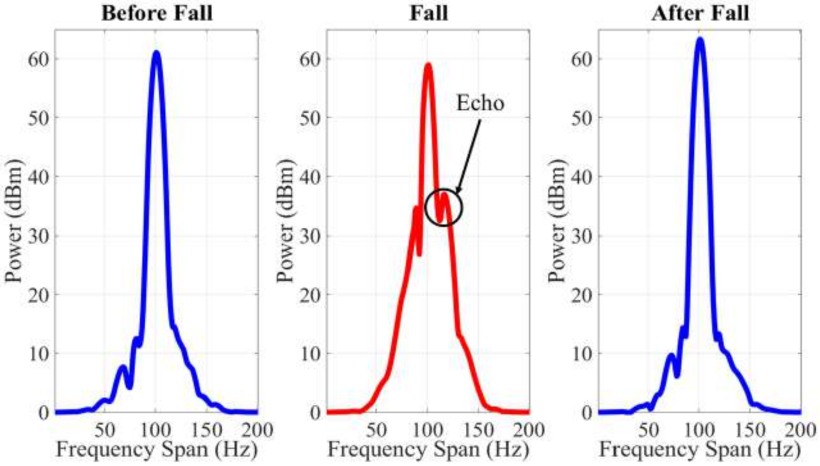

(b) Sequence of Doppler spectrums at a time $t_1 = 4.5s$ (before fall), $t_2 = 6s$ (fall) and $t_3 = 7.5s$ (after fall).

Figure 3.9: Experimental results using HH scenario setup: a) spectrogram, b) sequence of spectrums.

On the other hand, Figure 3.8b shows a sequence of the frequency spectrums before, during, and after the falling event. In the spectrum corresponding to falling event, echoes can be observed in the carrier signal. These echoes correspond to the fluctuations produced by the Doppler effect. Therefore, the configuration with the antennas in VV orientation achieved to capture the dispersions caused by the falls and the data could be used in the recognition stage.

The dataset of the HH scenario was processed following the same methodology. The results of the experiments with this orientation of the antennas are shown in Figure 3.9. In this case, the falling event was also recorded at 6 seconds. In Figure 3.9a the Doppler signatures at 6 seconds are distinguishable from the rest of the time samples recorded during the experimentation.

The data shows a clear difference between the two datasets. Figure 3.9b shows a higher amplitude echo in the HH scenario compared to the VV scenario shown in Figure 3.8b.

Both datasets capture dispersions caused by falling events. It is important to mention that both experiments were carried out under the same conditions and with the same angle of observation of the antennas. Nevertheless, the Doppler signatures in the HH case are more prominent. Therefore, the most prominent dispersion is achieved with this orientation.

To evaluate the impact of the antenna orientation, the frequency was taken as the feature of the Doppler spectrums. The feature space was reduced using the PCA for both scenarios. Figure 3.10 shows the comparison of the feature space obtained in each of the scenarios using a projection of the first two principal components. Figure 3.10a contains the numerical values obtained with the data from the VV scenario. The crosses in Figure 3.10a marks the identified falls. The rest of the features correspond to non-movement period and are shown as dots. The distribution of the data of both classes shows in multiple cases similarities between their numerical values. Figure 3.10a shows a low separability between the non-movement and the falling events features, this makes the classification process between both classes difficult.

On the other hand, the projection of the features of the HH scenario in Figure 3.10b shows a contrasting distribution compared to that of the VV scenario. Most of the features that correspond to falls have numerical values that can be differentiated from the rest. This separation between both classes determines that the features extracted from the spectrum where a fall occurred using the HH orientation of the antennas obtained a greater variability than the rest.

Classification was performed with SVM and the results are shown in Figure 3.11. Using the dataset of the VV scenario, an accuracy of 50% in the detection of falls was achieved (Figure 3.11a). Therefore, the false-negative rate was also 50%. This represents a high rate of false alarms in the system. The low percentage of accuracy is attributed to the sensing capability of the system when using a VV orientation of the antennas. After analyzing the principal components of the received signal in this scenario, it was shown that they have low variability and negatively impact the classification algorithm.

The results for the HH scenario dataset are shown in Figure 3.11b. In this case, the accuracy percentage increased. The evaluation results show a 92% accuracy in the detection of falls. The false negative rate decreased to 8%. This indicates that the sensing capabilities of the system can be increased by analyzing the effects related to the orientation of the antennas. This may represent a solution to the limitation of systems based on RF-WiFi signals without the need to increase the number of sensors in the indoor environment.

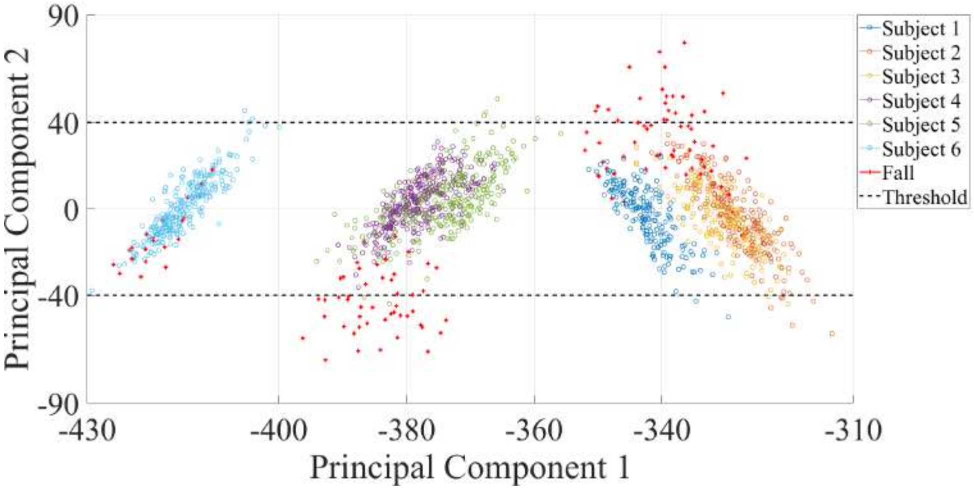

(a) VV scenario features

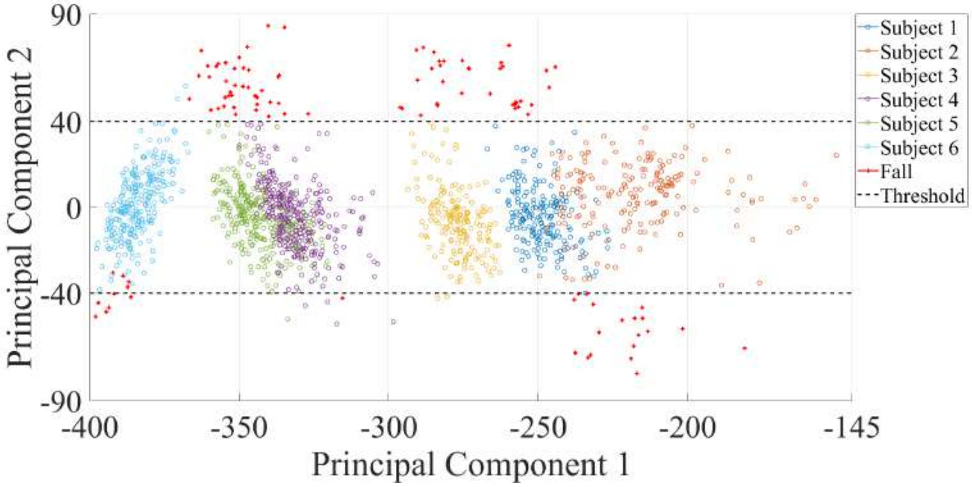

(b) HH scenario features

Figure 3.10: Projection of the first and second principal components.

Figure 3.12 and 3.13 show accuracy comparison between our experiments and two previously proposed systems. The comparison shows that classification accuracy is impacted by antenna orientation. Therefore, false negative rate is also affected. Although these systems use other features of the RF-WiFi signals for their recognition stage, the sensing stage is the common component in any system. WiFall-one link has a similar configuration to our system with only one T_X and one receiver. Nevertheless, with the HH scenario, higher accuracy percentages were achieved. WiFall-two links have two receiver sensors, our accuracy percentage (Figure 3.13) is very close to their results. Finally, Fall sense reported a 3% higher accuracy than the accuracy achieved by our experiments at the cost of increasing the number of sensor. Should be noted that in our experiments only one sensor was used and with a careful consideration of antenna orientation, a increase of

(a) VV scenario

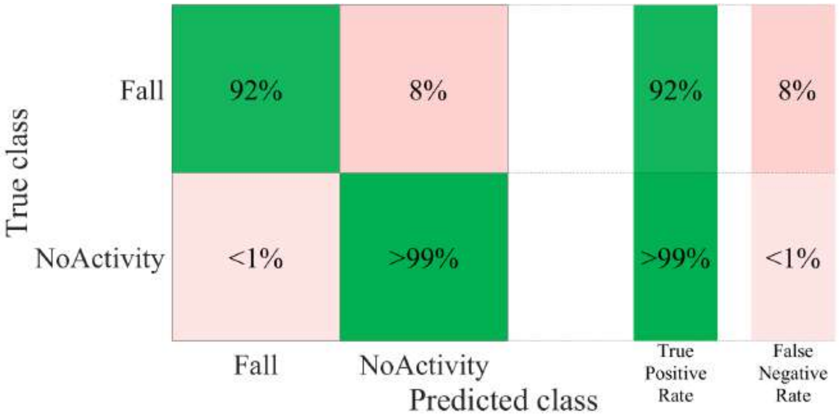

(b) HH scenario

Figure 3.11: Confusion matrix of the SVM algorithm.

12% was achieved. However, it is remarkable that orientation changes represent an important factor in the detection rate. Therefore, systems that consider these characteristics at the sensing stage can improve their accuracy and false-negative rate results. We expect that this configuration will help improve the difference between falls events and activities of daily living.

3.8 Discussion

Our preliminary results showed that the features extracted in the HH scenario corresponding to each participant have a trend in their values. The concordance of this indicates that under the same experimental conditions each person produced Doppler signatures different from those of the rest. Therefore, there is the possibility of characterizing the unique movement of each individual. This could close the gap with monitoring problems when there is the presence of more than one person moving near to the indoor

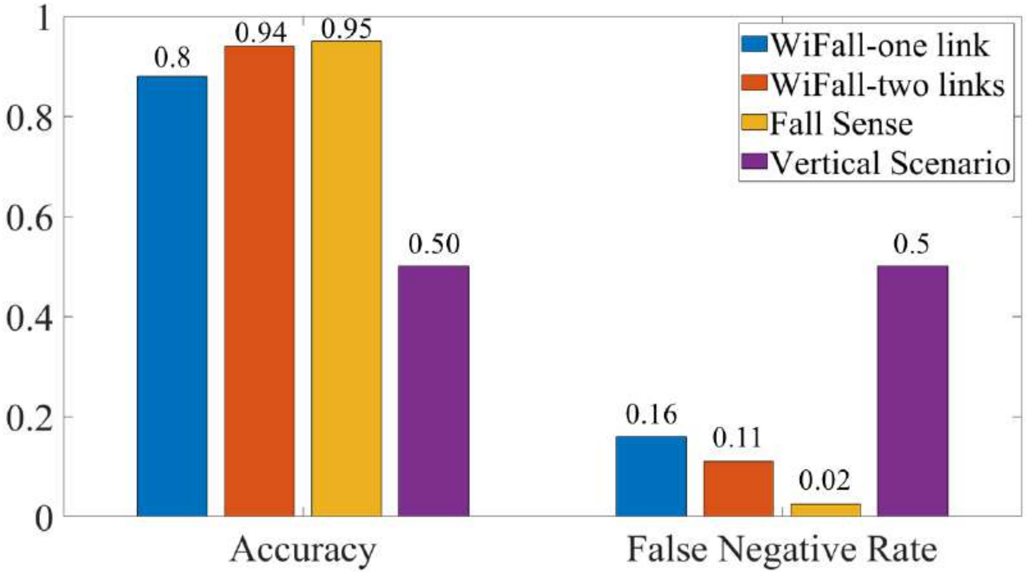

Figure 3.12: Comparison of Wifall, FallSense and VV scenario.

environment. Furthermore, this would allow the proposed scenario to be expanded to less controlled environments such as monitoring in public places.

When the different orientations of the antennas were analyzed, it was found that there is a relationship between the increase in the accuracy rate of the classification system and the alignment of the radiation and polarization pattern. In scenarios with an HH orientation, the LOS component between the antennas is very low, which highlights the non-LOS components. Outside the LOS of the antennas is where the information on the Doppler signatures is found. When the Doppler signatures are highlighted, it facilitates analysis techniques such as PCA to create separable data sets according to their characteristics. Our results show that for fall detection applications, it is necessary to consider a selection in the orientation of the antennas that decreases the contribution of the LOS in the antennas to reduce the complexity of classifying the Doppler signatures and improve the accuracy rates. However, a set of different activities should be measured to ensure the correct classification of a fall.

Human daily activities such as walking, walking waving arms or running, have a common characteristic, they produce a periodic Doppler shift as has been shown in [68]. However, seating and laying down are also non-periodic activities that do not produce a distinguishable Doppler shift as shown in a series of experiments measure with a 2.4 GHz radar [68]. In our future experiments, additional activities, such as walking towards or away from the stair, going up or down the stair and falling, should also be measured and analyzed to ensure that these activities can be distinguished from a fall. Additionally, feature extraction considering spatio-temporal evolution of the activities should be explored for classification of periodic and non-periodic

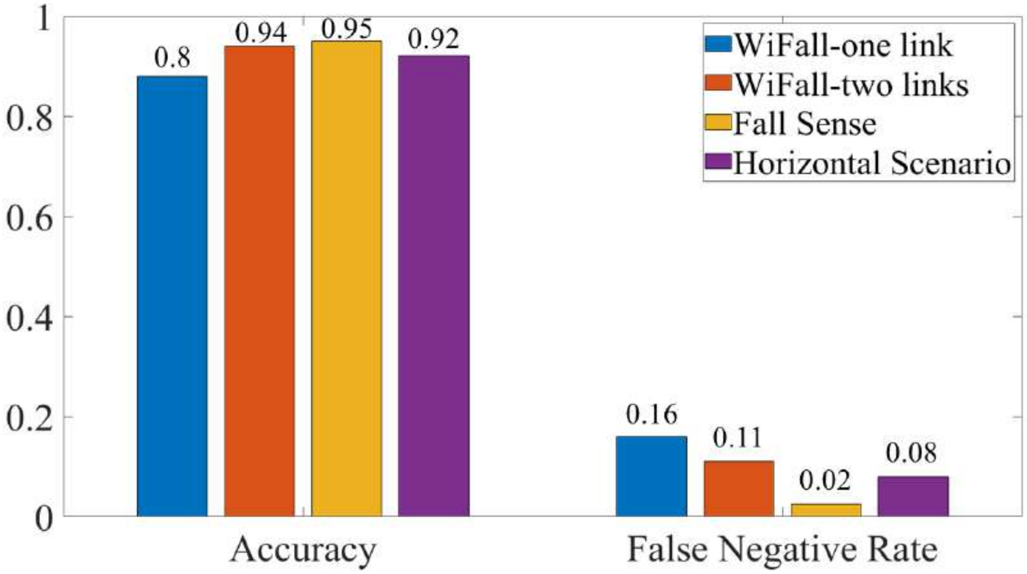

Figure 3.13: Comparison of Wifall, FallSense and HH scenario.

activities. Early experiments including several activities has led us to expect that those activities can be distinguished.

Besides, aged population is rising due to advanced medicine and higher life quality. However, world population reports higher susceptibility to age-related diseases that can be addressed by health technology. Wireless Body Area Network (WBAN) has been explored as a healthcare technology that can monitor blood pressure, blood sugar level or other physiological variable that prevent catastrophic events [69]. WBAN architecture involves a dense network of sensor and actuators distributed in the body that interact with a coordinator that sends information outside the WBAN, a smartphone is normally used as a gateway. WBAN uses the 2.4 GHz ISM band to communicate between sensors and coordinator. There are several communication technologies used for intra-WBAN including Bluetooth, ZigBee, and Ultra-wide band. The co-channel interference may occur due to the coexistence of WBAN with WiFi, ZigBee, Bluetooth, and cellular devices that share the same band. However, WiFi uses higher transmission power level than WBAN and consequently WiFi transmission dominates the medium [70]. Normally the gateway that sends information out of WBAN use WiFi, therefore, the interaction of WBAN with cloud-based services uses the same information channel that is used for the measure Doppler signatures. Quality of Service (QoS) measurements such as CSI or RSSI might be impacted by the interaction between these technologies, but Doppler signatures might not be affected.

Considering the above, it is possible to use the signals transmitted by commercial WiFi systems by analyzing Doppler signatures for fall detection without compromising coexistence. Furthermore, the analysis of the Doppler signatures allows the use of diversity techniques. In a WiFi system that transmits several pilot signals, the Doppler drifts will be replicated in each one. Therefore, the effects related to human movement can be compared in the same instant of time by more than one probe signal without the need to add a set of antennas to the system. This avenue has not been widely studied.

Finally, falling is a transient event that might be undetected due to the interruption of signal transmission. WiFi AP transmit their signal in burst, interrupting the sensing process for short periods of time. Then, in the current transmission protocol that might caused a falling event to be undetected. Therefore, should be considered to implement a continuous transmission mode with low power consumption that allows uninterrupted monitoring of the environment.

3.9 Conclusion

A study of the impact of antenna polarization in classification accuracy was performed. In order to determine this impact, an indoor WiFi platform was built with general-purpose equipment. The platform uses RF-WiFi signals to measure fluctuations caused by human movement without the need to carry any device. The design and development of the platform were presented as well as the fall experimentation protocol with volunteer subjects. At an operating frequency of 2.42 GHz we recorded the Doppler signatures on a series of spectrograms during testing. Two scenarios were proposed to characterize the effects caused by antenna orientation that impact the performance of the platform. The HH antenna scenario presented more prominent fluctuations during the tests. PCA was selected as a classification feature. It was shown that PCA component distribution shows difference in separability for the considered scenarios. A classification performed by SVM algorithm demonstrated that changing the orientation of the antennas can improve performance in detecting falling events. The results of the algorithms that used the data from the HH scenario showed that the accuracy system can be increased without increasing the number of sensors. This means that, in the design and implementation of sensing systems based on the analysis of RF signals, the antenna orientation that mitigates the effects of misalignment to a greater extent must be considered. This can be achieved through the PCA that provides an abstraction of the behavior of the data extracted from the signals, as is the case of the Doppler signatures. Therefore, the findings described in this work may have implications for the accuracy rates of other home health monitoring systems, considering it necessary to measure the effects of antenna orientation to ensure high-quality characteristics for their classification.

Chapter 4

Deep Learning Multi-Class Approach for Human Fall Detection Based on Doppler Signatures

Falling events are a global health concern with short- and long-term physical and psychological implications, especially for the elderly population. This work aims to monitor human activity in an indoor environment and recognize falling events without requiring users to carry a device or sensor on their bodies. A sensing platform based on the transmission of a Continuous Waveform (CW) Radio-Frequency (RF) probe signal was developed using general-purpose equipment. The CW probe signal is similar to the pilot subcarriers transmitted by commercial off-the-shelf WiFi devices. As a result, our methodology can easily be integrated into a joint radio sensing and communication scheme. The sensing process is carried out by analyzing the changes in phase, amplitude, and frequency that the probe signal suffers when it is reflected or scattered by static and moving bodies. These features are commonly extracted from the Channel State Information (CSI) of WiFi signals. However, CSI relies on complex data acquisition and channel estimation processes. Doppler radars have also been used to monitor human activity. While effective, a radar-based fall detection system requires dedicated hardware. In this chapter, we follow an alternative method to characterize falling events on the basis of the Doppler signatures imprinted on the CW probe signal by a falling person. A multi-class deep learning framework for classification was conceived to differentiate falling events from other activities that can be performed in indoor environments. Two neural network models were implemented, the first is based on a Long-Short-Term Memory Network (LSTM) and the second on a Convolutional Neural Net-

---

This chapter forms part of the paper titled Influence of the "Deep Learning Multi-Class Approach for Human Fall Detection Based on Doppler Signatures" published in *Int. J. Environ. Res. Public Health, MDPI.* The authors gave their consent to use their work as an integral part of this dissertation.

work (CNN). A series of experiments comprising 11 subjects were conducted to collect empirical data and test the system's performance. Falls were detected with an accuracy of 92.1% for the LSTM case, while for CNN, an accuracy rate of 92.1% was obtained. The results demonstrate the viability of human fall detection based on a radio sensing system like the one described in this chapter.

4.1 Introduction

According to the World Health Organization, in 2018 it was reported for the first time in history that the number of people over 65 exceeded the number of people under 5 years of age worldwide [71]. Therefore, it is estimated that by 2050 one in six people will belong to the elderly sector [72]. The fact that elderly people live alone raises concerns because they might not have access to continuous health status monitoring. Falls are the second leading cause of death worldwide, causing injuries that require immediate medical attention, otherwise, they can be fateful [25]. Unfortunately, the rate of deaths caused by falls continues to increase each year, and if this growth continues, it is anticipated that by 2030 there will be 7 fatalities every hour [73]. In addition, several studies show that if the falls are not fatal, there is a possibility that people present physical and psychological complications for the rest of their lives [74]. Some physical complications include restrictions in daily activities, joint pain, broken bones, or brain injuries, among others. Falls are the most common mechanism for causing traumatic brain injuries [75]. Psychologically, the person struggles with sadness, a lack of self-assurance, and a fear of falling again. On the other hand, statistics show that 80% of fall deaths are in low- and middle-income countries [25]. For this reason, the development of low-cost fall detection systems is a critical need.

This work aims at detecting human falls through radio sensing based on a continuous wave (CW) radio-frequency (RF) probe signal that can be transmitted as a pilot signal within the communications signal frame. Pilot signals do not carry information data and are used only for synchronization purposes between the transmitter and the receiver [53]. However, these signals are subject to frequency dispersions caused by the Doppler effect. Such frequency dispersions are known as Doppler signatures and have been widely used for sensing purposes [28, 76, 77]. The Doppler signatures produced by the interaction of the CW probe signal with a moving person can be analyzed to characterize falling events. We developed a CW probe signal transmission and reception system using general-purpose equipment that can be easily replicated. Unlike other works where a single-input multiple-output scheme is followed [36,52,78], our system only requires a single-input single-output (SISO) radio link. Furthermore, the platform allows the acquisition of the information from the probe signals through a less complex process than Channel State Information (CSI) or Received Signal Strength (RSSI) estimation.

In a previous study [18], we presented the influence of antenna orientation in fall detection systems using a Simple Input Simple Output (SISO) RF signal transmission platform. The results determined the orientation of the antennas with which the Doppler signatures of a fall are captured with the best resolution. However, this proof of concept was performed using a binary classification of events (falls and no activity). As a significant extension of this work, we seek to increase the robustness of the system using a multi-class classification approach and increase accuracy by implementing advanced deep learning (DL) techniques. DL is considered one of the core technologies of artificial intelligence capable of building intelligent systems [24]. Machine learning algorithms can be classified as Bag-of-Feature (BoF) or model algorithms [79]. BoF performs classification by a) extracting desirable features, b) generating a codebook, and c) generating a vector of features. The main problem in BoF is feature selection that guarantees separability between classes. Features must exhibit high information-packing properties, a high discrimination rate between classes, low within-class variability, and the ability to discard redundant information. Model-based machine learning, such as DL, performs feature extraction and classification within the designed network. The training process establishes which features are relevant to the desired classification. DL automatically selects the feature that achieves the best classification. In our methodology, the model will extract the required features from the received CW probe signals for the learning process. The system is trained to identify the Doppler signatures of different activities of the daily life and specific events such as walking, going up/down stairs, and falling. We implement and evaluate two one-dimensional neural network algorithms for this process: the long-short-term memory network (LSTM) and the convolutional neural network (CNN). The LSTM network is considered one of the most successful recurrent neural networks [24]. Our implementation achieved 92.1% accuracy in detecting falling events with the LSTM algorithm. On the other hand, CNN is a popular feature discriminator that automatically learns from the input signal without a feature extraction pre-process [80]. We assessed the CNN classification algorithm and we achieved an accuracy of 92.1% on falling events. Our results shows that the Doppler signatures of a CW probe signal are sufficient for accurately detecting falling events differentiating them from other activities.

The rest of the chapter is organized as follows. Section 4.2 provides a review of related work. Section 4.3 shows the materials and methods used for sensing and capturing de Doppler signatures from human activities. Section 4.4 describes the architectures of the implemented classification framework. Section 4.5 addresses the results and discussion of the proposed framework and its performance. Finally, Section 4.6 presents the conclusions.

4.2 Related work

Several systems have been proposed for fall detection using different sensing techniques. A machine vision technique can be implemented for this purpose. These systems are based on digital image processing and need to capture high-resolution images to achieve a high accuracy rate [81]. However, not all vision systems can deliver high image quality, and investing in equipment with higher resolution is an expensive solution. Furthermore, partial or complete occlusion of people by objects or walls reduces the detection of events [32]. Environment-based systems have the same disadvantages by requiring the installation of acoustic or vibration sensors throughout the entire indoor environment [4,5]. Due to their sophisticated implementations and high cost, they are not always viable. On the other hand, wearable devices have taken advantage of low-cost sensors embedded in general-purpose devices that people can wear to be monitored [43,82,83]. Nevertheless, the subject's will to wear such sensing devices is of prime importance because detection accuracy depends on it. However, users might find it uncomfortable to keep the device attached to their bodies. This approach is invasive and must be worn at all times in order to detect falls accurately.

An innovative approach to fall detection is through a RF technique. The operation of these systems is based on the transmission of RF signals that are reflected, diffracted, and scattered by static or moving human bodies [36]. Changes in such signals resulting from the interaction with the human body can thus be characterized to determine the nature of the movement performed. This means that the RF systems can monitor activities without the need for the user to wear a device on their body. The construction of these RF-based sensors can be implemented with relatively simple circuits to generate CW signals [84]. In addition, the health data provided by these signals can be monitored through technologies such as IEEE 802.11af which provides opportunistic access to licensed channels with the help of cognitive functions without any spectrum cost [85]. Therefore, the development of these technologies makes RF-based fall monitoring systems a low-cost alternative.

The RF signal transmitter that has had the greatest relevance in the field of monitoring systems is the WiFi access point (AP) [86]. These devices are ubiquitous in most indoor environments and are a commercial off-the-shelf technology. WiFi signals are commonly analyzed through the CSI [8, 17] or the RSSI [19]. The CSI provides information about changes in signal amplitude or phase during a falling event, whereas the RSSI measures changes in the average strength of the signal. In fall detection, CSI analysis has stood out above other approaches and has shown promising results. However, the technology available for the implementation of these systems is still limited principally by laborious offline processing. For example, sensing applications using CSI require a high rate of measurements which reduces network performance and efficiency [87]. Furthermore, the APs have to work in data transmission mode to compute the necessary Orthogonal Frequency Division Multiplexing (OFDM) signal for the CSI, which cannot always be guaranteed [88]. These aspects compromise the coexistence of joint radio sensing and communication systems. Therefore, it is necessary to define a new methodology that integrates both schemes.

Radar devices are another well-established sensing technology that is robust to the environment, small in size, and which has operating frequencies ranging from few GHz to hundreds of GHz [21]. Doppler radars have been widely used to monitor human activity. Unfortunately, these systems require specialized hardware, which can be expensive to develop. Furthermore signal processing for radar sensing requires information about the cross-correlation between surveillance and reference signals that are not part of the communications signal frame [46].

4.3 Materials and methods

4.3.1 System overview

Figure 4.1 shows an overview of the implemented platform for fall detection based on CW probe signals. In the experimental stage, the sensing of human movements is carried out through the transmission of RF probe signals in an indoor environment. Some of the signals are absorbed by the human body and others are reflected or scattered toward the receiver. Therefore, the reception of the signal occurs through more than one path and at different times. This is known as multipath propagation. The Doppler effect causes frequency shifts in RF signals and occurs when a moving body interacts with the transmitted signal. A Doppler signature is the frequency dispersion pattern imprinted on the probe signal during an activity or event. We intend to associate the falling events with the features of their generated Doppler signatures. Our efforts are focused on the implementation of two DL frameworks capable of accurately detecting falling events and distinguishing them from human activities. The LSTM network and CNN have shown remarkable success in performing fall detection tasks [78, 82, 89].

4.3.2 Sensing platform

We use general-purpose equipment to transmit and collect CW RF signals similar to those used by commercial WiFi systems. With a Keysight N9310A RF signal generator, we can emit a probe signal at a frequency between 9kHz and up to 3GHz, with a power of 20dBm. In this way, the platform is available to emit probe signals in the frequency range of the IEEE 802.11 b,g,n protocol. We consider the analysis of the Doppler signatures registered in the pilot carriers of these communication protocols used for channel estimation. Therefore, the platform guarantees not to interrupt or interfere with

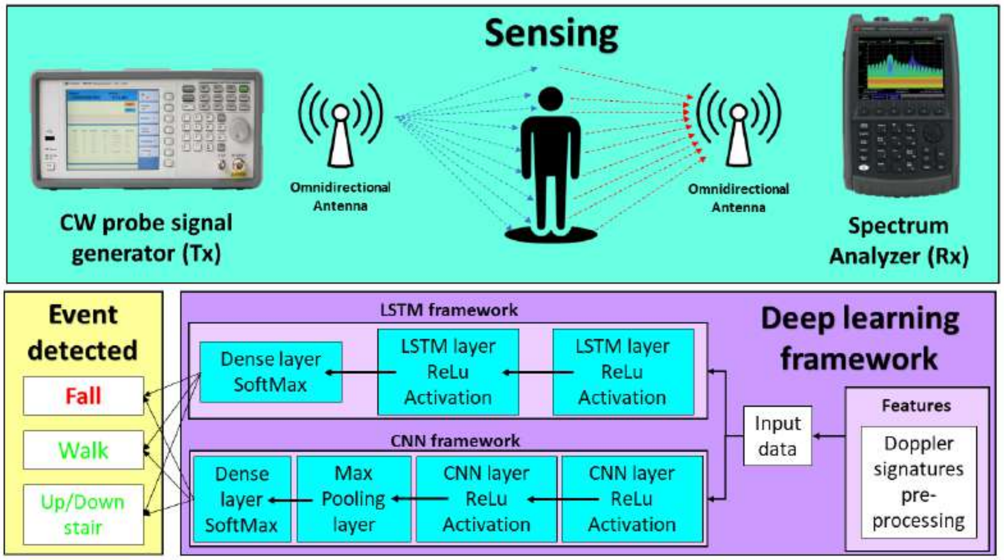

Figure 4.1: Overview of the fall detection system based on Doppler signatures.

the information transmitted.

Nonetheless, to calibrate the transmission and reception system, the characteristics of the antennas and the indoor environment that is being sensed must be considered. For this, it begins by characterizing the antennas used by the platform. In our case, the transmission is carried out with an omnidirectional monopole antenna (T_X) of 9 dBi gain that works in the 2.4-2.5 GHz band. Antennas with these characteristics are commonly used in WiFi. Furthermore, a Keysight FieldFox N9912A (R_X) spectrum analyzer was used to capture the transmitted signals and to characterize the coupling of the antennas with the transmitting and receiving equipment. According to our measurements, the monopole antennas had a better coupling at a frequency of 2.42 GHz. These antennas were fixed with a horizontal orientation for both T_X and R_X. This is in agreement with the results reported in our previous work where it was shown that this orientation improves the resolution with which the Doppler signatures are recorded [18]. Finally, the sweep time for detection was fixed at 271 ms with a frequency span of 1.5 kHz because the duration of a fall is between 1-1.5 s.

4.3.3 Recruitment of participants

The experiments in this study were conducted with a total of 11 adult participants. The age of the people involved was in a range between 21 and 48 years of age. Recruitment took place in the city of San Luis Potosí, Mexico, where the volunteers declared that they were in good physical health. Among the requirements to demonstrate good health is not having a his-

Table 4.1: Physical characteristics of the recruited participants.

Participant	Age	Gender	Height(m)	Weight(Kg)
1	21	Female	1.69	76
2	25	Female	1.57	50
3	26	Female	1.61	64
4	28	Female	1.64	59
5	47	Female	1.55	65
6	25	Male	1.67	70
7	29	Male	1.80	75
8	29	Male	1.63	93
9	30	Male	1.72	73
10	33	Male	1.65	72
11	48	Male	1.71	85

tory of musculoskeletal problems. The volunteer population was divided into 6 men and 5 women with different body masses and heights (Table 4.1). This variation in the physiognomy of the participants enables data to be obtained from activities performed at different speed. Furthermore, the amount of Doppler dispersion produced by the volunteers varies according to their weight or height. Before the experiments, the participants filled out informed consent forms about the risks of the study. Furthermore, all the experiments were carried out under the ethical standards that the Autonomous University of San Luis Potosí demands.

4.3.4 Experimental protocol

The sensing platform was located within the facilities of the Autonomous University of San Luis Potosí, Mexico. Each experiment was carried out in an indoor environment that simulates a two-story home. Figure 4.2 shows the dimensions of the test scenario and the position of the measurement equipment. The experiments were divided into four classes of activities to be carried out by the participants. To evaluate the robustness and generalization of the experimental model in different real-world situations, a walk at a constant speed of 7m in a forward direction was proposed as the first activity. Each participant performed 30 repetitions changing the direction in which they moved to cover the entire perimeter of the indoor environment. This allows a change of location of the people at all times, which adds randomness to the spatial location where the tests are carried out and allows the evaluation of the sensing quality in the scenario. The second activity was performed by going up and down a ten-step ladder for a total of ten repetitions per participant. Finally, the volunteers had to simulate a fall situation both in the case of fainting and a fall resulting from going down the stairs. For this, a thin mattress and an airbed were placed in the

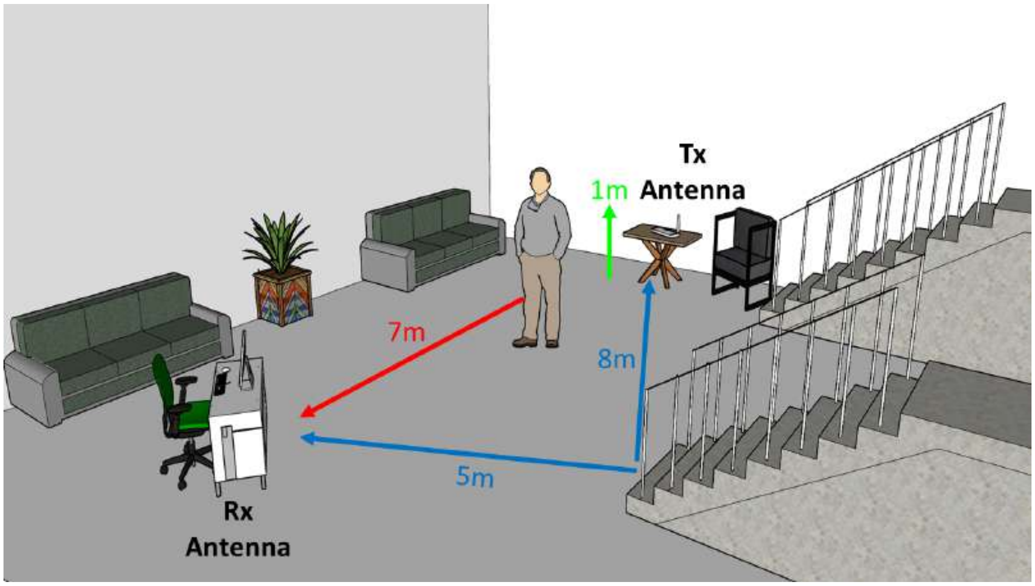

Figure 4.2: Test scenario for fall detection experiments and positioning of the measurement equipment.

Table 4.2: Summary of trials performed by the participants.

Activity/Event	Trials per participant	Total
Walk	30	330
Up/Down Stairs	10	110
Falls	10	110
No Activity	10	110

room to reduce the impact force caused by falls. In the scenario of a fainting event, the person was placed in the center of the room to perform the movement. The event was replicated five times per participant. On the other hand, in the event of a fall from the stairs, the participant stood two steps up and descended the stairs, ending with a falling movement towards the padded surface. Five repetitions of this event were performed. Furthermore, we included a series of experiments that did not require the presence of the participants. These experiments consisted of taking snapshots of the probe signal in the indoor environment without any human movement involved. The data collected in this experiment are categorized into a particular class of "no activity" and are used to determine when a person remains static. The summary of the activities and repetitions developed by the participants is shown in Table 4.2. The physical differences of the volunteers and the wide range of ages were taken into consideration to have a wide variety of movement speeds available when developing the tests. Therefore, our platform seeks to be evaluated under conditions that are as realistic as possible, including changes in location and variations in speed of movement.

4.3.5 Doppler signatures analysis

A methodology that allows visualizing the changes in the spectral density in a short observation time is necessary to differentiate the Doppler signatures recorded in the CW signals during the performance of activities. This has the objective of determining if the features of each signature are unique according to the activity to which they correspond. The spectrogram method is used to analyze time-varying and non-stationary signals such as those transmitted by our detection system. Therefore, we propose to compute spectrograms for the generation of a database containing the sequence of activities recorded by the platform.

The spectrogram of a received CW RF signal is calculated as $S(t';\nu) = |Y(t';\nu)|^2$, where t' is the observation time, $Y(t';\nu) = \int_{-\infty}^{\infty} y(t)w(t-t')e^{-j2\pi\nu t}\,\mathrm{d}t$ is the Fourier transform of $y(t)$ and $w(t)$ is a positive window and energy unit pair [49]. The shape and length of the window function $w(t)$ must be optimized to obtain a good resolution in frequency and a reduced spectral loss. A Gaussian window fits the time-frequency analysis requirements of the application at hand. Thereby, $w(t)$ can be given by

$$w(t) = (\sqrt{\pi}\sigma_s)^{-1/2}e^{-t^2/(2\sigma_s^2)}, \tag{4.1}$$

where σ_s is the dispersion parameter [56]. Examples of the spectrograms recorded during the four activities considered in our experiments are shown in Figure 4.3.

Doppler signatures pre-processing

The RF signal received by the platform contains an additive white noise component Gaussian $n_\sigma(t) \in \mathbb{C}$; $\mathbb{C}$ refers to the set of complex-valued numbers [18]. This component corrupts the signal mainly due to thermal noise from the measurement equipment and affects the resolution with which the signals are captured. Therefore, it can be challenging to extract and analyze the Doppler signatures. The noise contribution in the received signal is illustrated in Figure 4.4 which is a capture of the spectrogram of Figure 4.3a at a time $t' = 12s$. We observe that the RF signal dispersion caused by a falling person can be masked by noise. It is required to construct a pre-processing stage that enables us to sanitize the RF signals and remove the majority of the noise in order to account for these practical concerns. To compensate for these practical issues, it is necessary to implement a pre-processing stage. We propose a pre-processing methodology based on a denoising filter through a Gaussian mask. The masking is done through a Gaussian signal with an amplitude that properly covers the bandwidth of the sub-carrier signal and the Doppler generated by a person during a falling event. The mask was obtained by averaging the snapshots of the spectrograms captured during the experiments and was applied to the original values of the received

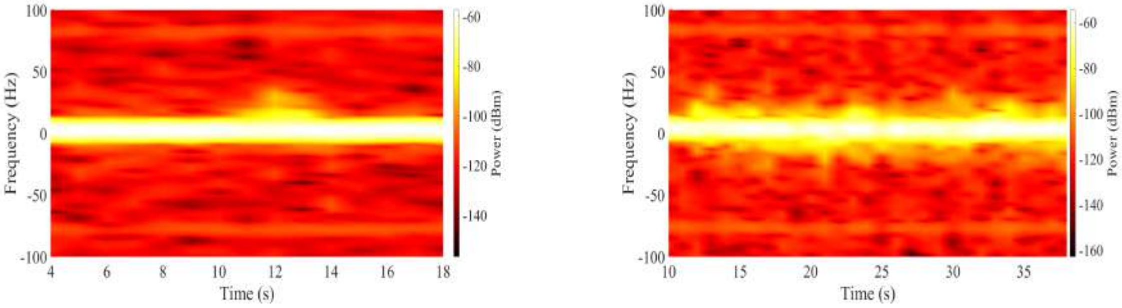

(a) Fall (b) Walk

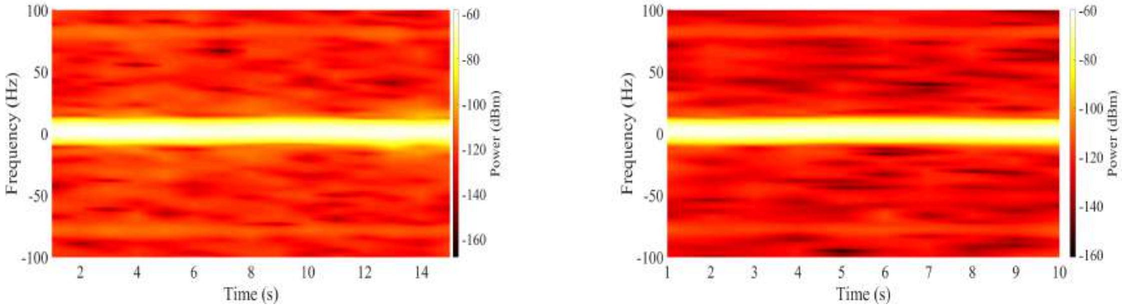

(c) Up/Down Stair (d) No Activity

Figure 4.3: Spectrograms of the four activities performed in the indoor environment.

signals. Figure 4.5 shows the result of applying the Gaussian mask to the spectrum of Figure 4.4, where the noise was smoothed in most of the signal. Furthermore, it is shown that the dispersion generated by the Doppler effect of the fall is preserved and is simpler to visualize. Figure 4.6 shows the calculated spectrograms after sanitizing the RF signals in all activities. These spectrograms are used to build the database for our fall detection platform. However, the sequences of activities do not have the same number of samples and it was necessary to take a fixed observation window. The observation window was set at ten samples per spectrogram because the dispersion of falls does not exceed three samples and is sufficient to capture a sequence of walking and going up or down stairs. According to Table 4.2 for a total of 660 calculated spectrograms, a database with 6600 samples was generated. Furthermore, after the probe signals are pre-processed, most of the information in the frequency spectrums is negligible (Figure 4.5). In our case, the maximum values of the power of the probe signal and its Doppler signatures were preserved in 82 values of the snapshots. These values are considered the principal features of the experiments.

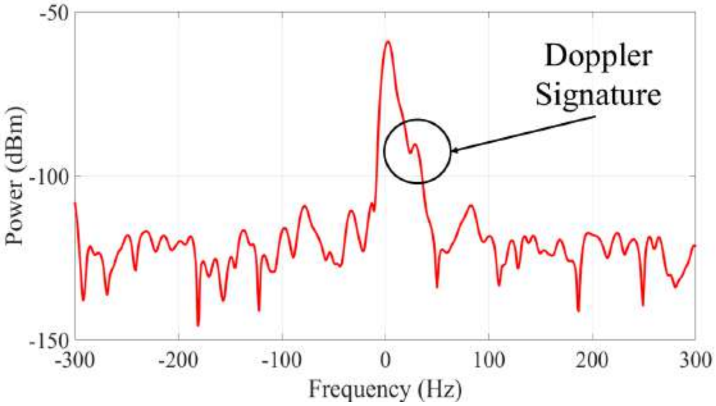

Figure 4.4: Snapshot of the probe signal during a falling event without applying a pre-processing stage.

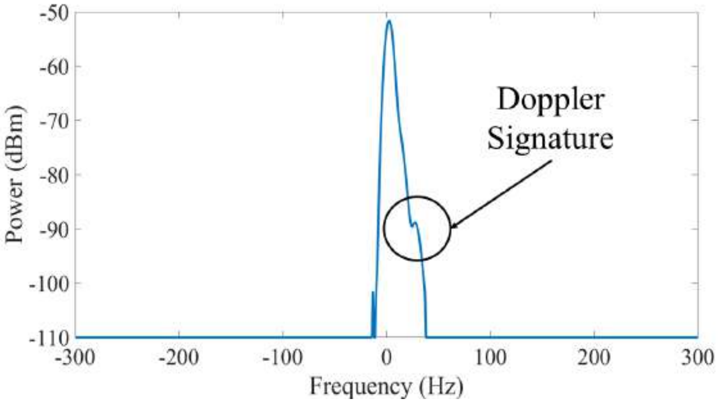

Figure 4.5: Probe signal pre-processed with denoising filter.

4.4 Deep learning framework

DL is a methodology that has been proposed to perform classification and regression tasks with significant results in the area of data science [24, 90]. DL algorithms are based on artificial neural networks to build computational models capable of extracting and learning the principal features of a data set. The first step in developing a DL model is to create a data set that includes measurements of various activities. The dispersion caused by the acceleration of falling bodies has a progressive and natural sequence. Moreover, human activities such as walking and going up or down stairs are also sequential activities. In order to analyze those activities, a sequence of spectrums conforming to an activity must be formed. A window that included ten spectrums allowed us to provide sequences where the activities could be observed. Each activity is measured with a sequence of spectrograms. Our dataset was built with a set of different experiments involving a predetermined set of activities. According to Table 4.2, a total of 660 sequences were captured and divided into four different classes. For the classification

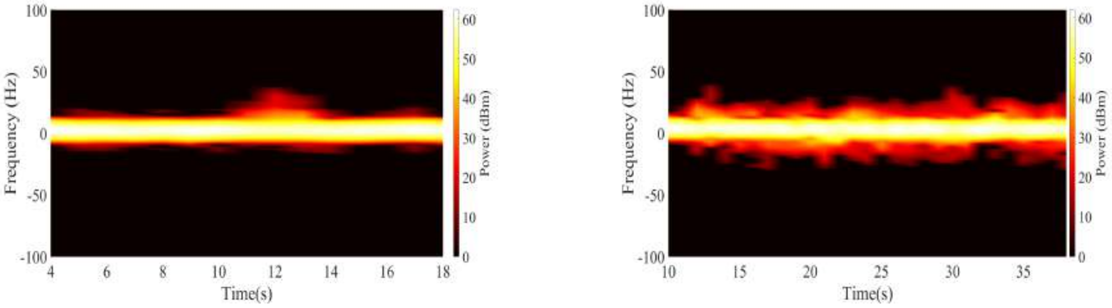

(a) Fall

(b) Walk

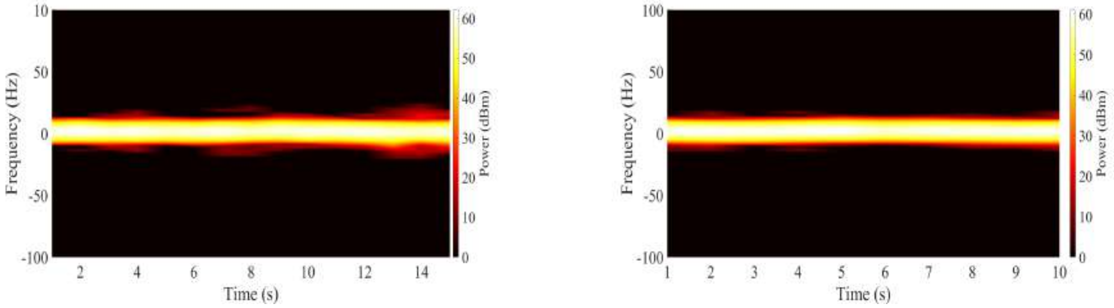

(c) Up/Down Stair

(d) No Activity

Figure 4.6: Spectrograms of the four activities performed in the indoor environment.

process, the algorithms need one data set for training and another for validation and testing. Our training data corresponds to 80% of the total captured sequences and the remaining 20% was used for validation and testing.

In this work, we consider two architectures with different supervised learning approaches to compare the features they are capable of extracting and determine which have better classification results. The first architecture is the LSTM network which has a generative approach. We selected this network for its capability to learn from the contextual relationships in the data. Furthermore, in the experimental protocol, sequential data of activities such as walking are considered. The LSTM model can process a particular input considering previous inputs. This is essential in our application since the recognition depends on the context of the activity. Moreover, in high-dimensional data sets, LSTM networks prevent the loss of important information over long periods. Therefore, unlike other recurrent neural networks (RNN) based learning models, LSTM has greater potential for fall detection.

The other architecture used was a CNN which has a discriminative approach. This model uses convolution operations to extract the most relevant features from a data set. This allows us to recognize patterns in the information automatically and highlights the information that is most related to each other. In our case, the Doppler signatures of the falls are locally related data, and the CNN model is ideal for highlighting them from the rest of the activities in the data set. Therefore, within artificial neural networks, the CNN algorithm has multiple advantages for our platform.

4.4.1 Long short-term memory network

LSTM networks are a variation of RNN and are used in sequential data analysis applications [77,91]. These networks have a state cell which is a memory block that stores data for long periods. This solves the vanishing gradients problem, which makes it difficult for the network to remember important information from the beginning of the sequence as the sequence increases. The memory block is divided into three gates: the forget gate, the input gate, and the output gate. The forget gate has the task of determining what information from the previous state cell will be stored and what information can be discarded. On the other hand, the input gate decides the data to enter the state cell and the output gate controls the outputs. Therefore, we can use a larger volume of input data to increase the efficiency of network learning without losing information over long periods.

The architecture of our classification algorithm using LSTM networks is shown in Figure 4.7. The input data in these networks must be a three-dimensional array. The first dimension is the one that represents the batch size, the second dimension corresponds to the time steps and finally, the third dimension is the number of units or features in an input sequence. The batch size was 5,391 samples for the training set and 1,191 samples for the validation and test set. Which correspond to 80% and 20% of the total samples of the database respectively. The time step taken has a value of 10, considering the size of the observation window of the pre-processing stage. The features entered into the network were the 82 most relevant values of the probe signals (Section 4.3.5). Once the data is entered into the algorithm, it is processed by two LSTM network layers using a rectified linear unit (ReLU) activation function. The number of input artificial neurons in both layers was 100. Finally, the output is a dense layer that classifies the samples into the four given activity classes using a Soft-max activation function.

4.4.2 Convolutional neural network

CNNs are classification models that can reduce the dimensionality of the input data and extract the principal features without requiring a supervised extraction stage. This architecture is mainly based on the implementation of convolution layers to discriminate a data set. The convolution is computed through multiple digital filters that sweep the input data and create a feature map. Pooling layers are used for dimensionality and operation reduction as well as feature summarization. A max-pooling layer takes only the maximum value of a portion of the feature map given by a defined kernel and discards the rest. This process reduces the computational cost of algorithms by

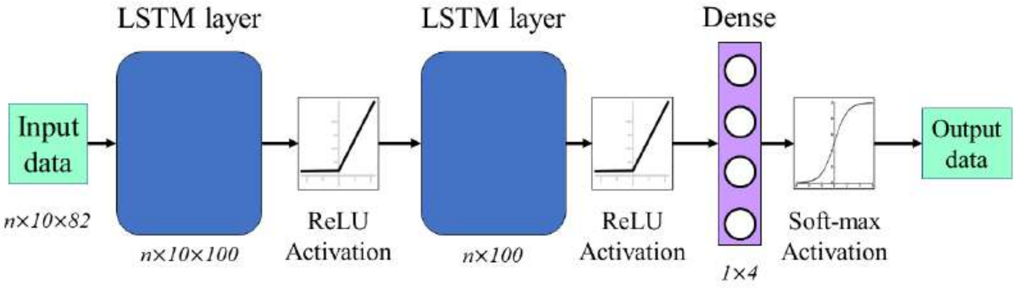

Figure 4.7: The architecture of the LSTM network implemented for the classification process, where n is the size of the input data set.

extracting and preserving only the dominant features of the dataset. Finally, a fully connected layer called a dense layer is used to determine the class to which each extracted feature belongs. For this, it is first necessary that a flatten layer must process the data extracted from the convolution layer to adjust its dimensions to those of the dense layer. Therefore, the proposed CNN architecture for fall detection is defined in Figure 4.8. The input data of the algorithm has to be a three-dimensional array represented by the batch size, the time step, and the number of features. In our implementation, 16 filters were used in each of the convolution layers. The stride, which defines the input of the given data, was set to 1 for all layers. We select a kernel value of 3 to reduce the computational cost without losing excessive details on the features. The convolution layers were built using a ReLU activation function. Finally, for the fully connected layer, a Soft-max activation was selected for the dense layer.

4.4.3 Performance evaluation

We use the confusion matrix to visualize the results and determine the percentage of activities classified correctly. In a confusion matrix, 4 possible results can be obtained: True Positive (TP), True Negative (TN), False Negative (FN), and False Positive (FP). Positive true values are the number of samples that were correctly classified in the class being evaluated. The true negatives are the samples correctly classified in the rest of the classes. On the other hand, the false negatives are the samples of the evaluated class that were classified as another activity. Finally, the false positives, contrary to the false negatives, are the samples of other activities that were classified as the evaluated class. To evaluate the classification performance of the classes from the confusion matrices, some metrics can be used, including accuracy, precision, recall, and specificity. These metrics are computed using the following equations:

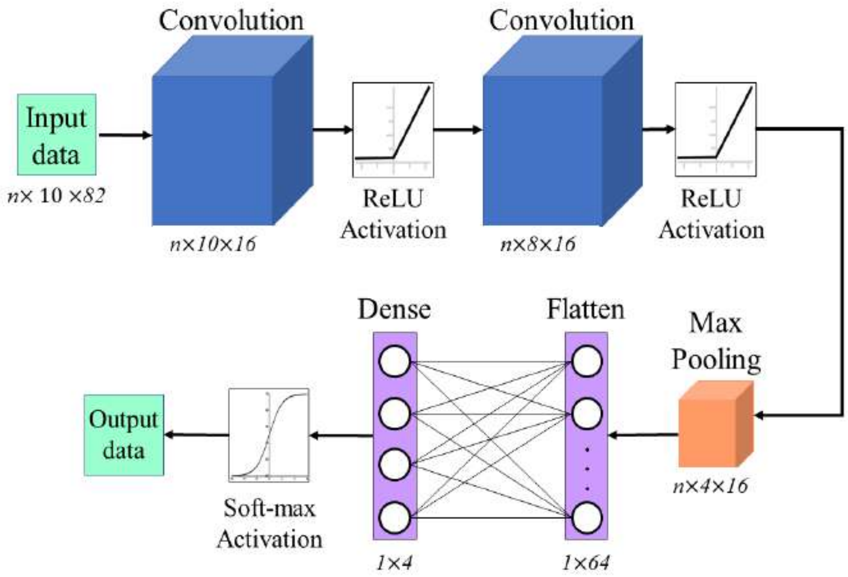

Figure 4.8: The architecture of the CNN network implemented for the classification process, where n is the size of the input data set.

$$Accuracy = \frac{TP + TN}{TP + FP + FN + TN} \tag{4.2}$$

$$Precision = \frac{TP}{TP + FP} \tag{4.3}$$

$$Recall = \frac{TP}{TP + FN} \tag{4.4}$$

$$Specificity = \frac{TN}{TN + FP} \tag{4.5}$$

where accuracy refers to how close the result is to its true value, precision is how close the results are to each other, recall is the proportion of TP that were correctly classified, and specificity is the rate of TN which expresses how well the model can detect a class. The set of results of equations [4.2-4.5] are in a normalized range between 0 and 1, corresponding to 0% and 100% respectively. Furthermore, based on the performance evaluation by confusion matrices, the Receiver-Operating Characteristic (ROC) curve can be computed. This is a graph used to visualize the performance of the model and it represents two parameters: sensitivity and specificity. The Area Under the ROC Curve (AUC) measures the two-dimensional area under the ROC and provides an aggregate measure of performance. The AUC measures how well the predictions of each class are classified and their quality. AUC values range from 0 to 1, where 0 represents that all predictions were incorrect and 1 that they were all correct.

4.5 Results and discussion

The performance of the fall detection platform based on a DL framework was evaluated by taking the results of the LSTM and CNN classification algorithms. The classification was performed with a multi-class approach, taking four different activities from the generated database. The sequence of samples of each activity was assigned a numerical label such that: no activity corresponds to class 1, walking to class 2, going up and down stairs corresponds to class 3 and the falling event is class 4. The confusion matrix generated with the results of the LSTM algorithm is shown in Figure 4.9. From this confusion matrix, we computed the performance metrics that are listed in Table 4.3. The accuracy achieved for this framework was 82.20%. Furthermore, during the training of the network, the loss function of the model was estimated to measure how well the data was learned. In this case, at the end of the training stage, the loss function had a loss value of less than 0.01. The lower this value, the better the model fits the data.

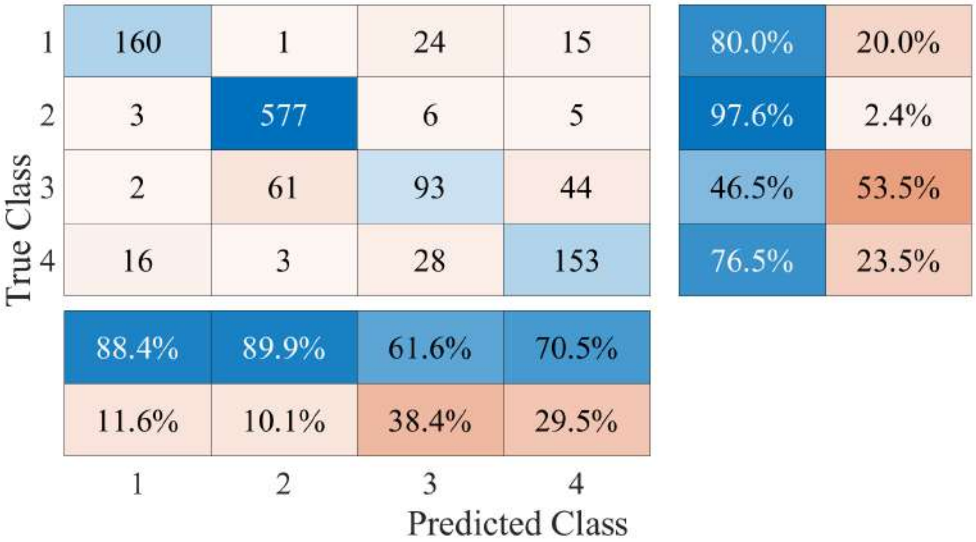

Figure 4.9: LSTM multi-class classification confusion matrix results, where the classes correspond to (1) no activity, (2) walking, (3) going up/down stairs, and (4) falling.

Table 4.3: Results of the metrics computed from the confusion matrices in the LSTM algorithm.

Metric	No activity	Walk	Up/Down stair	Fall
Precision	88.40%	89.90%	61.60%	70.50%
Recall	80.00%	97.60%	46.50%	76.50%
Specificity	97.51%	86.19%	93.88%	92.84%

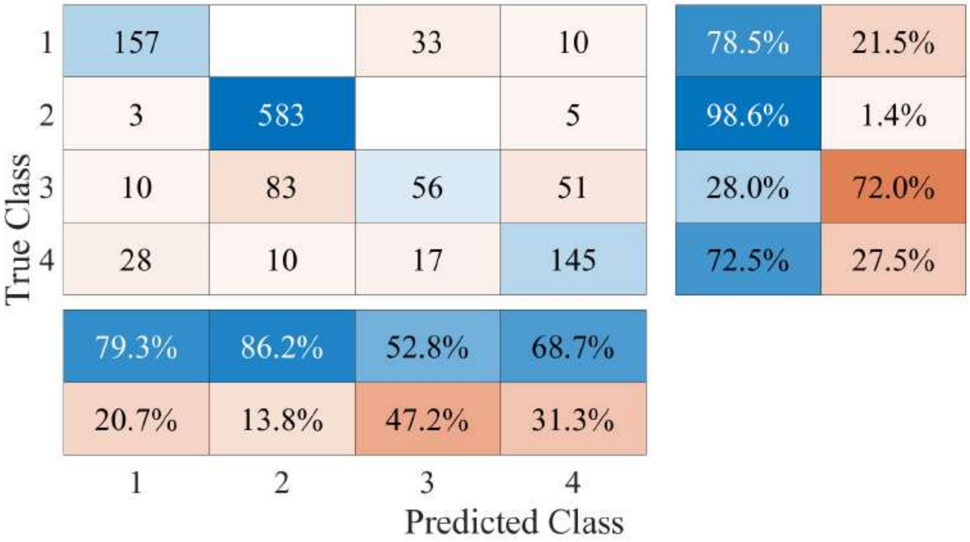

Figure 4.10: CNN multi-class classification confusion matrix results, where the classes correspond to (1) no activity, (2) walking, (3) going up/down stairs, and (4) falling.

Table 4.4: Results of the metrics computed from the confusion matrices in the CNN algorithm.

Metric	**No activity**	**Walk**	**Up/Down stair**	**Fall**
Precision	79.30%	86.20%	52.80%	68.70%
Recall	78.50%	98.60%	28.00%	68.70%
Specificity	95.03%	79.37%	94.65%	92.34%

On the other hand, Figure 4.10 shows the confusion matrix generated with the results of the CNN. Considering the values registered in the matrix, the metrics were calculated to evaluate the performance and are shown in Table 4.4. In this case, the accuracy achieved in the classification of all activities was 78.09%. The loss function of this algorithm was approximately 0.05. Therefore, the CNN classification model was better adapted to learning the data of all the activities.

Comparing the results, the LSTM algorithm obtained the best performance. The performance success rate demonstrates that Doppler signatures can be used as the main feature of classification systems and activity recognition applications. However, the aim of the platform is not to recognize human activities, but to differentiate falls from other classes. This means that the most relevant class is falling, and they must have the highest percentage of precision possible so that elderly people receive the corresponding medical attention. In total, 70.50% of the falling events were correctly detected and classified for the LSTM case and, 68.70% for the CNN. These results indicate that there is a high rate of falls that cannot be detected or are misclassified.

A deeper analysis of the loss function during the validation stage provides us with an overview of how the classification model fits the input data. In the case of the LSTM network, the final value of the loss function had an approximate value of 1.45, which indicates a considerable increase compared to the training. In the case of CNN, the loss value was approximately 0.09. This represents that the model had a loss of performance in identifying the Doppler signatures. Furthermore, as can be seen in Figures 4.9 and 4.10, going up and down stairs activity has the highest percentage of FP that affects the fall class. The complications in distinguishing between these two classes may be because the model had an overfit with the features of these classes during training due to the similarity between the data of both. Therefore, the precision percentage decreases and causes falls to not be correctly detected.

There are several reasons why there might be this difference between activity precision rates. However, we can highlight two in particular. The first reason has to do with the resolution with which the Doppler signatures are captured by the sensing platform. For example, if the spectrograms of Figure 4.6 are considered, it is visible that the fluctuations vary depending on the acceleration that the body has during the development of a specific activity. Walking is an activity that involves a constant and sequential acceleration of the volunteers, which causes the dispersions to be repeated over a long period, and it is sometimes the one with the highest energy. However, even though the activity of going up and down stairs is also sequential, the distance from the antennas and the resolution of the measurement equipment cause the dispersions to be of a lower intensity. Furthermore, empirically, it can be determined that some of these dispersions are similar to those caused by a fall. Therefore, the activity of going up and down stairs can influence the accuracy rate of falls, decreasing their detection.

Another reason that causes a difference in the precision rate of all the activities considered in the experiments with the platform is the number of samples captured. Because the sequential activities represent long periods of experimentation in which the movement can be repeated and sensed for a long time, the data we obtained was extensive. However, in the case of falls, subjecting volunteers to a large number of falls can compromise their health. This is why the number of samples of falls is less than that of other activities. Therefore, there is an imbalance that can cause the fall accuracy rate to decrease in comparison with the other activities.

There are some techniques that can be used to acquire Doppler signatures with higher resolution during experiments. For instance, improved feature extraction inside the network can be achieved by using better RF signal acquisition resolution. Measurement equipment with higher performance can be used to avoid the loss of power of the signals in long-distance indoor environments. Furthermore, sophisticated pre-processing methods

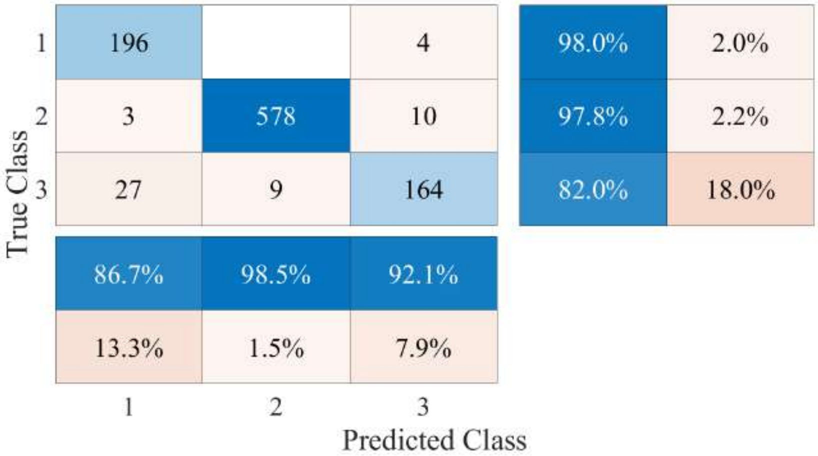

(a) LSTM multi-class classification confusion matrix results.

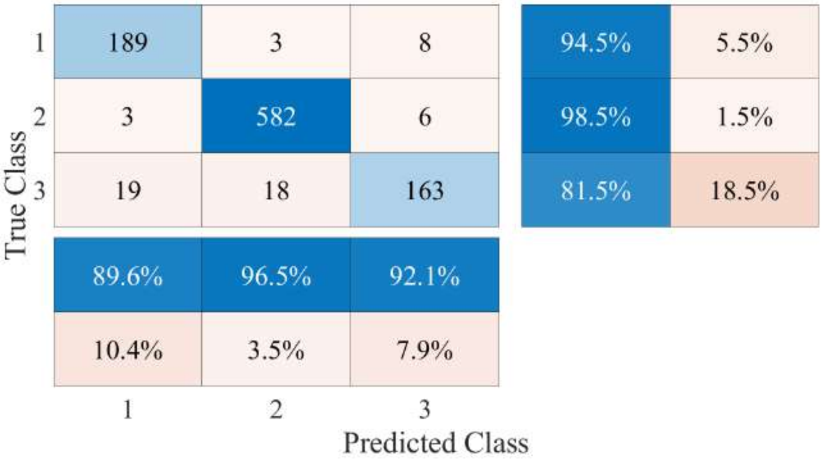

(b) CNN multi-class classification confusion matrix results.

Figure 4.11: Confusion matrices of both classification frameworks where the classes correspond to (1) no activity, (2) walking, and (3) falling.

can be used to enhance classification. However, due to the physical difficulties and the risk involved for an elderly person going up and down stairs. This sector of the population has been limited to living in one-story houses. Therefore, we can limit the range of activities in our multi-class approach to only those that generate enough Doppler spread to be captured by the sensing platform. Following the sensing process previously described, the experimental protocol was repeated only by considering the classes of no activity, walking, and falls. In this way, the same DL architectures were used for data classification. The system was tested and analyzed following these metrics and the results were used to compute the confusion matrices shown in Figure 4.11. From the confusion matrix in Figure 4.11a, the accuracy of the LSTM algorithm was calculated and a value of 94.95% was obtained. This result had a considerable increase when compared to the scheme that

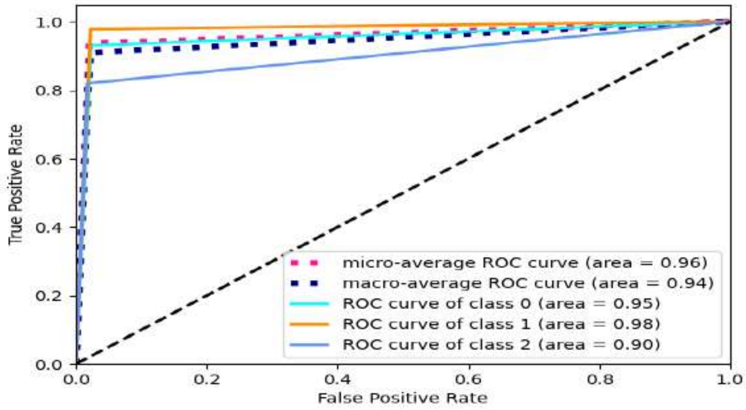

(a) LSTM ROC curves.

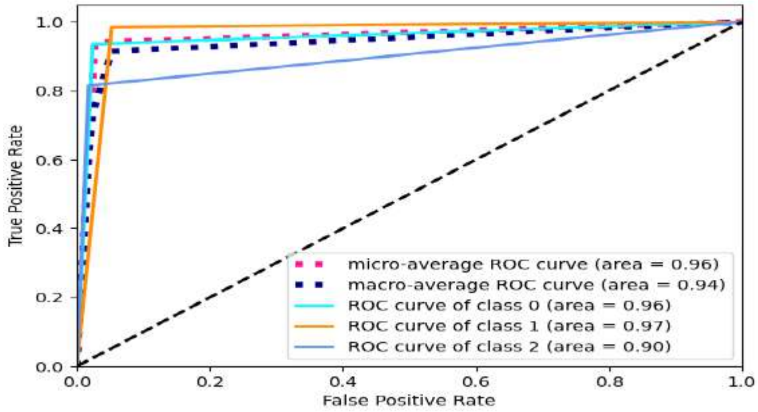

(b) CNN ROC curves.

Figure 4.12: ROC curves computed for both classification frameworks where class 0 corresponds to no activity, class 1 to walking, and class 2 to falling.

considers the 4-class classification. The precision in falls also had an improvement with a percentage of 92.1% and a recall of 82.0%. On the other hand, using the CNN architecture, the accuracy achieved was 94.25%, an improvement of more than 16%. Falls reported a precision of 92.1% with a sensitivity of 81.5%. Notably, the results in both algorithms were very similar, in addition, they reported a false alarm rate with a maximum of 7.90%.

The other metric implemented to compare both classification frameworks was the ROC and whose graphs are shown in Figure 4.12. The graphs in figures 4.12a and 4.12b show a low rate of FP for both classifiers. This behavior is expected in falling detection applications where the model's performance needs to be maintained during the learning stage of the different classes of activities. The AUC for both schemes was 90%, which means that the quality of the predictions made by the algorithms is desirable.

The precision values of a human fall detection system have to be as close to 100% as possible. This is because if there is an error in the sensing and a fall is not detected correctly, it can trigger a series of complications in the health of the elderly. As could be observed, our efforts were focused on increasing the precision values of the falls above any other activity. The results obtained validate our platform as a high-precision sensing system comparable to the majority of works published in this area. For example, in [78] the authors computed the CSI of WiFi signals and with a CNN methodology, they obtained a percentage of 93.3% in fall detection. Works such as those presented in [21] and [77] used specialized high-resolution equipment such as Doppler radars to analyze the spectrograms of the signal. In this case, 95.00% and 95.60% precision were obtained in the fall class, respectively. Our platform achieves similar levels of accuracy without the need for specialized equipment such as radars or complex feature extraction, as in the case of CSI estimation. Furthermore, the system was tested under extensive indoor environment conditions, with antenna locations up to 7 m. Therefore, our human fall recognition system prioritizes the precision rate to be as high as possible and achieves this using SISO communication without involving multiple antennas.

4.6 Conclusions

In this chapter, we analyze the performance of a fall detection platform based on CW RF signals using a multi-class DL framework. Using this platform, we collected data from probe signals containing Doppler signatures generated by people movement in an indoor environment. The activities of the experimentation protocol included: walking, going up and down stairs, non-activity, and falls. Furthermore, we compute the spectrograms of each sequence of activities in the collected data to extract the features of the Doppler signatures. The spectrograms were divided into a training set and a validation and test set to be used in a DL framework. We compared the performance of two different multi-class classification approaches, an LSTM network, and a CNN. The results showed an overall accuracy of 82.20% for the LSTM algorithm, with an precision of 70.50% in fall detection. On the other hand, CNN reported an overall accuracy of 78.09% and a fall detection precision of 68.70%. We note that elderly people have physical limitations to perform complex or highly mobile activities such as going up and down stairs. Therefore, we consider an experimental scenario where these kinds of activities are not carried out. We center our efforts on sensing the activities of elderly people that live independently in one-story homes. In this way, the overall accuracy of the LSTM algorithm reached 94.95% and a precision of 92.1% in fall detection. Moreover, CNN also increased the overall accuracy and reached 95.25%. In this case, the fall detection precision also achieved 92.1%. These results demonstrate that the features extracted from the Doppler signatures can be used in different classification frameworks with high levels of accuracy. Therefore, our platform could be used to monitor and detect falling events with a high accuracy rate. In addition, our methodology allows the integration of radio sensing and joint communications by using an RF probe signal similar to the pilot subcarriers of commercial WiFi systems. Nevertheless, the platform cannot be used to distinguish low-acceleration activities from the human body and is limited by these sensing capabilities. As future work, we will seek to increase the resolution of the captured Doppler signatures using other pre-processing techniques and a methodology to capture the signals with a better balance between acquisition time and frequency resolution.

Chapter 5

Fall Detection using WiFi Signals with Doppler Frequency Diversity

Human fall sensing using radio frequency (RF) signals transmitted by WiFi access points is considered a low-cost and non-invasive solution for elderly home care. Several proposals have considered the use of multiple sensors to diversify the information gathered from RF signals and, as a result, extract more redundant features that improve system precision. In consequence, the system demands high-performance signal processing and complex hardware, resulting in an expensive solution. Frequency dispersions called Doppler signatures are produced when RF signals interact with human movement. Systems for detecting falls can involve Doppler signature analysis. In a frequency diversity radio sensing (RS) scheme, the Doppler signature information is diversified through the multiple transmitted subcarriers without increasing the number of sensors. However, this RS scheme needs to demonstrate its feasibility in fall detection and determine if diversification of features improves the accuracy. This work presents the proof of concept of this scheme, where the results obtained in fall detection reached up to 98.10% precision.

5.1 Introduction

Wireless local area networks (WLAN) are ubiquitous communication systems available in various environments such as homes, offices, industries, universities, hospitals, etc. Recently, radio frequency (RF) signals transmitted by these communication systems have been used to develop sensing applications. This is possible because radio sensing (RS) systems share similar hardware and signal processing characteristics with WLAN. The main

---

This chapter forms part of the paper titled 'Fall Detection using WiFi Signals with Doppler Frequency Diversity" submitted in *Consumer Electronics Magazine, IEEE*. The authors gave their consent to use their work as an integral part of this dissertation.

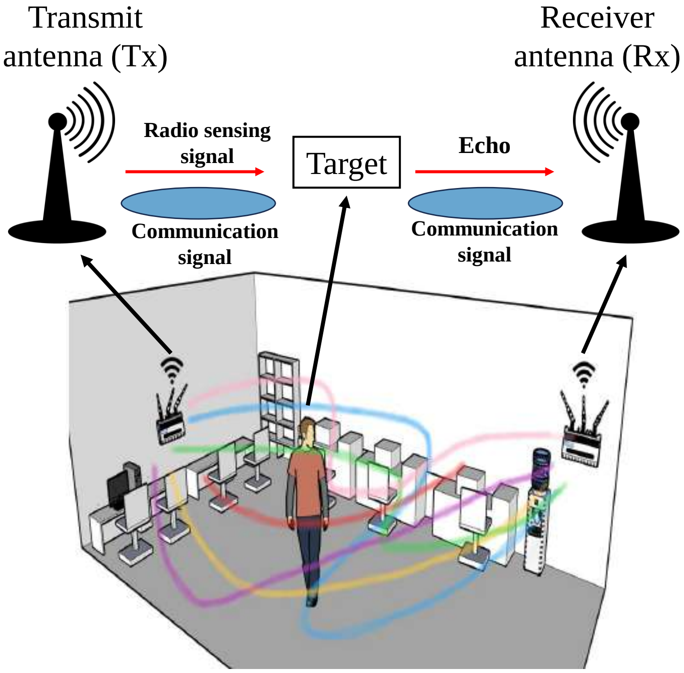

Figure 5.1: Overview of the operation of a joint radio sensing and communication system.

idea is to use the signals received by consumer electronic devices, such as WiFi access points (AP), to extract the characteristics that describe their propagation. Afterward, human activities can be characterized using signal propagation modeling. Thereby, joint RS and communication (JRSAC) systems can be developed to reduce the infrastructure cost for their operation and promote non-invasive sensing. An illustration of the operation of these systems is shown in Figure 5.1.

The detection of human falls is one of the RS applications for indoor environments that has drawn the most attention. This is the second most common reason for preventable death worldwide [25]. Additionally, it is important to identify and report falls in senior persons who live independently as soon as possible in order to lower the risk of complications that could harm their quality of life. Furthermore, prompt medical attention can reduce the incidence of fatalities.

Several proposals have been presented for the RS of falls using or emulating simple point-to-point WiFi communication systems [20,92,93]. However, the accuracy of these systems has been limited because when the same human activity is observed from different angles of the AP antennas, the characteristics extracted from the signals differ and are complex to characterize [18]. One solution to this has been the deployment of multiple antennas to diversify the information collected in the same indoor environment. Nevertheless, adding more hardware implies the design of new platforms and complicates the reuse of consumer electronics and grows the demand of computational resources for signal processing.

An alternative to the deployment of multiple antennas is to use signal diversity techniques to take advantage of the propagation properties of wireless signals and diversify the information on the effects generated by human movement. The frequency diversity technique involves transmitting a carrier signal at different frequencies. This mitigates frequency selective vanishing by averaging the propagation effects across multiple frequencies. Therefore, more redundant information can be extracted from the effects registered in each subcarrier that facilitates the characterization of its principal features.

One of the propagation effects, which has shown its potential for fall detection, is the dispersion in frequency called the Doppler signature [18]. Doppler signatures are caused when a moving object interferes with the propagation of a continuous wave and forms a characteristic pattern of shifted frequencies. Furthermore, in a wireless signal propagation scheme using frequency diversity techniques, this pattern is recorded by the multiple subcarriers. However, the information that can be extracted using this scheme has not been analyzed for fall detection applications. Therefore, it is necessary to demonstrate that frequency diversity is a viable alternative for the diversification of the information collected by RF signals for fall detection.

This chapter describes an RS fall detection strategy that employs a frequency diversity technique for broadening the propagation effects information. To demonstrate its feasibility, three pilot sub-carriers with characteristics similar to those used by the IEEE 802.11 g, n communication protocols were used. With these signals, a series of fall events were sensed to capture their characteristic Doppler signatures. The unique patterns generated are characterized to be distinguished from other activities of daily living, such as walking. Automation in the characterization process of these two events can be accomplished through artificial intelligence models, such as deep learning (DL). Due to the event-sequential nature of our experimental protocol, a variation of the recurrent neural networks (RNN) used in DL known as long-short-term memory was selected. The results showed that the data collected with the frequency diversity technique supplied enough information to classify falls with up to 98.10% accuracy without increasing the number of sensors.

5.2 Background and motivation

Accuracy in fall detection through JRSAC has been limited primarily by scarce real-world fall data [21, 40].Although experiments have been carried out to collect data from volunteers, due to the nature of falls, a large amount of information is needed to characterize the random movements of each person [20,92,93]. Therefore, it is necessary to obtain feedback or diversification of the propagation effects that RF signals have when interfered with by human movement during a fall to favor the learning process of classification models and thus increase their accuracy.

Another concern that has arisen during the collection of data on human falls is the observation angle that RS equipment has. The effective range of sensing obtained with RF signals can fluctuate depending on the size of the experimental scenario or the influence on the orientation and positioning of the antennas [18, 40]. This means that the propagation effects in the signals can be attenuated or differ in the information extracted if the same activity is observed in a different location. Therefore, the fall characterization process can become complex and limit the accuracy rate in its classification.

The deployment of multiple antennas has been proposed as a solution to the diversification issues and the variations in propagation effects of the data collected during the RS. The authors in [92] diversified WiFi channel state information (CSI) using 2x2 MIMO communication having four pairs of antennas for each captured subcarrier signal. On the other hand, in [93], the authors used the information on the angle of arrival of the CSI obtained through two receivers positioned in the same indoor environment. However, using these schemes with multiple inputs and outputs requires more hardware and high-performance signal processing, resulting in an expensive solution. Furthermore, it moves away from the objective of the JRSAC systems, which is intended to reuse consumer electronics.

This has motivated research to explore other methods, such as the frequency diversity technique, to expanding the information gathered in RF signals. This technique is already implemented in consumer electronic devices such as AP that operate under the IEEE 802.11 g and n communication standards. In this case, various pilot subcarrier signals are transmitted at different frequencies to estimate and compensate for transmission channel effects. However, with this frequency separation, the information on particular propagation effects, such as Doppler signatures, can be diversified. This is because all subcarriers transmitted in a communication frame are equally affected by interference from human movement. Therefore, more significant information can be extracted from the same event without the need to use more antennas.

The information from the Doppler signatures gathered in RF probe signals with similar characteristics to the pilot carriers has already been used for fall detection with promising results [20]. However, it has not been demonstrated that the diversification of its principal features through a scheme based on the frequency diversity technique improves the accuracy rate of intelligent classification models. Therefore, it is necessary to demonstrate that the Doppler frequency diversity RS scheme is a viable alternative to improve fall detection without introducing more antennas.

5.3 Overview of the RS system for fall detection using frequency diversity technique

RS systems based on Doppler signatures use a transmitter (T_X) of RF signals to propagate them in an indoor environment. If the system uses a frequency diversity technique, the subcarriers must have a separation between them to avoid interference. These separations can vary depending on the needs of the communication channel, but the parameters established in protocols such as IEEE 802.11 g, n can be considered where multiple pilot carriers are transmitted.

Once the signals are transmitted in the indoor environment, a receiver (R_X) captures them. Through signal processing techniques, the information of the Doppler signatures can be extracted and characterized depending on the event that generated them. However, in applications that require continuous sensing, the amount of information collected is extensive. Furthermore, considering the use of the frequency diversity technique, the number of subcarriers that can be analyzed is also increased. Therefore, in these systems, the use of intelligent detection techniques is required, which can automate the analysis and characterization of high-dimensional data.

Intelligent fall detection can be performed through different data analysis techniques based on artificial intelligence models. In these models, a learning process is used to classify the Doppler signatures that are entered as input. Also, some of these models improve their learning process if the dimensionality of the data is more extensive. Therefore, for the design of fall detection systems, it is necessary to compare and determine the model that best adapts to the analysis of the information provided by the Doppler signatures.

5.3.1 Frequency diversity using general-purpose measurement equipment

For the proof of concept of this system, we transmit three continuous wave probe signals that resemble the pilot carriers in the AP WiFi but can be generated by general-purpose equipment. This methodology makes it possible to focus the analysis of the Doppler signature information without directly involving the communication system. As T_X, we use a Keysight N9310A RF generator that allows the probe signals to be transmitted with a separation of up to 500 Hz between them. Furthermore, we use a pair of commercial omnidirectional monopole antennas for WiFi AP. The best coupling of these devices was obtained when using a central transmission frequency of 2.42 GHz. At this operating frequency, our system is within the IEEE 802.11 g, n standard, where multiple pilot carriers are also considered.

On the other hand, the Rx was a Keysight FieldFox N9912A spectrum analyzer. This was configured to capture the probe signal frame with an approximate acquisition time of 0.27 s and a frequency span of 1.5 kHz. The acquisition time and the resolution with which the subcarriers are captured are directly related, and it is necessary to find a balance since the falls occur in a very short period.

5.4 Experimental measurements

A measurement campaign was carried out to collect as much information as possible to capture the Doppler signatures frequency diversity of the fall events. Furthermore, it is essential to measure other activities of daily living that can be compared with falls to determine if there are unique patterns that help differentiate them. In our case, we divided the experiments into two different classes: the falling class and the walking class. Walking is a sequential movement carried out at an almost constant speed and is one of the most common in elderly people. Therefore, the Doppler signatures of both motions can be compared to determine if their features can be differentiated.

The participation of eleven adults was requested, who were physically evaluated so as not to put their health at risk during the experiments. Furthermore, the participants signed an informed consent report required for this type of experimentation. Each of the subjects simulated a falling event during a faint for a total of 20 repetitions. On the other hand, for the activity of walking, the participants moved constantly in a space of 7 meters performing 30 repetitions in total.

5.5 Pre-processing and Doppler signature analysis

One of the issues when capturing probe signals is that they are affected by the additive white Gaussian noise of the measurement equipment. The contribution of this noise component is not of interest to the analysis of the Doppler signatures and it is necessary to eliminate it. For this, we consider a thresholding process where signal values below the average noise level are discarded. In our case, the RF CW signal has the contribution of the Gaussian noise, the pilot sub-carrier signal, and the Doppler spread generated by the movement. The average noise level is measured by omitting the contribution of the pilot subcarrier, of which we know its center frequency and bandwidth in each received RF signal. Once measured, this noise value is set as the threshold value. To ensure that significant features of the Doppler signatures were not removed using this thresholding, the formula for measuring the maximum Doppler obtained during a falling event was used, such that

$$\Delta f_{\max} = \frac{2v}{c} f_c, \tag{5.1}$$

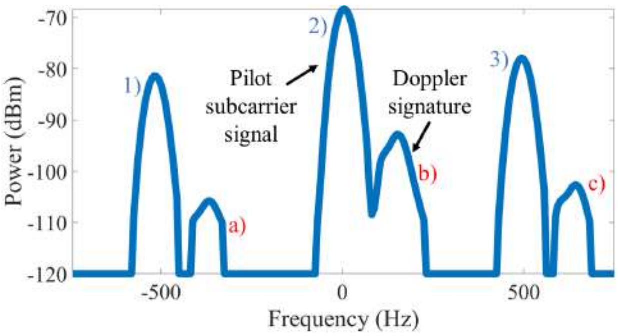

Figure 5.2: Frequency spectrum during a falling event.

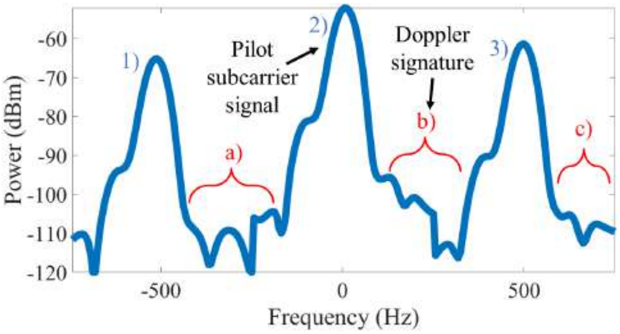

Figure 5.3: Frequency spectrum during a walking event.

where the average speed that an adult person reaches during the fall is $v = 5\ m/s$, $c = 3 \times 10^8\ m/s$ is the constant of the speed of light, and f_c is the central frequency of 2.42 GHz. Therefore, during the thresholding process, values within the range of the maximum Doppler frequency and the center frequency of the pilot subcarrier were preserved. The signals resulting from this pre-processing and their principal components are shown in Figures 5.2 and 5.3.

On the other hand, the variations of the Doppler signatures can be analyzed using a great variety of time-frequency analysis techniques. However, the analysis of spectrograms is a technique that has been widely used in non-stationary RF signals and the identification of interferences since it provides a graphical representation of the signal components. Furthermore, it shows the spectral density of the signal over time, which can be used to analyze how its energy is distributed and determine the patterns of each experimental scenario. The spectrograms of each event recorded during the experiments were computed using the concepts presented in [49]. Figure 5.4 shows the spectrogram of a fall event and some of its principal frequency components. The Figure 5.5 shows a spectrogram in a scenario where a constant walk was performed. The changes in the Doppler signatures at these time intervals demonstrate that characteristics of Doppler signatures can be profiled to differentiate between them. Therefore, we selected this technique to construct a Doppler Signature Frequency Diversity dataset that can be

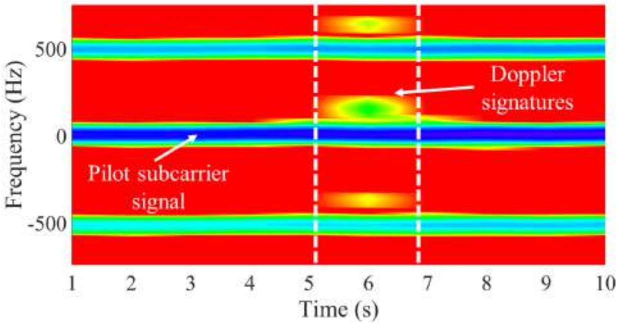

Figure 5.4: Spectrogram computed for falling event.

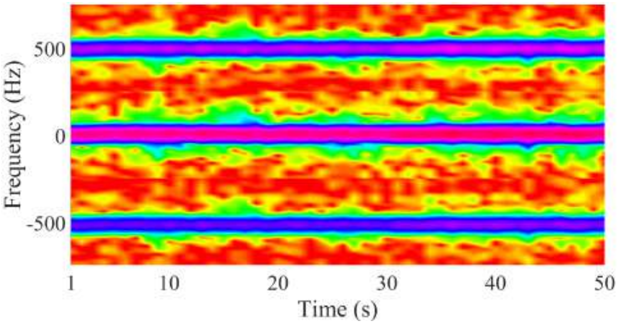

Figure 5.5: Spectrogram computed for walking event.

analyzed and characterized by automatic learning classification models.

5.6 Doppler signatures as features in a classification model

Different classification methods based on artificial intelligence can be applied to categorize Doppler signals and use them as a detection parameter in a fall detection system. These techniques have the advantage that they can be used to build intelligent data-based systems capable of automating applications with a high data dimension, such as monitoring human activities. They can be divided into two main approaches: feature-based and model-based.

5.6.1 Feature-based

In the feature-based classification approach, a set of desired features is initially extracted, which will then be clustered according to the class they belong to, as shown in Figure 5.6. With these algorithms, the separability of the classes depends on the variability of the extracted features, so it must be guaranteed that redundant information will be discarded. In our case, walking is a sequential low-speed activity, while when a person falls,

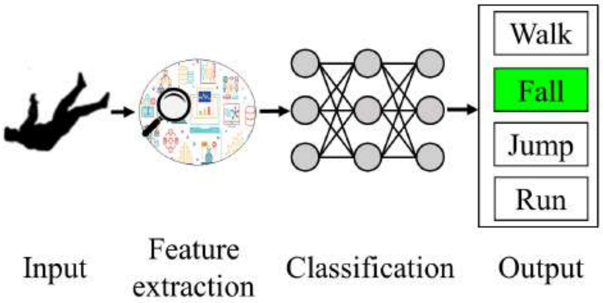

Figure 5.6: Feature-based classification approach.

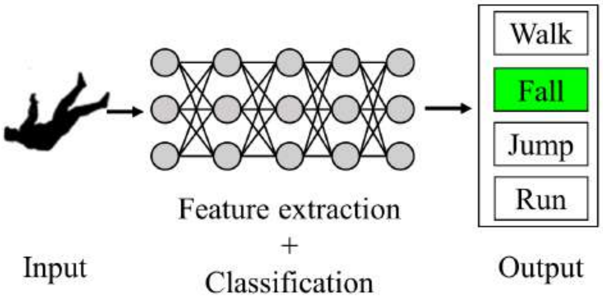

Figure 5.7: Model-based classification approach.

it is unexpectedly at a high speed. However, as shown in Figures 5.2 and 5.3, the Doppler signatures have similar dispersion and power, making the information redundant and complex to discard. Therefore, with this classification approach, the automation of falling sensing and detection requires many additional processes and analyses.

5.6.2 Model-based

On the other hand, in the model-based approach, the feature extraction stage is carried out automatically (Figure 5.7). This is possible because the data is abstracted as information models using discriminative functions that extract its highest-level features [24]. Furthermore, DL is a model-based approach that uses artificial neural networks (ANN) with different discriminative functions depending on the application. There is a neural network that has been used to analyze and discriminate information from time-series data known as RNN [91]. These networks are well suited to applications that contain sequential event data such as a person's walking and can detect transient anomalies in those patterns such as falls. Specifically, we use a variant of these networks known as LSTM because it minimizes gradient fading issues [24].

We take the architecture of a LSTM network following the methodology

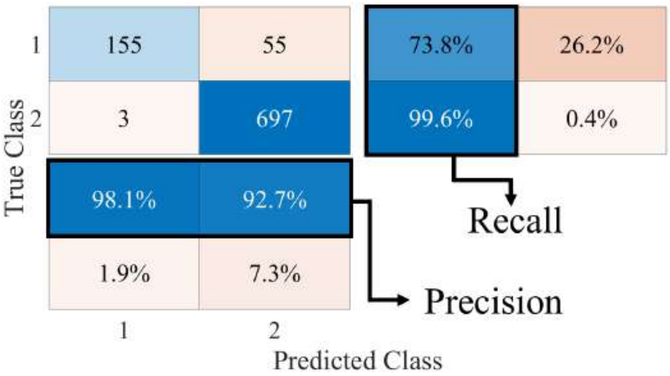

Figure 5.8: LSTM multi-class confusion matrix results, where the classes correspond to (1) falling event and (2) walking.

shown in [20]. In our case, the LSTM network took 80% of the computed spectrograms to construct the training set of the network and 20% for the test. Furthermore, two sequential layers of 100 artificial neurons activated by a rectified linear unit (ReLU) were taken. In the network, a dense layer with a soft-max activation function was used to classify the two activities. Finally, the performance of the network can be measured through the confusion matrix and its associated metrics (accuracy, precision, recall, and specificity) [26]. These metrics will determine if the Doppler signatures contain the necessary information to distinguish each of the activities and be used as the main feature of fall detection systems.

5.7 Results

In Figure 5.8, we present the confusion matrix that is generated with the data resulting from the LSTM classification model. The class marked as 1 corresponds to the event of falls whose Doppler signatures were recorded in the spectrograms. Class 2 includes all the events where the walking of a person was recorded.

The system's accuracy was 93.63%, which indicates that most of the samples were correctly classified and the performance of the model is high. The precision of the system detecting falls was 98.10%. These values indicate that the model can extract the most relevant information from the Doppler signatures of a fall and accurately predict the class to which they were assigned. Therefore, a DL system with these characteristics can be adjusted to the analysis of this data and have an adequate performance to detect the majority of falling events. However, it is necessary to compare the performance obtained with these metrics with the others provided by the confusion matrix to have a complete vision of the model.

Table 5.1 presents the results of the rest of the performance metrics that were computed using the output data of the LSTM classification algorithm.

Table 5.1: Performance metrics computed from the resulting confusion matrix of LSTM algorithm.

Metric	Falling	Walking
Precision	98.10%	92.70%
Recall	73.80%	99.60%
Specificity	98.10%	92.68%

The values show that by using the information from the Doppler signatures, the accuracy rates detecting both movements are elevated. This represents an increase in precision in detecting multiple classes compared to systems that only use the information of a single carrier signal such as those shown in [20]. However, the recall in the detection of falls was 73.80%. A low recall percentage indicates that some samples did not register a pattern in the Doppler signatures close enough to that learned by the model, so they were not detected.

One of the reasons that the Doppler signatures did not record redundant dispersion patterns across all measurements was variations in the acceleration of falls. Our experiments involved a series of fall simulations with a group of people with different physical characteristics. In some individuals, the acceleration recorded during their movement was low, causing the frequency dispersion to have values similar to the noise components or static objects. Therefore, it is necessary to consider a measurement equipment configuration that allows a suitable trade-off between resolution and acquisition time.

Finally, another of the considerations is the bandwidth of the pilot subcarriers. When the subcarrier signals have an adequate separation, noise decorrelation is promoted, which prevents the appearance of artifacts or interference. In our case, three subcarriers were used with a separation between them limited by the general-purpose measurement equipment. This separation may not be enough to avoid interference between the dispersions of each subcarrier. Therefore, the extraction of features from Doppler signatures is a challenge for DL algorithms. However, if it is considered that the same scheme can operate under the characteristics of the IEEE 802.11 g and n communication protocols where the separation between carriers is up to 20 MHz, these problems can be mitigated.

5.8 Conclusions

This chapter has introduced a RS scheme for fall detection using a frequency diversity technique to improve the accuracy rate by spreading the information extracted from Doppler signatures. The main contribution of this work was to use general-purpose equipment to demonstrate that frequency diversity is an alternative technique to using multiple antennas to extract more redundant data from RF signals. The precision rates obtained for the experiments with authentic fall events showed the feasibility of integrating this scheme into the joint RS and communications paradigm. Furthermore, the information on the Doppler signatures recorded by the pilot subcarriers can be extracted without a complex process. Therefore, they are features that can be exploited for falling events detection in a signal diversity scheme.

The principal features of the Doppler signatures were extracted by a DL-based classification model. This is the model that best adapted to the needs of the system after having made a comparison between the two most used approaches for data classification. Due to the recurring nature of the recorded movements, the LSTM algorithm was used to determine if the precision rate in detecting falls could reach high percentages. The results demonstrated the feasibility of using this scheme for RS systems in interior environments. However, the recall of the system needs to be increased to prevent the rate of true negatives from being high. In future work, we will use the frequency diversity technique under conditions more similar to those used by commercial devices to improve the resolution-capture time trade-off and improve recall.

Chapter 6

Experimental Assessment of a Forward-Collision Warning System Fusing Deep Learning and Decentralized Radio Sensing

Connected and autonomous vehicles rely on a variety of sensors for timely detection of nearby vehicles, whose proximity and trajectory could pose a collision threat. In this context, radio sensing (RS) is emerging as a complement to the capacities of acoustic, infrared, laser, and video sensors. RS is gaining momentum also due to its potential for seamless integration with radio communication systems, through a common design paradigm known as joint RS and communications (JRSAC). However, current proposals for vehicular RS are based on radar systems, whose integration into the JRSAC framework is far from trivial, as the waveforms and signal frame structure of radars are not tailored for data transport. Moreover, vehicular radar systems follow a centralized approach in which each vehicle independently performs the transmission, reception, and processing of its own radar signal. The integration of this centralized sensing approach with vehicular communication systems (VCS) operating in half-duplex mode is also a nontrivial open problem. This chapter explores an alternative for RS based on a decentralized approach where a vehicle in receiving mode employs a continuous waveform (CW) transmitted by a second vehicle as a probe signal to detect oncoming vehicles and warn the driver of a potential forward collision. Such a CW can easily be incorporated as a pilot signal within the data frame of current multicarrier VCS. Detection of oncoming vehicles is performed by a deep-learning (DL) module that analyzes the features of the Doppler

---

This chapter forms part of the paper titled "Experimental Assessment of a Forward-Collision Warning System Fusing Deep Learning and Decentralized Radio Sensing" submitted in *Intelligent Transportation Systems Magazine, IEEE.* The authors gave their consent to use their work as an integral part of this dissertation.

signature imprinted on the CW probe signal by a rapidly approaching vehicle. This decentralized CW RS approach was validated experimentally using data collected by a series of field trials conducted in a high-speed highway near the city of San Luis Potosí, México. Detection performance was evaluated for two different DL models: a long short-term memory network and a convolutional neural network. The obtained results demonstrate the feasibility of a forward collision warning system based on the fusion of DL and decentralized CW RS.

6.1 Introduction

Forward collisions between vehicles are road accidents that cost many lives each year [72]. Such accidents are caused mainly by driver distractions and external factors affecting the driver's capacity to perceive other vehicles, such as weather and traffic conditions. This problem has prompted the development of driving assistance systems that employ a variety of sensors for automatic detection and alerting of vehicles whose proximity and trajectory could pose a collision threat. The sensors employed for such applications are primarily based on ultrasonic [94], infrared [95], video [1,2], and laser [3] technology. These sensing technologies are well understood and already incorporated in modern smart vehicles. Nonetheless, further research is still required to cover the limitations inherent to each type of sensors. For example, ultrasonic and infrared sensors are affected by weather factors like fog, snow, and rain. On the other hand, video sensors depend on good lighting, whereas laser-based sensors rely on a precise pointing to target.

Radio sensing (RS) is emerging as an option to complement the capacities of the aforementioned sensors. This technology leverages on the mechanisms of reflection, scattering and Doppler dispersion of radio-frequency (RF) signals for target detection, i.e., for the detection of nearby vehicles. Environmental conditions and the lack of a line-of-sight (LOS) with the target do not represent major limitations for RS systems. Moreover, the interest in RS has increased in recent years due to the potential of this technology for seamless integration with vehicular communication systems, through a design paradigm known as joint RS and communications (JRSAC) [96]. In this paradigm, the sensing process and the transmission of data between vehicles are simultaneously performed by means of a common RF signal. This can be accomplished because the hardware resources required for both applications are similar and can be shared to transmit and receive a single signal that serves both purposes.

Radars are the prevailing form of RS. In fact, some forward collision warning systems based on radar technology have already been developed and are in the verge of market deployment. However, the integration of radars into the JRSAC framework is a challenging research problem, mainly because the waveforms and signal frame structure of radars are not tailored for data transport. An increasing number of research projects are currently underway with the aim of finding efficient solutions to this problem, e.g., see [97,98]. The integration of radars within the JRSAC framework is further complicated by the centralized approach of these sensing systems, whereby each vehicle independently performs the transmission, reception, and processing of its own radar signal. Such a centralized approach entails full-duplex transmission capacities. This is in contrast with the characteristics of vehicular communication systems (VCS) based on current dedicated short-range communications (DSRC) [22] and cellular vehicle-to-everything (C-V2X) [23] standards, whose specifications consider a half-duplex (simplex or dual-simplex) transmission mode.

In this chapter, we explore an alternative for automatic forward collision alerting that follows a decentralized RS approach, where a vehicle in receiving mode employs an RF signal transmitted by a second vehicle as a probe to detect other oncoming vehicles. The probe signal is a continuous waveform (CW) that can be easily appended to the data signal in a process analogous to the transmission of pilot subcarriers within the data frame of modern multicarrier communication systems. Oncoming vehicles are detected by the receiver (R_X) based on the Doppler signature that a rapidly approaching vehicle imprints on the CW signal. A deep-learning (DL) module is employed for the timely recognition of such Doppler signatures. We assessed the feasibility of such a decentralized CW RS approach by a series of field trials conducted in a high-speed highway near the city of San Luis Potosí, México. The aim of these experiments was to collect realistic information about the Doppler signatures produced by vehicles approaching the R_X on a potential collision path. The aim was also to gather an empirical data set comprising a variety of Doppler signatures produced not only by oncoming vehicles but also by other relevant events. Using this data set, we evaluated the detection performance of our decentralized CW RS system by considering two different DL models: a long short-term memory (LSTM) network and a convolutional neural network (CNN). To the best of the authors' knowledge, this is the first experimental demonstration of a forward collision warning system based on the fusion of DL and a decentralized CW RS approach. We note, nonetheless, that a CW RS system for vehicle-to-infrastructure communications was presented previously in [99]. However, this system follows a centralized approach.

The remainder of this chapter is organized as follows. The RS scenario that motivates this research work is described in detail in Section 6.2. Section 6.3 provides an overview of our measurement platform and experimental protocol. The empirical data collected during our measurement experiments are described in Sections 6.4 and 6.5. Section 6.6 shows the architecture of the DL algorithms and the data set generated by the experiments. In Section 6.7 we present and discuss the results of the system performance evaluation. Finally, we give our conclusions in Section 6.8.

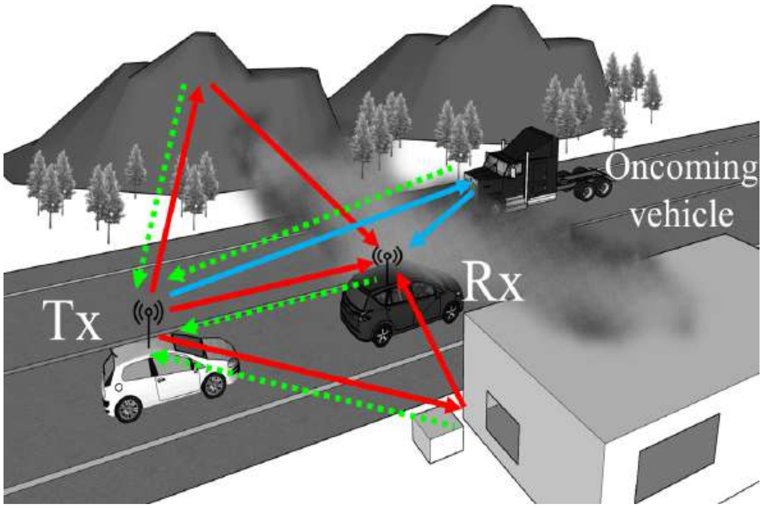

Figure 6.1: Centralized approach for a JRSAC system, where the solid blue and red lines correspond to the communication link and the dotted green lines represent the reflected component of the signal for the RS.

6.2 The forward-collision warning system based on decentralized CW RS and DL

The focus of this research work is on the automatic alerting of a potential forward collision under the conditions illustrated in Fig. 6.1. In particular, we consider a RS scenario where two vehicles are driving in the same direction, one behind the other. The rear vehicle transmits a large number of data frames on an uninterrupted basis to the vehicle in front, as in the case of video streaming. The communications between the transmitter (T_X) and R_X are assumed to follow a half-duplex vehicular communications standard, implying that only one vehicle can transmit at a time. The two vehicles are approached from ahead by a third vehicle driving on an adjacent lane, in a trajectory that poses a potential risk of frontal collision for the R_X. In the centralized JRSAC framework, each vehicle relies on the transmission of its own RF signal for threat detection. Hence, in the scenario illustrated in Fig. 6.1, the T_X would be in capacity of detecting the oncoming vehicle, but the R_X would be unable to do it, as it should remain silent during the reception of data of the T_X. The situation can be even more critical for the R_X if its visibility toward the oncoming vehicle is compromised, e.g., by a fog bank, as depicted in Fig. 6.1. The R_X could of course maintain its sensing capacities, for example, if it switches from a JRSAC mode to a disjoint mode in which the transmission of a pure sensing signal is activated at a frequency band different from that of the communications signal. However, this solution requires additional hardware resources and is not in line with the premise of using the same signal for data transmission and sensing.

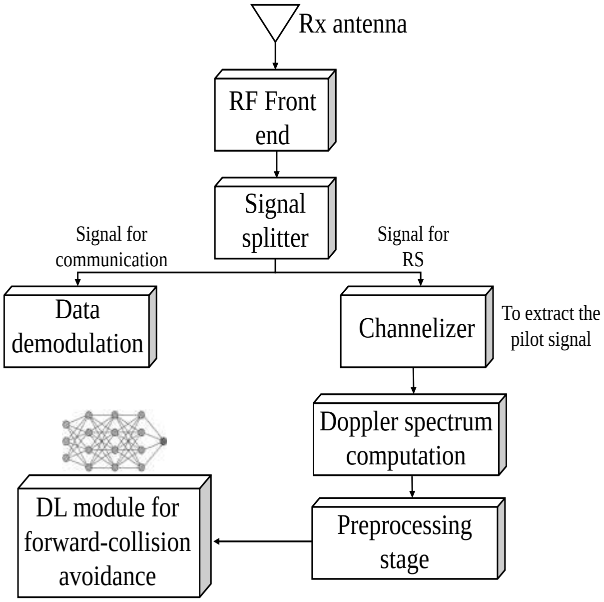

Figure 6.2: Block diagram of the forward collision warning system in the R_X.

An alternative that does not depend on additional hardware resources is to extract information about events happening around the R_X directly from the data signal of the T_X. This can be accomplished, e.g., by analyzing the spectral features of the signal reflected toward the R_X by the oncoming vehicle (the trajectory of this signal is indicated by the blue arrows in Fig. 6.1). Such a decentralized RS approach does not require re-engineering of the multicarrier waveforms of current VCS. This is because the spectral signature of the oncoming vehicles can be detected by computing and analyzing the Doppler spectrogram of the pilot signals embedded in these waveforms. The features of the Doppler signature imprinted by the oncoming vehicle on the spectrogram of any of such pilot signals can be characterized and classified with the aid of modern DL techniques. A flow diagram of the received signal processing required to implement this idea is shown in Fig. 6.2. This detection strategy is similar to that described in [20] for the detection of human falls employing WiFi signals for RS. However, the feasibility of this idea for decentralized RS in vehicular environments has yet to be verified. This paper aims to provide insight in that regard by employing empirical data to train and assess the performance of a DL-based system for the automatic detection of oncoming vehicles. The first step toward this goal is the gathering of empirical data to obtain a realistic description of the Doppler signatures of oncoming vehicles. Such a task is described in the following section.

Table 6.1: Overview of the measurement equipment configurations.

Equipment	Parameter	Value
Transmitter (T_X)	Carrier frequency	760 MHz 2.5 GHz
	Output level	20 dBm
Receiver (R_X)	Central frequency	760 MHz 2.5 GHz
	Frequency span	1.5 kHz 2 kHz
	Sample points	1001
	Resolution bandwidth	10 Hz
	Sweep time	0.40 s
	Attenuation	0 dB
	Pre-amp	Off

6.3 The Experimental Setup

6.3.1 The Measurement Platform

For our measurement experiments, we employed a CW channel sounding platform as the one described in [28] to mimic the transmission and reception of an unmodulated pilot signal. The platform is comprised of a RF signal generator that is carried by the T_X and a spectrum analyzer mounted on the R_X. We conducted our experiments by considering two different frequencies for the CW probe signals: one frequency at 760 MHz, and the other at 2.5 GHz. The former frequency is reserved in some countries, such as Japan, for VCS applications. The latter frequency is in the range of the IEEE 802.11g standard for WiFi transmissions [53]. We did not include measurements at the frequency band of the DSRC standards, i.e., at 5.9 GHz, because this band is beyond reach to the measurement equipment that was available for our experiments. Table 6.1 provides an overview of the values chosen to configure the RF generator and spectrum analyzer for the two frequencies of our experiments. The T_X and the R_X were also equipped with video recording and global positioning system (GPS) modules. These components are necessary to extract information of velocity, position, and for identification of the events that occurred around the R_X during the experiments.

6.3.2 The measurement scenario

The location chosen for our field trials was a high-speed highway near the city of San Luis Potosí, México. Specifically, our measurement route was a 21 km stretch of the Mexican federal highway 80D, as shown in Fig. 6.3.

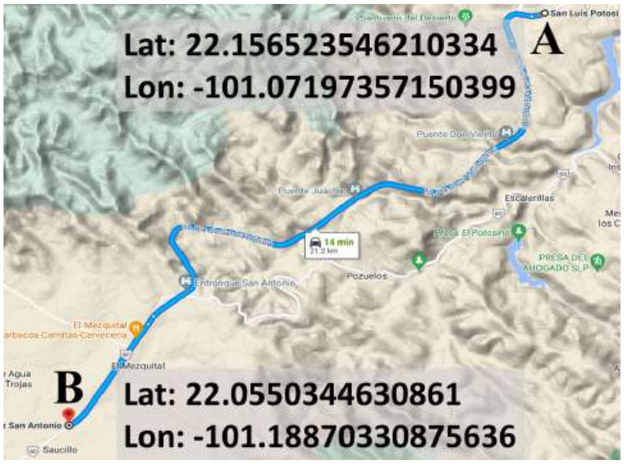

Figure 6.3: The route followed by the vehicles during the experiments.

This highway presents the characteristics of the RS scenario described in the previous section: a high-speed two-lanes wide road that passes through a mountainous chain [100]. Data was recorded along a measurement circuit between points A and B in Fig. 6.3. This circuit takes 30 to 35 minutes to complete, depending on traffic conditions. The T_X remained behind the R_X at all times during the experiments, maintaining a separation distance with the R_X between 100 and 250 m. The speed of these vehicles ranged from 80 to 120 km/h. For each of the two frequencies (760 MHz and 2.5 GHz) of the CW signal, a data set was recorded uninterruptedly along a route comprising two circuits.

6.4 Empirical characterization of the Doppler signature of an oncoming vehicle

With the settings of Table 6.1, our measurement platform was able to record almost three snapshots per second of the received CW signal's Doppler spectrum. Figure 6.4 shows two snapshots of the Doppler spectra recorded at 760 MHz (Fig. 6.4a) and 2.5 GHz (Fig. 6.4b) during time instants at which the R_X was being approached by an oncoming vehicle. These two spectra illustrate the typical frequency dispersion effects produced by the Doppler effect and multipath propagation during the mobile reception of a CW signal. Specifically, we can identify the LOS component of the received signal as the spectral spike of the highest power, which is located around the origin (Doppler shift equal to zero). In addition, we can observe the presence of other high-power elements within a frequency band centered at the origin and bounded by a frequency of ±169 Hz for the spectrum at 760 MHz and ±402 Hz for the spectrum at 2.5 GHz. The spectral elements in this band correspond to the non-LOS (NLOS) components of the received signal arriving at the R_X by the mechanisms of reflection and scattering from static objects around the road. The boundaries of this band of NLOS power can be determined following the well-known formula of the maximum Doppler shift due to reflection/scattering by static objects

$$\Delta f_{\max} = \frac{v_T(t) + v_R(t)}{c} f_c \tag{6.1}$$

where $v_T(t)$ and $v_R(t)$ are the instantaneous speeds of the T_X and the R_X respectively, c is the speed of light and f_c is the carrier frequency. For frequencies outside the interval $[-\Delta f_{\max}, \Delta f_{\max}]$, the measured Doppler spectra comprise mostly noise. However, the examples shown in Fig. 6.4 show an additional spectral spike above the noise level and located at a frequency outside of $[-\Delta f_{\max}, \Delta f_{\max}]$. This term is caused by the reflection of the CW signal from the oncoming vehicle. In fact, we can infer that the oncoming vehicle is approaching the R_X if the frequency of such a spectral spike is larger than $\Delta f_{\max}$, as in the case shown in Fig. 6.4a. In turn, we can infer that the oncoming vehicle has already passed by the R_X and is driving away if this spectral spike has a negative frequency smaller than $\Delta f_{\max}$, as in Fig. 6.4b.

Figure 6.5 shows a complete sequence of contiguous Doppler spectra recorded during an event involving an oncoming vehicle. The spectral signature shown in this figure contains all the information required by the R_X to detect the oncoming vehicle. Nonetheless, only the first part of the signature is relevant for the detection of the approaching vehicle, i.e., the part where the frequency of the spectral spike observed outside of $[-\Delta f_{\max}, \Delta f_{\max}]$ is positive and nearly constant. The middle part, where an abrupt drift from a positive frequency to a negative frequency is observed, is not helpful because this drifting effect indicates that the two vehicles are practically one besides the other, which would imply a possible collision.

6.5 Empirical data sets for the DL-based detection of oncoming vehicles

The automatic classification and identification of the first part of the Doppler signature of an oncoming vehicle is addressed in this paper by applying DL tools. To apply these tools, it is necessary to denoise and correct the slow frequency drift of the measured Doppler spectra resulting from temperature variations of the measurement equipment. We followed the methods described in [28] to correct such issues and to synchronize the obtained data sets with the corresponding video files for visual inspection. Figure 6.6 shows two examples of the pre-processed (sanitized) Doppler spectrograms recorded at 760 MHz and 2.5 GHz. The LOS components of the received signal can be identified by the line in magenta, whereas the frequency band

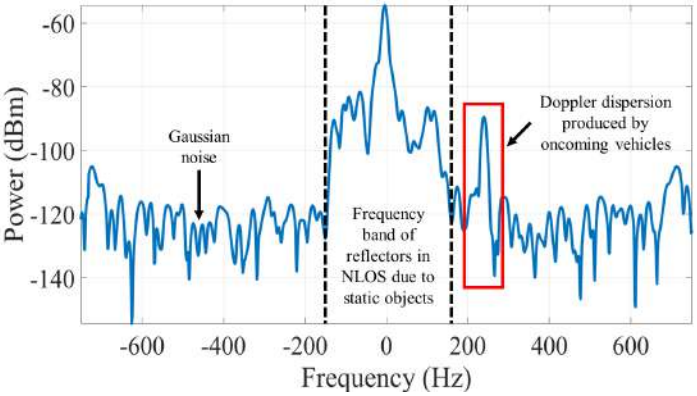

(a) Snapshot of a spectrum at 760 MHz.

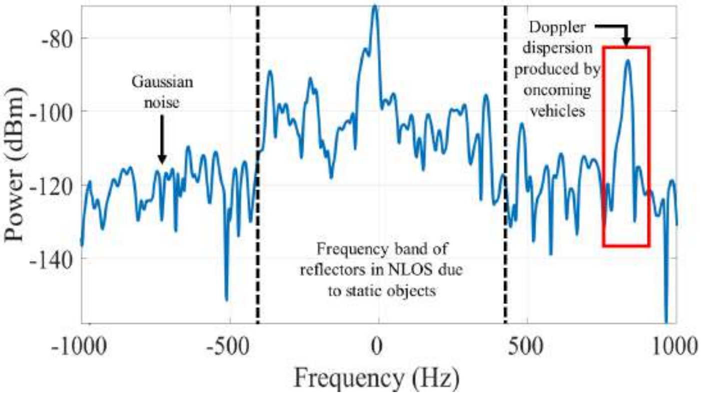

(b) Snapshot of a spectrum at 2.5 GHz.

Figure 6.4: Components identified in the Doppler spectra using the maximum Doppler shift formula.

containing NLOS power received via reflections from static objects forms the contour shown in blue/light-blue. The length of both spectrograms spans only one half of the measurement circuit between points A and B. The absence of NLOS power at the beginning and the end of these spectrograms is due to the fact that the T_X and R_X made full stops for a few minutes after completing each trip between points A and B. This was done for recording short control data sequences.

Each data set collected at 760 MHz and 2.5 GHz is comprised of four spectrograms like those shown in Fig. 6.6. The data set at 760 MHz is formed by a sequence of 6,553 Doppler spectra, for a total of 6,553×1001 = 6,559,553 time-frequency (TF) samples. On the other hand, the data set at 2.5 GHz comprises a sequence of 6,047 spectra, for a total of 6,047×1001 = 6,053,047 TF samples. It is convenient to reduce the bulk of data that needs to be processes in order to speed-up the execution time of the DL algorithms. From our analysis of the principal components of the recorded spectra, the data set at 760 MHz reveals that the meaningful TF samples are within the interval of ±600 Hz. This allows to reduce the number of

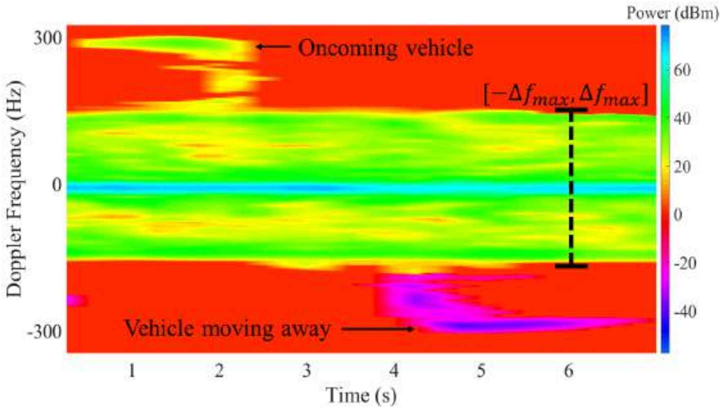

Figure 6.5: A sequence of characteristic Doppler signatures of an event involving an oncoming vehicle.

frequency samples per measured spectrum from 1001 to 425, resulting in a total of 2,785,025 TF samples to be processed by the DL algorithms. However, such a dimensionality reduction is not possible for the data set at 2.5 GHz, because the Doppler dispersion at 2.5 GHz is more than three times higher than that observed at 760 MHz and the meaningful bandwidth of analysis is within $\pm 1,000$ Hz for the signal transmitted at 2.5 GHz.

For the automatic detection of oncoming vehicles, the measured Doppler spectra in each data set were classified by considering four distinct events: static T_X and R_X (no-activity), moving T_X and R_X and no oncoming vehicle (no-oncoming vehicle), moving T_X and R_X and an oncoming vehicle approaching the R_X (vehicle approaching), moving T_X and R_X and an oncoming vehicle driving away from the R_X (vehicle driving away). Figure 6.7 shows examples of the spectrograms recorded for each class. The spectrogram shown in Fig. 6.7a illustrates the case where both the T_X and the R_X are static, therefore producing no frequency dispersion of the received CW signal. Figure 6.7b shows the case where these two vehicles are in motion and no other vehicle is nearby. The event when an oncoming vehicle is approaching the R_X is exemplified in Fig. 6.7c, whereas Fig. 6.7d illustrates the event when the oncoming vehicle is driving away from the R_X.

6.6 Deep learning for forward-collision avoidance

The use of data science for vehicular applications has been widely explored [101, 102]. One of the techniques that has raised most interest is DL [24]. This mathematical model aims to learn certain features of a data set by applying multiple layers of artificial neural networks. The typical architecture of a DL-based classification algorithm is comprised of a data training stage, a testing stage, and a third stage for the interpretation or validation of the

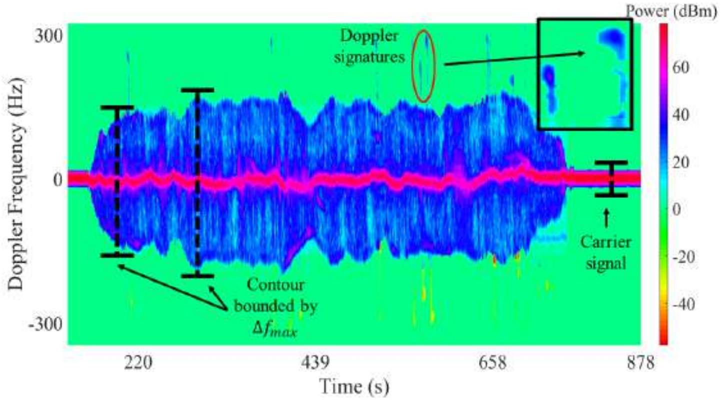

(a) Spectrogram pre-processed using the data set of signals at 760 MHz.

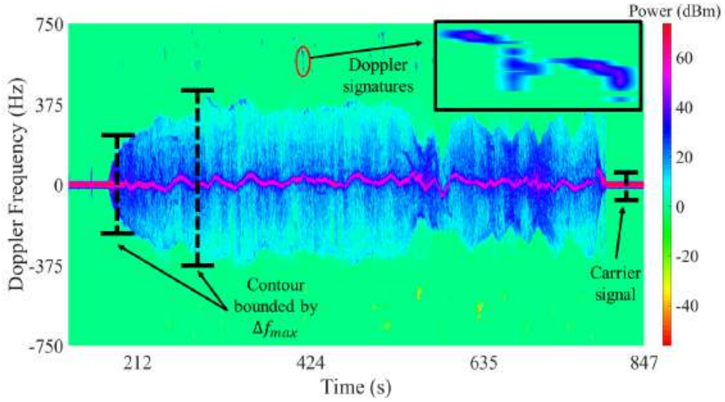

(b) Spectrogram pre-processed using the data set of signals at 2.5 GHz.

Figure 6.6: Pre-processed spectrograms delimiting the contour and preserving the Doppler signatures.

algorithm. One of the advantages by which DL surpasses other techniques is that the extraction of the principal features of the data is done automatically. Furthermore, once DL models learn to recognize the principal features through the training stage, they can use them to classify new data. This reduces the computational cost once the network is inferred [103, 104]. However, the accuracy in this case directly depends on the amount of data entered into the networks [24]. Therefore, it is important to have a large data set that allows algorithms to improve their performance.

6.6.1 Long short-term memory network

In the analysis of sequential data, recurrent neural networks (RNN) have been widely used [105, 106]. However, in systems where the data sequences are very long, these networks present issues with the vanishing gradient. This makes it difficult for the network to have "memory" of the previous

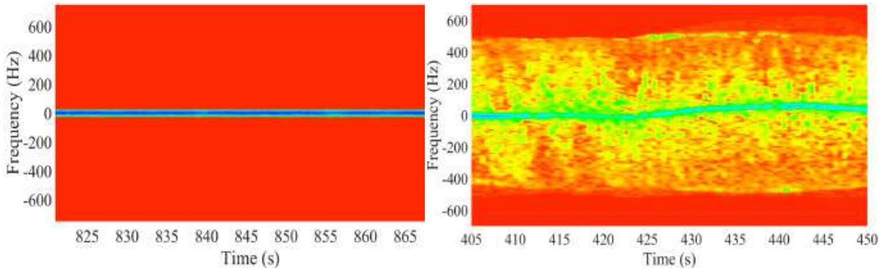

(a) No activity (b) No oncoming vehicle

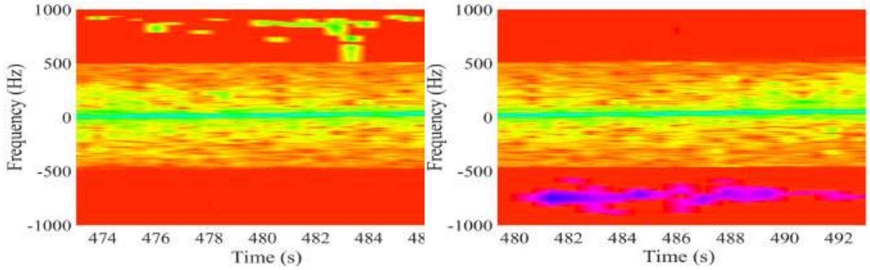

(c) Vehicle approaching (d) Vehicle driving away

Figure 6.7: Spectrograms of each registered event that were labeled and separated into 4 different classes within the data set.

data. A variant of RNN known as an LSTM network has become popular to compensate for these practical issues. The use of LSTM networks in vehicular applications has presented relevant results already [101,107]. We use two LSTM layers for the design of our classification system. The architecture of our LSTM network is shown in Fig. 6.8. The input data must have a three-dimensional representation corresponding to the batch size, the time step, and the number of features of the data set. The time step was set equal to one since we considered taking the smallest value of the observation window. This is because response time is essential to avoid possible collisions. Taking a larger window size would reduce the response time of our collision warning system. On the other hand, the number of features corresponds to the data registered in each frequency spectrum and depends on the frequency span of the measurement. The network setting is shown in Table 6.2. Finally, the network uses a dense layer at the output to classify the samples into any of the four classes that were defined in Section 6.5.

6.6.2 Convolutional neural network

The measured spectrograms are a long data sequence that can be challenging for RNNs to analyze. Hence, to circumvent this issue, we implemented a different DL technique. CNN are popular because their architecture allows them to learn directly from input data without the need for a human-supervised feature extraction stage. Furthermore, this model can reduce the dimensionality of the data and maintain only the principal features [102]. In

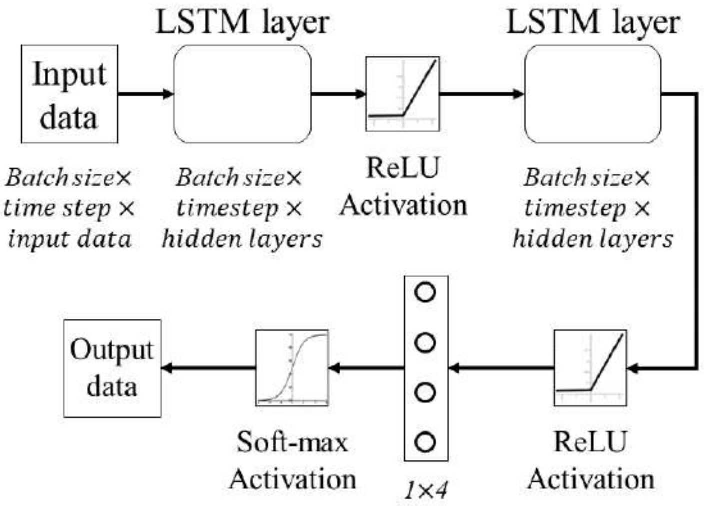

Figure 6.8: Neural network architecture using two layers of LSTM for feature extraction and a dense layer for classification.

Table 6.2: LSTM network setting.

Parameter	Value
Epoch	800
Batch size (training)	5227
Batch size (test)	1326
Time step	1
Hidden nodes	100
Features	(425-1001)

CNN, a series of digital filters are used to compute the convolution of the input data and build a feature map for the classification process. The elements of our CNN are shown in Fig. 6.9. Data is processed by two convolution layers with an activation function for each set of filters and a specified kernel size. The number of filters can change according to the application in which they are used and depends on the feature map that is desired to be obtained. However, the filters must be sufficient to extract the most relevant features without consuming many computational resources for their implementation. As in the case of the LSTM network, data is feed in a configuration that includes batch size, time step, and the number of features. The chosen batch size is the same as for the LSTM case. The time step oscillates because in a CNN, the information is reduced by the network and it is necessary to maintain at least a minimum size to carry out the operations. A minimum range between 5 and 10 samples in the window observation size was selected to minimize the response time of the system. The number of features in this case also depends on the frequency span of the experimentation. On

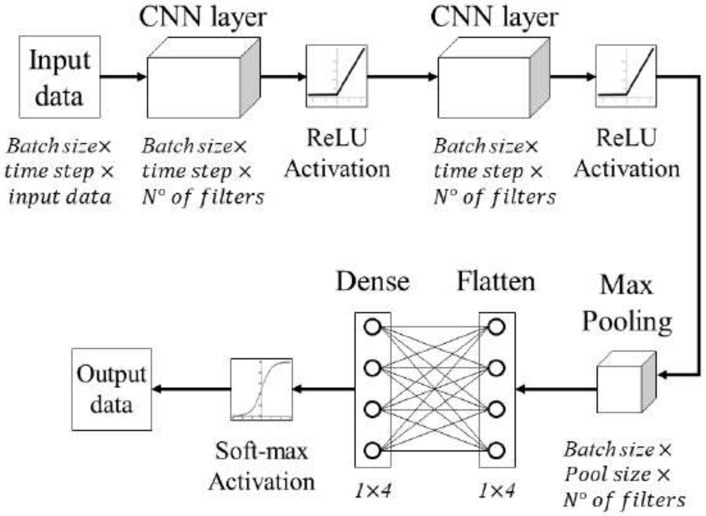

Figure 6.9: Neural network architecture using two layers of CNN for feature extraction, a max pooling layer for data reduction and a dense layer for classification.

Table 6.3: CNN setting.

Parameter	Value
Epoch	800
Batch size (training)	5227
Batch size (test)	1326
Stride	1
Time step	(5-10)
Number of filters	(8-64)
Kernel size	3
Pool size	2
Features	(425-1001)

the other hand, the reduction in data dimensionality is carried out by the pooling layers. In a max pooling layer, the maximum values of the feature map of the convolution layer are taken and the rest are discarded. Furthermore, the size of the pooling operation has to be less than the size of the feature map and is commonly reduced by a factor of two. The last layer of the architecture is a fully connected layer that is used to process the reduced data and order it in such a way that the dense layer can receive it. This is achieved through a flatten layer. The summary of the values used in the network configuration is shown in Table 6.3.

6.6.3 Neural networks performance metrics

We considered four metrics to evaluate and compare the performance of the LSTM and CNN algorithms: accuracy, precision, recall, and specificity [26]. These metrics are in a normalized range that goes from zero to one (0% and 100%, respectively). Accuracy refers to how close the classification result was to the true values analyzed. Precision indicates how well each class was classified. The recall is the proportion of correctly classified data versus incorrectly classified data. And specificity expresses how effectively the model fits into identifying the classes. These metrics are computed using the true positives (TP), true negatives (TN), false negatives (FN), and false positives (FP) values. A TP is the number of samples correctly classified for a class. The TN refers to when the model has succeeded in properly classifying the samples that do not belong to the class being identified. The FN are the misclassified samples of a class. FP are samples from other classes that were classified as part of a class to which they do not belong. Therefore, performance metrics are defined as follows:

$$Accuracy = \frac{TP + TN}{TP + FP + FN + TN}, \tag{6.2}$$

$$Precision = \frac{TP}{TP + FP}, \tag{6.3}$$

$$Recall = \frac{TP}{TP + FN}, \tag{6.4}$$

$$Specificity = \frac{TN}{TN + FP}. \tag{6.5}$$

Furthermore, we use the R_X-operating characteristic (ROC) curve and the area under the ROC curve (AUC) which are obtained from the relationship between the rates of TP and FP values. This allows us to quantitatively estimate the performance of the model. An AUC close to 1 indicates a better capacity to distinguish classes. The results of all these metrics are shown in the next section.

6.7 Results and discussion

Using the data sets obtained for the CW probe signals at 760 MHz and 2.5 GHz, we classified the samples through the LSTM and CNN algorithms. For the learning stage, 80% of the randomly selected samples were used and the remaining 20% were used for validation. The accuracy obtained in the case of experiments at 760 MHz was 96.94% this represents that the majority of the events of all the classes were correctly classified. With the data obtained from the 2.5 GHz signal, the accuracy was 96.53%. However, even though the accuracy values in both cases are high, the class of vehicle approaching is the most important and determines the efficiency of the system.

Table 6.4: LSTM performance evaluation.

Metric	No activity		No oncoming vehicle		Vehicle approaching		Vehicle driving away	
	760 MHz	2.5 GHz	760 MHz	2.5 GHz	760 MHz	2.5 GHz	760 MHz	2.5 GHz
Precision	97.60%	98.70%	98.00%	96.40%	**88.50%**	**98.60%**	90.00%	98.00%
Recall	99.60%	98.70%	97.80%	99.10%	75.40%	90.80%	95.70%	93.60%
Specificity	99.41%	99.68%	95.53%	95.31%	99.51%	99.80%	99.15%	99.70%
ROC	100%	99.00%	97.00%	97.00%	87.00%	95.00%	97.00%	97.00%

Table 6.5: CNN performance evaluation.

Metric	No activity		No oncoming vehicle		Vehicle approaching		Vehicle driving away	
	760 MHz	2.5 GHz	760 MHz	2.5 GHz	760 MHz	2.5 GHz	760 MHz	2.5 GHz
Precision	96.78%	97.70%	96.10%	92.90%	**68.40%**	**94.50%**	78.70%	97.90%
Recall	97.50%	97.70%	94.80%	97.90%	63.90%	79.10%	90.40%	91.10%
Specificity	99.18%	99.46%	91.11%	90.58%	98.48%	99.31%	98.00%	99.70%
ROC	98.00%	99.00%	93.00%	94.00%	81.00%	89.00%	94.00%	95.00%

The results of the performance parameters of the LSTM model using both data sets are shown in Table 6.4. We compare the precision and sensitivity of this class for both data sets. It was found that there is a higher percentage in the experiments with signals at 2.5 GHz. The 98.60% precision means that a high rate of samples was correctly classified and the system can detect if a car is approaching. Therefore, in a collision avoidance system, the results using the 2.5 GHz data set have better reliability.

On the other hand, for the CNN classification model, the accuracy of the system using the signals captured at 760 MHz was 93.68%. Using the data set obtained with the 2.5 GHz signals, the algorithm obtained an accuracy of 94.61%. These results were calculated to measure, in general terms, the capacity of the system to classify the multiple classes. The results of the performance parameters computed with both data sets are shown in Table 6.5. In this case, it can be seen that the detection accuracy of oncoming vehicles was 68.40% for the 760 MHz data set and 94.50% for the 2.5 GHz data. In both cases, the precision rates are lower than those obtained by the LSTM algorithm. Furthermore, examining the results in general terms, a clear difference between the two data sets is highlighted. This indicates that by using a higher central frequency of the CW signal the resolution of the Doppler signatures of relevant events increases and facilitates their characterization.

Table 6.6 shows the classification performance results for each model using the different data sets. As can be seen, the calculated AUC values were close to 1 for most classes. This indicates that the evaluated models had a high performance during their execution. According to these results, the DL LSTM algorithm obtained the highest classification performance in the event of approaching vehicles when using the data set containing the

Table 6.6: Area under the ROC curve (AUC).

Dataset DL model	760 MHz LSTM	 CNN	2.5 GHz LSTM	 CNN
AUC no activity	1.0	0.98	0.99	0.99
AUC no oncoming vehicle	0.97	0.93	0.97	0.94
AUC vehicle approaching	0.87	0.81	0.95	0.89
AUC vehicle driving away	0.97	0.94	0.97	0.95

signals captured at 2.5 GHz. This model is known to have difficulties in retaining relevant information during the training stage. However, even though our data set contains several features, the classification model has satisfactory performance. In the case of the models that used the data set containing the signals captured at 760 MHz, it is shown that the model had the lowest performance in classifying the approaching vehicles. This may be because, during the pre-processing stage of the Doppler signatures, some of its principal features faded. Therefore, it is necessary to consider that the pre-processing stage has to be adapted if the carrier frequency is in another range to adequately preserve the features of their Doppler signatures.

Our system detects oncoming vehicles with a precision that can be compared to some of the published works on vehicle detection and recognition. Figure 6.10 shows a comparison between the precision percentages achieved by the different configurations of our platform and the methodologies used in other works. For example, in [108] (methodology #1) they used the WiFi channel state information to detect vehicles with a methodology based on machine learning and a support vector machine algorithm. Our system uses a DL approach and the accuracy achieved was, in some cases, higher. In [3] (methodology #2) a fusion between a vision system and the information from a laser sensor was used to detect vehicles at night. Therefore, the implementation requires specialized equipment which makes it expensive. In our case, we use general-purpose equipment to perform vehicle sensing under different environmental conditions. The authors in [109] (methodology #3) proposes an innovative fusion of a radar and a vision system to assist autonomous cars. The resolution that radar systems can achieve is very practical for vehicle maneuver detection tasks. However, this requires specialized equipment and cannot be easily integrated into VCS. In the case of [1] (methodology #4), a panoramic camera and a DL approach were used, implementing a deep CNN network architecture. The principal disadvantage is that these systems must always maintain a direct LOS with the car, which cannot always be guaranteed. Our methodologies (#5-#8) work using the multi-path effect so they do not require a direct LOS and oncoming vehicles can be detected with a high precision rate.

Another critical component in this class of systems is the time it takes

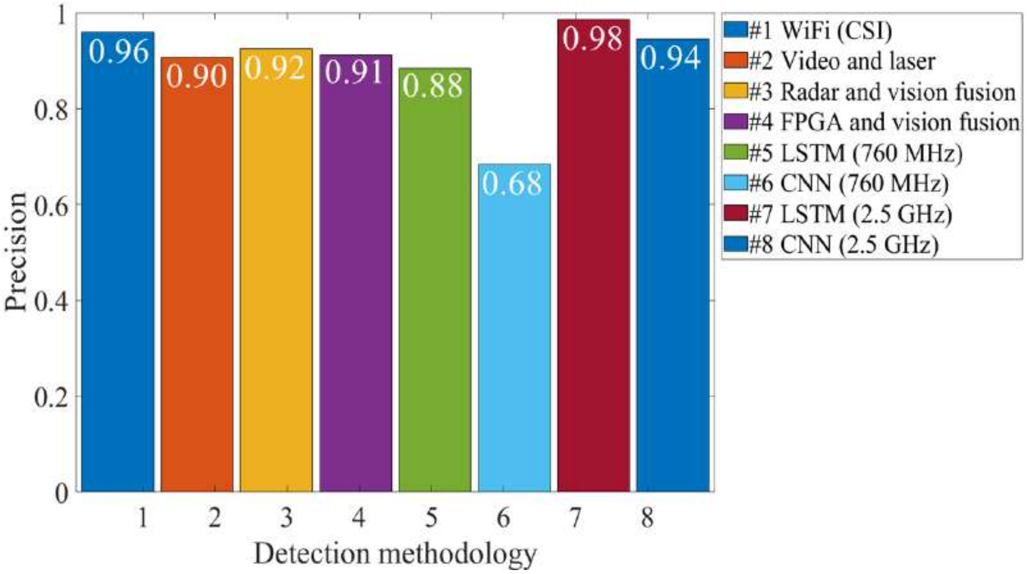

Figure 6.10: Comparison of precision achieved by different vehicle detection systems.

for vehicles to be warned of oncoming vehicles. Our DL models take this into account as part of their architecture. Both DL algorithms are trained with a sequential data set on which the warning signal can be emitted once the first Doppler signature of an oncoming vehicle is captured. In the case of the 760 MHz configuration, drivers could be alerted 0.92 s on average before intersecting an oncoming vehicle, with a standard deviation of 0.75 s. Furthermore, the maximum time for the alert was 4.4s before a possible collision. On the other hand, with a configuration using the 2.5 GHz signal, the average detection time was 0.94s with a standard deviation of 1.04 s. Moreover, the maximum detection time before the intersection was 9.2 s. According to several investigations, on average, people need between 390 and 600 milliseconds to detect and react to hazards on the road [110]. Therefore, both systems based on a decentralized approach fused with DL classification algorithms are capable of warning drivers with a sufficient time window for decision-making.

Finally, the system had a favorable performance in the detection of events through the classification algorithms. The proposed models reduce the computational cost of the algorithms by not involving complex processes in their architecture. Furthermore, the selected observation windows reduce the reaction time of the system involving a minimum of samples to take a decision. Therefore, several of these settings can be taken into consideration for real-time event detection in future works.

6.8 Conclusion and open research problems

In this article, we experimentally validate the feasibility of a forward-collision avoidance system based on a decentralized RS approach and the analysis of the Doppler signatures of an oncoming vehicle. To compare and determine the highest accuracy that our system can achieve, the performance of both DL algorithms was compared using two different data sets. For both data sets, 4 different classes of activities were labeled to test the robustness of the system against different events. After several evaluations and tests by the classification algorithms, it was found that the highest accuracy of the system is achieved with the data set recorded at 2.5 GHz. Furthermore, with the LSTM algorithm, it is possible to detect 98.6% of approaching vehicles with a response time for the driver of up to 9.6 s. This demonstrates that the decentralized RS approach described here is a feasible alternative for forward-collision warning systems based on the new JRSAC paradigm.

On the other hand, it is necessary to explore different DL models that can further improve the system accuracy, and increase the detection time in order to allow for a timely reaction to these events. We address the exploration of CNN algorithms that reduce the dimensionality of the data and in this way, fewer operations are necessary to perform the classification. However, in our case, it is still required to readjust the models to increase the performance of the classification. In future work, we will look for the fusion of both DL models presented here (CNN-LSTM), since the principal characteristics of each one can be exploited.

Chapter 7

Conclusions

7.1 General conclusions

The present work showed the impact of the polarization and the radiation pattern of the antennas of a RS system on the classification performance of indoor environment events [18]. For this, a sensing platform was developed using general-purpose equipment. Furthermore, the platform used an RF probe signal to measure fluctuations caused by the human movement for a fall detection application. The information on the Doppler signatures recorded during the experiments was processed to compute the spectrograms. To measure the impact of the orientation of the antennas, two experimental scenarios were proposed, the scenario with the antennas in HH orientation and the antennas in VV orientation. Afterward, the extraction of the features of the spectrograms computed in both scenarios was through the PCA. The extracted features were fed into an SVM-based classification algorithm with which accuracy rates were obtained and compared. The highest accuracies detecting falling events were obtained using the HH scenario setup. Although, within the setting only the orientation of the antennas changed, the VV scenario obtained accuracy rates below the HH scenario. The results were compared with other RS systems that use a larger number of antennas to increase their accuracy and I obtained a similar performance. Therefore, the results showed that some limitations of RS-based fall detection systems can be mitigated by considering the orientation of the antennas.

The performance of a fall detection platform based on CW RF signals was analyzed using a DL framework [20]. For this, a measurement campaign was carried out to sense different activities and human falls using the measurement platform. Activities include: walking, going up and down stairs, a control activity where there was no movement, and falls. Subsequently, the spectrograms of the received signals were computed. These include the characteristic Doppler signatures of each activity. The LSTM network showed an overall accuracy of 82.20% with a precision of 70.50% in detecting falls.

CNN reported an accuracy of 78.09% and detecting falls obtained a precision of 68.70%. Although these results, it was found that the platform did not have the necessary resolution to capture the dispersions caused by the movements of going up and down stairs. Therefore, a protocol that did not include this activity was considered because elderly people who live independently tend to live in one-story houses. In this way, the LSTM algorithm reached an accuracy of 94.95% and a precision of 92.10% in detecting falls. On the other hand, the CNN improved its accuracy to 95.25% and a precision of 92.10% in detecting falls. These considerations demonstrated that the sensing platform has high performance in identifying falling events, but is not optimized to distinguish slow-moving activities.

The feasibility of using a frequency diversity technique to diversify the information gathered to the RF signals of an RS-based fall detection system was demonstrated. This technique does not require increasing the number of antennas in the system and can be used to extract more remarkable information from some signal propagation effects. The propagation effect that was used to demonstrate the feasibility of the frequency diversity technique was the spread in the frequency of the Doppler signatures. The information from the Doppler signatures of three pilot subcarriers generated by general-purpose measurement equipment was extracted. Finally, the data set was fed to a DL-based LSTM classification algorithm to determine the system's accuracy. The results showed high precision values can be achieved in fall detection but with a low recall rate. Therefore, it was shown that classification performance can be improved without increasing the number of antennas by using a frequency diversity technique.

Finally, the feasibility of a forward collision warning system based on a decentralized RS approach was validated experimentally. To determine how high the accuracy percentages could be in detecting oncoming vehicles, two DL algorithms were compared: LSTM and CNN. Furthermore, two data sets were used that included 4 different classes of events recorded during a road trip. From each data set, the Doppler signature information contained in the signal spectrograms was extracted and entered them as inputs into the algorithms. It was shown that the maximum system accuracy rate was obtained using the data set with 2.5 GHz signals. The accuracy of detecting oncoming vehicles was 98.60% when using the LSTM algorithm with a response time of 9.6 s for the drivers. Therefore, it was demonstrated that a warning system using a decentralized RS approach can be a feasible alternative to the JRSAC systems paradigm.

A summary of the most outstanding results of this work is shown in the Table 7.1. These results are intended to establish an overview of the efficiency of our proposed system and the principal applications.

Table 7.1: Principal results obtained in the different works presented.

Application	Technique / Model	Precision	Recall	Specificity	ROC
Fall Detection	CW single probe signal / LSTM 3 classes	**92.10%**	82.00%	94.41%	90.00%
Fall Detection	CW single probe signal / CNN 3 classes	**92.10%**	81.5%	98.21%	90.00%
Fall Detection	Frequency diversity / LSTM 2 classes	**98.10%**	73.80%	98.10%	87.00%
Vehicle Detection	CW RF signal 2.5 GHz / LSTM 4 classes	**98.60%**	90.80%	99.80%	95.00%
Vehicle Detection	CW RF signal 2.5 GHz / CNN 4 classes	**94.50%**	79.10%	99.31%	89.00%

7.2 Future work

Future work in the wireless perception research line includes the use of different techniques and methodologies to improve the performance of the RS platform. An interesting extension of the work includes the use of software-defined radios to be able to adapt our signals to a greater number of communication standards and verify the feasibility of their use. Furthermore, one of our purposes is to find a setup that allows me to capture the Doppler signatures of low-speed movements with fine granularity. In this way, the multi-class analysis for fall detection can be more robust by differentiating between a more significant number of activities. Another of the major drawbacks in the field of fall detection was the trade-off of the platform between acquisition time and frequency resolution. Therefore, the use of other pre-processing or capture techniques to optimize these parameters remains future work. Finally, the decision stages with which our platform will be able to send alert messages about the detection of events were outside the scope of this work, so they will be addressed in future works.

On the other hand, in the detection of oncoming vehicles, it is still necessary to explore different DL approaches, which can reduce the processing time for real-time applications. It is then proposed to explore some alternatives that include the fusion of different layers of neural networks that reduce the dimensionality of the data and others that are more adapted to a sequential analysis of data. Furthermore, the platform sensing capabilities will be tested by changing the RS approach to a centralized one using the same CW probe signal. This extension of the work can be used to compare the performance of both systems and demonstrate which is the best proposal to adapt within the JRSAC paradigm.

Appendix A: Effects of Antenna Orientation in Fall Detection Systems Based on WiFi Signals

The global increase in human life expectancy has created a need for healthcare and remote monitoring technology suitable for the elderly. One of the biggest health treats to older adults are falls occurring at home during daily activities. This reality has prompted the design of device-free fall detection systems that employ WiFi signals as sensing probes. Several works have addressed the design and development of these detection platforms. However, these works have not considered the impact of the antenna orientation on the system's sensing capabilities. To close the gap, we present a systematic analysis of the effects of antenna orientation on the performance of a WiFi-based fall detection systems. The analysis was conducted on the grounds of an experimental platform that transmits WiFi-like waveforms from which the Doppler signature of a fall event can be computed. Our work shows how the orientation of the antenna affects spectrograms of the received probe signal. The results also show that signals transmitted with a horizontal positioning improve the performance in the classification stage.

A.1 Introduction

The share of the world population aged 65 years or more will experience a large growth in the next years. The percentage of elderly population in 1990 was 6%, but in 2019, the percentage of elderly population was 9%. Therefore, in the past 30 years, the elderly population had a 3% growth. This proportion is expected to rise to 16% by 2050. These estimates create a need for healthcare and monitoring systems suitable to provide elderly care [31].

This chapter forms part of the paper titled 'Effects of Antenna Orientation in Fall Detection Systems Based on WiFi Signals" published in *IEEE Latin American Communications Conference (LATINCOM) proceedings.* I and the other authors gave consent to use our work as an integral part of this dissertation.

According to the World Health Organization, 37.3 million of elderly people require medical attention each year for injuries caused by falls [25]. For this reason, fall detection automation has become a research topic of great interest. A fall is a sporadic action in which the persons lose control of their body and precipitate to the ground.

There are several approaches to human activity monitoring that can be employed to detect when a human fall event has occurred. Systems for event detection based on activity monitoring have been developed using different sensing techniques. A vision system can be used to detect an event. However, these systems are expensive and require a direct line of sight (LOS) with the person under monitoring. Another disadvantage is the violation of user privacy [34]. Another approach is the use of wearable devices with accelerometers or gyroscopes. However, these devices must always be carried by the users, making them invasive. A further approach has emerged in the last years: device-free fall detection based on radio frequency (RF) signals. In this approach, a transmitted probe signal is processed at the receiver to obtain information of ranging and Doppler dispersion caused by moving people [35]. These systems have several advantages: they are not invasive, they do not require a LOS with the moving person and they offer a communication mechanism to send alerts if falls occur. Fall detection systems based on WiFi are under intense research and development due to the ubiquity of these wireless local area networks [38, 46, 47].

However, previous research works on WiFi-based fall detection have not considered the impact of the antenna orientation on the system's sensing capabilities. In [40], the accuracy of a fall detection system called WiFall was analyzed by considering different heights of the antennas. Nonetheless, the effect of the antenna orientation was not addressed. Huang et. al. considered different sensing regions of the antennas by introducing multiple sensors in the indoor environment [37]. Notwithstanding, increasing the sensors also increases the system's cost. This previous work did not consider the impact of antenna orientation in the sensing regions.

In this chapter, we present an experimental platform for fall detection that allows identifying signal variations caused by the orientations of antennas. This platform emits a pure tone in the range of RF WiFi signals. The signal is transmitted by a typical WiFi monopole antenna. The objective is to replicate the operation conditions of commercial access points but allowing a flexible positioning of the transmitting and receiving antennas. Thereby, it is possible to assess the signal dispersion caused by the multipath effects. In order to measure the impact of the orientation of the antenna, we conducted a series of experiments involving falls of young and middle-age adults from the top of a three-step ladder within an indoor environment.

The analysis of the Doppler signatures of the received probe signal is carried out in accordance with the concept of spectrogram. Spectrograms are used to analyze time-varying and non-stationary signals. These signals provide information on the variations in time of the frequency spectrum. This is performed by estimating the dispersions of the signal's spectral signatures stemming from human motion. Finally, result validation is carried out by extracting the features of the spectrograms using Principal Component Analysis (PCA). The numerical values obtained by this technique are used to quantitatively determine the variations between Doppler signatures of fall events and those of static states.

The remainder of this chapter is organized as follows. In Section A.2, a review of spectrogram analysis through Doppler signatures for fall detection is presented. Then, the instrumental implementation necessary for the sensing platform is described in Section A.3. The results obtained are shown in the Section A.4. Finally, the conclusions are given in Section A.5.

A.2 Doppler Signatures and Spectrogram Analysis

The computation of Doppler signatures starts with the transmission of an unmodulated RF signal in an indoor setting. When the signal impinges on a moving body, the carrier signal suffers a frequency shift known as the Doppler effect. This frequency shift together with the multipath propagation generates sidebands in the received signal's spectrum known as Doppler signatures. During a fall event, the speed of the falling body produces certain Doppler signatures that can be characterized to determine the nature of the event. Doppler signatures can be studied using spectrogram analysis. A spectrogram provides information about the spectral density of a signal that varies over time [49].

A spectrogram is calculated by dividing the span of a time-varying signal into short-time segments. These segments are a representation of the signal in a short period of time. Then, a Short Time Fourier Transform is applied to each segment as shown in Eq. A.1.

$$X(f,t) = \int_{-\infty}^{\infty} x(t)h(\tau - t)e^{-j2\pi ft}dt. \tag{A.1}$$

According to (A.1) $x(t)$ is a signal that varies in time t and $h(\tau - t)$ is an even and positive window function. The spectrogram $S(f,t)$ is defined as

$$S(f,t) = |X(f,t)|^2. \tag{A.2}$$

Once the spectrogram of the signal has been calculated, an analysis of the Doppler signatures can be performed. The spectrogram provides a visual map of a signal's spectral variations over time. Doppler signatures are obtained from analyzing a series of spectrograms. The process of obtaining a Doppler signature involves examining a large set of data. There are several techniques that can be used to extract valuable information of a large set of data. The most popular technique is PCA. PCA is based on singular value decomposition and it unveils important features of a high-dimensional data collection with only a few components [66].

The first two components computed using by PCA contain the most significant features of the frequency spectrums. These components are used to classify the Doppler signatures into two categories: a fall event or a state of no movement. Furthermore, the classification achieved by using the principal components of the signal can be used to compare the effects of varying position and orientation of the antennas in the experiment setting.

A.3 Sensing System for Fall Detection

A.3.1 Experimental Setup

A fall detection system is composed of three stages: sensing, recognition and decision. A general diagram of a fall detection platform is illustrated in Fig. A.1. Our work focuses on the sensing stage of the system. In the sensing stage, an RF signal is transmitted by a transmitter (Tx) through an indoor environment and captured by a receiver (Rx). In our experiments, a platform operating in the frequency range of commercial WiFi systems (IEEE 802.11) was implemented. Furthermore, this platform allowed us to experiment with different orientation and positions of the antennas. The transmitted signals are collected by a spectrum analyzer that makes it possible to record a series of snapshots of the signal's dispersion in the frequency domain throughout the indoor environment. With this information it is possible to compute the spectrograms of the signal.

The experiments are conducted in a controlled environment to avoid interfering signals generated by reflections from moving objects other than the target. The indoor environment includes three-step ladder. The falls were developed by a group of subjects who made it possible to record signal's dispersions during this event.

The spectrograms computed during the experiments are processed in the recognition stage to reduce the noise generated by the measurement equipment and extract the principal features. The feature extracted are analyzed by a classification algorithm to determine if they correspond to a falling event or a non-moving state. The accuracy of the recognition stage determines the number of false alarms that can occur in the decision stage. The output of the decision stage is an alert message that is prompted when the event occurs. However, in this work the recognition stage is limited to identifying the differences caused by varying the rotation of the antennas. The experimental process adopted in this paper is summarized in the diagram shown in Fig. A.2.

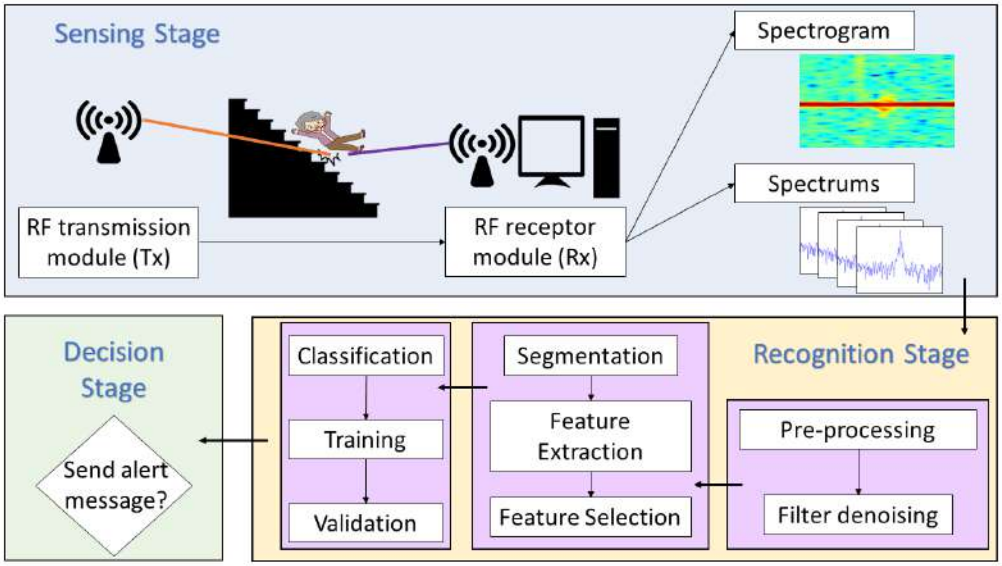

Figure A.1: General diagram of a fall detection system based on radio frequency signals.

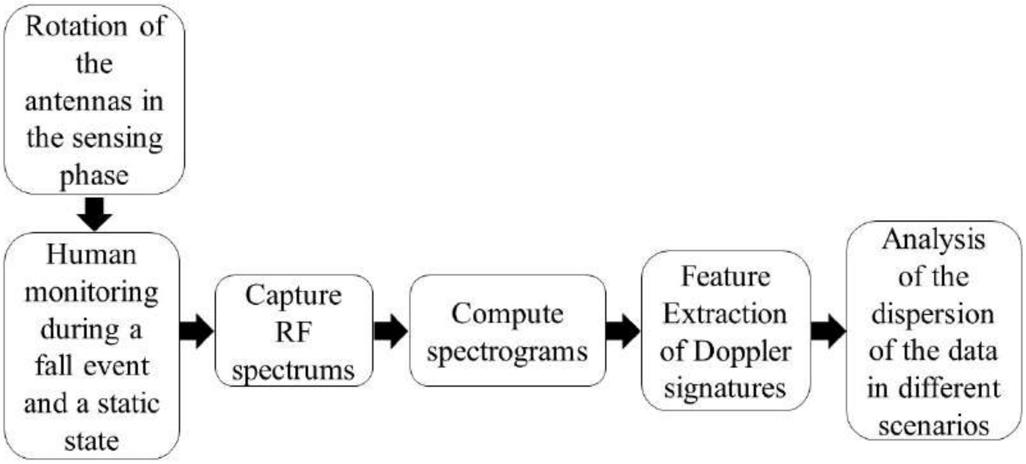

Figure A.2: Block diagram of the experimental process.

A.3.2 Hardware Design

The hardware employed in our experiments includes a RF generator Keysight N9310A, a spectrum analyzer FieldFox N9912A, two 2.4-2.5 GHz omni-directional antennas, one 3.9 GHz Intel(R) i7 CPU 8 GHz RAM computer with Matlab$^{\text{TM}}$ software installed. The positioning of the instruments is shown in the schematic in Fig. A.3. The omni-directional antennas were characterized using the FieldFox spectrum analyzer in its cable and antenna test mode. For a 2.42 GHz frequency, the antennas have a 32.4 dB in return losses, an impedance of $50+j0.70$ Ohms and a voltage standing wave ratio of 1.042. At this frequency the antennas operate with their best performance.

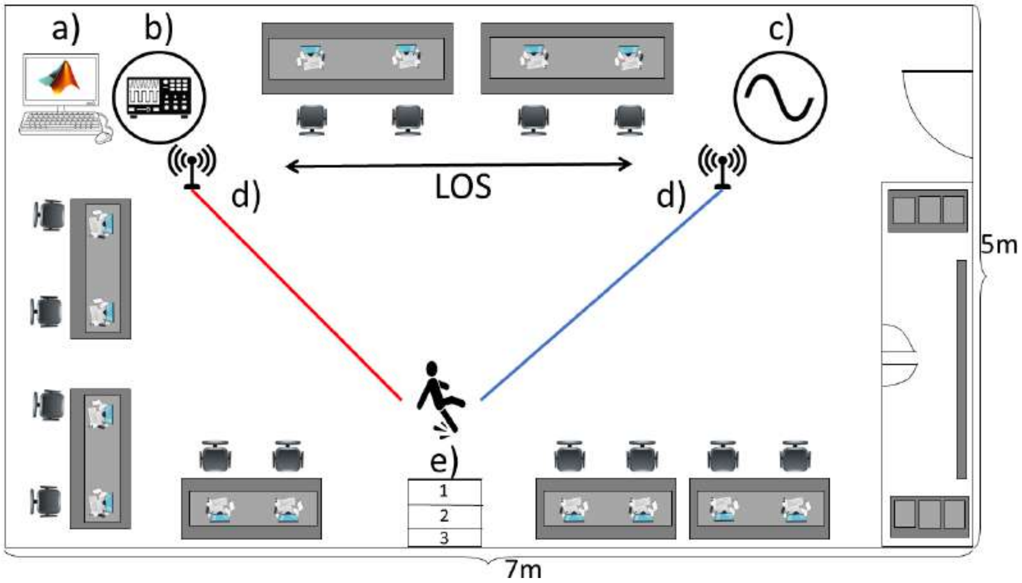

Figure A.3: Schematic of the test scenario: a) control and analysis computer, b) spectrum analyzer (Tx), c) RF generator (Rx), d) omni-directional antennas, e) ladder.

Therefore, the RF generator was configured with a center frequency of 2.42 Ghz and a transmission power of 20 dBm for the best performance of the system. Furthermore, during the experiments the spectrum analyzer was configured to capture signals with a sweep time of 271 ms for 1001 points with 1 KHz of span.

A.3.3 Experimental Scenarios

The experiments were conducted within an indoor space of the Faculty of Sciences of the Autonomous University of San Luis Potosí. The location corresponds to an office room. The room has a dimension of $7m \times 5m$ and has furniture such as tables, chairs and computer equipment (Fig. A.3). The Tx transmitter was installed in the top right corner of the room according to Fig. A.3b with one of the omni-directional antennas. The Rx receiver was positioned in the top left corner of the room (Fig. A.3c) with the second omni-directional antenna. Both antennas were placed at a height of 2 m.

The antennas are omnidirectional monopole used by commercial WiFi systems. The experimental platform allows changing the position and orientation of the antennas. Nevertheless, when the orientation is changed, certain transmission features are affected in the antennas. Therefore, when fixing any position of the sensing equipment in the environment, it is necessary to carry out a study of two principal features given an orientation.

The first feature is the radiation pattern, where the power density is represented. The radiation pattern of the antennas is shown in Figure A.4.

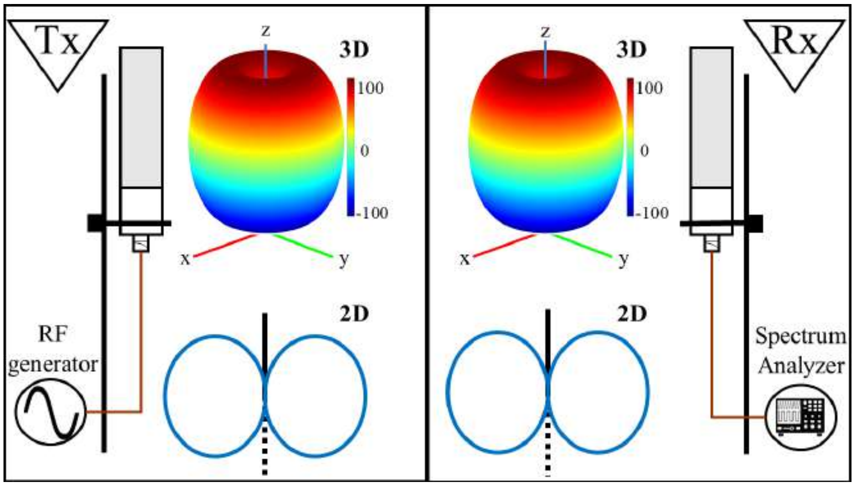

(a) Radiation pattern of antennas in vertical position.

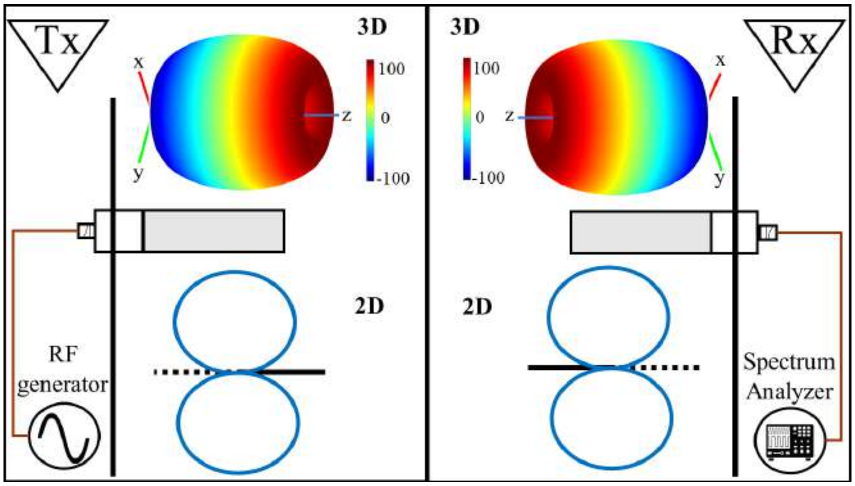

(b) Radiation pattern of antennas in horizontal position.

Figure A.4: Radiation pattern of antennas configuration in 2D and 3D view.

A vertical scenario is defined as the orientation commonly used in antennas at access points (Figure A.4a). In the vertical position, the maximum radiation points can be determined. An important feature of this class of antennas is that their radiation pattern creates zones where the power density is very low. A signal capture in a low radiation area presents disturbances. Therefore, it is important to know how our sensing channel operates.

On the other hand, in the horizontal scenario the antennas are oriented in direction of the LOS (Figure A.4b). In this scenario, the direction of the radiation pattern is changed. The horizontal and vertical scenarios allow us to register the effect in the classification stage of the signals.

It is true that a large number of orientations can be defined to vary this feature. However, this work focuses only on the two cases defined as vertical and horizontal scenarios. The configuration of these two scenarios is followed below.

Vertical positioning scenario

According to Fig. A.4a, both antennas were positioned 5m apart from each other. The ladder was positioned near the middle of the room, from that position the falls were performed.

Horizontal positioning scenario

In this case the antennas were configured as in Fig. A.4b at 5 m distance from each other. As in the case of vertical positioning, the falls were performed on a ladder approximately 3m away from the platform.

The second feature is the linear polarization of the antennas. In this case, the electric fields of the monopole antennas oscillate in only one direction depending on their orientation. In Figure A.5a, the power received by an Rx antenna is shown depending on the polarization of the transmitted signal. This means that the signals captured with a perpendicular polarization is null. This is a very important concept in fall detection systems. Even though the antennas are positioned with the same polarization in the LOS, they are affected by the multi-path effect. This effect causes a signal to propagate through different paths. The result is a signal formed by the interaction of the different signals that have traveled to different paths (Figure A.5b).

The signals propagated by the transmitting antenna impinges the surfaces in the indoor space, including the human body. The signals that are reflected undergo a change in their polarization perpendicular to the plane of incidence. Therefore, if a signal cannot be detected during a fall event, it can generate false alarms (Figure A.5a). This is the importance of the polarization state of antennas in detection systems.

Our fall detection platform allows to register the effect of the horizontal and vertical scenarios. In these scenarios it is possible to measure the variation of different angles of fall observation and determine the antenna orientation that reduces false alarms.

A.3.4 Experimental Protocol

With the sensing platform implemented in the indoor environment, 6 test subjects were selected to perform the experiments. This group of people developed a sequence of falls to a fixed height of 59 cm. This is the average height of the third step of a ladder.

The protocol that the participants followed was to place themselves on the corresponding step and remain still. Then, they received a visual and audible signal sent by the control computer to indicate the start of the test. The next instruction was to perform a falling motion from their starting position toward a padded surface to cushion the impact against the ground. Once the participants were on the ground, they had to remain in that position until a new audio signal indicated the end of the test. This allowed the

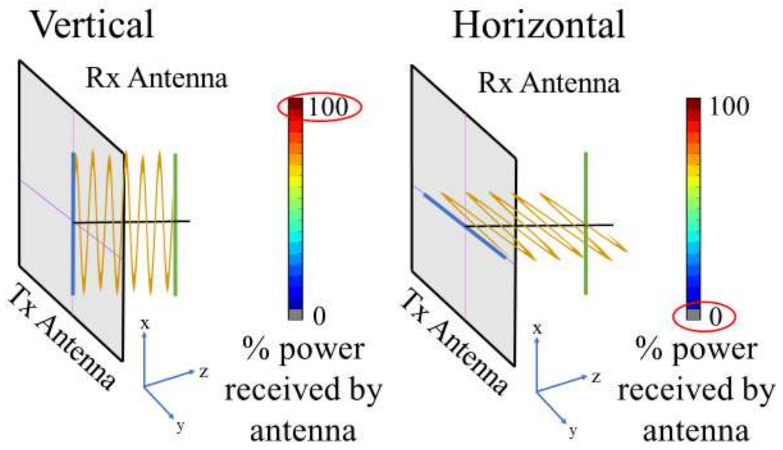

(a) Effects of polarization on the power received by the antennas.

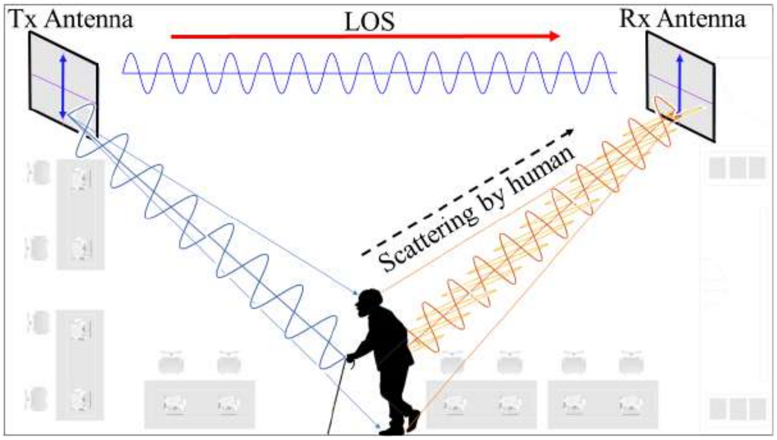

(b) Change of polarization caused by the multipath effect and reflection.

Figure A.5: Characteristics of the polarization in antennas.

platform to only record the movement of the fall. In total, a sequence of 10 falls was carried out in each of the experimental scenarios designed.

The selected participants were people between 23 and 48 years of age in good physical condition. We consider that an older age could put the integrity of the participants at risk. However, the variation of ages provides a record of how a person falls over the years. In addition, the group has another series of physical characteristics to be studied. Some of these are shown in the Table A.1. Finally, all the experiments were recorded by the platform and a video recording system. The video recording had the purpose of providing visual evidence and also a timestamp during the development of the experiments.

Table A.1: Physical characteristics of test subjects

Subject	**Age**	**Gender**	**Height (m)**	**Weight (Kg)**
1	23	Female	1.61	60
2	24	Male	1.75	77
3	27	Male	1.72	73
4	38	Female	1.55	58
5	47	Female	1.55	65
6	48	Male	1.71	85

A.4 Results

In this chapter we developed an analysis of the variations in a fall detection systems caused by the multiple observation angles of the sensing equipment. For this purpose, a database with 60 falls from 6 different people was used. The database was generated by experimentation in two different scenarios using our sensing platform based on RF-WiFi signals. The result of this was a database containing the spectrums captured throughout the time of experimentation. The spectrograms were separated into two groups. The first group contains the spectrums captured using the vertical positioning on the WiFi antennas. The second group is that of horizontal positioning. Both groups were subjected to a pre-processing stage. At this stage, a Gaussian-type high-pass filter was applied to the spectrograms. Furthermore, a bandwidth of 200 Hz was defined. The result of this is shown in the Figure A.6.

Figure A.6 shows a comparison between the spectrograms of the sensing group using antennas with vertical orientation (Figure A.6a) and the group of antennas with horizontal orientation (Figure A.6b). In the vertical case, the fall was recorded in sample 12. This was determined according to the timestamp provided by the video recording equipment. This spectrogram shows how the signal power suffered a slight disturbance caused by the acceleration of the falling body. However, within the spectrograms of the horizontal case the dispersion registered in the Doppler signatures is more prominent. In Figure A.6b, the fall was also recorded in sample 12. A noticeable difference is recorded in the experiments, both scenarios have the same angle of observation of the event but different antenna orientation. The dispersion register in the spectrum during the fall is larger in the horizontal scenario. Therefore, the classification stage provides a better differentiation due to the larger effect recorded in the spectrums.

To validate these results, we use PCA. This technique was applied to each of the spectrums captured in both scenarios. In our case we use the numerical results of the first two components. These components contain most of the energy of the signal and can be used to project the differences between all the spectrums.

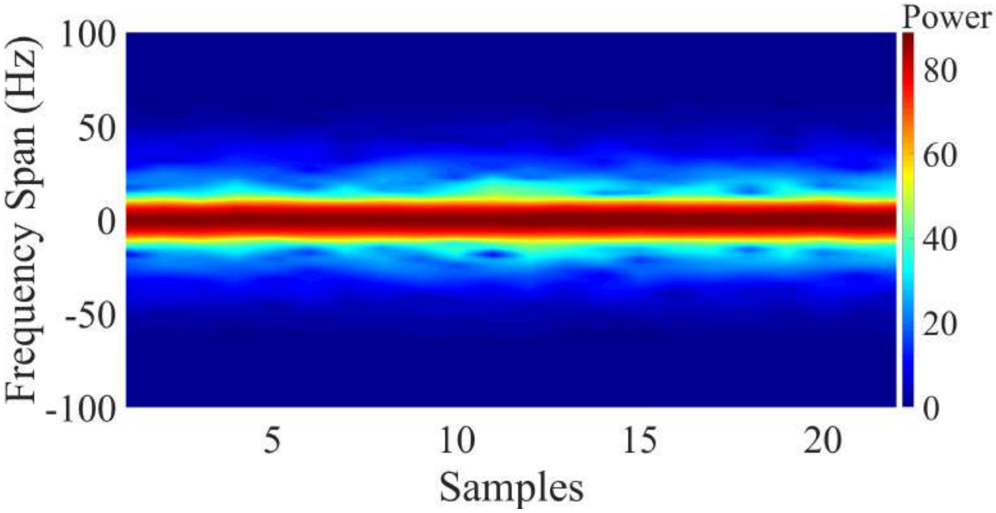

(a) Vertical orientation antennas with the fall recorded in sample 12.

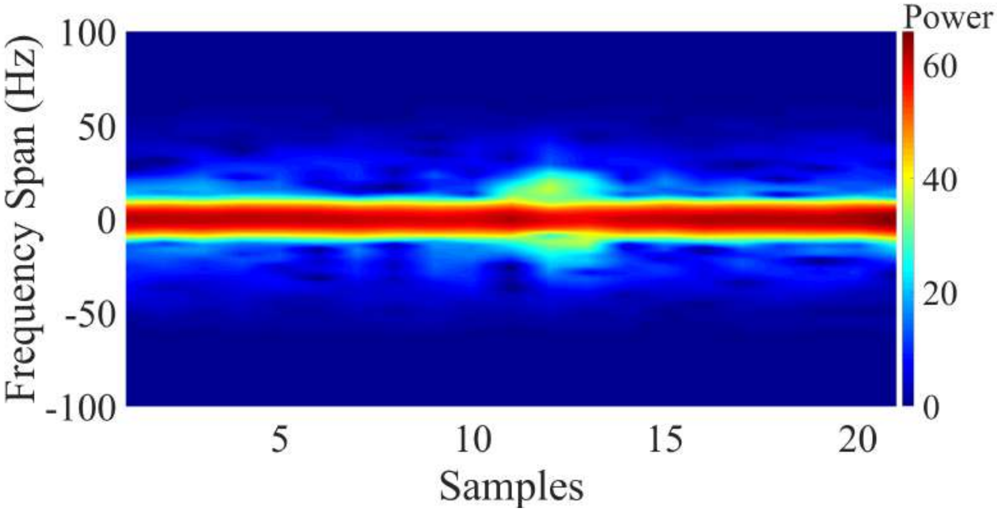

(b) Horizontal orientation antennas with the fall recorded in sample 12.

Figure A.6: Spectrograms collected by the fall detection platform: a) Vertical scenario, b) Horizontal scenario.

Figure A.7 shows the comparative graphs for the experiments in the vertical and horizontal case. These graphs show the numerical values of the first and second principal components. The dots correspond to the values obtained for the spectrums where no movement was recorded. The falls are identified by crosses.

In both cases, the data for each of these two classes tend to cluster. However, in the horizontal case a threshold can be easily determined between these two classes. The vertical case does not show a clear separation of the classes. The horizontal scenario recorded a greater dispersion in the Doppler signatures of the spectrograms, and these dispersions allows a clear distinction between falls and no movement classes.

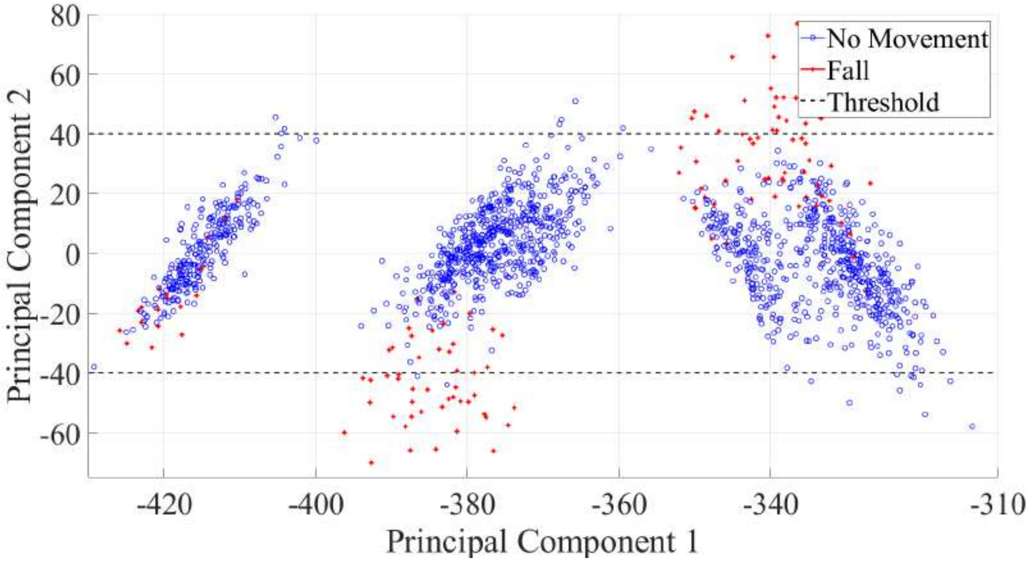

(a) Vertical antenna.

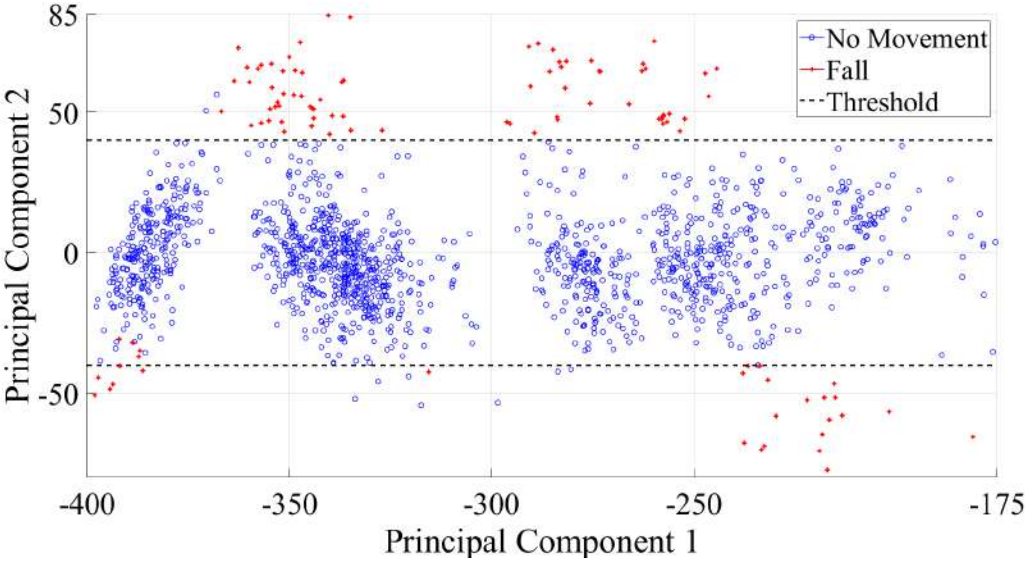

(b) Horizontal antenna.

Figure A.7: Projection of the first and second principal components.

The orientation of the antennas has a great impact on Doppler signature dispersion. The horizontal orientation of the antenna positively impacts the distinction of the two characterized classes: falls and no movement. This evident separation reduces the possibility of false alarms. Taking this into account, it is possible to design or improve a fall detection systems based on RF-WiFi signals. This platform allows to reduce the errors caused by the observation angle without increasing the number of sensors in the same indoor environment. Furthermore, the results were obtained using a platform designed with general-purpose measurement equipment. For this reason our platform is affordable and easy to replicate.

On the other hand, it is necessary to add new activities in the experimental protocol such as: walking, sitting or going up and down stairs. In this way the proposed sensing platform can be compared with other similar works, such as those in [40] and [37]. For that purpose, it is necessary to consider classification algorithms that allow to compute the precision of detection in terms of probability. Our platform is designed in blocks. Therefore, it is possible to incorporate additional elements without modifying the other parts of the system. These are key elements in the continuous evaluation of the performance of the platform.

A.5 Conclusion

In this chapter, we develop a fall detection platform based on sensing RF-WiFi signals. The platform is used to study the effects of the antennas orientation and improve the performance of the fall detection systems. Spectrograms were captured during experiments involving a series of falls that capture the dispersion in the Doppler signatures created by the event. The recorded spectrograms were analyzed to establish how antenna orientation affected the dispersion. In this case, the orientation in the horizontal scenario allowed us to observe a larger dispersion at the moment of the fall event. Furthermore, the principal component analysis was used to extract the features of the spectrograms. The principal features were used to analyze the differences between the spectrums that record a fall and those that did not. The PCA results shows that horizontal scenario provides a clear separation between no movement and falls. Therefore, the effects caused by the orientation of the antennas impact the performance of the classification stage of the fall detection systems.

Appendix B: Doppler Spectrum Measurement Platform for Narrowband V2V Channels

This chapter describes the implementation of a Doppler spectrum measurement platform for narrowband frequency-dispersive vehicle-to-vehicle (V2V) channels. The platform is based on a continuous-wave (CW) channel sounding approach widely used for path-loss and large-scale fading measurements, but whose effectiveness to measure the Doppler spectrum of V2V channels is not equally known. This channel sounding method is implemented using general-purpose hardware in a configuration that is easy to replicate and that enables a partial characterization of frequency-dispersive V2V channels at a fraction of the cost of a dedicated channel sounder. The platform was assessed in a series of field experiments that collected empirical data of the instantaneous Doppler spectrum, the mean Doppler shift, the Doppler spread, the path-loss profile, and the large-scale fading distribution of V2V channels under realistic driving conditions. These experiments were conducted in a highway scenario near San Luis Potosí, México, at two different carrier frequencies, one at 760 MHz and the other at 2,500 MHz. The transmitting and receiving vehicles were moving in the same direction at varying speeds, ranging from 20 to 130 km/h and dictated by the unpredictable traffic conditions. The obtained results demonstrate that the presented measurement platform enables the spectral characterization of narrowband V2V channels and the identification of their Doppler signatures in relevant road-safety scenarios, such as those involving overtaking maneuvers and rapid vehicles approaching the transmitter and receiver in the opposite direction.

This chapter forms part of the paper titled 'Doppler Spectrum Measurement Platform for Narrowband V2V Channels" published in *IEEE Access*. I and the other authors gave consent to use our work as an integral part of this dissertation.

B.1 Introduction

Vehicular communication systems are an emerging technology aimed at applications related to road safety, traffic management, and on-board infotainment services [111–118]. Early efforts to equip vehicles with communication capabilities focused on the development of dedicated short-range communication (DSRC) technologies. In the U.S. and Europe, the DSRC technology is based on the specifications of the IEEE 802.11 Standard [119]. These specifications encompass the protocols for wireless access in vehicular environments [113, 114], including vehicle-to-vehicle (V2V) and vehicle-to-infrastructure (V2I) communications in the 5.9 GHz band [119]. Japan has also contributed to the development of DSRC technology for vehicular communications [114–116]. In this country, local regulatory agencies issued specifications for vehicular networks in the 700 MHz band [120]. In recent years, the Third Generation Partnership Project (3GPP) defined specifications for Vehicle-to-Everything (V2X) communications based on the infrastructure of the long-term evolution (LTE) cellular network [121–123]. With the fast development of fifth-generation (5G) networks, the 3GPP updated those specifications and defined new use cases for V2X communications within the 5G ecosystem [124]. These cellular-based V2X communication protocols also adopt the 5.9 GHz band for direct V2V communications [117, 123, 124].

Regardless of the particular frequency bands and communication protocols, the design of vehicular communication systems faces several technical challenges related to the transmission of information through the rapidly-changing and highly-dispersive vehicular channel [125, 126]. The vehicles' mobility, paired with the short-range communication links, produces rapid variations of the channel's response that compromise the system performance [127–133]. Moreover, depending on the propagation conditions, the transmitted signal can arrive at the receiver through multiple interactions with interfering objects in the environment, resulting in worse-than-Rayleigh fading [134–136]. Hence, a thorough understanding and a correct characterization of the vehicular channel are crucial for the efficient design of V2X communication systems.

Theoretical V2V channel models have been developed to characterize wireless propagation in vehicular environments [137–141]. Typically, these models are derived by making certain assumptions on the mobility conditions and propagation environments. For instance, V2V channel models have been often developed assuming uniform motion, i.e., vehicles moving with constant speed over linear trajectories [135, 142]. Since this assumption is not always valid in practice, recent research efforts are aiming at the formulation of V2V channel models with non-uniform motion, i.e., assuming acceleration components and non-linear trajectories [143–145]. Regarding the propagation environment, some assumptions are made on the distributions of interfering objects for particular scenarios [146]. Conventional approaches consider isotropic or non-isotropic distributions of interfering objects around the vehicles [131]. For more realistic scenarios, ray-tracing models provide accurate representations of the propagation environments by considering the exact positions and electromagnetic properties of the interfering objects [147].

Besides the theoretical characterization of V2X channels, empirical data are also needed to gain insights into the behavior of realistic channels [148–152]. Empirical data are obtained following a specific channel sounding principle, e.g., CW, direct pulse, or correlation-based [153, 154]. The selection of the sounding principle depends on the channel characteristics that need to be analyzed. For example, the frequency-dispersive characteristics of time-varying V2V channels require a sounding approach aimed at capturing traces of the channel's Doppler spectrum. In turn, a sounding method with a focus on the channel's power delay profile (PDP) is required for the analysis of the time-dispersive characteristics of frequency-selective V2V channels [155]. Most high-performance channel sounding platforms employ specialized equipment to sample the Doppler spectrum and/or the PDP with a high resolution (e.g., see [156–159]). While desirable, such platforms are rare assets, as their high cost and specific purpose make their purchase the least priority to most universities and research centers. This limitation creates a need for innovative solutions to construct V2V channel sounding platforms with more accessible general-purpose equipment.

In response to this need, this paper describes the implementation of a Doppler spectrum measurement platform for frequency-dispersive V2V channels. The platform is based on a narrowband channel sounding principle that employs an analog radio-frequency (RF) signal generator to transmit a CW probe signal and a spectrum analyzer (SA) to measure the channel's Doppler spectrum for a given carrier frequency. This measurement setup has been widely used for path-loss and large-scale fading measurements, e.g., see [160]. However, the effectiveness of such a setup to measure the Doppler spectrum of V2V channels is not equally known. The resulting measurement platform is easy to replicate since it comprises general-purpose hardware commonly available in universities and research centers. It is, therefore, adequate not only for research but also for educational purposes, e.g., to illustrate the Doppler effect in mobile radio communications to undergraduate and graduate students.

This chapter is the culmination of our previous work presented in [161]. The scope and contributions of [161] are extended here as follows:

- We provide a detailed discussion of the theoretical foundations of our implementation. This discussion is intended to help the reader to understand how our implementation works, and to identify its capabilities and limitations. We bring attention to a practical issue that affects the computation of the Doppler spectrum and that passed unnoticed in [161]: the presence of artifacts due to cross-terms in the measured channel's spectrogram. Moreover, we discuss the configuration of the hardware parameters that set the trade-off between acquisition time and Doppler frequency resolution.

- We present a methodology to pre-process the measured spectrograms and circumvent the limitations of generic RF hardware. In particular, we address: (i) the frequency drifts in the transmitted signal caused by the operation of the signal generator; and (ii) the artifacts caused by cross-terms in the measured spectrograms.

- Finally, to demonstrate the capabilities of our measurement platform, we present the results of a measurement campaign at 760 MHz and 2,500 MHz in a highway scenario near San Luis Potosí, México. The experiments were conducted on a highway since this is a diverse and challenging environment where the effects of high mobility and the unpredictable dynamics of vehicular traffic can be observed clearly. We analyze the empirical Doppler signatures of the V2V channel in relevant road-safety scenarios, namely those involving overtaking maneuvers and rapid vehicles approaching the transmitter and receiver in the opposite direction. In addition, we characterize the distributions of the instantaneous mean Doppler shift and Doppler spread, the path-loss profile, and the large-scale fading distribution. While our platform does not measure the time-dispersive characteristics of wideband V2V channels, the obtained results demonstrate that it successfully captures the Doppler profile of frequency-dispersive V2V channels in realistic driving conditions.

The remainder of the chapter is organized as follows. Section B.2 provides a review of related work. The theoretical background and the details of our implementation are discussed in Sections B.3 and B.4, respectively. Section B.5 addresses the hardware configuration and describes the highway scenario in which we tested the platform. Section B.6 presents our Doppler spectrum measurement results. SectionB.7 addresses the computation of the path-loss profile and large-scale fading distribution from the measured Doppler spectra. Finally, Section B.8 summarizes our conclusion.

B.2 Motivation and Related Work

Substantial research efforts have focused on measuring the V2V channel at 5.9 GHz. Most approaches to measuring V2V channels seek high time resolution due to the rapid fluctuations of the V2V channel [156–158]. Measurements in [156, 157, 162, 163] were performed using a multiple-input multiple-output (MIMO) channel sounder based on a switched-array principle. This architecture employs rubidium clocks for time reference synchronization to record accurate versions of the channel response with a digital signal processor as an interface. Measurements in [158] were conducted using a sounding platform that employs a software-defined radio to generate an unmodulated version of the IEEE 802.11p signal [164]. The transmission of this signal is repeated during the experiment and sampled by a data acquisition card with a high sample rate. Furthermore, measurements at 700 MHz have been conducted using a sounding platform based on a pulse-compression technique [165]. This platform employs a real-time SA to record the channel response. In particular, these implementations have been employed to effectively analyze channel characteristics in both time and frequency domains. Nevertheless, the experiments are not easy to reproduce due to the stringent hardware requirements of the channel sounding platforms.

Although the analysis of the channel's delay domain properties is important, a partial characterization of the V2V channel only in the Doppler frequency domain is also relevant. Measurements in [166, 167], follow a CW sounding principle using a vector spectrum analyzer to record the channel's Doppler spectrum. In this platform, the time information obtained by Global Positioning System (GPS) receivers is employed for data synchronization. In particular, CW sounding principles have been mainly employed for the characterization of attenuation effects through zero-span measurements. However, the accuracy of these measurements is compromised when the signal generator is subject to frequency drifts due to temperature effects. This practical issue can be solved by increasing the frequency span to a few Hertz and correcting the observed drifts. Furthermore, such a solution can also be harnessed to measure the channel's Doppler spectrum by further increasing the frequency span. The CW sounding principle has two main advantages: (i) CW channel sounders might have simple architectures; and (ii) CW sounding platforms have sampling rates that enable continuous data acquisition over long trajectories.

While most channel sounders for V2V channels have stringent hardware requirements [156–158, 166, 167], general-purpose devices can be used to implement simpler architectures. In contrast to dedicated channel sounding platforms, the reconfiguration of general-purpose devices is straightforward and enables users to perform tests at different frequencies. The characterization of V2V channels at different frequencies is particularly relevant since the defined carriers might differ for different communication protocols (e.g., see [120, 123, 124, 164]).

B.3 Preliminaries

In this section, we describe the theoretical foundations of our measurement platform. We discuss the main concepts of the V2V channel response and present the CW sounding principle harnessed in our implementation.

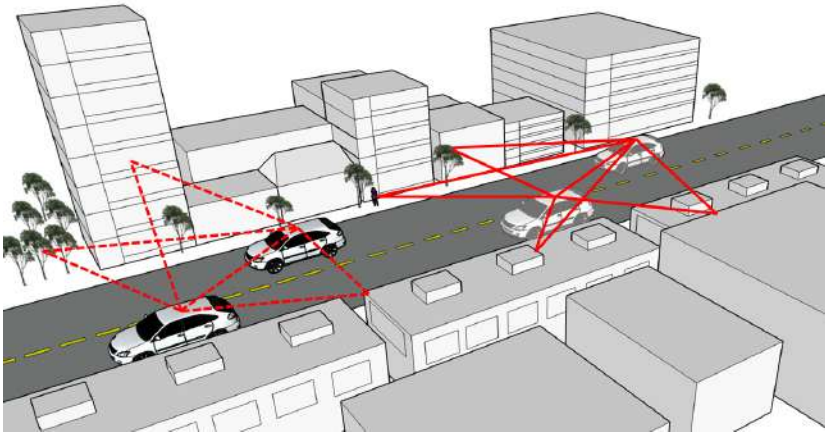

Figure B.1: Time-varying multipath propagation in vehicular environments (red-solid lines: propagation paths at time instant $t = t_1$, red-dashed lines: propagation paths at time instant $t = t_2$).

B.3.1 Theoretical Background

In a vehicular radio communication system, the received signal is the superposition of multiple replicas of the transmitted signal that arrive at the receiver over different propagation paths, one of which can be a Line of Sight (LOS) path, as illustrated in Fig. B.1. Hence, by neglecting the effects of additive noise, the received multipath signal can be modeled in the complex base-band equivalent by

$$y(t) = \sum_{n=1}^{N(t)} g_n(t) e^{-j[2\pi f_c \tau_n(t) + \theta_n(t)]} x(t - \tau_n(t))\,. \tag{B.1}$$

In this equation, $x(t)$ stands for the transmitted signal, f_c is the carrier signal frequency, $N(t)$ denotes the number of replicas of $x(t)$ that arrive at the receiver at the time instant t, whereas $g_n(t)$, $\theta_n(t)$, and $\tau_n(t)$ are the instantaneous attenuation factor, phase shift, and propagation delay of the nth received replica. The latter four parameters are characterized by time-dependent variables since the propagation conditions in vehicular environments may change at any moment due to the vehicles' high mobility and the short-range communication link (see Fig. B.1).

In turn, the V2V channel can be modeled by a linear time-varying (LTV) system. An LTV system is uniquely characterized by its impulse response, $h(t;\tau)$, or equivalently, by its frequency response, $H(t;f) = \int_{-\infty}^{\infty} h(t;\tau) e^{-j2\pi f \tau}\, \mathrm{d}\tau$ [168–170]. Since (B.1) is the output of an LTV system to an input $x(t)$, i.e., $y(t) = h(t;\tau) * x(t)$ with $*$ denoting the convolution operation, we can characterize the V2V channel by

$$h(t;\tau) = \sum_{n=1}^{N(t)} g_n(t) e^{-j[2\pi f_c \tau_n(t) + \theta_n(t)]} \delta(\tau - \tau_n(t)) \tag{B.2}$$

$$H(t;f) = \sum_{n=1}^{N(t)} g_n(t) e^{-j[2\pi (f_c + f) \tau_n(t) + \theta_n(t)]} \tag{B.3}$$

where $\delta(t)$ denotes the Dirac delta function. Equation (B.3) shows that the V2V channel is a linear system whose response varies not only in the time domain, but also in the frequency domain. The channel's time and frequency variations cause a spectral dispersion of the transmitted signal. In particular, the channel's variation in time causes dispersion in the frequency domain, whereas its frequency variations cause dispersion in the time domain [155]. These effects can be analyzed in the joint domain of the Doppler frequency variable, ν, and the delay variable, τ, by the Doppler-delay spreading function $s(\nu;\tau) = \int_{-\infty}^{\infty} \int_{-\infty}^{\infty} H(t;f) e^{-j2(\nu t - f\tau)} \, \mathrm{d}t \, \mathrm{d}f$. Alternatively, the channel dispersion can be analyzed in the Doppler domain on the grounds of the frequency-dependent Doppler-spread function

$$D(\nu;f) = \int_{-\infty}^{\infty} H(t;f) e^{-j2\pi\nu t} \, \mathrm{d}t \tag{B.4}$$

or in the delay domain, with respect to $h(t;\tau)$, which is a time-dependent delay-spread function dual to $D(\nu;f)$. We refer the reader to [169–172] for a detailed discussion on the system functions of mobile radio channels.

From the definition of $h(t;\tau)$, it follows that the response of the V2V channel can be measured in practice by transmitting a signal of a very short duration, e.g., those designed for spread spectrum and ultra-wideband communications [173–176]. Also, from the definition of $H(t;f)$, the channel response can be measured by transmitting multiple unmodulated complex sinusoids of different frequency, either sequentially (as in frequency-hopping communication systems [177, 178]) or simultaneously (as in orthogonal frequency division multiplexing systems [158, 159, 179, 180]). However, the transmission of these signals relies on costly equipment, such as vector waveform/function generators, and their detection requires the implementation of sophisticated receivers that rely on accurate synchronization with the transmitter.

B.3.2 Narrowband Channel Sounding Principle

The complexity and high cost of implementing a V2V channel sounder are further exacerbated by the difficulty in measuring the channel response with a high resolution in time and frequency. An alternative to simplify the channel sounder architecture is to measure the channel response only in one dimension. For mobile communications in rapidly time-varying channels, the time-domain response is critical to assess the impact of signal dispersion in the Doppler frequency domain [181–184]. To measure the response of the V2V channel only in the time domain, it suffices to transmit a CW probe waveform, $x(t) = 1$, i.e., an unmodulated carrier signal. Thereby, the received signal is given by

$$c(t) = \sum_{n=1}^{N(t)} g_n(t) e^{-j[2\pi f_c \tau_n(t) + \theta_n(t)]} \,. \tag{B.5}$$

where $c(t)$ can be identified as the channel complex envelope (CCE) since $c(t) = H(t;f)\Big|_{f=0}$. The reception process can be simplified further if the channel's instantaneous power, $z(t) = |c(t)|^2$, is measured instead of the CCE. This narrowband channel sounder can be implemented with general-purpose hardware, such as an analog RF signal generator and an SA. Measurement platforms of this type are typically employed to gather empirical information about the fading statistics of narrowband channels. However, the same platform can be employed to characterize the channel dispersion in the Doppler frequency domain. To show this, we note that an SA produces traces of the received signal's spectrogram

$$S(\nu, t') = |Y(\nu, t')|^2 \tag{B.6}$$

where the variable t' denotes a particular observation time instant, and

$$Y(\nu, t') = \int_{-\infty}^{\infty} c(t) w(t - t') e^{-j2\pi\nu t} \, \mathrm{d}t \tag{B.7}$$

is the STFT of $c(t)$, where $w(t)$ is a real-valued even function given such that $w(t) > 0$ for $|t| < T_0/2$, $w(t) = 0$ for $|t| > T_0/2$, $\int_{-\infty}^{\infty} w^2(t)dt = 1$, and $T_0 > 0$ [185]. In practice, the constant quantity T_0 can be associated to the sweep time of an SA. Assuming that the number of multipath components of the channel response remains constant within an observation interval of length T_0, we can write the STFT of the CCE for a given discrete time, $t'_k = kT_0$, for $k \in \mathbb{Z}$, as

$$\begin{aligned} Y(\nu, t'_k) = & \sum_{n=1}^{N_k} g_{k,n} e^{-j\theta_{k,n}} \\ & \times \int_{-\infty}^{\infty} w(t - t'_k) e^{-j2\pi[\nu t + f_c \tau_{k,n}(t)]} \, \mathrm{d}t \,. \end{aligned} \tag{B.8}$$

In this equation, N_k is the number of resolvable multipath components of $c(t)$ within the kth observation interval, $\left(k - \frac{1}{2}\right) T_0 < t' \leq \left(k + \frac{1}{2}\right) T_0$, whereas $g_{k,n}$, $\theta_{k,n}$, and $\tau_{k,n}(t)$ are the corresponding attenuation factor, phase shift, and time-varying propagation delay, respectively, of the nth received replica of $x(t)$ within the kth observation interval. Assuming also that the received signal is given by the superposition of N_k electromagnetic plane waves, the time-varying propagation delays $\tau_{k,n}(t)$ are equal to

$$\tau_{k,n}(t) = \tau_{k,n}^{(0)} - t\frac{\nu_{k,n}}{f_c} \tag{B.9}$$

where $\tau_{k,n}^{(0)}$ and $\nu_{k,n}$ are the initial propagation delay and the Doppler shift, respectively, of the nth plane wave received within the kth observation interval [186]. In particular, the Doppler shift $\nu_{k,n}$ can be expressed as

$$\nu_{k,n} = f_{k,n}^{S} + \frac{\dot{f}_{k,n}^{A}(t)}{2} \tag{B.10}$$

where $f_{k,n}^{S}$ and $\dot{f}_{k,n}^{A}(t)$ are Doppler shifts caused by the vehicles' speed and acceleration for the nth plane wave received within the kth observation interval, respectively. The first component depends on the initial speeds of the vehicles, whereas the second term is a time-varying quantity that depends on the vehicles' acceleration profiles.

Thereby, we have

$$Y(\nu, t_k') = \sum_{n=1}^{N_k} g_{k,n} W(\nu - \nu_{k,n}) e^{j\left[2\pi\left(\nu t_k' - f_c \tau_{k,n}^{(0)}\right) - \theta_{k,n}\right]} \tag{B.11}$$

where $W(\nu)$ is the Fourier transform of the windowing function $w(t)$. The STFT of the CCE provides a time-dependent description of the channel dispersion in the Doppler domain. The function $Y(\nu, t_k')$ is similar in that regard to the frequency-dependent Doppler-spread function defined in (B.4). In fact, if the number of multipath components is constant for all t, then, in the limit when $T_0 \to \infty$, one can verify that $Y(\nu, 0) = D(\nu, 0) = \sum_{n=1}^{N_0} g_n e^{j\left[2\pi f_c \tau_n^{(0)} - \theta_n\right]} \delta(\nu - \nu_n)$. From (B.6) and (B.11), it follows that the spectrogram of the CCE is equal to

$$S(\nu, t_k') = S_A(\nu, t_k') + S_C(\nu, t_k') \tag{B.12}$$

where the spectral function

$$S_A(\nu, t_k') = \sum_{n=1}^{N_k} g_{k,n}^2 W^2(\nu - \nu_{k,n}) \tag{B.13}$$

contains the auto-terms of the CCE. This function has a clear physical meaning as it can be interpreted as the channel's time-varying Doppler spectrum [185]. In turn, the function

$$\begin{aligned} S_C(\nu, t_k') = & \sum_{n=1}^{N_k} \sum_{\substack{m=1 \\ m \neq n}}^{N_k} g_{k,m} g_{k,n} W(\nu - \nu_{k,m}) W(\nu - \nu_{k,n}) \\ & \times e^{j\left[2\pi f_c\left(\tau_{k,m}^{(0)} - \tau_{k,n}^{(0)}\right) + \left(\theta_{k,m} - \theta_{k,n}\right)\right]} \end{aligned} \tag{B.14}$$

contains the cross-terms of $S(\nu, t'_k)$. In contrast to $S_A(\nu, t'_k)$, $S_C(\nu, t'_k)$ does not have a physical meaning since the cross-terms are artifacts caused by the windowing function $w(t)$. In the case of a super-heterodyne SA, the cross-terms are also related to the dynamic range of the frequency mixers [30].

Equations (B.12)–(B.14) show that the Doppler spectrum of a V2V channel can be measured in practice by employing a narrowband channel sounder that follows the principle described in this section. One of the challenges of implementing such a platform is to find the value of the SA's sweep time that maximizes the contribution of the spectrogram's auto-terms and minimizes that of the cross-terms. It can be shown that the spectrogram's cross-terms vanish in the limit when $T_0 \to \infty$ [185]. However, this asymptotic scenario is of little relevance in practice since the sweep time of an SA cannot extend to infinity. Moreover, short sweep times are required to ensure that the time variations of $N(t)$, $g_n(t)$, and $\theta_n(t)$ are negligible within the observation window of length T_0. Nevertheless, the sweep time cannot be too short either since this will reduce the SA's capability to resolve the spectrogram's auto-terms that are in close proximity to each other. There is, therefore, a critical tradeoff in finding a proper value for the sweep time.

In practice, the sweep time is determined by the resolution bandwidth (RBW), video bandwidth (VBW), and frequency span [30]. In modern SAs, such parameters are coupled to avoid measurement errors. Therefore, setting a subset of parameters will update the others automatically. For example, the VBW is coupled linearly with the RBW. In the case of measuring CW probe signals, the RBW should be set to the smallest possible value [187]. Nevertheless, this configuration will affect the time resolution significantly since decreasing the RBW will increase the sweep time [30, 187]. Therefore, we need to find a compromise between a sufficiently small RBW (typically a few Hertz) and a suitable sweep time.

B.4 The Measurement Platform

In this section, we present the implementation of our Doppler spectrum measurement platform for frequency-dispersive V2V channels. We describe the main components and considerations to assemble the transmitter and receiver stations according to the theoretical concepts revised in the previous section. The discussion is intended to guide the interested readers to replicate the platform with their own hardware.

B.4.1 Implementation

The particular devices in our implementation are the Keysight N9310A Radio-Frequency (RF) signal generator [188], and the Keysight Fieldfox N9913A in SA mode [189]. The N9310A RF signal generator enables the transmission of an RF wave in frequencies that range from 9 kHz to 3 GHz.

The highest power level that this device provides is 20 dBm. Since this is an RF device built with non-ideal components, the probe signal may be subject to frequency drifts due to temperature effects. An approach to tackle this particular issue will be discussed in the next subsection.

The N9913A is a portable device that includes the SA mode. This device can measure signals with frequencies that range from 30 kHz to 4 GHz. The proper configuration of the SA is important for this specific application since it involves the tradeoff between time and frequency resolution. The flexibility of these two devices enables us to measure the Doppler spectra of V2V channels at different frequencies by reconfiguring some of the hardware parameters.

In addition to the described devices, the measurement platform requires pairs of antennas at specific frequencies, cabling, and adapters. Furthermore, other components are needed to gather complementary information to analyze the V2V channel characteristics effectively. In particular, GPS receivers are crucial to obtain time-stamped position information of the vehicles. This information is used to determine the instantaneous separation distances among vehicles, which are particularly important to describe the path-loss profile. Laptop computers are required to record the position information and control the measurement hardware. Video cameras are also useful in this context to record how the propagation scenario changes during the experiments, e.g., to establish the time intervals measured under LOS conditions. Table B.1 summarizes the list of employed materials.

A block diagram of the transmitter station is illustrated in Fig. B.2. The CW probe signal is produced by the N9310A RF signal generator and transmitted by a dipole antenna at 760 MHZ (or 2,500 MHz). In particular, we set the carrier frequency to 760 MHZ (or 2,500 MHz) and the RF output level to 20 dBm. Before performing any experiment, we power on, configure, and allow this device to warm up for half an hour. The warm up reduces the effects of temperature on the frequency drift of the probe signal during the experiments. Once turned on, this device will continuously transmit the probe signal without requiring any control device. We equip this station with a GPS receiver and a laptop to record the position information. Moreover, we consider a video camera in this station to record the propagation scenario from the transmitter perspective.

A block diagram of the receiver station is illustrated in Fig. B.3. The signal is received by a dipole antenna at 760 MHz (or 2,500 MHz) connected to the N9913A in SA mode. This station is also equipped with a GPS receiver, a laptop, and a video camera. The laptop in this station runs a MATLAB script to configure the SA's parameters automatically via the TCP/IP protocol. We use the same protocol to initiate and stop the data recording in the SA by sending control commands. In particular, the measured data was stored in the SA's internal memory since this required less time than recording directly in the computer by querying the spectrogram's data via

Materials	Company	Model/Description
SA	Keysight	FieldFox N9913A
RF signal generator	Keysight	N9310A
GPS receivers	Digilent	PmodGPS
Antennas	Generic	Half wavelength dipoles at 760 MHz and 2,500 MHz
Cabling	Generic	RG-6 cables of different lengths
Adapters	Generic	N-type male to F-type female
Laptops	Generic	Control computers equipped with MATLAB© software
Ethernet cable	Generic	For communication between a control computer and the SA
Video cameras	Generic	For recording the changes of the propagation scenario

Table B.1: List of materials and hardware for the measurement platform.

the TCP/IP protocol. While the SA records the spectrogram's data, the laptop stores the time-stamped position information from the GPS receiver. The SA is configured according to the parameters shown in Table B.2. The central frequency is set to the frequency of the probe signal (760 MHz or 2,500 MHz). We consider a frequency span of 1,500 Hz for the probe signal at 760 MHz, and of 2,000 Hz for the signal at 2,500 MHz. We also consider the maximum number of frequency span sample points (1001) supported by the SA to measure the Doppler spectrum of V2V channels with sufficient resolution. In low mobility conditions, the frequency span can be further reduced according to the considered speed range. As discussed in the previous section, the choice of the RBW compromises the sweep time. Since the measured spectrogram is stored in the SA's internal memory (or directly in the computer), the RBW should be set also taking into account the recording time. We set the RBW to 10 Hz since it enables suitable sweep times to perform the experiments without compromising the capability to resolve the spectral components. In this regard, the aim is to find a small value of the RBW that avoids the distortion of a pure tone measured in controlled conditions and does not yield a large sweep time. The average sweep time obtained in this setting was 0.27 s, but the total acquisition time including the latency due to data recording in the SA internal memory was about

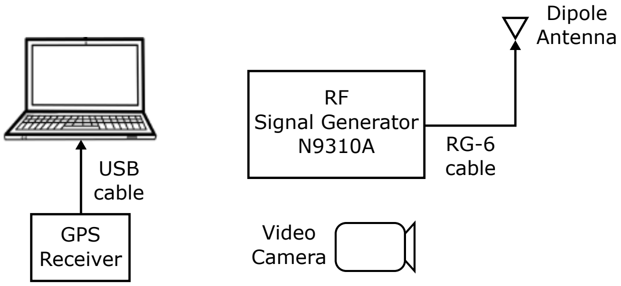

Figure B.2: Block diagram of the transmitter station.

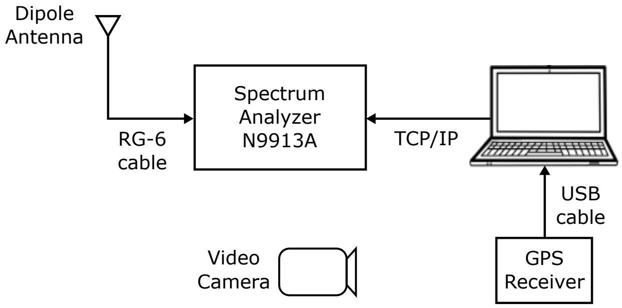

Figure B.3: Block diagram of the receiver station.

Parameter	**Value**
Central frequency	760 MHz 2,500 MHz
Frequency span	1,500 Hz (@760 MHz) 2,000 Hz (@2,500 MHz)
Sample points	1001
RBW	10 Hz
Attenuation	0 dB
Pre-amp	On

Table B.2: List of parameters for the configuration of the SA.

0.40 s.

B.4.2 Practical Aspects

In practice, the measured spectrograms are subject to several impairments caused by the non-ideal RF components of the hardware. We address here two practical aspects of our implementation: (i) the frequency drifts of the transmitted signal due to temperature effects on the RF signal generator; and (ii) the presence of artifacts caused by the cross-terms in the measured spectrograms.

To compensate for the practical issues of our platform, we conducted reference measurements in controlled laboratory conditions and in-field with static vehicles. The first control measurements were taken with the output of the RF signal generator connected directly to the input of the SA while setting the transmitting power to -40 dBm. We attenuated the transmitting power for such experiments to prevent an overload in the SA's input. Figure B.4 shows a 500 Hz window of a spectrogram measured at 2,500 MHz over 210 s. This spectrogram illustrates the two practical issues mentioned above. The first effect is observed in the deviation of the received signal from the central frequency over time. The second effect is observed in the undesirable contributions above noise level that appear around the carrier frequency (yellow lines). Note that the probe signal is not a monochromatic signal, as it does not have a zero bandwidth. It occurs since, in practice, the signal spectrum is widened over a few Hertz due to filtering and time windowing stages. In the following, we discuss each issue separately and our approach to addressing them in the pre-processing stage.

The frequency drifts of the transmitted signal are caused by the continuous operation of the RF signal generator. The frequency drifts of the spectrogram with respect to the central frequency are shown in Fig. B.5. This plot shows that the carrier frequency of the received signal shifts to negative frequencies in this particular experiment. The frequency drift appears to change linearly with small variations due to the uncertainty of the signal detection in the SA. This issue can be compensated in practice by taking control measurements during short intervals at the beginning and the end of each experiment run. The transmitter and receiver should remain completely stationary during such control intervals to avoid the probe signal's spectral dispersion caused by the combined effects of multipath and the Doppler effect. The spectrogram's snapshots recorded with the vehicles in static conditions allow to identify the initial and final trend of the frequency drift. The rest of the snapshots, obtained with the vehicles in motion, are realigned employing frequency drift estimates obtained from a piece-wise linear regression of the reference heading and trailing snapshots.

As discussed in the previous section, the cross-terms of the measured spectrogram are undesirable artifacts that corrupt the Doppler spectrum. The presence of such artifacts can be masked by the additive noise. The effects of the cross-terms are illustrated in Fig. B.6, which shows a snapshot of the spectrogram presented in Fig. B.4 with the frequency drift corrected. Figure B.7 presents a time average of the spectrogram shown in Fig. B.4 after the correction of the frequency drift. The average operation smooths the additive noise's variations around its average power and highlights the presence of artifacts around the carrier frequency. In practice, these artifacts can mask propagation effects that are important to the statistical analysis of the measured V2V channels. Our approach to address this issue consists of computing the correlation of each snapshot in the measured spectrogram with a proper spectrogram mask. The spectrogram masks are obtained by

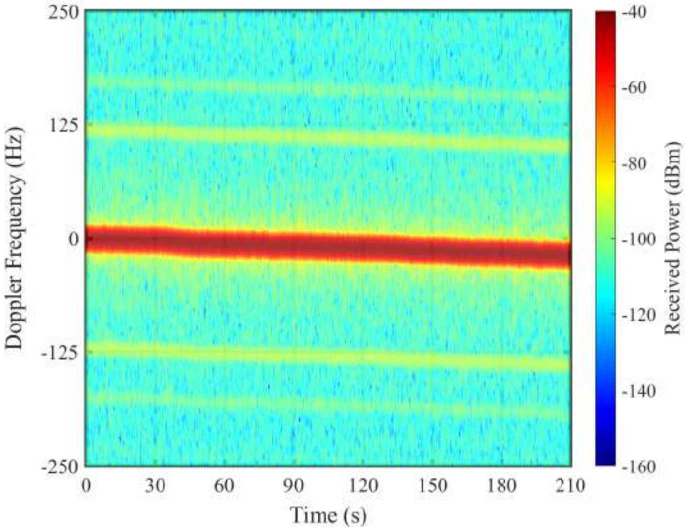

Figure B.4: A measured spectrogram to illustrate the practical issues of our implementation. The carrier frequency of the probe signal is 2,500 MHz.

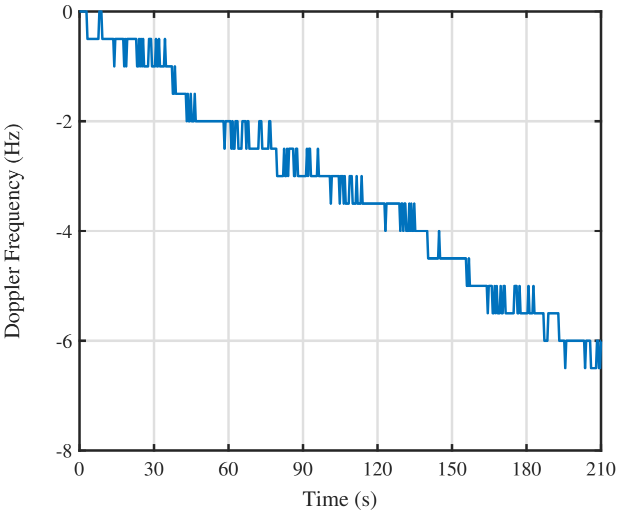

Figure B.5: Frequency drift of a received signal over time.

averaging snapshots of spectrograms measured in laboratory conditions at the corresponding carrier frequencies, such as that shown in Fig. B.7. To complete the pre-processing stage, we readjust the amplitudes and scale them to the original values in the measured spectrogram. Finally, we apply a threshold to clip the noise level. After addressing the two practical aspects by pre-processing the raw data, we obtain the spectrogram $\tilde{S}(\nu, t'_k)$ that can be used to compute the channel's statistics.

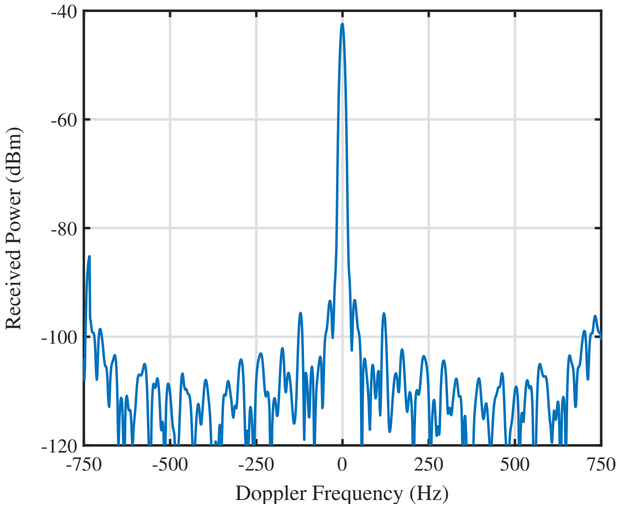

Figure B.6: A snapshot of a measured spectrogram. The carrier frequency of the probe signal is 2,500 MHz.

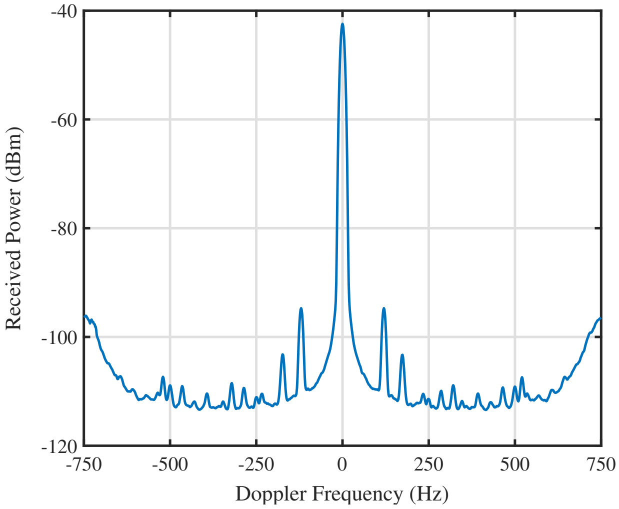

Figure B.7: Averaged snapshot of a measured spectrogram. The contributions of the spectrogram's cross-terms appear above the noise level.

B.5 The Measurement Campaign

In this section, we discuss how to assemble the measurement platform on the test vehicles and how we perform a measurement campaign. Moreover, we discuss the particular scenario where we performed our experiments.

B.5.1 The Measurement Setup

First, the RF signal generator and the SA are installed on the vehicles' main storage compartments using base plates. Moreover, the antennas and GPS receivers are placed on the vehicles' roofs using permanent magnets.

Then, we connect the antennas and GPS receivers to the corresponding devices. Finally, we configure the hardware according to the discussion in Section B.4.1 and allow it to warm up before performing any experiment. Each test vehicle is equipped with a portable power generator that supplies the devices.

To perform the experiments, a passenger in each vehicle is in charge of a laptop computer. The passenger in the receiver station controls the SA and coordinates the experiments. In the transmitter station, the passenger with the computer receives the instructions to initiate or stop the acquisition of the position information. We synchronize the position information offline using the time stamp of each sample. Besides, one passenger in each vehicle records the video of the propagation scenario. The role of these two passengers is to provide comments on the propagation and traffic conditions that we observe during the experiments, e.g., the availability of LOS conditions, the speed of the corresponding vehicle, and what maneuvers are the drivers attempting.

B.5.2 The Measurement Scenario

The measurement campaign was performed on the Mexican Federal Highway 80D in a mountainous area on the outskirts of the city of San Luis Potosí, México. The route over this highway is shown in Fig. B.8, where the labels *A* and *B* indicate the route's starting and ending points, respectively. This route spans 25 km and is completed in approximately 15minutes, depending on traffic conditions. A total of sixteen circuits were completed for the measurements, eight with the probe signal centered at 760 Hz and eight more with the signal at 2,500 Hz. During the experiments, the test vehicles were moving in the same direction. The receiver was most of the time in front of the transmitter, and occasionally and momentarily, they changed position to perform overtaking maneuvers. Both vehicles seek to maintain a velocity between 80 and 120 km/hr and a separation distance between 100 and 250 m. However, they were subject to arbitrary velocity variations caused by the changing traffic conditions over the route. Also, the separation distance was increased to up to 500 m in some sections of the road to expand our assessment of path-loss and large-scale fading.

The relevant road sections can be described as follows:

- Scenario #1: Road sections that pass through mountain cutouts. In these sections, tall and long rock walls carved through the mountain are found on both sides of the road. Some of the walls are long enough to flank both vehicles at the same time, as illustrated in Fig. B.9a, whereas others are shorter and border only one vehicle at a time, as shown in Fig. B.9b. The rock walls have a slight inclination, and produce strong multipath around the transmitter and/or the receiver. Multipath stemming from double scattering or double reflections is possible in this scenario, as discussed in the following subsection. Some of these road sections also pass under bridges, e.g., see Fig. B.10. These elevated structures produce strong reflections and a large Doppler shift, as the signals reflected off the bridge arrive from the front (or the back) of the receiving vehicle.

- Scenario #2: Road sections that go around the mountains. In these sections, the vehicles are flanked by a rock wall only on one side, whereas the other side is clear and goes downwards following the mountain's slope, as shown in Fig. B.11. Reflections off the rock wall produce strong multipath with a highly non-isotropic profile, implying that the mean Doppler shift of the channel will be different from zero.

- Scenario #3: Road sections in the open field. Reflectors and scattering clusters of large dimensions (such as rock walls or hillsides) are far off, as illustrated in Fig. B.12. Weak multipath stemming from the irregular terrain prevails in these road sections. However, the multipath is occasionally intensified by strong replicas of the probe signal reflected by man-made objects, such as road signs and metallic safety barriers.

The road also presents sections with sharp curves bordered by steep mountain walls. These curved sections are interesting since the walls can hinder a prompt visual detection of oncoming vehicles, as in the scenario shown in Fig. B.11b Furthermore, such sharp curves can obstruct the LOS path between communicating vehicles. This latter situation is illustrated in Fig. B.9b, where the receiver is about to lose LOS contact with the transmitter as both vehicles take a long curve stretch that passes through a mountain cutout. During the experiments, we observed LOS blockages also in straight sections of the road. These blockages were caused by vehicles of large dimensions that found themselves momentarily placed between the transmitter and the receiver, as in the instance shown in Fig. B.12b

The traffic dynamics of the Federal Highway 80D allowed us to record the probe signal's spectral dispersion during overtaking maneuvers. The test vehicles performed these maneuvers on each other in a controlled sequence that was coordinated using portable two-way radios. Figure B.12a shows the transmitting vehicle performing an overtaking on the receiving vehicle. In addition to these coordinated maneuvers, spontaneous overtaking, involving a third party and one of the test vehicles, were prompted arbitrarily by the traffic conditions. One of such non-coordinated maneuvers is depicted in Fig. B.11a , where a truck is overtaking the transmitting vehicle.

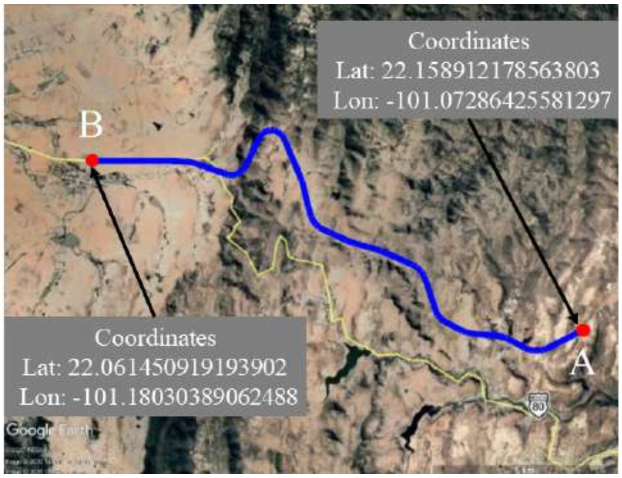

Figure B.8: Map showing the route of the measurement campaign.

(a) Receiver camera

(b) Transmitter camera

Figure B.9: Two sections of the road with steep rock walls on both sides.

B.6 Measurement Results of the Doppler Spectrum

This section presents the empirical Doppler spectrum recorded during our experiments. The discussion focuses on the relevant Doppler statistics of time-varying V2V channels. We describe the processing methods used to compute the Doppler spectrograms and the corresponding moments from the empirical data.

Figure B.10: Section of the road with steep mountains on both sides and an under bridge pass (Receiver camera).

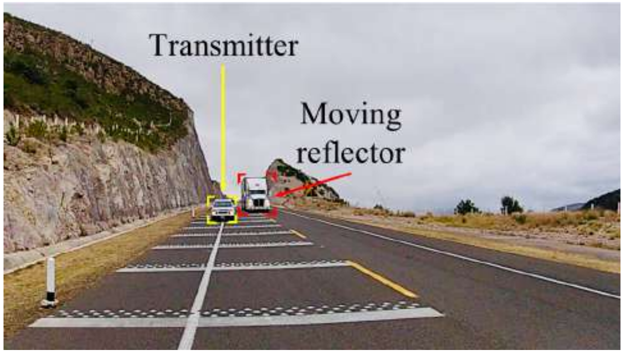

(a) Receiver camera

(b) Transmitter camera

Figure B.11: Two sections of the road with a steep rock wall on one side.

B.6.1 Pre-Processing

Before computing the channel's statistics from the measured data, a data pre-processing stage is necessary to address the practical issues of our channel sounding platform that are discussed in Section B.4.2. The pre-processing stage consists of the following actions:

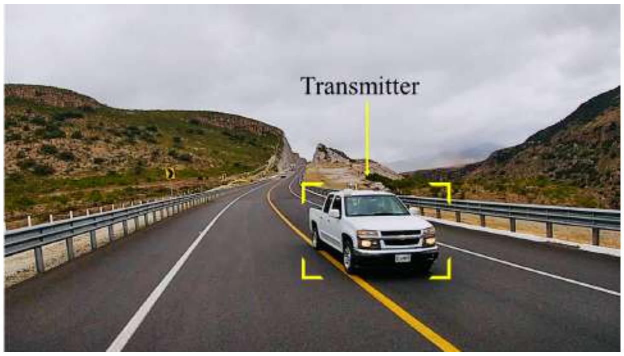

(a) Receiver camera

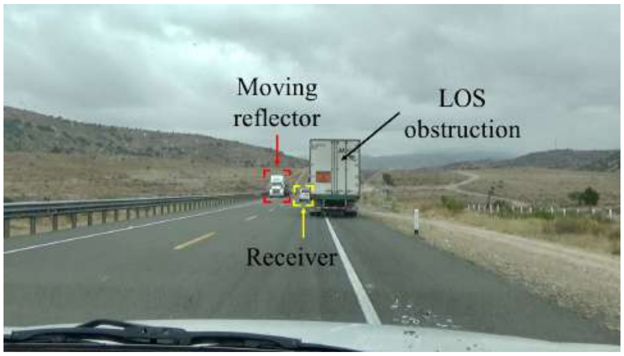

(b) Transmitter camera

Figure B.12: Two sections of the road in open field with mountains in the distance.

1. Center the snapshots of the measured spectrogram, i.e., correct the frequency drifts due to temperature effects.
2. Compute correlation with a proper mask to mitigate the effects of cross-terms in the measured spectrogram.
3. Scale the processed spectrogram's values back to the original power levels.
4. Apply a noise floor threshold to set all values below this threshold to the same level.

Figures B.13 and B.14 show the raw spectrograms of two measurement runs, one at 760 MHz and the other at 2,500 MHz, respectively. In Fig. B.13, the measurement route went from point A to point B (cf. Fig. B.8), whereas in Fig. B.14, it went from B to A. Both figures show the header and tail control snapshots that we used as a reference to correct the frequency drift due to temperature effects. This impairment, observed in both figures, does not change significantly over time. However, the received signal's frequency is deviated from the central frequency due to drifts in past observations.

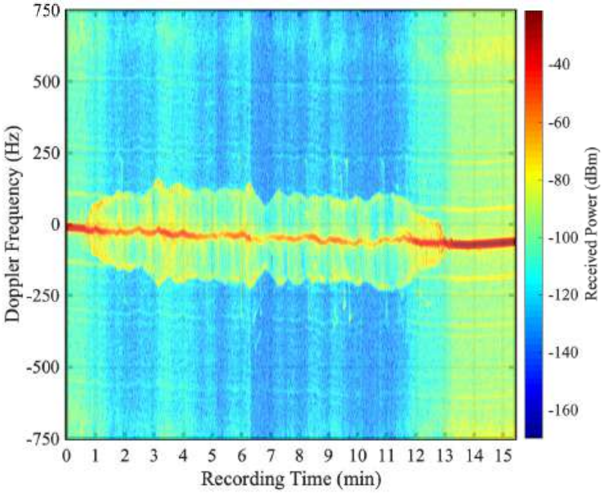

Figure B.13: A raw spectrogram recorded at 760 MHz.

The pre-processed version of the raw spectrograms in Figs. B.13 and B.14 are presented in Figs. B.15 and B.16, respectively. These sanitized spectrograms were obtained following the procedures described in Section B.4.2 for frequency drift correction and noise clipping. The frequency dispersion of the probe signal, which is caused by multipath propagation and the Doppler effect, can be observed clearly in Figs. B.15 and B.16. As soon as the vehicles start to move, part of the probe signal's power is spread out, forming a contour bounded by the instantaneous maximum Doppler shift, $\nu_{\max}^{sta}(t)$, due to static reflectors. This frequency shift is given by

$$\nu_{\max}^{sta}(t) = \frac{v_T(t) + v_R(t)}{\lambda} \tag{B.15}$$

where $v_T(t)$ and $v_R(t)$ denote the instantaneous speed of the transmitter and receiver, respectively [142]. The maximum Doppler shift is observed when the probe signal is reflected by an object located either in front (or nearly in front) of the receiver, or behind the transmitter. These propagation conditions are recurring in the route of our experiments due to the presence of traffic signs, rocky hillsides, or bridges. For the measurements at 760 MHz, the largest maximum Doppler shift was produced when the transmitting and receiving vehicles were moving at a speed of about 110 km/h, causing a peak value of $\nu_{\max}^{sta}(t)$ of around 169 Hz. Likewise, for the measurements at 2,500 MHz, the maximum Doppler shift was produced for $v_T(t) \approx v_R(t) \approx$ 120 km/h, corresponding to $\nu_{\max}^{sta}(t) \approx 555$ Hz. The frequency dispersion of the probe signal changed frequently throughout the measurement route due to the traffic dynamics. Indeed, Figs. B.15 and B.16 show the spreading (and despreading) effects of the vehicles' acceleration (and deceleration) on the signal frequency dispersion. Such effects are more evident when the vehicles begin and conclude their transit, but can also be identified along the route by the unceasing widening and narrowing of the recorded spectrogram.

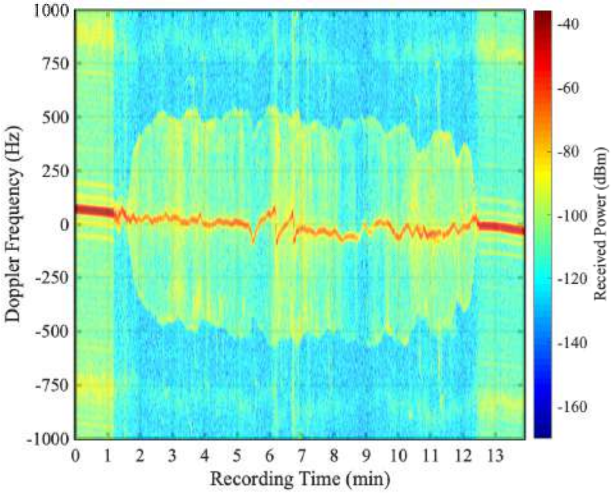

Figure B.14: A raw spectrogram recorded at 2,500 MHz.

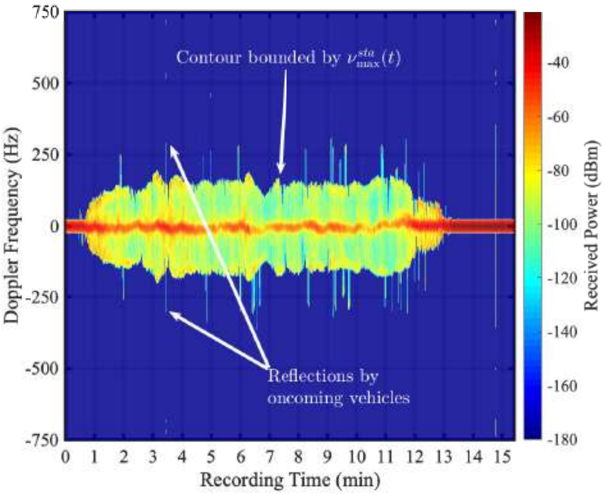

Figure B.15: A pre-processed spectrogram recorded at 760 MHz.

B.6.2 Doppler Signatures of Relevant Road Safety Events

The spectrograms presented in Figs. B.13– B.16 show that the measurement platform described in Section B.4 is capable of recording the frequency dispersion caused by multipath propagation and the Doppler effect. A close inspection of the measured spectrograms suggests that the platform allows recording the Doppler signatures of relevant events to road safety, as those produced by rapidly oncoming vehicles and overtaking maneuvers. Fig. B.17 exemplifies a common road event by extracting a segment of eleven seconds of the spectrogram in Fig. B.15. This segment was recorded on an open-field road section when a large truck was approaching, passing by, and driving away. During this event, the transmitter and receiver vehicles always maintained a LOS path with the truck. Figure B.18 presents three pictures of this event captured by the transmitter's video camera at the time instants

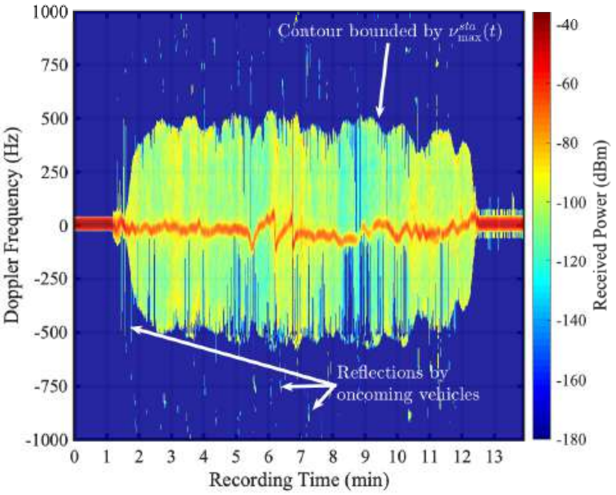

Figure B.16: A pre-processed spectrogram recorded at 2,500 MHz.

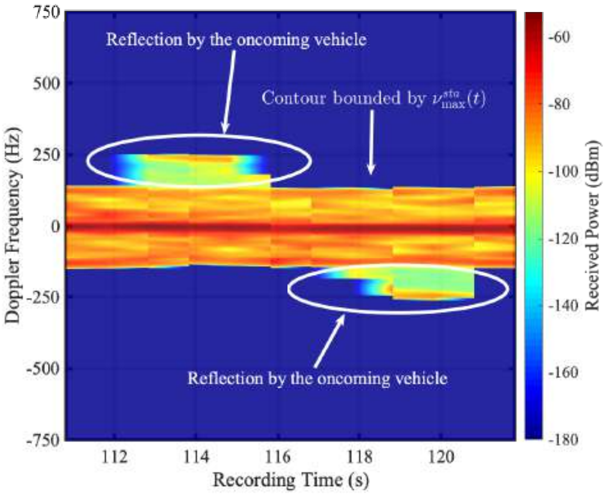

Figure B.17: An interval of a pre-processed spectrogram recorded at 760 MHz during an event involving a rapidly oncoming vehicle in an open-field road segment.

at which: the reflection from the oncoming truck was detected (Fig. B.18a) , the truck and the receiver were side by side (Fig. B.18b) , and the truck was driving away and the reflected signal was about to disappear (Fig. B.18c) . Fig. B.19 shows the corresponding Doppler spectra of these three time instants. We can observe from Figs. B.17 and B.19 that the reflection of the oncoming truck produces a tall spectral spike that commutes from an initial positive frequency of around 250 Hz to a negative frequency of -250 Hz. This behavior is consistent with the theoretical models of electromagnetic wave propagation when the source and the observer are in motion [143, 144].

Figure B.20 shows another segment of the spectrogram given in Fig. B.15 during a second event involving a rapidly oncoming truck. However, this

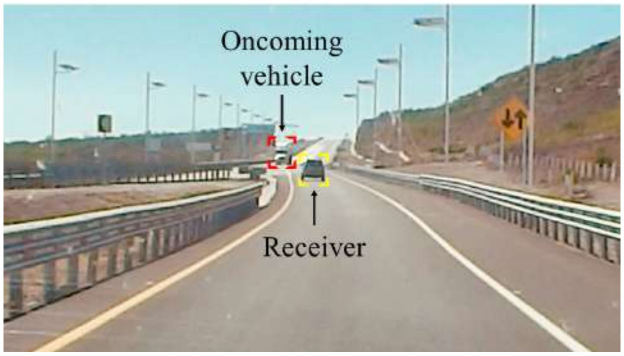

(a) Oncoming vehicle approaching the receiver (time instant $t_a = 112.8$ s)

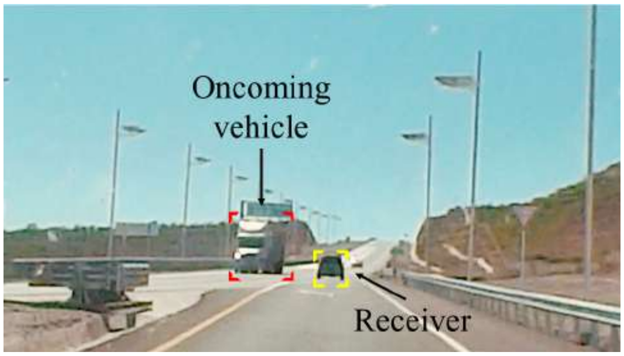

(b) Oncoming vehicle side-by-side wih the receiver (time instant $t_b = 115.8$ s)

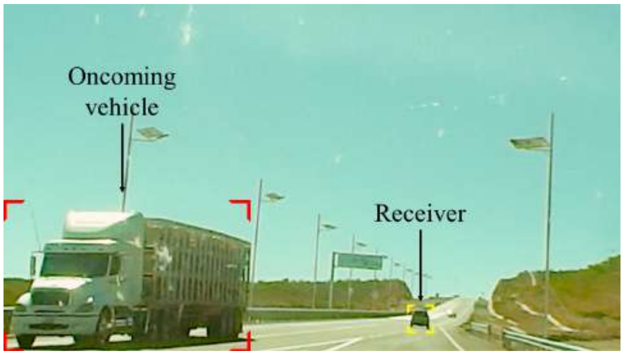

(c) Oncoming vehicle driving away from the receiver (time instant $t_c = 119.8$ s)

Figure B.18: Photo sequence of an event in which a rapidly oncoming vehicle passes by the receiver in an open-field road section.

event took place on a curved stretch bordered on the right-hand side (from the test vehicles' perspective) by a long and tall hillside, and on the left-hand side by a short rocky wall. Fig. B.21 presents a sequence of pictures of

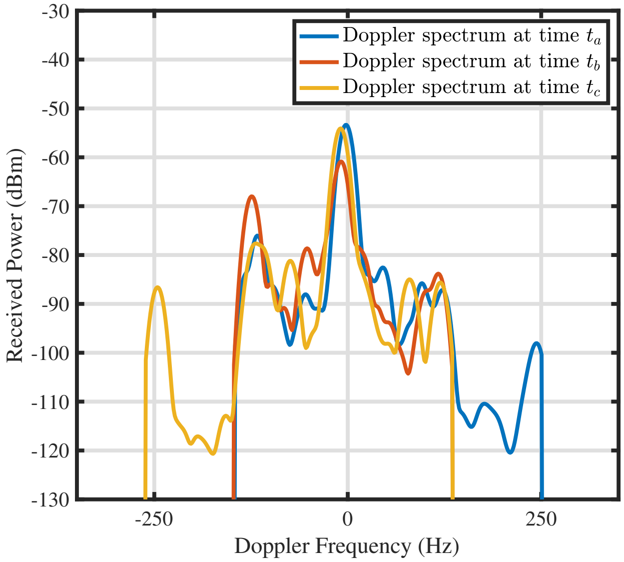

Figure B.19: Doppler spectrum recorded at 760 MHz and three different time instants ($t_a = 112.8$ s, $t_b = 115.8$ s, $t_c = 119.8$ s) during an event involving a rapidly oncoming vehicle in an open-field road section.

the propagation scenario taken by the transmitter at different time instants during the event. The corresponding Doppler spectra recorded at such time instants are shown in Fig. B.22. An important difference with the previous event is that the LOS path with the oncoming truck was obstructed for most of the event duration. First, an initial blockage between the transmitter and the truck was caused by the short rocky wall (see Fig. B.21a). Then a subsequent blockage between this truck and the receiver was yielded by a second truck located right in front of the receiver (see Fig. B.21b). Despite such blockages, a NLOS link among the transmitter, the oncoming truck, and the receiver was presumably maintained at all times during the event by a double reflection mechanism. Note that the initial LOS obstruction between the transmitter and the oncoming truck can be circumvented if the probe signal is reflected either by the long hillside or by the second truck (cf. Fig. B.21a). Then, the signal can be reflected once more by the oncoming truck in the direction of the receiver. This is plausible, as the LOS between the receiver and the oncoming truck was not blocked at the beginning of the event, since the road's curvature kept the second trailer (in front of the receiver) out of the visual field. Such a doubly-reflected signal produces a spectral spike whose frequency would be Doppler shifted to a positive value exceeding the maximum Doppler shift, $\nu_{\max}^{sta}(t)$, caused by static reflectors. It occurs under the aforementioned conditions as the doubly-reflected signal's direction of arrival and the receiver's direction of motion are nearly the same. A spectral spike with such characteristics, located at a frequency of 270 Hz, was recorded at the beginning of the event, as observed in Fig. B.22.

The event becomes even more interesting when the LOS path between the

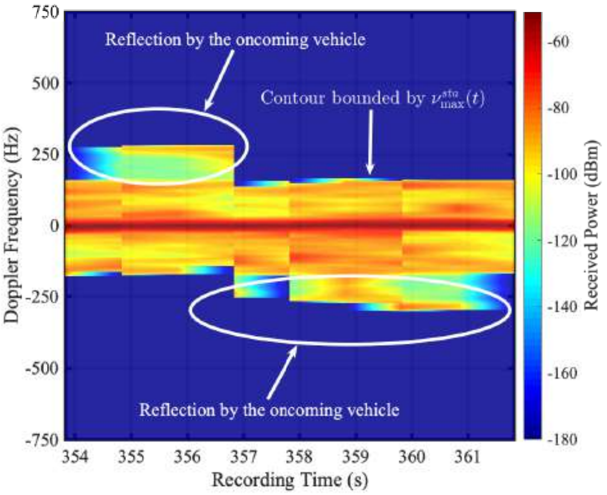

Figure B.20: An interval of a pre-processed spectrogram recorded at 760 MHz during an event involving a rapidly oncoming vehicle in a curved road section.

receiver and the oncoming truck is obstructed by the second truck, whereas the transmitter has a LOS path to both the receiver and the oncoming truck, as illustrated in Fig. B.21b. The obstruction by the second truck hinders a direct reception of the signal reflected by the oncoming truck. However, the geometrical configuration of the propagation scenario allows the reflected signal to propagate back to the transmitter and undergo a second reflection off this latter vehicle in direction to the receiver. The resulting doubly-reflected signal will produce a spectral spike at a negative frequency smaller than $-\nu_{\max}^{sta}(t)$ because the signal's direction of arrival, and the receiver's direction of motion are nearly opposite in this case. This explains the spectral spikes at -260 and -280 Hz in Fig. B.22.

Several events similar to the two analyzed above were recorded along the measurements route. These events, which involved even small vehicles, can be identified in Figs. B.15 and B.16 by the small white spots and vertical whiskers (lines) coming out of the contour bounded by $\nu_{\max}^{sta}(t)$.

Regarding the Doppler signatures of overtaking maneuvers, Fig. B.23 shows a thirty-one seconds segment of a spectrogram recorded at 2,500 MHz in an open-field road scenario. This segment corresponds to the moments where the transmitter increased its velocity to approach the receiver, changed lanes, performed the overtaking, and reincorporated to its original lane. The maneuver was conducted in a coordinated manner using portable two-way radios and with the test vehicles having a LOS path to each other. At the beginning of the maneuver, and as a result of the transmitter's acceleration, the probe signal's frequency shifts slightly away from the origin toward positive frequencies. Then, as the transmitter passes by the receiver, the signal's frequency drifts rapidly to the negative frequencies. Finally, when the transmitter changes lanes again and decelerates to complete the maneu-

(a) Oncoming vehicle hidden to the transmitter by the rock wall on the left-hand side (time instant $t_d = 354.8$ s)

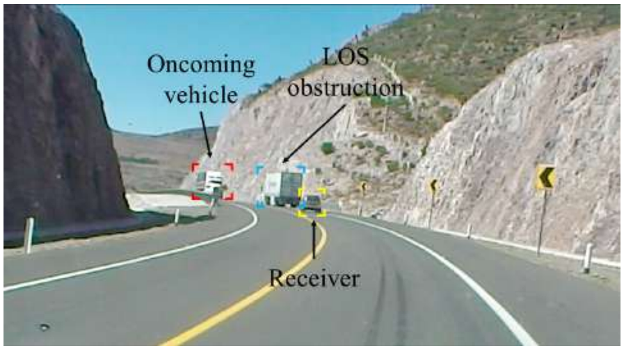

(b) Oncoming vehicle hidden to the receiver by a second truck (time instant $t_e = 357.8$ s)

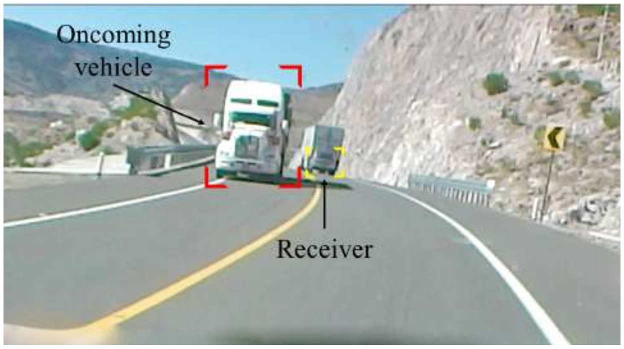

(c) Oncoming vehicle driving away from the receiver (time instant $t_f = 359.8$ s)

Figure B.21: Photo sequence of an event in which a rapidly oncoming vehicle passes by the receiver in a curved road section.

ver, the probe signal's frequency drifts once again in direction to positive frequencies to relocate around the origin. A similar Doppler signature was observed when the transmitter was overtaken by the receiver.

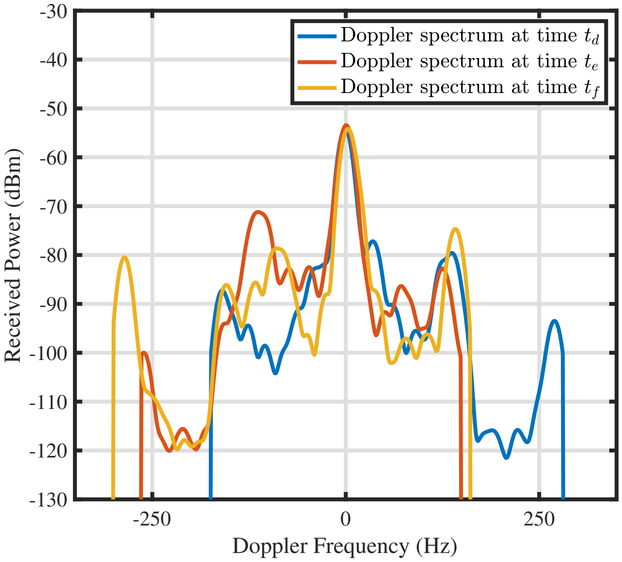

Figure B.22: Doppler spectrum recorded at 760 MHz and three different time instants (t_d = 354.8 s, t_e = 357.8 s, t_f = 359.8 s) during an event involving a rapidly oncoming vehicle in a curved road section.

B.6.3 Doppler statistics

The spectral moments of the empirical instantaneous Doppler spectrum can also be computed from the data recorded during our experiments. Two important moments of the Doppler spectrum are the mean Doppler shift and the Doppler spread [170]. The mean Doppler shift describes the mean frequency drift that the signal experiences due to the relative motion between the transmitting and receiving vehicles. In turn, the Doppler spread describes the frequency spread that the signal experiences during the transmission. By considering the empirical Doppler spectrum $\tilde{S}(\nu, t'_k)$, the instantaneous mean Doppler shift can be computed as

$$B_1(t'_k) = \frac{\int_{-\infty}^{\infty} \nu \tilde{S}(\nu, t'_k)\,\mathrm{d}\nu}{\int_{-\infty}^{\infty} \tilde{S}(\nu, t'_k)\,\mathrm{d}\nu}. \tag{B.16}$$

The empirical instantaneous Doppler spread is given by

$$B_2(t'_k) = \sqrt{\frac{\int_{-\infty}^{\infty} \left(\nu - B_1(t'_k)\right)^2 \tilde{S}(\nu, t'_k)\,\mathrm{d}\nu}{\int_{-\infty}^{\infty} \tilde{S}(\nu, t'_k)\,\mathrm{d}\nu}}. \tag{B.17}$$

In practice, the range of measured frequencies does not extend to infinity. Therefore, we compute these statistics by integrating only over the measured frequency window.

In addition to the instantaneous values of $B_1(t'_k)$ and $B_2(t'_k)$, we also computed the empirical distributions of these two spectral moments and tested their fitting against several well-known theoretical distributions. The

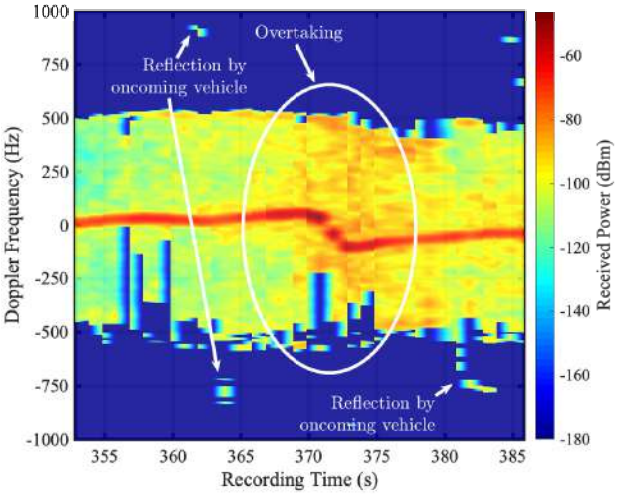

Figure B.23: An interval of a pre-processed spectrogram recorded at 2,500 MHz during an overtaking maneuver.

parameters of such theoretical distributions were obtained via maximum likelihood estimation using the `fitdist` function of MATLAB©. This function allows testing twenty-one different distributions. Nonetheless, for the analysis of $B_1(t'_k)$, we can only work with six distributions, as the other sixteen are not valid for continuous random variables, or their range is limited to positive values. However, for the analysis of $B_2(t'_k)$, we can test nineteen different continuous distributions. Furthermore, we conducted a goodness-of-fit test on each estimated theoretical distribution to determine whether a particular theoretical model is suitable for the measured data. Specifically, we considered the Kolgomorov-Smirnov goodness-of-fit (KSGOF) test at a significance level of 5%. In addition, we computed the Jensen-Shannon divergence (JSD) to determine which of the distributions that passed the test provide the best fit against the measured data.

Mean Doppler shift

We first analyze the mean Doppler shift of the spectrograms presented in Figs. B.15 and B.16. The waveform of $B_1(t'_k)$ computed at 760 MHz is shown in Fig. B.24. For this particular waveform, the time-averaged mean Doppler shift,

$$\overline{B}_1 = \frac{1}{K}\sum_{k=1}^{K} B_1(t'_k) \tag{B.18}$$

is equal to $\overline{B}_1 = -5.13\,\text{Hz}$, whereas the standard deviation of $B_1(t'_k)$

$$\overline{\sigma}_1 = \sqrt{\frac{1}{K}\sum_{k=1}^{K}[B_1(t'_k) - \overline{B}_1]^2} \tag{B.19}$$

is equal to $\overline{\sigma}_1 = 10.72\,\text{Hz}$. From Fig. B.24, we can observe that the mean Doppler shift fluctuates slightly around the central frequency, but it has

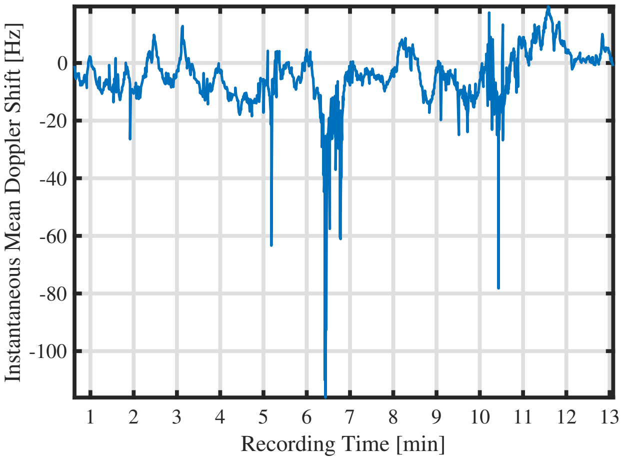

Figure B.24: Instantaneous mean Doppler shift of a measured spectrogram at 760 MHz.

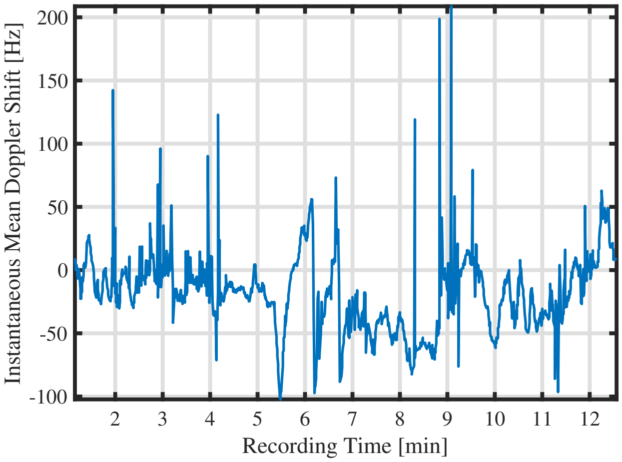

Figure B.25: Instantaneous mean Doppler shift of a measured spectrogram 2,500 MHz.

sharp peak values of up to -60, -80, and -116 Hz. The videos recorded over the route reveal that these peak values correspond to scenarios in which the transmitter was left behind by a rapidly accelerating receiver. In fact, the largest values at -80 and -116 Hz were recorded under NLOS conditions. On the other hand, Fig. B.25 shows the waveform of $B_1(t'_k)$ computed from the spectrogram at 2,500 MHz. For this waveform, we have $\overline{B}_1 = -18.19$ Hz and $\overline{\sigma}_1 = 31.0729$ Hz. The largest peak value of $B_1(t'_k)$, which is of about 205 Hz and can be observed in Fig. B.25 at $t \approx 9$ min, was caused by an accelerating transmitter in a maneuver to shorten the distance to the receiver.

The empirical probability distribution function (PDF) and cumulative distribution function (CDF) of $B_1(t'_k)$, computed from the spectrogram recorded at 760 MHz, are presented in Fig. B.26. The theoretical distributions that passed the KSGOF test namely, the Stable and t Location-Scale distribu-

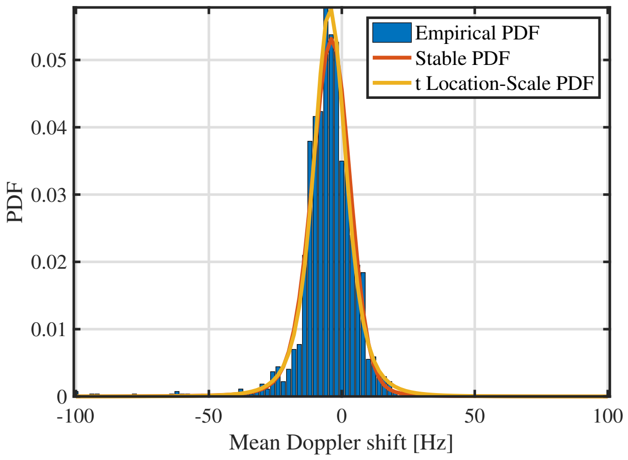

(a) PDF

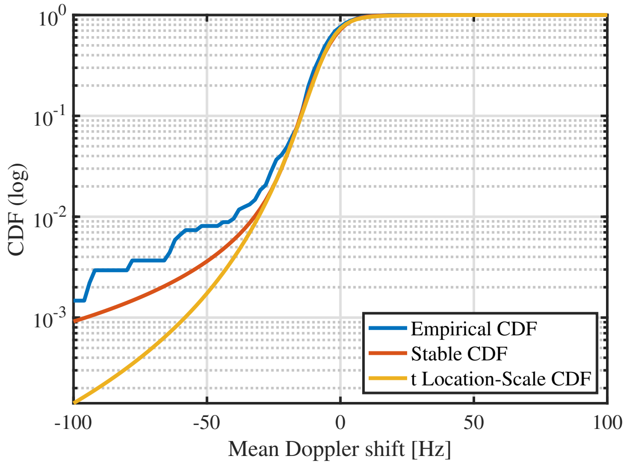

(b) CDF

Figure B.26: Empirical distribution of the instantaneous mean Doppler shift at 760 MHz.

tions, are also shown in Fig. B.26. The JSD was equal to 0.0100 and 0.0103, for the Stable and t Location-Scale distributions, respectively. Based on this metric, we conclude that the best fitting is obtained for the Stable distribution with parameters $\alpha = 1.76$, $\beta = -0.37$, $\gamma = 5.32$, and $\delta = -3.99$.

Likewise, the empirical distribution of the instantaneous mean Doppler shift at 2,500 MHz is shown in Fig. B.27. We observe that the mean Doppler shift spreads over a larger range of values. This occurs because the Doppler shift is larger as the carrier frequency increases. Moreover, the values are distributed around the proximity of the central frequency. The Logistic and t Location-Scale distributions were the models that passed the KSGOF test and their corresponding JSD was equal to 0.0133 and 0.0128, respectively. Based on the JSD, it follows that the t Location-Scale distribution provides

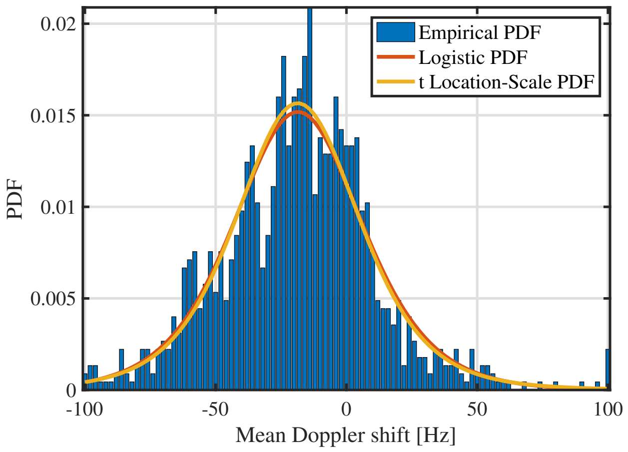

(a) PDF

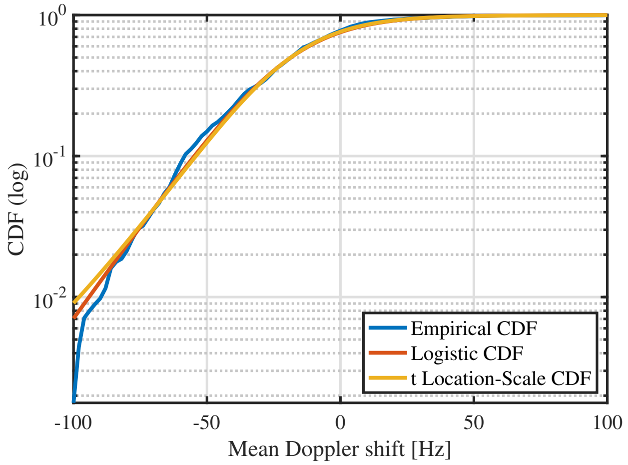

(b) CDF

Figure B.27: Empirical distribution of the instantaneous mean Doppler shift at 2,500 MHz.

the best fitting. For this distribution, the estimated parameters are equal to $\mu = -18.64$, $\sigma = 24.32$, $\nu = 5.42$.

The empirical and theoretical distributions of $B_1(t'_k)$ presented in Figs. B.26 and B.27 show that the measured instantaneous mean Doppler shift is distributed almost symmetrically around its average value, $\overline{B}_1$. This observation is consistent with the geometry of the three propagation scenarios described in Section B.4. Moreover, the fact that the time-averaged value of $B_1(t'_k)$ is negative for the two carrier frequencies suggests that the multipath signal was arriving at the receiver mainly from a direction opposite to the direction of motion of this vehicle. This is also consistent with how the experiments were carried out. Hence, the obtained results indicate that our measurement platform provides coherent information about the statistics of $B_1(t'_k)$.

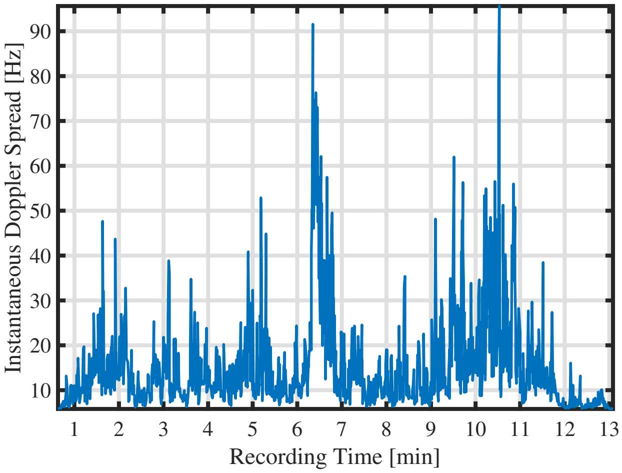

Figure B.28: Instantaneous Doppler spread of a measured spectrogram at 760 MHz.

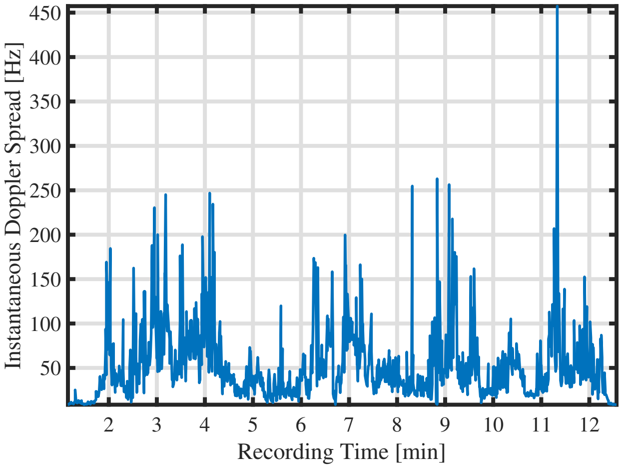

Figure B.29: Instantaneous Doppler spread of a measured spectrogram at 2,500 MHz.

Doppler spread

We next analyze the Doppler spread of the pre-processed spectrograms in Figs. B.15 and Fig. B.16. The instantaneous Doppler spread, $B_2(t'_k)$, computed from the spectrogram at 760 MHz is shown in Fig. B.28, whereas the waveform of $B_2(t'_k)$ computed from the spectrogram at 2,500 MHz is presented in Fig. B.29. Both figures show that the smallest values recorded for this spectral moment are not equal to zero. This occurs because the transmitted probe signal is not a perfect impulse function, as shown in Fig. B.7. Therefore, the received power is not concentrated at a single frequency. Instead, it is distributed over a narrow bandwidth, causing a small bias in the computation of $B_2(t'_k)$. However, such a bias can be compensated easily. The behavior of the Doppler spread at 2,500 MHz is similar to the one observed at 760 MHz. Nonetheless, larger Doppler spread values are obtained at 2,500 MHz due to the larger spectral dispersion that results from increasing the carrier frequency. The effects of the carrier frequency on the Doppler spread are highlighted by the analysis of the time-averaged Doppler spread

$$\overline{B}_2 = \frac{1}{K}\sum\nolimits_{k=1}^{K} B_2(t'_k) \tag{B.20}$$

and the standard deviation of $B_2(t'_k)$

$$\overline{\sigma}_2 = \sqrt{\frac{1}{K}\sum\nolimits_{k=1}^{K}[B_2(t'_k) - \overline{B}_2]^2}. \tag{B.21}$$

For the waveform of $B_2(t'_k)$ at 760 MHz, we have $\overline{B}_2 = 15.84$ and $\overline{\sigma}_2 = 11.35$, whereas $\overline{B}_2 = 52.21$ and $\overline{\sigma}_2 = 40.3754$ for the waveform at $2,500$ MHz.

Regarding the distribution of $B_2(t'_k)$, Figs. B.30 and B.31 show curves of the empirical PDFs and CDFs of the waveforms presented in Figs. B.28 and B.29. For the probe signal at 760 MHz, the empirical distribution of $B_2(t'_k)$ can be fitted against the Burr, the Generalized Extreme Value, the Log-Logistic, and the Stable distributions, as these four theoretical distributions passed the KSGOF test. In that same order, the obtained JSD was equal to 0.0065, 0.0050, 0.0043, 0.0055. The best fitting was therefore against the Log-Logistic distribution with parameters $\mu = 1.80$ and $\sigma = 0.6594$. On the other hand, for the probe signal at $2,500$ MHz, the empirical distribution of $B_2(t'_k)$ can be fitted only against the Generalized Extreme Value and the Stable distributions. The JSD of these two distributions was equal to 0.0167 and 0.0180, respectively, meaning that the best fitting was against the Generalized Extreme Value distribution. The estimated parameters of this distribution were $k = 0.28$, $\sigma = 20.97$ and $\mu = 24.18$.

The statistical results presented in Figs. B.26, B.27, B.30 and B.31 demonstrate that our measurement platform is an effective tool for the empirical characterization of the Doppler spectrum of V2V channels. However, such results are site specific, as they were obtained without considering the differences between the variety of propagation scenarios along the measurements route. To provide results that are meaningful beyond the particular location of our measurement experiments, we present in Table B.3 the empirical statistics of $B_1(t'_k)$ and $B_2(t'_k)$ by considering a classification of propagation scenarios. Specifically, the classification is based on the three propagation scenarios described in SectionB.5.2. The results in Table B.3 can be used as guidelines for the spectral moments analysis of V2V channels in highway scenarios having characteristics similar to those described in SectionB.5.2.

B.7 Path-loss and Large-Scale Fading

The measurement set up described in Section B.4 is commonly used to characterize the path-loss profile and large-scale fading distribution. In this sec-

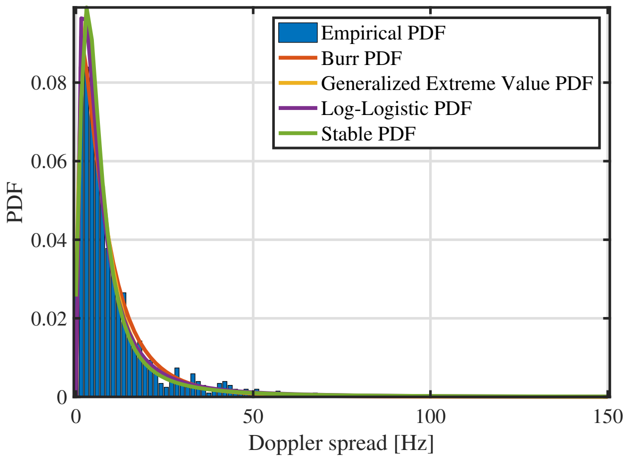

(a) PDF

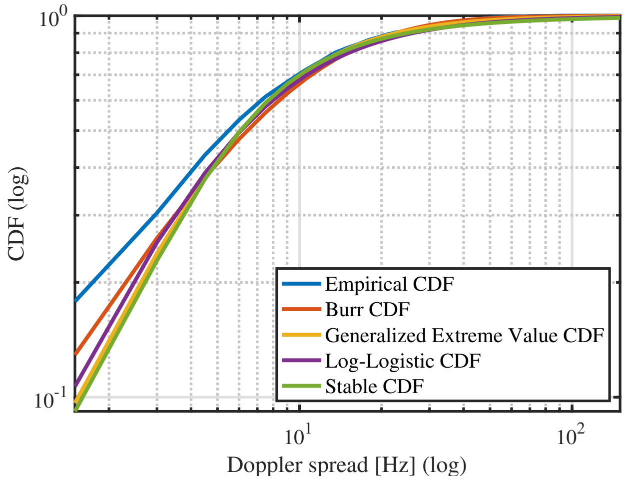

(b) CDF

Figure B.30: Empirical distribution of the instantaneous Doppler spread at 760 MHz.

tion, we address the computation of these two statistics from the recorded Doppler spectrograms. Our analysis begins by decoupling the total received power into its path-loss and fading components.

By neglecting the power of the additive noise,[1] the instantaneous total received power in decibels (dB) of the Doppler spectrum $\tilde{S}(\nu, t'_k)$ is given by

$$\mathcal{P}(t'_k) = 10 \log_{10} \left(\int_{-\infty}^{\infty} \tilde{S}(\nu, t'_k) \, \mathrm{d}\nu \right). \tag{B.22}$$

In practice, the integration is computed only over the range of measured frequencies. The total received power can be separated into the contributions of the average power and the small-scale fading

$$\mathcal{P}(t'_k) = \mathcal{P}_\mathrm{a}(t'_k) + \mathcal{P}_\mathrm{s}(t'_k) \tag{B.23}$$

---

[1] This consideration is justified since we apply a noise floor threshold to the measured spectrograms in the pre-processing stage.

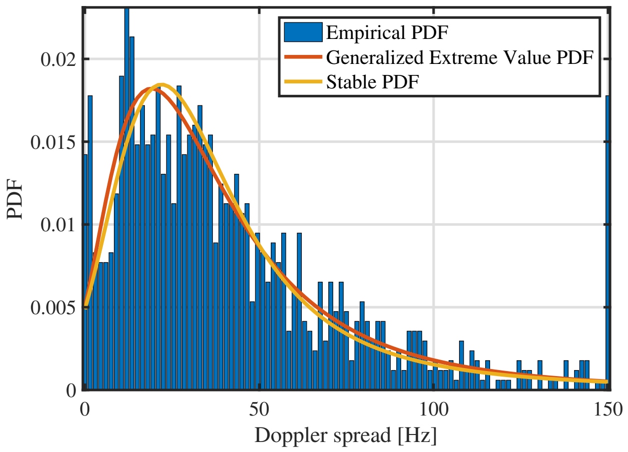

(a) PDF

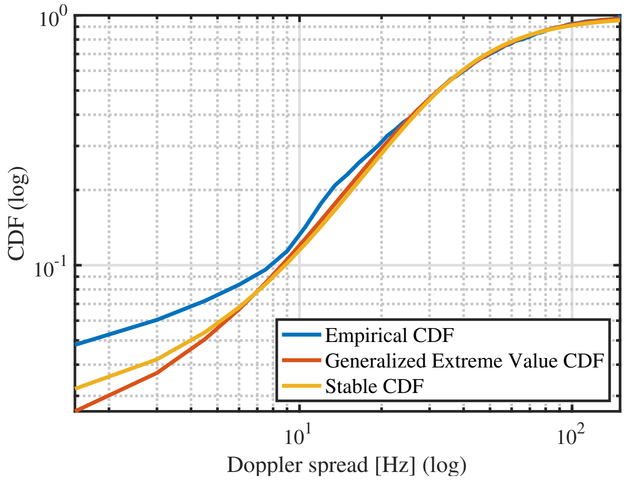

(b) CDF

Figure B.31: Empirical distribution of the instantaneous Doppler spread at 2,500 MHz.

where $\mathcal{P}_\mathrm{a}(t'_k)$ is the average received power (in dB) and $\mathcal{P}_\mathrm{s}(t'_k)$ is the power of the small-scale fading (also in dB). The average power is computed here using a window filter over multiple observations of the total received power. The window filter vanishes the fluctuations of the total received power due to small-scale fading. In turn, the average received power is decoupled into two components as

$$\mathcal{P}_\mathrm{a}(t'_k) = \mathcal{P}_\mathrm{d}(t'_k) + \mathcal{P}_\mathrm{l}(t'_k) \tag{B.24}$$

where $\mathcal{P}_\mathrm{d}(t'_k)$ is the received power level due to path-loss effects given as a function of the distance, and $\mathcal{P}_\mathrm{l}(t'_k)$ are the contributions of the large-scale fading. The path-loss profile can be described by the linear function

$$\mathcal{P}_\mathrm{d}(t'_k) = \mathcal{P}_0 - Kd(t'_k) \tag{B.25}$$

where $\mathcal{P}_0$ is a reference power level, K is a constant related to the signal loss

Table B.3: Statistics of the mean Doppler shift (MDS) and Doppler spread (DS) for the two carrier frequencies and the three scenarios described in SectionB.5.2.

Scenario	$\overline{B}_1$	$\overline{\sigma}_1$	$\overline{B}_2$	$\overline{\sigma}_2$	MDS PDF	MDS PDF Parameters	DS PDF	DS PDF Parameters
#1 @760 MHz	-7.44	11.17	17.35	12.97	Stable	$\alpha = 1.67$, $\beta = -0.63$, $\gamma = 4.60$, $\delta = -5.49$	Log-Logistic	$\mu = 1.85$, $\sigma = 0.67$
#2 @760 MHz	-7.86	9.68	15.65	9.11	Stable	$\alpha = 1.63$, $\beta = -0.99$, $\gamma = 3.98$, $\delta = -5.31$	Generalized Extreme Value	$k = 0.34$, $\sigma = 4.64$, $\mu = -0.22$
#3 @760 MHz	-0.64	8.94	13.77	9.36	Stable	$\alpha = 1.95$, $\beta = -0.99$, $\gamma = 5.75$, $\delta = -5.49$	Stable	$\alpha = 0.99$, $\beta = 0.99$, $\gamma = 2.46$, $\delta = 3.41$
#1 @2,500 MHz	-21.76	29.43	58.95	39.44	Logistic	$\mu = -22.02$, $\sigma = 15.23$	Log-Logistic	$\mu = 3.65$, $\sigma = 0.49$
#2 @2,500 MHz	-21.48	37.63	49.10	37.52	Generalized Extreme Value	$k = -0.12$, $\sigma = 33.11$, $\mu = -37.19$	Log-Logistic	$\mu = 3.34$, $\sigma = 0.65$
#3 @2,500 MHz	-12.64	29.73	45.10	41.18	t Location-Scale	$\mu = -12.37$, $\sigma = 19.09$, $\nu = 2.97$	Exponential	$\mu = 36.51$

and $d(t'_k)$ is the instantaneous separation distance between vehicles at time t'_k.

To obtain the power statistics, we compute the instantaneous separation distance among the transmitting and receiving vehicles and decouple the corresponding power levels following (B.23)-(B.25). First, the instantaneous separation distances between vehicles are computed from the measured latitudes and longitudes using the haversine formula. Next, we compute the average received power by means of a window filter and perform linear regression to obtain the empirical path-loss profile. Finally, we compute the empirical distributions of the large-scale fading. The empirical distributions of the fading statistics were computed harnessing all the experimental data measured at the corresponding frequencies. We fit the empirical fading distributions to theoretical PDFs. For our experiments, the best fitting was obtained against the log-normal distribution for the empirical large-scale fading.

The proper identification of the availability of LOS conditions in the measured intervals is obtained by inspecting the recorded videos synced with the time information of the measured spectrograms. The visualization of the instantaneous power measures and the availability of LOS conditions enables us to observe and understand the effects of attenuation due to the separation distance and fading, as well as the repercussions of losing the LOS paths.

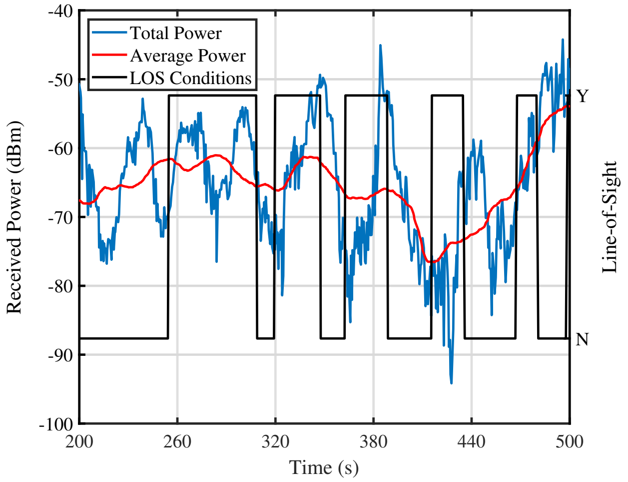

Figure B.32: Received power of a measured spectrogram at 760 MHz.

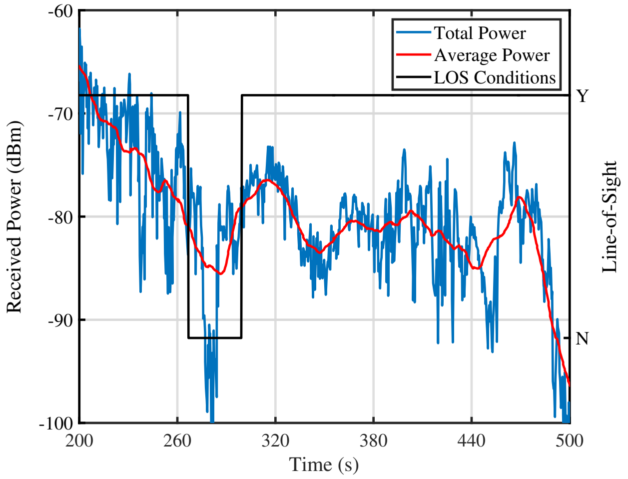

Figure B.33: Received power of a measured spectrogram at 2,500 MHz.

The instantaneous received power during a time interval of a measured spectrogram at 760 MHz is depicted in Fig. B.32. We plotted the total received power, the average received power and the indicator of the availability of LOS conditions. The empirical data were obtained for the pre-processed spectrogram in Fig. B.15. The total received power presents multiple fluctuations due to small-scale fading. The average received power has a more uniform behavior since the vehicles' motion profiles were almost constant during the observed time interval. However, the unavailability of LOS conditions paired with the separation distance among vehicles produce losses in the average received power, e.g., in the interval from 190 to 210 s.

Figure B.33 shows the received power during an interval of a measured spectrogram at 2,500 MHz. This figure presents curves of the total received power, the average received power, and the indicator of the availability of LOS conditions corresponding to the spectrogram in Fig. B.16. In this

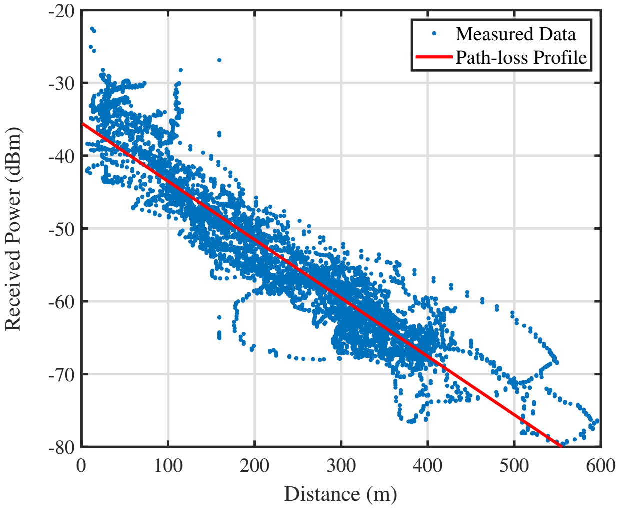

Figure B.34: Empirical path-loss profile at 760 MHz.

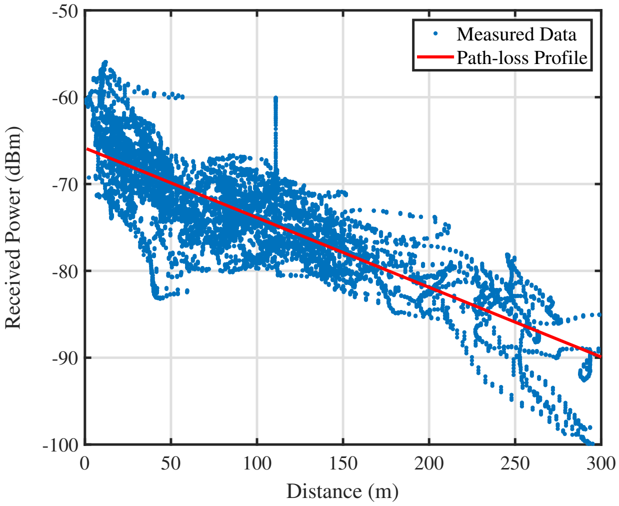

Figure B.35: Empirical path-loss profile at 2,500 MHz.

particular interval, the LOS conditions were available in most observations. In this spectrogram segment, the transmitting and receiving vehicles were accelerating to increase their speeds and separation distance. Indeed, this effect is observed during the first 70 s of the interval, where the received power decays over time as the vehicles separate. A second power decay is shown at the end of this interval, in which the separation distance among vehicles increases and the signal attenuates. Moreover, we can observe the effects of losing the LOS conditions in the interval from 70 to 90 s, where the signal experiences a severe attenuation.

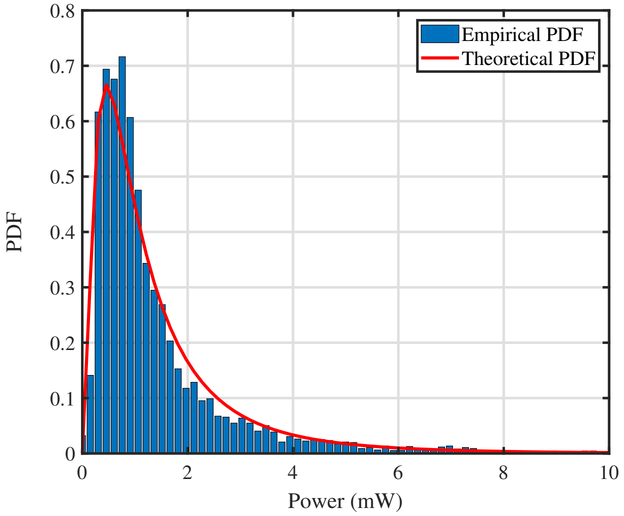

Figure B.36: Empirical large-scale fading distribution at 760 MHz.

Path-loss

We first focus our attention on the empirical path-loss profiles of the measured data at 760 MHz and 2,500 MHz. The empirical path-loss profile of the measured spectrograms at 760 MHz is depicted in Fig. B.34. This plot shows the constellation of the measured data and the linear function that describes the path-loss profile. The constellation of measured data shows that most experiments were performed with separation distances between 100 and 400 m. The obtained parameters for this empirical path-loss profile are $P_0 = -35.50$ dBm and $K = 0.08$. Moreover, Fig. B.35 shows the empirical path-loss profile of the measured spectrograms at 2,500 MHz. The separation distances of the experiments performed at 2,500 MHz were mainly between 50 and 150 m. The corresponding parameters for the empirical path-loss profile at 2,500 MHz are $P_0 = -65.85$ dBm and $K = 0.08$. These results show that the path-loss profile varies with the carrier frequency. Indeed, the losses at a higher frequency are more significant, as can be observed in the spectrograms shown in Figs. B.15 and B.16.

Large-scale fading

We next analyze the empirical distributions of the power of large-scale fading for both measured carrier frequencies at 760 MHz and 2,500 MHz. The empirical distribution of the large-scale fading at 760 MHz is depicted in Fig. B.36. The empirical distribution was fitted against a log-normal distribution with $\mu = 0$ and $\sigma = 0.89$. The theoretical PDF has a shape similar to the empirical distribution and fits well the data for most power levels. Furthermore, Fig. B.37 shows the empirical distribution of the large-scale fading for the carrier frequency at 2,500 MHz. This empirical result is similar to the one obtained for the measurements at 760 MHz with small differences in the

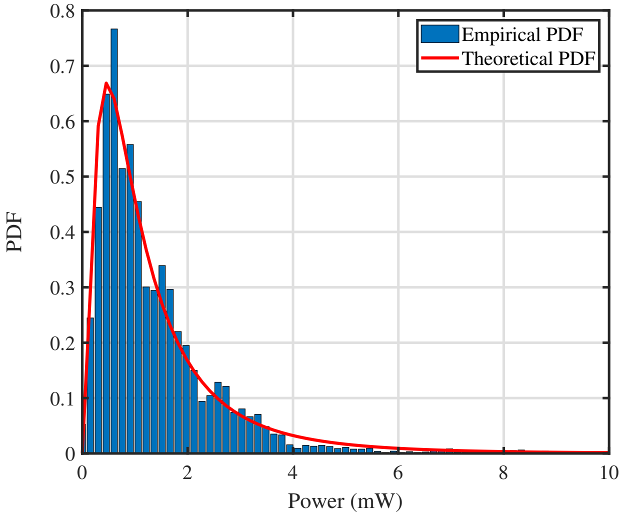

Figure B.37: Empirical large-scale fading distribution at 2,500 MHz.

tail of the distribution. The theoretical PDF fitted to the latter empirical data follows a log-normal distribution with $\mu = 0$ and $\sigma = 0.87$, which verify the similarity between both empirical distributions.

B.8 Final Remarks

In this paper, we described the implementation of a Doppler spectrum measurement platform for time-varying V2V channels that can be assembled using general-purpose hardware. This platform employs an RF signal generator and an SA to record traces of the channel's Doppler spectrum. Similar platforms have been widely employed to gather empirical data of the channel's path-loss profile and fading statistics. However, we have shown here that the same channel sounding architecture can be harnessed as well to measure the channel's time-varying Doppler spectrum.

We assessed the capabilities of our implementation by performing field experiments at 760 MHz and 2,500 MHz in highway scenarios near San Luis Potosí, México. The obtained results demonstrate that our measurement platform lends itself for the empirical characterization of the channel's time-varying spectral moments. The results also show that our platform allows to identify the Doppler signatures of the V2V channel during events relevant to road safety. In fact, the spectral signature of one of the events analyzed in this paper shows that the transmitted signal may reach the receiver by a double-reflection mechanism. While this propagation mechanism has been previously reported and modeled in the literature, the results presented here suggest that the body of the transmitting vehicle can also be involved in such a double reflection path. To the best of the authors' knowledge, the role of the transmitter (and by extension, of the receiver) as a potential reflector has not been considered for the modeling of double-reflection (or double-scattering) multipath V2V channels.

We also analyzed the empirical statistics of the instantaneous mean Doppler shift and Doppler spread for three different propagation scenarios that are commonly found on a mountainous road, namely: A scenario with rock walls on both sides of the road, a scenario with rock walls only on one side of the road, and an open field road. The mean Doppler shifts were distributed almost symmetrically around their average value. The largest Doppler spread was observed in the former scenario (two rock walls), whereas the smallest was observed in the latter (open field), as one would expect. In addition, we computed the empirical path-loss profile and the empirical distributions of the large-scale fading. The path-loss profile of our measured data was modeled by a linear function, whereas the empirical distribution of the large-scale fading provided a good fitting against the log-normal PDF.

Appendix C: Informed consent

CARTA DE CONSENTIMIENTO INFORMADO

Universidad Autónoma de San Luis Potosí
Facultad de Ciencias

El presente documento es dirigido a estudiantes de la Facultad de Ciencias de la Universidad Autónoma de San Luis Potosí (UASLP) y publico en general que deseen participar en el las experimentaciones del proyecto:

Detección de Caídas Empleando la Información del Estado del Canal WiFi.

Las personas deben declarar no presentar afecciones como osteoporosis, artritis, lesiones o traumatismos que puedan comprometer su salud al momento de desarrollar las experimentaciones. Además, deberán realizar ejercicios de calentamiento para evitar cualquier tipo de lesión durante la ejecución de los movimientos. Las experimentaciones serán supervisadas por el M.C.A. Jorge Daniel Cárdenas Amaya, estudiante del Doctorado en Ciencias de la Ingeniería de la Facultad de Ciencias, UASLP. El protocolo se desarrollara dentro de las instalaciones del Laboratorio de Comunicaciones Inálambricas de la Facultad de Ciencias. Si usted decide participar en este estudio, es importante que considere la siguiente información.

INTRODUCCIÓN

La mejora de la calidad de vida se ha traducido en un aumento de la esperanza de vida. En 2019, la población mayor de 65 años tuvo un crecimiento del 3% en comparación con 1990. La expansión poblacional proyectada indica que las personas mayores representarán el 16% de la población mundial para 2050. Gran parte de este sector de la sociedad tiende a vivir de forma independiente. Por este motivo, es necesario proporcionar sistemas de monitoreo y asistencia médica a distancia. Según la Organización Mundial de la Salud, 37.3 millones de personas mayores requieren atención médica cada año por lesiones causadas por caídas. Por lo tanto, nuestras experimentaciones se enfocan en la detección de estos eventos en particular.

OBJETIVO

Este trabajo busca realizar un análisis sistemático de los efectos de la orientación de las antenas en un sistema de detección de caídas basado en las firmas Doppler de señales WiFi. Por lo tanto, se requiere generar una base de datos que contenga los cambios producidos por el movimiento humano en presencia de señales de radiofrecuencia WiFi dentro de un ambiente interior.

PROCEDIMIENTO

Su participación consistirá en seguir las siguientes instrucciones durante el desarrollo de las n pruebas establecidas:

- Antes de realizar las pruebas se le pedirá que realice algunos ejercicios de calentamiento. Estos movimientos consisten en estiramientos para evitar sufrir una lesión.

- Todas las pruebas serán realizadas en una habitación donde solamente se encontrara presente el participante. Por lo tanto, el inicio y fin de las pruebas es indicado a través de alarmas visuales y auditivas para iniciar y detener las acciones de los voluntarios.

- Durante la primer prueba usted caminara dos metros y medio a un ritmo constante en una dirección fija delimitada en el suelo del lugar de experimentación. Después repetirá la trayectoria en sentido contrario, estas actividades serán repetidas hasta escuchar el sonido correspondiente al fin de la prueba.

- La segunda prueba consiste en caminar dos metros y medio en dirección perpendicular a las antenas de la experimentación. Se realizarán 5 repeticiones de esta trayectoria.

- En la tercer prueba usted comenzara desde la posición estática en el punto más alto de la escalera y al iniciar la prueba descenderá por los escalones de la escalera hasta el nivel del suelo. Una vez llegada a esta posición final, tendrá que permanecer estático hasta escuchar el sonido de finalización.

- La cuarta prueba comenzará desde el ultimo punto de la prueba tres, en este caso la indicación visual y auditiva le indicara que tiene que comenzar su movimiento. En esta prueba se ascenderá por la escalera hasta el punto más alto y se permanecerá estático al concluir esta actividad.
- La prueba tres y cuatro serán alternadas por cada repetición que sea requerida.
- La quinta prueba se realiza desde el nivel del suelo y comienza en un estado estático estando de pie. En este caso, usted permanecerá inmóvil hasta que sea indicado el inicio de la prueba. Una vez iniciada la prueba, usted procederá a caer sobre una superficie acolchada donde una vez que haga contacto permanecerá inmóvil hasta la indicación auditiva.
- La sexta prueba se llevará a cabo en el tercer escalón de la escalera del ambiente interior. Partiendo de una posición de pie y permaneciendo estático en el escalón, usted realizará un movimiento de caída hasta la superficie acolchada al frente de la escalera. Una vez realizado el movimiento se le pedirá que permanezca inmóvil hasta la indicación de finalización.
- Las actividades necesarias para las ultimas pruebas serán una combinación de todas las anteriores y consisten en: 1) Bajar escalera, caminar paralelamente a las antenas y bajar escalera. 2) Subir escalera, caminar paralelamente a las antenas, subir escalera. 3) caminar paralelamente a las antenas y caer a la superficie acolchada. 4) caminar perpendicularmente a las antenas y caer en la superficie acolchada. Y 5) bajar escalera y caer desde el tercer escalón a la superficie acolchada.
- Todas las pruebas serán repetidas un número de 5 veces para cada uno de los dos escenarios que serán implementados en la habitación. Esto da un total de 10 repeticiones en cada prueba y un total de 70 movimientos que serán registrados.
- El tiempo de experimentación total es de 1 hora y media aproximadamente.

BENEFICIOS

No recibirá ninguna compensación monetaria por su participación en el estudio. Sin embargo, si usted acepta participar, estará contribuyendo en el desarrollo de un sistema para la detección de caídas libre de dispositivos. Esto representa un avance en el cuidado de la salud de personas mayores y la prevención de eventos fatales.

CONFIDENCIALIDAD

Toda la información que usted proporcione para el estudio será de carácter estrictamente confidencial. Su información será únicamente en beneficio de la investigación del estudio. Ninguno de los datos recabados estará disponible para ningún otro propósito. Los resultados de este estudio serán publicados con fines científicos, pero se presentarán de tal manera que no podrá ser identificado(a).

PARTICIPACIÓN VOLUNTARIA

Su participación en este estudio es absolutamente voluntaria. Usted está en plena libertad de negarse a participar o de retirar su participación del mismo en cualquier momento. Su decisión de participar o no en el estudio no implicará ningún tipo de consecuencia o lo afectará de ninguna manera.

RIESGOS

Los riesgos durante su participación en el estudio son de mínimo riesgo y se enlistan a continuación:

1. Heridas leves.
2. Contusiones leves.
3. Rozaduras.
4. Torceduras.
5. Luxaciones.

En caso de que ocurriera alguno de estos accidentes, se le canalizara al módulo de atención médica de la Facultad de Ciencias.

CONTACTO

Para cualquier duda o aclaración sobre lo aquí presentado o durante la ejecución de la experimentación, ponemos a su disposición los siguientes contactos:

1. M.C.A Jorge Daniel Cárdenas Amaya.

- Responsable del estudio.
- Tel. 4444-92-32-48
- Correo: j.cardenas@ieee.org

2. Dr. Carlos A. Gutierrez.
    - Asesor del estudio.
    - Tel. 8262300 ext. 5670
    - Correo: cagutierrez@ieee.org
3. Dra. Ruth Mariela Aguilar Ponce.
    - Asesor del estudio.
    - Tel. 8262300 ext. 5671
    - Correo: rma1294@gmail.com

DECLARACIÓN

- He leído y entendido el contenido de este documento.
- Se me han explicado los procedimientos y riesgos que conlleva mi participación durante la experimentación.
- Todas mis dudas fueron aclaradas por los responsables del estudio.
- Declaro que no presento ninguna de las enfermedades que han sido mencionadas por lo que mi salud no se encontrara comprometida durante la ejecución de las experimentaciones.

Declaro mi conformidad en participar en este estudio y autorizo que mi información sea utilizada conforme a lo establecido en este documento.

PARTICIPANTE:

Nombre: ____

Fecha y Hora: ____________________

____

Firma del Participante

Bibliography

[1] L. Chen, Q. Zou, Z. Pan, D. Lai, L. Zhu, Z. Hou, J. Wang, and D. Cao, "Surrounding Vehicle Detection Using an FPGA Panoramic Camera and Deep CNNs," *IEEE Trans. Intell. Transp. Syst.*, vol. 21, no. 12, pp. 5110–5122, 2020.

[2] J. G. Wang, S. J. Chen, L. B. Zhou, K. W. Wan, and W. Y. Yau, "Vehicle Detection and Width Estimation in Rain by Fusing Radar and Vision," *2018 15th Int. Conf. Control. Autom. Robot. Vision, ICARCV 2018*, pp. 1063–1068, 2018.

[3] R. H. Zhang, F. You, F. Chen, and W. Q. He, "Vehicle Detection Method for Intelligent Vehicle at Night Time Based on Video and Laser Information," *Int. J. Pattern Recognit. Artif. Intell.*, vol. 32, no. 4, pp. 1–20, 2018.

[4] J. M. Sim, Y. Lee, and O. Kwon, "Acoustic Sensor Based Recognition of Human Activity in Everyday Life for Smart Home Services," *Int. J. Distrib. Sens. Networks*, vol. 2015, 2015.

[5] C. Liu, Z. Jiang, X. Su, S. Benzoni, and A. Maxwell, "Detection of human fall using floor vibration and multi-features semi-supervised SVM," *Sensors*, vol. 19, no. 17, 2019.

[6] S. Palipana, D. Rojas, P. Agrawal, and D. Pesch, "FallDeFi," *Proc. ACM Interactive, Mobile, Wearable Ubiquitous Technol.*, vol. 1, no. 4, pp. 1–25, 2018.

[7] F. Liu, Y. Cui, C. Masouros, J. Xu, T. X. Han, Y. C. Eldar, and S. Buzzi, "Integrated Sensing and Communications: Toward Dual-Functional Wireless Networks for 6G and Beyond," *IEEE J. Sel. Areas Commun.*, vol. 40, no. 6, pp. 1728–1767, 2022.

[8] D. Zhang, D. Wu, K. Niu, X. Wang, F. Zhang, J. Yao, D. Jiang, and F. Qin, "Practical Issues and Challenges in CSI-based Integrated

Sensing and Communication," *2022 IEEE Int. Conf. Commun. Work. ICC Work. 2022*, pp. 836–841, 2022.

[9] J. A. Zhang, M. L. Rahman, K. Wu, X. Huang, Y. J. Guo, S. Chen, and J. Yuan, "Enabling Joint Communication and Radar Sensing in Mobile Networks - A Survey," *IEEE Commun. Surv. Tutorials*, vol. 24, no. 1, pp. 306–345, 2022.

[10] R. Gao, W. Li, Y. Xie, E. Yi, L. Wang, D. Wu, and D. Zhang, "Towards Robust Gesture Recognition by Characterizing the Sensing Quality of WiFi Signals," *Proc. ACM Interactive, Mobile, Wearable Ubiquitous Technol.*, vol. 6, no. 1, 2022.

[11] Y. Gu, X. Zhang, Y. Wang, M. Wang, H. Yan, Y. Ji, Z. Liu, J. Li, and M. Dong, "Wigrunt: Wifi-enabled gesture recognition using dual-attention network," *IEEE Transactions on Human-Machine Systems*, vol. 52, no. 4, pp. 736–746, 2022.

[12] R. Guo, H. Li, D. Han, and R. Liu, "Feasibility Analysis of Using Channel State Information (CSI) Acquired from Wi-Fi Routers for Construction Worker Fall Detection," *Int. J. Environ. Res. Public Health*, vol. 20, no. 6, p. 4998, 2023.

[13] X. Zhang, Y. Gu, H. Yan, Y. Wang, M. Dong, K. Ota, F. Ren, and Y. Ji, "Wital: A cots wifi devices based vital signs monitoring system using nlos sensing model," *IEEE Transactions on Human-Machine Systems*, pp. 1–13, 2023.

[14] F. Firoozi, A. Borhani, and M. Patzold, "Experimental characterization of mobile fading channels aiming the design of non-wearable fall detection radio systems at 5.9 GHz," in *2016 IEEE Int. Conf. Commun. Syst. ICCS 2016*, 2017.

[15] D. Halperin, W. Hu, A. Sheth, and D. Wetherall, "Tool release," *ACM SIGCOMM Comput. Commun. Rev.*, vol. 41, no. 1, pp. 53–53, 2011.

[16] Y. Xie, Z. Li, and M. Li, "Precise power delay profiling with commodity wifi," in *Proceedings of the 21st Annual International Conference on Mobile Computing and Networking*, ser. MobiCom '15. New York, NY, USA: ACM, 2015, p. 53–64. [Online]. Available: http://doi.acm.org/10.1145/2789168.2790124

[17] B. A. Alsaify, M. Almazari, R. Alazrai, S. Alouneh, and M. I. Daoud, "A CSI-Based Multi-Environment Human Activity Recognition Framework," *Appl. Sci.*, vol. 12, no. 2, 2022.

[18] J. D. Cardenas, C. A. Gutierrez, and R. Aguilar-Ponce, "Influence of the antenna orientation on wifi-based fall detection systems," *Sensors*, vol. 21, no. 15, 2021.

[19] S. Sadowski and P. Spachos, "RSSI-Based Indoor Localization with the Internet of Things," *IEEE Access*, vol. 6, pp. 30 149–30 161, 2018.

[20] J. D. Cardenas, C. A. Gutierrez, and R. Aguilar-Ponce, "Deep Learning Multi-Class Approach for Human Fall Detection Based on Doppler Signatures," *Int. J. Environ. Res. Public Health*, vol. 20, no. 2, p. 1123, jan 2023. [Online]. Available: https://www.mdpi.com/1660-4601/20/2/1123

[21] A. Bhattacharya and R. Vaughan, "Deep Learning Radar Design for Breathing and Fall Detection," *IEEE Sens. J.*, vol. 20, no. 9, pp. 5072–5085, 2020.

[22] *IEEE Standard for Information technology—Local and metropolitan area networks—Specific requirements—Part II: Wireless LAN Medium Access Control (MAC) and Physical Layer (PHY) Specifications Amendment 6: Wireless Access in Vehicular Environments*, IEEE Std 802.11p-2010, July 2010.

[23] I. Soto, M. Calderon, O. Amador, and M. Urueña, "A survey on road safety and traffic efficiency vehicular applications based on C-V2X technologies," *Veh. Commun.*, vol. 33, p. 100428, 2022. [Online]. Available: https://doi.org/10.1016/j.vehcom.2021.100428

[24] I. H. Sarker, "Deep Learning: A Comprehensive Overview on Techniques, Taxonomy, Applications and Research Directions," *SN Comput. Sci.*, vol. 2, no. 6, p. 420, nov 2021. [Online]. Available: https://link.springer.com/10.1007/s42979-021-00815-1

[25] W. H. Organization, "Falls," 2018. [Online]. Available: https://www.who.int/news-room/fact-sheets/detail/falls

[26] E. Bisong, *Building Machine Learning and Deep Learning Models on Google Cloud Platform*, 1st ed. Apress Berkeley, CA, 2019.

[27] J. Cardenas, C. A. Gutierrez, and R. Aguilar-Ponce, "Effects of Antenna Orientation in Fall Detection Systems Based on WiFi Signals," in *Proc. - 2020 IEEE Latin-American Conf. Commun. LATINCOM 2020*, 2020, pp. 1–6.

[28] C. A. Gomez-Vega, J. Cardenas, J. C. Ornelas-Lizcano, C. A. Gutierrez, M. Cardenas-Juarez, J. M. Luna-Rivera, and R. M. Aguilar-Ponce, "Doppler Spectrum Measurement Platform for Narrowband V2V Channels," *IEEE Access*, vol. 10, pp. 27 162–27 184, 2022.

[29] V. Chen, *The Micro-Doppler Effect in Radar, Second Edition*, ser. Artech House radar library. Artech House, 2019. [Online]. Available: https://books.google.com.mx/books?id=SVCQDwAAQBAJ

[30] C. Rauscher, V. Janssen, and R. Minihold, *Fundamentals of Spectrum Analysis*, 5th ed. Munich, Germany: Rohde & Schwarz, 2007.

[31] U. Nations, “World Population Ageing 2019: Highlights,” Department of Economic and Social Affairs, Population Division, Tech. Rep., 2019.

[32] J. Zhang, C. Wu, and Y. Wang, “Human fall detection based on body posture spatio-temporal evolution,” *Sensors*, vol. 20, no. 3, 2020.

[33] J. Hauth, S. Jabri, F. Kamran, E. W. Feleke, K. Nigusie, L. V. Ojeda, S. Handelzalts, L. Nyquist, N. B. Alexander, X. Huan, J. Wiens, and K. H. Sienko, “Automated Loss-of-Balance Event Identification in Older Adults at Risk of Falls during Real-World Walking Using Wearable Inertial Measurement Units,” *Sensors*, vol. 21, no. 14, pp. 1–13, 2021.

[34] L. Chen, J. Hoey, C. D. Nugent, D. J. Cook, and Z. Yu, “Sensor-based activity recognition,” *IEEE Trans. Syst. Man Cybern. Part C Appl. Rev.*, vol. 42, no. 6, pp. 790–808, 2012.

[35] K. Woyach, D. Puccinelli, and M. Haenggi, “Sensorless sensing in wireless networks: Implementation and measurements,” in *2006 4th Int. Symp. Model. Optim. Mobile, Ad Hoc Wirel. Networks, WiOpt 2006*. IEEE, 2006, pp. 1–8.

[36] P. W. Lee, W. K. Seah, H. P. Tan, and Z. Yao, “Wireless sensing without sensors-an experimental study of motion/intrusion detection using RF irregularity,” *Meas. Sci. Technol.*, vol. 21, no. 12, 2010.

[37] M. Huang, J. Liu, Y. Gu, Y. Zhang, F. Ren, X. Wang, and J. Li, “Your WiFi Knows You Fall: A Channel Data-Driven Device-Free Fall Sensing System,” in *IEEE Int. Conf. Commun.*, vol. 2019-May, 2019.

[38] W. Wang, A. X. Liu, M. Shahzad, K. Ling, and S. Lu, “Device-Free Human Activity Recognition Using Commercial WiFi Devices,” *IEEE J. Sel. Areas Commun.*, vol. 35, no. 5, pp. 1118–1131, 2017.

[39] C. A. Gutiérrez, J. C. Ornelas-Lizcano, and M. Pätzold, “Geometrical modeling of non-stationary polarimetric vehicular radio channels,” in *2019 IEEE 2nd Connect. Autom. Veh. Symp. CAVS 2019 - Proc.*, 2019.

[40] Y. Wang, K. Wu, and L. M. Ni, “WiFall: Device-Free Fall Detection by Wireless Networks,” *IEEE Trans. Mob. Comput.*, vol. 16, no. 2, pp. 581–594, 2017.

[41] C. Rougier, J. Meunier, A. St-Arnaud, and J. Rousseau, “Robust video surveillance for fall detection based on human shape deformation,” *IEEE Trans. Circuits Syst. Video Technol.*, vol. 21, no. 5, pp. 611–622, 2011.

[42] X. Su, H. Tong, and P. Ji, “Activity recognition with smartphone sensors,” *Tsinghua Sci. Technol.*, vol. 19, no. 3, pp. 235–249, 2014.

[43] P. Zurbuchen, N.; Wilde, A.; Bruegger, “A Machine Learning Multi-Class Approach for Fall Detection Systems Based on Wearable Sensors with a Study on Sampling Rates,” *Sensors*, vol. 21, no. 3, p. 23, 2021.

[44] K. I. Withanage, I. Lee, R. Brinkworth, S. Mackintosh, and D. Thewlis, “Fall Recovery Subactivity Recognition with RGB-D Cameras,” *IEEE Trans. Ind. Informatics*, vol. 12, no. 6, pp. 2312–2320, 2016.

[45] O. Kerdjidj, N. Ramzan, K. Ghanem, A. Amira, and F. Chouireb, “Fall detection and human activity classification using wearable sensors and compressed sensing,” *J. Ambient Intell. Humaniz. Comput.*, vol. 11, no. 1, pp. 349–361, 2020. [Online]. Available: http://dx.doi.org/10.1007/s12652-019-01214-4

[46] S. Di Domenico, M. De Sanctis, E. Cianca, F. Giuliano, and G. Bianchi, “Exploring Training Options for RF Sensing Using CSI,” *IEEE Commun. Mag.*, vol. 56, no. 5, pp. 116–123, 2018.

[47] D. Wu, D. Zhang, C. Xu, H. Wang, and X. Li, “Device-Free WiFi Human Sensing: From Pattern-Based to Model-Based Approaches,” *IEEE Commun. Mag.*, vol. 55, no. 10, pp. 91–97, 2017.

[48] B. Erol and M. Amin, “Effects of range spread and aspect angle on radar fall detection,” *Proc. IEEE Sens. Array Multichannel Signal Process. Work.*, vol. 2016-Septe, pp. 1–5, 2016.

[49] M. Patzold and N. Youssef, “Spectrogram analysis of multipath fading channels,” *IEEE Int. Symp. Pers. Indoor Mob. Radio Commun. PIMRC*, vol. 2015-Decem, no. 4898, pp. 2214–2219, 2015.

[50] A. Chelli and M. Pätzold, “A Machine Learning Approach for Fall Detection Based on the Instantaneous Doppler Frequency,” *IEEE Access*, vol. 7, pp. 166 173–166 189, 2019.

[51] T. D. H. Nguyen and H. N. H. Nguyen, “Towards a Robust WiFi-based Fall Detection with Adversarial Data Augmentation,” in *2020 54th Annu. Conf. Inf. Sci. Syst. CISS 2020*, 2020.

[52] J. Ding and Y. Wang, “A WiFi-Based Smart Home Fall Detection System Using Recurrent Neural Network,” *IEEE Trans. Consum. Electron.*, vol. 66, no. 4, pp. 308–317, 2020.

[53] I. C. S. L. S. Committee, “IEEE Standard for Information technology-Telecommunications and information exchange between systems-Local and metropolitan area networks-Specific requirements Part 11 : Wireless LAN Medium Access Control (MAC) and Physical Layer (PHY) Specifications,” *IEEE Std 802.11ˆ<TM>*, 2007. [Online]. Available: http://ci.nii.ac.jp/naid/10030068811/en/

[54] N. Ida, *Engineering Electromagnetics*, 3rd ed. Springer Cham, 2015.

[55] W. Dahech, M. Pätzold, C. A. Gutiérrez, and N. Youssef, “A Non-Stationary Mobile-to-Mobile Channel Model Allowing for Velocity and Trajectory Variations of the Mobile Stations,” *IEEE Trans. Wirel. Commun.*, vol. 16, no. 3, pp. 1987–2000, 2017.

[56] M. Pätzold and C. A. Gutierrez, “Enhancing the resolution of the spectrogram of non-stationary mobile radio channels by using massive MIMO techniques,” *IEEE Veh. Technol. Conf.*, pp. 1–7, 2017.

[57] P. Kyritsi, D. C. Cox, R. A. Valenzuela, and P. W. Wolniansky, “Effect of antenna polarization on the capacity of a multiple element system in an indoor environment,” *IEEE J. Sel. Areas Commun.*, 2002.

[58] H. Zhang and T. Ngo, “Linear-Polarization-Insensitive Rectenna Design for Ground-to-Air Microwave Power Transmission,” *IEEE Access*, vol. 8, pp. 101 702–101 707, 2020.

[59] U. Gpu, “A Novel PCA-Firefly Based XGBoost Classification Model for Intrusion Detection in Networks,” *Electron.*, vol. 9, no. 2, p. 16, 2020.

[60] R. Gottumukkal and V. K. Asari, “An improved face recognition technique based on modular PCA approach,” *Pattern Recognit. Lett.*, vol. 25, no. 4, pp. 429–436, 2004.

[61] T. R. Gadekallu, N. Khare, S. Bhattacharya, S. Singh, P. K. R. Maddikunta, I. H. Ra, and M. Alazab, “Early detection of diabetic retinopathy using pca-firefly based deep learning model,” *Electron.*, vol. 9, no. 2, pp. 1–16, 2020.

[62] H. M. Ebied, “Feature extraction using PCA and Kernel-PCA for face recognition,” in *2012 8th Int. Conf. Informatics Syst. INFOS 2012*, 2012, pp. 72–77.

[63] Z. Yuan, J. Zhang, Y. Zhang, P. Tang, and L. Tian, “A Novel Complex PCA-based Wireless MIMO Channel Modeling Methodology,” in *IEEE Veh. Technol. Conf.*, vol. 2020-Novem, no. 1, 2020.

[64] A. Hadri, K. Chougdali, and R. Touahni, “Intrusion detection system using PCA and Fuzzy PCA techniques,” in *2016 Int. Conf. Adv. Commun. Syst. Inf. Secur. ACOSIS 2016 - Proc.* IEEE, 2017.

[65] A. Rehman, A. Khan, M. A. Ali, M. U. Khan, S. U. Khan, and L. Ali, “Performance Analysis of PCA, Sparse PCA, Kernel PCA and Incremental PCA Algorithms for Heart Failure Prediction,” in *2nd Int. Conf. Electr. Commun. Comput. Eng. ICECCE 2020*, no. June, 2020, pp. 20–24.

[66] S. L. Brunton and J. N. Kutz, “Data Driven Science & Engineering - Machine Learning, Dynamical Systems, and Control,” p. 572, 2017. [Online]. Available: databook.uw.edu

[67] J. Shlens, “A Tutorial on Principal Component Analysis,” 2014. [Online]. Available: http://arxiv.org/abs/1404.1100

[68] Y. Kim and H. Ling, “Human activity classification based on micro-doppler signatures using an artificial neural network,” *2008 IEEE Int. Symp. Antennas Propag. Usn. Natl. Radio Sci. Meet. APSURSI*, vol. 2, pp. 2–5, 2008.

[69] Q. Liu, K. G. Mkongwa, and C. Zhang, “Performance issues in wireless body area networks for the healthcare application: a survey and future prospects,” *SN Appl. Sci.*, vol. 3, no. 2, pp. 1–19, 2021. [Online]. Available: https://doi.org/10.1007/s42452-020-04058-2

[70] M. J. Ali, “Wireless body area networks : co-channel interference mitigation & avoidance,” Ph.D. dissertation, Université Sorbonne Paris, 2019.

[71] U. Nations, “Ageing,” 2019. [Online]. Available: https://www.un.org/en/global-issues/ageing

[72] W. H. Organization, “Road traffic injuries,” 2022. [Online]. Available: https://www.who.int/news-room/fact-sheets/detail/road-traffic-injuries

[73] Centers for Disease Control and Prevention, “Older Adult Fall Prevention,” 2021. [Online]. Available: https://www.cdc.gov/falls/facts.html

[74] A. Orihuela-Espejo, F. Álvarez-Salvago, A. Martínez-Amat, C. Boquete-Pumar, M. De Diego-Moreno, M. García-Sillero,

A. Aibar-Almazán, and J. D. Jiménez-García, “Associations between Muscle Strength, Physical Performance and Cognitive Impairment with Fear of Falling among Older Adults Aged 60 Years: A Cross-Sectional Study,” *Int. J. Environ. Res. Public Health*, vol. 19, no. 17, p. 10504, 2022.

[75] T. E. Jager, H. B. Weiss, J. H. Coben, and P. E. Pepe, “Traumatic Brain Injuries Evaluated in U.S. Emergency Departments, 1992-1994,” *Acad. Emerg. Med.*, vol. 7, no. 2, pp. 134–140, feb 2000. [Online]. Available: https://onlinelibrary.wiley.com/doi/10.1111/j.1553-2712.2000.tb00515.x

[76] A. Abdelgawwad, A. C. Mallofre, and M. Patzold, “A Trajectory-Driven 3D Channel Model for Human Activity Recognition,” *IEEE Access*, vol. 9, pp. 103 393–103 406, 2021.

[77] L. M. Kenshi Saho, Sora Hayashi, Mutsuki Tsuyama and M. Masugi, “Machine Learning-Based Classification of Human Behaviors,” *Sensors*, vol. 22, no. 1721, pp. 1–15, 2022.

[78] M. Muaaz, A. Chelli, M. W. Gerdes, and M. Pätzold, “Wi-Sense: a passive human activity recognition system using Wi-Fi and convolutional neural network and its integration in health information systems,” *Ann. des Telecommun. Telecommun.*, vol. 77, no. 3-4, pp. 163–175, 2022.

[79] Z. K. Senturk and R. Kara, “Breast Cancer Diagnosis Via Data Mining: Performance Analysis of Seven Different Algorithms,” *Comput. Sci. Eng. An Int. J.*, vol. 4, no. 1, pp. 35–46, feb 2014. [Online]. Available: http://www.airccse.org/journal/cseij/papers/4114cseij04.pdf

[80] Y. LeCun, L. Bottou, Y. Bengio, and P. Haffner, “Gradient-based learning applied to document recognition,” *Proc. IEEE*, vol. 86, no. 11, pp. 2278–2323, 1998.

[81] S. Zhang, Z. Wei, J. Nie, L. Huang, S. Wang, and Z. Li, “A Review on Human Activity Recognition Using Vision-Based Method,” *J. Healthc. Eng.*, vol. 2017, 2017.

[82] A. Choi, T. H. Kim, O. Yuhai, S. Jeong, K. Kim, H. Kim, and J. H. Mun, “Deep Learning-Based Near-Fall Detection Algorithm for Fall Risk Monitoring System Using a Single Inertial Measurement Unit,” *IEEE Trans. Neural Syst. Rehabil. Eng.*, vol. 30, pp. 2385–2394, 2022.

[83] R. Tanwar, N. Nandal, M. Zamani, and A. A. Manaf, “Pathway of Trends and Technologies in Fall Detection: A Systematic Review,” *Healthc.*, vol. 10, no. 1, pp. 1–27, 2022.

[84] H. C. Kumawat and A. A. B. Raj, “SP-WVD with Adaptive-Filter-Bank-Supported RF Sensor for Low RCS Targets’ Nonlinear Micro-Doppler Signature/Pattern Imaging System,” *Sensors*, vol. 22, no. 3, 2022.

[85] M. E. Bayrakdar, “Priority based health data monitoring with IEEE 802.11af technology in wireless medical sensor networks,” *Med. Biol. Eng. Comput.*, vol. 57, no. 12, pp. 2757–2769, 2019.

[86] H. Jiang, C. Cai, X. Ma, Y. Yang, and J. Liu, “Smart Home Based on WiFi Sensing: A Survey,” *IEEE Access*, vol. 6, pp. 13 317–13 325, 2018.

[87] Y. Ma, G. Zhou, and S. Wang, “WiFi sensing with channel state information: A survey,” *ACM Comput. Surv.*, vol. 52, no. 3, 2019.

[88] B. Tan, Q. Chen, K. Chetty, K. Woodbridge, W. Li, and R. Piechocki, “Exploiting WiFi Channel State Information for Residential Healthcare Informatics,” *IEEE Commun. Mag.*, vol. 56, no. 5, pp. 130–137, 2018.

[89] J. Wu, J. Wang, A. Zhan, and C. Wu, “Fall detection with cnn-casual lstm network,” *Inf.*, vol. 12, no. 10, 2021.

[90] D. Akgün, A. T. Kabakuş, Z. Karapinar Şentürk, A. Şentürk, and E. Küçükkülahli, “A transfer learning-based deep learning approach for automated COVID-19 diagnosis with audio data,” *Turkish J. Electr. Eng. Comput. Sci.*, vol. 29, no. 8, pp. 2807–2823, 2021.

[91] F. J. Ordóñez and D. Roggen, “Deep convolutional and LSTM recurrent neural networks for multimodal wearable activity recognition,” *Sensors (Switzerland)*, vol. 16, no. 1, 2016.

[92] T. Nakamura, M. Bouazizi, K. Yamamoto, and T. Ohtsuki, “Wi-Fi-CSI-based Fall Detection by Spectrogram Analysis with CNN,” *2020 IEEE Glob. Commun. Conf. GLOBECOM 2020 - Proc.*, 2020.

[93] S. Chen, W. Yang, Y. Xu, Y. Geng, B. Xin, and L. Huang, “Afall: Wi-fi-based device-free fall detection system using spatial angle of arrival,” *IEEE Transactions on Mobile Computing*, vol. 22, no. 8, pp. 4471–4484, 2023.

[94] P. Krishnan, “Design of Collision Detection System for Smart Car Using Li-Fi and Ultrasonic Sensor,” *IEEE Trans. Veh. Technol.*, vol. 67, no. 12, pp. 11 420–11 426, 2018.

[95] S. Mita, X. Yuquan, K. Ishimaru, and S. Nishino, “Robust 3D perception for any environment and any weather condition using thermal

stereo," *IEEE Intell. Veh. Symp. Proc.*, vol. 2019-June, no. Iv, pp. 2569–2574, 2019.

[96] A. Zhang, M. L. Rahman, X. Huang, Y. J. Guo, S. Chen, and R. W. Heath, "Perceptive Mobile Networks: Cellular Networks with Radio Vision via Joint Communication and Radar Sensing," *IEEE Veh. Technol. Mag.*, vol. 16, no. 2, pp. 20–30, 2021.

[97] R. C. Daniels, E. R. Yeh, and R. W. Heath, "Forward Collision Vehicular Radar with IEEE 802.11: Feasibility Demonstration Through Measurements," *IEEE Trans. Veh. Technol.*, vol. 67, no. 2, pp. 1404–1416, 2018.

[98] D. Cong, S. Guo, S. Dang, and H. Zhang, "Vehicular Behavior-Aware Beamforming Design for Integrated Sensing and Communication Systems," *IEEE Trans. Intell. Transp. Syst.*, pp. 1–13, 2023.

[99] J. Fang, H. Meng, H. Zhang, and X. Wang, "A low-cost vehicle detection and classification system based on unmodulated continuous-wave radar," *IEEE Conf. Intell. Transp. Syst. Proceedings, ITSC*, no. September 2007, pp. 715–720, 2007.

[100] C. A. Gutiérrez, W. Harrison, M. Rice, B. Jensen, K. Norman, B. Redd, A. Twitchell, and M. Cardenas-Juarez, "Envelope distribution and Doppler spectrum of V2V channels at 5.9 GHz in mountainous roads," *Veh. Commun.*, vol. 39, p. 100570, 2023. [Online]. Available: https://doi.org/10.1016/j.vehcom.2022.100570

[101] B. Tian, G. Wang, Z. Xu, Y. Zhang, and X. Zhao, "Communication delay compensation for string stability of CACC system using LSTM prediction," *Veh. Commun.*, vol. 29, p. 100333, 2021. [Online]. Available: https://doi.org/10.1016/j.vehcom.2021.100333

[102] S. Jeong, B. Jeon, B. Chung, and H. K. Kim, "Convolutional neural network-based intrusion detection system for AVTP streams in automotive Ethernet-based networks," *Veh. Commun.*, vol. 29, p. 100338, 2021. [Online]. Available: https://doi.org/10.1016/j.vehcom.2021.100338

[103] Y. Lu, L. Zhang, and W. Xie, "YOLO-compact: An Efficient YOLO Network for Single Category Real-time Object Detection," *Proc. 32nd Chinese Control Decis. Conf. CCDC 2020*, pp. 1931–1936, 2020.

[104] A. A. Gonzalez, "Implementation of an FPGA Hardware Accelerator for a Moving Object Detection Model (YOLOv4)," Ph.D. dissertation, Autonomous University of San Luis Potosi, 2021.

[105] W. Liu and Y. Shoji, “DeepVM: RNN-Based Vehicle Mobility Prediction to Support Intelligent Vehicle Applications,” *IEEE Trans. Ind. Informatics*, vol. 16, no. 6, pp. 3997–4006, 2020.

[106] A. Miglani and N. Kumar, “Deep learning models for traffic flow prediction in autonomous vehicles: A review, solutions, and challenges,” *Veh. Commun.*, vol. 20, p. 100184, 2019. [Online]. Available: https://doi.org/10.1016/j.vehcom.2019.100184

[107] L. Lin, W. Li, H. Bi, and L. Qin, “Vehicle Trajectory Prediction Using LSTMs With Spatial–Temporal Attention Mechanisms,” *IEEE Intell. Transp. Syst. Mag.*, vol. 14, no. 2, pp. 197–208, mar 2022. [Online]. Available: https://ieeexplore.ieee.org/document/9349962/

[108] M. Won, S. Zhang, and S. H. Son, “WiTraffic: Low-cost and non-intrusive traffic monitoring system using WiFi,” *2017 26th Int. Conf. Comput. Commun. Networks, ICCCN 2017*, 2017.

[109] Q. Jiang, L. Zhang, and D. Meng, “Target Detection Algorithm Based on MMW Radar and Camera Fusion,” in *2019 IEEE Intell. Transp. Syst. Conf.*, vol. PartF16898. Auckland, New Zealand: IEEE, 2019, pp. 1–6. [Online]. Available: https://ieeexplore.ieee.org/document/8917504/

[110] R. Wolfe, B., Seppelt, B., Mehler, B., Reimer, B., & Rosenholtz, “Rapid holistic perception and evasion of road hazards,” *J. Exp. Psychol.*, vol. 149, no. 3, pp. 490–500, 2020.

[111] P. Papadimitratos, A. D. L. Fortelle, K. Evenssen, R. Brignolo, and S. Cosenza, “Vehicular communication systems: Enabling technologies, applications, and future outlook on intelligent transportation,” vol. 47, no. 11, pp. 84–95, Nov. 2009.

[112] G. Dimitrakopoulos and P. Demestichas, “Intelligent transportation systems: Systems based on cognitive networking principles and management functionality,” vol. 5, no. 1, pp. 77–84, 2010.

[113] J. B. Kenney, “Dedicated short-range communications (DSRC) standards in the United States,” vol. 99, no. 7, pp. 1162–1182, Jul. 2011.

[114] G. Karagiannis, O. Altintas, E. Ekici, G. Heijenk, B. Jarupan, K. Lin, and T. Weil, “Vehicular networking: A survey and tutorial on requirements, architectures, challenges, standards and solutions,” vol. 13, no. 4, pp. 584–616, Fourth 2011.

[115] G. Rafiq, B. Talha, M. Patzold, J. G. Luis, G. Ripa, I. Carreras, C. Coviello, S. Marzorati, G. P. Rodriguez, G. Herrero, and M. Desaeger, “What’s new in intelligent transportation systems?: An

overview of European projects and initiatives," vol. 8, no. 4, pp. 45–69, Dec. 2013.

[116] T. G. McGiffen, S. Beiker, and A. Paulraj, "Motivating network deployment: Vehicular communications," vol. 12, no. 3, pp. 22–33, Sept. 2017.

[117] G. Naik, B. Choudhury, and J.-M. Park, "IEEE 802.11bd & 5G NR V2X: Evolution of radio access technologies for V2X communications," *IEEE Access*, vol. 7, pp. 70 169–70 184, 2019.

[118] Z. H. Mir, J. Toutouh, F. Filali, and Y.-B. Ko, "Enabling DSRC and C-V2X integrated hybrid vehicular networks: Architecture and protocol," *IEEE Access*, vol. 8, pp. 180 909–180 927, 2020.

[119] *IEEE Standard for Information Technology–Telecommunications and Information Exchange between Systems - Local and Metropolitan Area Networks–Specific Requirements - Part 11: Wireless LAN Medium Access Control (MAC) and Physical Layer (PHY) Specifications.* IEEE Std 802.11-2020 (Revision of IEEE Std 802.11-2016), 2021.

[120] *700 MHz Band Intelligent Transport Systems.* ARIB STD-T109, 2013.

[121] H. Seo, K. Lee, S. Yasukawa, Y. Peng, and P. Sartori, "LTE evolution for vehicle-to-everything services," vol. 54, no. 6, pp. 22–28, 2016.

[122] S. Chen, J. Hu, Y. Shi, Y. Peng, J. Fang, R. Zhao, and L. Zhao, "Vehicle-to-everything (V2X) services supported by LTE-based systems and 5G," *IEEE Commun. Standards Mag.*, vol. 1, no. 2, pp. 70–76, 2017.

[123] *3rd Generation Partnership Project; Technical Specification Group Services and System Aspects; Release 14 Description; Summary of Rel-14 Work Items (Release 14).* 3GPP TR 21.914 V14.0.0 (2018-05) , 2018.

[124] *3rd Generation Partnership Project; Technical Specification Group Services and System Aspects; Release 16 Description; Summary of Rel-16 Work Items (Release 16) .* 3GPP TR 21.916 V0.4.0 (2020-03), 2019.

[125] J. Gozalvez, M. Sepulcre, and R. Bauza, "Impact of the radio channel modelling on the performance of VANET communication protocols," *Telecommun. Syst.*, vol. 50, no. 3, pp. 149–167, Jul. 2012.

[126] C. Mecklenbräuker, A. Molisch, J. Karedal, F. Tufvesson, A. Paier, L. Bernadó, T. Zemen, O. Klemp, and N. Czink, "Vehicular channel characterization and its implications for wireless system design and performance," vol. 99, no. 7, pp. 1189–1212, Jul. 2011.

[127] J. A. Fernandez, K. Borries, L. Cheng, B. V. K. Vijaya Kumar, D. D. Stancil, and F. Bai, “Performance of the 802.11p physical layer in vehicle-to-vehicle environments,” vol. 61, no. 1, pp. 3–14, 2012.

[128] Y. M. Khattabi and M. M. Matalgah, “Alamouti-OSTBC wireless cooperative networks with mobile nodes and imperfect CSI estimation,” vol. 67, no. 4, pp. 3447–3456, 2018.

[129] L. Hu, H. Wang, and Y. Zhao, “Performance analysis of DSRC-based vehicular safety communication in imperfect channels,” *IEEE Access*, vol. 8, pp. 107 399–107 408, 2020.

[130] S. Yadav and A. Pandey, “Secrecy performance of cognitive vehicular radio networks: Joint impact of nodes mobility and imperfect channel estimates,” in *2020 IEEE International Black Sea Conference on Communications and Networking (BlackSeaCom)*, 2020, pp. 1–7.

[131] J. J. Jaime-Rodríguez, C. A. Gómez-Vega, C. A. Gutiérrez, J. M. Luna-Rivera, D. U. Campos-Delgado, and R. Velázquez, “A non-WSSUS channel simulator for V2X communication systems,” *Electronics*, vol. 9, no. 8, pp. 1–25, 2020.

[132] S. Bolufé, C. A. Azurdia-Meza, S. Céspedes, S. Montejo-Sánchez, R. D. Souza, and E. M. G. Fernandez, “POSACC: Position-accuracy based adaptive beaconing algorithm for cooperative vehicular safety systems,” *IEEE Access*, vol. 8, pp. 15 484–15 501, 2020.

[133] E. Meesa-ard and S. Pattaramalai, “Evaluating the mobility impact on the performance of heterogeneous wireless networks over η-μ fading channels,” *IEEE Access*, pp. 1–16, 2021, to appear.

[134] Y. Alghorani, G. Kaddoum, S. Muhaidat, S. Pierre, and N. Al-Dhahir, “On the performance of multihop-intervehicular communications systems over n*Rayleigh fading channels,” vol. 5, no. 2, pp. 116–119, 2016.

[135] C. A. Gutiérrez, J. J. Jaime-Rodríguez, J. M. Luna-Rivera, D. U. Campos-Delgado, and J. Vázquez Castillo, “Modeling of non-WSSUS double-Rayleigh fading channels for vehicular communications,” *Wireless Communications and Mobile Computing*, vol. 2017, pp. 1–15, 2017.

[136] A. Pandey and S. Yadav, “Joint impact of nodes mobility and imperfect channel estimates on the secrecy performance of cognitive radio vehicular networks over Nakagami-m fading channels,” *IEEE Open J. Veh. Technol.*, vol. 2, pp. 289–309, 2021.

[137] P. Almers, E. Bonek, A. Burr, N. Czink, M. Debbah, V. Degli-Esposti, H. Hofstetter, D. L. P. Kyösti, G. Matz, A. F. Molisch, C. Oestges,

and H. Özcelik, “Survey of channel and radio propagation models for wireless MIMO systems,” *EURASIP J. Wireless Commun. and Netw.*, vol. 2007, no. 1, pp. 1–19, Feb. 2007.

[138] D. W. Matolak, “Modeling the vehicle-to-vehicle propagation channel: A review,” *Radio Science*, vol. 49, no. 9, pp. 721–736, Sept 2014.

[139] M. Boban, J. Barros, and O. K. Tonguz, “Geometry-based vehicle-to-vehicle channel modeling for large-scale simulation,” vol. 63, no. 9, pp. 4146–4164, Nov. 2014.

[140] A. Molisch, F. Tufvesson, J. Karedal, and C. Mecklenbräuker, “A survey on vehicle-to-vehicle propagation channels,” vol. 16, no. 6, pp. 12–22, Dec. 2009.

[141] Y. Ma, L. Yang, and X. Zheng, “A geometry-based non-stationary MIMO channel model for vehicular communications,” *China Communications*, vol. 15, no. 7, pp. 30–38, Jul. 2018.

[142] C. A. Gutiérrez, J. T. Gutiérrez-Mena, J. M. Luna-Rivera, D. U. Campos-Delgado, R. Velázquez, and M. Pätzold, “Geometry-based statistical modeling of non-WSSUS mobile-to-mobile Rayleigh fading channels,” vol. 67, no. 1, pp. 362–377, Jan. 2018.

[143] W. Dahech, M. Pätzold, C. A. Gutiérrez, and N. Youssef, “A non-stationary mobile-to-mobile channel model allowing for velocity and trajectory variations of the mobile stations,” vol. 16, no. 3, pp. 1987–2000, March 2017.

[144] K. Jiang, X. Chen, Q. Zhu, L. Chen, D. Xu, and B. Chen, “A novel simulation model for nonstationary Rice fading channels,” *Wireless Communications and Mobile Computing*, vol. 2018, pp. 1–9, 2018.

[145] S. Imbert, X. Leturc, and C. J. LeMartret, “On the simulation of correlated mobile-to-mobile fading channels for time-varying velocities,” in *Proc. 2018 International Conference on Military Communications and Information Systems (ICMCIS 2018)*, Warsaw, Poland, May 2018, pp. 1–8.

[146] Z. Xu, L. Bernadó, M. Gan, M. Hofer, T. Abbas, V. Shivaldova, K. Mahler, D. Smely, and T. Zemen, “Relaying for IEEE 802.11p at road intersection using a vehicular non-stationary channel model,” in *Proc. 2014 IEEE 6th International Symposium on Wireless Vehicular Communications (WiVeC 2014)*, Sep. 2014, pp. 1–6.

[147] P. Paschalidis, J. Nuckelt, K. Mahler, M. Peter, A. Kortke, M. Wisotzki, W. Keusgen, and T. Kürner, “Investigation of MPC

correlation and angular characteristics in the vehicular urban intersection channel using channel sounding and ray tracing," vol. 65, no. 8, pp. 5874–5886, 2016.

[148] C. Mecklenbräuker, A. Molisch, J. Karedal, F. Tufvesson, A. Paier, L. Bernadó, T. Zemen, O. Klemp, and N. Czink, "Vehicular channel characterization and its implications for wireless system design and performance," vol. 99, no. 7, pp. 1189–1212, Jul. 2011.

[149] K. Mahler, W. Keusgen, F. Tufvesson, T. Zemen, and G. Caire, "Measurement-based wideband analysis of dynamic multipath propagation in vehicular communication scenarios," vol. 66, no. 6, pp. 4657–4667, 2017.

[150] T. Abbas, J. Nuckelt, T. Kürner, T. Zemen, C. F. Mecklenbräuker, and F. Tufvesson, "Simulation and measurement-based vehicle-to-vehicle channel characterization: Accuracy and constraint analysis," vol. 63, no. 7, pp. 3208–3218, July 2015.

[151] K. Mahler, P. Paschalidis, A. Kortke, M. Peter, and W. Keusgen, "Realistic IEEE 802.11p transmission simulations based on channel sounder measurement data," in *Proc. 2013 IEEE 78th Vehicular Technology Conference (VTC Fall)*, 2013, pp. 1–5.

[152] F. Talebi and T. Pratt, "Channel sounding and parameter estimation for a wideband correlation-based MIMO model," vol. 65, no. 2, pp. 499–508, 2016.

[153] S. Salous, *Radio Propagation Measurement and Channel Modeling*, 1st ed. John Wiley and Sons, 2013.

[154] N. Costa and S. Haykin, *Multiple-Input Multiple-Output Channel Models: Theory and Practice*, 1st ed. John Wiley and Sons, 2010.

[155] B. Sklar, "Rayleigh fading channels in mobile digital communication systems. I. characterization," vol. 35, no. 7, pp. 90–100, Jul 1997.

[156] L. Bernadó, T. Zemen, F. Tufvesson, A. Molisch, and C. F. Mecklenbräuker, "Delay and doppler spreads of nonstationary vehicular channels for safety-relevant scenarios," vol. 63, no. 1, pp. 82–93, Jan. 2014.

[157] ——, "The (in)validity of the WSSUS assumption in vehicular radio channels," in *Proc. 23rd IEEE International Symposium on Personal, Indoor, and Mobile Radio Communications (PIMRC'12)*, Sidney, Australia, Sep. 2012, pp. 1757–1762.

[158] M. Rice, W. Harrison, B. Jensen, K. Norman, B. Wood, and C. A. Gutiérrez, "V2V propagation in mountainous terrain: Part

I—Experimental configuration and measurement results," in *2019 IEEE Latin-American Conference on Communications (LATINCOM)*, 2019, pp. 1–6.

[159] C. A. Gutiérrez, W. Harrison, and M. Rice, "V2V propagation in mountainous terrain: Part II—Modeling results," in *Proc. 2019 IEEE Latin-American Conference on Communications (LATINCOM)*, 2019, pp. 1–6.

[160] H. Fernández, L. Rubio, V. M. Rodrigo-Peñarrocha, and J. Reig, "Path loss characterization for vehicular communications at 700 MHz and 5.9 GHz under LOS and NLOS conditions," vol. 13, pp. 931–934, 2014.

[161] C. A. Gómez-Vega, C. A. Gutiérrez, J. J. Jaime-Rodríguez, J. Vázquez Castillo, D. U. Campos-Delgado, J. M. Luna-Rivera, and M. A. Díaz-Ibarra, "Doppler spectrum measurements of vehicular radio channels using a narrowband sounder," *Revista Facultad de Ingeniería Universidad de Antioquia*, pp. 32 – 40, 12 2019.

[162] A. Paier, J. Karedal, N. Czink, H. Hofstetter, C. Dumard, T. Zemen, F. Tufvesson, A. F. Molisch, and C. F. Mecklenbräuker, "Car-to-car radio channel measurements at 5 GHz: Pathloss, power-delay profile, and delay-Doppler spectrum," in *Proc. 2007 4th International Symposium on Wireless Communication Systems*, Oct. 2007, pp. 224–228.

[163] A. Paier, L. Bernadó, J. Karedal, O. Klemp, and A. Kwoczek, "Overview of vehicle-to-vehicle radio channel measurements for collision avoidance applications," in *Proc. 2010 IEEE 71st Vehicular Technology Conference*, May 2010, pp. 1–5.

[164] *IEEE Standard for Information technology– Local and metropolitan area networks– Specific requirements– Part 11: Wireless LAN Medium Access Control (MAC) and Physical Layer (PHY) Specifications Amendment 6: Wireless Access in Vehicular Environments.* IEEE Std 802.11-2007 (Revision of IEEE Std 802.11-1999), 2010.

[165] R. Sevlian, C. Chun, I. Tan, A. Bahai, and K. Laberteaux, "Channel characterization for 700 MHz DSRC vehicular communication," *Journal of Electrical and Computer Engineering*, vol. 2010, pp. 1–9, 2010.

[166] L. Cheng, B. Henty, D. D. Stancil, F. Bai, and P. Mudalige, "A fully mobile, GPS enabled, vehicle-to-vehicle measurement platform for characterization of the 5.9 GHz DSRC channel," in *Proc. 2007 IEEE Antennas and Propagation Society International Symposium*, June 2007, pp. 2005–2008.

[167] L. Cheng, B. E. Henty, D. D. Stancil, F. Bai, and P. Mudalige, "Mobile vehicle-to-vehicle narrow-band channel measurement and characterization of the 5.9 GHz dedicated short range communication (DSRC) frequency band," vol. 25, no. 8, pp. 1501–1516, 2007.

[168] Y. Shmaliy, *Continuous-Time Systems.* Dordrecht, The Netherlands: Springer, 2007.

[169] J. S. Bendat and A. G. Piersol, *Random Data Analysis and Measurement Procedures*, 3rd ed. New York: John Wiley and Sons, 2000.

[170] M. Pätzold, *Mobile Radio Channels*, 2nd ed. Chichester, UK: John Wiley and Sons, 2011.

[171] P. H. Bello, "Characterization of randomly time-variant linear channels," vol. 11, no. 4, pp. 360–393, Dec. 1963.

[172] G. Matz, "On non-WSSUS wireless fading channels," *IEEE Trans. Wireless Commun.*, vol. 4, no. 5, pp. 2465–2478, Sep. 2005.

[173] M. Z. Win and R. A. Scholtz, "Impulse radio: How it works," vol. 2, no. 2, pp. 36–38, Feb. 1998.

[174] ——, "Ultra-wide bandwidth time-hopping spread-spectrum impulse radio for wireless multiple-access communications," vol. 48, no. 4, pp. 679–691, Apr. 2000.

[175] D. Cassioli, M. Z. Win, and A. F. Molisch, "The ultra-wide bandwidth indoor channel: From statistical model to simulations," vol. 20, no. 6, pp. 1247–1257, Aug. 2002.

[176] M. Z. Win and R. A. Scholtz, "Characterization of ultra-wide bandwidth wireless indoor communications channel: A communication-theoretic view," vol. 20, no. 9, pp. 1613–1627, Dec. 2002.

[177] M. Chiani, A. Conti, and O. Andrisano, "Outage evaluation for slow frequency hopping mobile radio systems," vol. 47, no. 12, pp. 1865–1874, Dec. 1999.

[178] H. Schulze and C. Lüders, *Theory and Applications of OFDM and CDMA Wideband Wireless Communications.* Chichester, England: John Wiley and Sons, 2005.

[179] F. Zabini, B. M. Masini, A. Conti, and L. Hanzo, "Partial equalization for MC-CDMA systems in non-ideally estimated correlated fading," vol. 59, no. 8, pp. 3818–3830, Oct. 2010.

[180] A. Conti, B. M. Masini, F. Zabini, and O. Andrisano, "On the downlink performance of multi-carrier CDMA systems with partial equalization," vol. 6, no. 1, pp. 230–239, Jan. 2007.

[181] M. Chiani, A. Conti, and C. Fontana, "Improved performance in TD-CDMA mobile radio system by optimizing energy partition in channel estimation," vol. 51, no. 3, pp. 352–355, Mar. 2003.

[182] E. Salazar, C. A. Azurdia-Meza, D. Zabala-Blanco, S. Bolufé, and I. Soto, "Semi-supervised extreme learning machine channel estimator and equalizer for vehicle to vehicle communications," *Electronics*, vol. 10, no. 8, 2021.

[183] A. Conti, M. Z. Win, and M. Chiani, "Slow adaptive M-QAM with diversity in fast fading and shadowing," vol. 55, no. 5, pp. 895–905, May 2007.

[184] L. Toni and A. Conti, "Does fast adaptive modulation always outperform slow adaptive modulation?" vol. 10, no. 5, pp. 1504–1513, May 2011.

[185] M. Pätzold and N. Youssef, "Spectrogram analysis of multipath fading channels," in *Proc. 2015 IEEE 26th Annual Int. Symposium on Personal, Indoor, and Mobile Radio Communications PIMRC (2015)*, Sep. 2015, pp. 2214–2219.

[186] C. A. Gutiérrez *et al.*, "Doppler shift characterization of wideband mobile radio channels," *IEEE Trans. Veh. Technol.*, vol. 68, no. 12, pp. 12 375–12 380, Dec. 2019.

[187] C. A. Hammerschmidt, R. T. Johnk, P. M. McKenna, and C. R. Anderson, *Best Practices for Radio Propagation Measurements.* NTIA Technical Memorandum TM-19-535, 2018.

[188] *Keysight N9310A Signal Generator*, 3rd ed., Keysight Technologies, Chengdu, China, 2014.

[189] *Keysight FieldFox Analyzers: User's Guide*, 4th ed., Keysight Technologies, Santa Rosa, CA, 2017.